On the Fundamentals of Stochastic Spatial Modeling and Analysis of Wireless Networks and its Impact to Channel Losses

Mouhamed Abdulla

A Thesis

in

The Department

of

Electrical and Computer Engineering

Presented in Partial Fulfillment of the Requirements

for the Degree of Doctor of Philosophy at

Concordia University

Montréal, Québec, Canada

September, 2012

CONCORDIA UNIVERSITY

SCHOOL OF GRADUATE STUDIES

This is to certify that the thesis prepared

By: **Mouhamed Abdulla**

Entitled: **On the Fundamentals of Stochastic Spatial Modeling and Analysis of Wireless Networks and its Impact to Channel Losses**

and submitted in partial fulfillment of the requirements for the degree of

DOCTOR OF PHILOSOPHY (Electrical & Computer Engineering)

complies with the regulations of the University and meets the accepted standards with respect to originality and quality.

Signed by the final examining committee:

_____ Chair
Dr. D. Dysart-Gale

_____ External Examiner
Dr. B. Champagne

_____ External to Program
Dr. J. Dargahi

_____ Examiner
Dr. A.K. Elhakeem

_____ Examiner
Dr. W. Hamouda

_____ Thesis Supervisor
Dr. Y.R. Shayan

Approved by _____
Dr. J.X. Zhang, Graduate Program Director

September 12, 2012

_____
Dr. Robin A.L. Drew, Dean
Faculty of Engineering and Computer Science

Abstract

On the Fundamentals of Stochastic Spatial Modeling and Analysis of Wireless Networks and its Impact to Channel Losses

Mouhamed Abdulla, Ph.D.
Concordia University, 2012

With the rapid evolution of wireless networking, it becomes vital to ensure transmission reliability, enhanced connectivity, and efficient resource utilization. One possible pathway for gaining insight into these critical requirements would be to explore the spatial geometry of the network. However, tractably characterizing the actual position of nodes for large wireless networks (LWNs) is technically unfeasible. Thus, stochastical spatial modeling is commonly considered for emulating the random pattern of mobile users. As a result, the concept of random geometry is gaining attention in the field of cellular systems in order to analytically extract hidden features and properties useful for assessing the performance of networks.

Meanwhile, the large-scale fading between interacting nodes is the most fundamental element in radio communications, responsible for weakening the propagation, and thus worsening the service quality. Given the importance of channel losses in general, and the inevitability of random networks in real-life situations, it was then natural to merge these two paradigms together in order to obtain an improved stochastical model for the large-scale fading. Therefore, in exact closed-form notation, we generically derived the large-scale fading distributions between a reference base-station and an arbitrary node for uni-cellular (UCN), multi-cellular (MCN), and Gaussian random network models. In fact, we for the first time provided explicit formulations that considered at once: the lattice profile, the users' random geometry, the spatial intensity, the effect of the far-field phenomenon, the path-loss behavior, and the stochastic impact of channel scatters. Overall, the results can be useful for analyzing and designing LWNs through the evaluation of performance indicators.

Moreover, we conceptualized a straightforward and flexible approach for random spatial inhomogeneity by proposing the area-specific deployment (ASD) principle, which takes into account the clustering tendency of users. In fact, the ASD method has the advantage of achieving a more realistic deployment based on limited planning inputs, while still preserving the stochastic character of users' position. We then applied this inhomogeneous technique to different circumstances, and thus developed three spatial-level network simulator algorithms for: controlled/uncontrolled UCN, and MCN deployments.

Keywords: Cellular Systems, Network Planning, Network Modeling, Spatial Deployment, Random Geometry, Stochastical Inference, Channel Propagation, Large-Scale Fading, Network Performance, Random Generation, and Monte Carlo Simulations.

This doctoral dissertation is dedicated to:

My Mother: (*Houda*)	*All that I am today would have never happened if it were not for your affection, dedication, effort, and guidance. Mom, you are my heart, my genuine love, and my moral compass in life.*
My Brother: (*Ahmed*)	*You are my mentor, my role model, my best friend, and above all you are my oxygen. Bro, I love you more than words or actions can ever demonstrate.*
The Soul of My Father: (*Prof./Dr. Abdul Baki Abdulla*)	*It has been more than 20yrs that you have left us, yet my love, admiration, and respect for you has never faded because your legacy continues to inspire. I hope your sons will always make you proud. R.I.P. Dad.*

Acknowledgments

Sir Isaac Newton was absolutely right when he famously said that *If I have seen further, it is by standing on the shoulders of giants*. And so, I am forever indebted to all the giants who were a source of inspiration and support during the course of my research work.

First of all, I would like to express my utmost gratitude to my advisor, Prof. Yousef R. Shayan, for his guidance, encouragements, patience, and wisdom. I am also very grateful for the external examiner Prof. Benoît Champagne from McGill University who agreed to participate and took the necessary time to read and assess my dissertation; his suggestions were considerably helpful in reorganizing and refining the structure of the dissertation. Also, I would like to thank my committee members: Prof. Ahmed Elhakeem, Prof. Walaa Hamouda, and Prof. Javad Dargahi, for their constructive insight in order to make the dissemination of my research results more lucid and informative. Moreover, I am grateful to Prof. Ali Ghrayeb, Prof. Reza Soleymani, and Prof. Rajamohan Ganesan for their feedback during earlier versions of this treatment. On the whole, I am more than fortunate to have had the opportunity to interact and learn from these highly regarded scholars.

Furthermore, I am very thankful to Pamela Fox, the ECE Coordinator for Graduate Programs, and Sharon Carey from the School of Graduate Studies. They were both phenomenal for untiredly answering my logistical questions while at the same time keeping a pleasant smile.

Last, but definitively not least, I would like to thank my mother and my brother for believing in me and for always being there when I needed them the most. To me, these two individual represent everything that is good in life.

Mouhamed Abdulla

Montréal, Québec, Canada

Table of Contents

List of Figures

List of Tables

List of Symbols

Functions and Operators

$\mathbf{1}_A(x), \mathbf{1}_A(x,y)$	1D and 2D indicator functions, where unity is the case when $x \in A \subseteq \mathbb{R}$ and $(x,y) \in A \subseteq \mathbb{R}^2$
$Binomial(x,n,p)$	binomial probability mass function for getting x successes in n trials, where each successful event has probability p
$\mathrm{E}[\blacksquare], \langle \blacksquare \rangle$	statistical expectation and averaging operators
$erf(x)$	error function
$erfc(x)$	complementary error function
$\inf_{x \in A}\{f(x)\}$	optimization operator that determines the infimum of the input function $f(x)$ over $x \in A$
$\mathbf{I}_n$	identity matrix of size n
$J(r,\theta)$	2D Jacobian matrix in polar notation
$\max_{x \in A}\{f(x)\}$	optimization operator that determines the maximum of the input function $f(x)$ over $x \in A$
$\min_{x \in A}\{f(x)\}$	optimization operator that determines the minimum of the input function $f(x)$ over $x \in A$
$a \bmod b$	modulo operator used to obtain the remainder of the rational number a/b
$\mathcal{N}(m, \sigma^2)$	Gaussian density function with mean $m \in \mathbb{R}$ and standard deviation $\sigma \in \mathbb{R}_+^*$
$\mathcal{N}(\boldsymbol{m}, \boldsymbol{\Sigma})$	multivariate Gaussian density function with mean vector $\boldsymbol{m} \in \mathbb{R}^k$ and covariance matrix $\boldsymbol{\Sigma} \in \mathbb{R}^{k \times k}$, $k \in \mathbb{N}^*$
$O(\blacksquare)$	big-O notation for assessing the growth rate

$\Pr\{x \in D\}$	probability measure for the input argument
$Q(x)$	Q-function, which is a variation of the error function
$Rayleigh(\sigma)$	Rayleigh density function with parameter $\sigma \in \mathbb{R}_+^*$
$\vec{x}_{sorted} = \text{sort}(\vec{x})$	algorithm that sorts the input vector $\vec{x} \in \mathbb{R}^k$, $k = 2,3,\cdots$ in ascending order
$\sup_{x \in A}\{f(x)\}$	optimization operator that determines the supremum of the input function $f(x)$ over $x \in A$
$T_{cost}(\blacksquare)$	worst case computational time complexity of an algorithm
$\mathcal{U}(a,b)$	continuous uniform density function bounded by $[a,b] \in \mathbb{R}^2$
$\mathcal{U}_D(n_1,n_2)$	discrete uniform distribution function bounded by $[n_1,n_2] \in \mathbb{Z}^2$

Geometrical Analysis

α_1, α_2	angular limits of a circular ring sector (rad)
β_d	distribution index for achieving an inhomogeneous spatial network
γ	largest number of sectors in a particular UCN layer
Δ_i	width of the i-th deployment layer for automatic emulation of heterogeneous UCN (unit of length)
Δ_L	width of a circular ring (unit of length)
θ	angular coordinate for polar notation (rad)
$\Theta = \left[\theta_{(i,j)}\right]_{\substack{i=1,2,\cdots,n_L \\ j=1,2,\cdots,n_{\text{sec}}^{(i)}-1}}$	clusters angular matrix for heterogeneous random deployment of a UCN
μ	cellular radius to the close-in distance ratio (RCR)
ρ_0, ρ_A	areal number density of a random network (no./unit of area)
σ_G	spatial intensity of a Gaussian random network

ϕ	cluster network rotation angle (rad)
$\phi_{(l,j)}$	rotation angle of a random cluster for MCN modeling
χ	set of arguments for the infimum of $f_X(x)$
A_0, A_N	surface area of a network lattice (unit of area)
A_{FF}	deployment area that takes into consideration the effect of far-field for large-scale fading analysis (unit of area)
A_G	gap area created by adjacently positioned cells (unit of area)
A_H, A_R, A_T	random network deployment area for hexagonal, rhombus, and triangular lattice shapes (unit of area)
A_{RS}	deployment area of a network cluster for a circular ring sector (unit of area)
dA	infinitesimal area element
d_{BS}	separation distance between adjacent base-stations (unit of length)
D_{FF}, D_{FF}^P	support domain for the deployment surface with the impact of far-field in Cartesian and polar formats
D_H, D_R, D_T	support domain for the deployment surface over hexagonal, rhombus, and triangular lattice shapes
D_{RS}, D_{RS}^P	support domain for the deployment surface over a circular ring sector in Cartesian and polar formats
D^T	truncated deployment surface support for a Gaussian network
D_X, D_{XY}	1D and 2D domain of the marginal/joint probability density function
D_i, A_i, n_i, ρ_i	support domain, surface area, quantity of nodes, and number density of the i-th ASD sub-region
$f_{XY}(x, y)$	spatial density function of a network cluster in Cartesian coordinate system
$f_{XY}^T(x, y)$	truncated spatial density function of a network cluster
$f_X(x), F_X(x)$	marginal probability density, and its cumulative distribution function for random network geometry along the *x*-axis

$f_X^{\max}$	maximum value of the marginal probability density function along the *x*-axis
$f_{Y\|X=\hat{x}}(y)$	conditional probability density function of a random network along the *y*-axis
$f_{R\theta}(r,\theta)$	joint polar probability density function of a random network
$f_R(r), F_R(r)$	internodal distance density, and its cumulative distribution function
$f_R^T(r), F_R^T(r)$	truncated internodal distance density, and its cumulative distribution function
$f_R^{\max}$	maximum value of the radial probability density function
$f_\theta(\theta)$	angular probability density function of a random network
h_{AP}, h_{node}	elevation above ground of the access point/nodal antenna (unit of length)
(h_u, k_v)	centroid position of a cell with (u,v) indexing in a MCN grid
k_{FF}, k_{RS}	intensity of the homogeneous spatial density for MCN and UCN models
k_L	k_L-th UCN layer that contains the largest number of sectors
L	predefined size of the cellular radius (unit of length)
L_1, L_2	inner and outer cell radii of a circular ring sector (unit of length)
$\mathbf{L}=[u_i, v_i]_{i=1,2,\cdots,n_C}$	cellular location matrix for heterogeneous MCN deployment
n_0	amount of random nodes enclosed by a network lattice or cluster
n_{av}	average amount of nodes per deployment sector in an uncontrolled inhomogeneous UCN
n_C	number of cells for inhomogeneous MCN deployment
n_{in}	amount of random nodes deployed in the innermost layer of an automatically emulated inhomogeneous UCN
n_L	number of layers for inhomogeneous UCN deployment
$n_{L-\max}$	maximum arbitrary number of deployment layers possible for achieving spatial inhomogeneity

n_{out}	amount of random nodes deployed in the outer layers of an automatically emulated inhomogeneous UCN
$n_{\text{sec}}^{(i)}$	number of sectors within the i-th layer considered for inhomogeneous UCN deployment
$n_{\text{sec-total}}$	overall number of sectors considered in UCN and MCN deployment
$\mathbf{N}=\left[n_{(i,j)}\right]_{\substack{i=1,2,\cdots,n_L \\ j=1,2,\cdots,n_{\text{sec}}^{(i)}}}$	matrix for heterogeneous UCN deployment that contains the amount of randomly positioned nodes in each cluster
$\mathbf{P}=\left[p_{(i,j)}\right]_{\substack{i=1,2,\cdots,n_L \\ j=1,2,\cdots,2\gamma}}$	matrix of the network plan used for heterogeneous random deployment of a UCN
$\mathbf{P}_i, \tilde{\mathbf{P}}_i$	original and new position of a node within a random cluster
r	random sample of the interpoint distance (unit of length)
r_i	spatial gap between a reference and the $i \in \mathbb{N}^*$ arbitrary node (unit of length)
$\left(r_i, \theta_i\right)_{i=1,2,\cdots,n}$	coordinates of a random cluster in polar format
r_j	rate of nodal quantity per cellular sector
$r_{\max}$	farthest internodal separation between a master and a slave within a square cell (unit of length)
r_T	constant power transmission radius (unit of length)
$\mathbf{R}=\left[r_i\right]_{i=1,2,\cdots,n_L}$	layers radii for heterogeneous random deployment of a UCN
$\mathbf{R}_C$	rotation matrix for a random cluster
S, S_x, S_y	scaling factor of a random cluster
s_i	number of sectors within the i-th cell considered for inhomogeneous MCN deployment
$\mathbf{S}=\left[s_i\right]_{i=1,2,\cdots,n_C}$	sectors information array for MCN deployment
$\mathbf{S}_C$	scaling matrix for a random cluster

$\mathbf{T}_C = [h \quad k]$	translation vector for a random cluster (unit of length)^2
(x, y)	spatial instance of a node over the deployment lattice
(X, Y)	random variables representing the geometrical coordinate pair of a source node
$(x_i, y_i)_{i=1,2,\cdots,n}$	original coordinates of a random cluster
$(\tilde{x}_i, \tilde{y}_i)_{i=1,2,\cdots,n}$	coordinates of a random cluster following geometrical maneuvering

Channel Propagation

(α, β)	path-loss parameters for a particular link (dB)
Δ_{PL}	span of the domain for the large-scale fading density (dB)
η_{dBW}^{S}	sensor sensitivity for detection
λ_0	radiation wavelength of a transmitting source (unit of length)
$\vec{\Lambda}$	array of generic attributes for the large-scale fading distribution
$\mu_0 = \mu_0(l)$	evaluation limit for the large-scale fading density at the close-in distance
$\mu_L = \mu_L(l)$	evaluation limit for the large-scale fading density at the cell border
σ_Ψ	standard deviation of shadowing (dB)
τ	variable of integration for large-scale fading distribution
Ψ_{S-dB}	shadowing element emulating in-field scatterers
$c \approx 3\times10^8$	speed of light in vacuum (m/s)
d	propagation distance away from a transmitting antenna (unit of length)
d_0	close-in distance for a directional antenna (unit of length)
d_1, d_2, d_3	boundary values for the EM radiation regions of an antenna (unit of length)
d_f	Fraunhofer distance (unit of length)
d_S	Fresnel distance (unit of length)

D_A	largest dimension of an antenna or its aperture width (unit of length)
f_0	operating frequency of a radiating emitter (Hz)
$f_0(\tau)$	integrand for large-scale fading distribution
$f_\Psi(l)$	distribution function of shadowing
$f_{L_{PL}}\left(l,\vec{\Lambda}\right), F_{L_{PL}}\left(l,\vec{\Lambda}\right)$	generic probability density, and its cumulative distribution function for large-scale fading
$f_{L_{PL}}^{\max}$	maximum value of the probability density function for large-scale fading
$f_W(w)$	density of the average decay
l	random sample of large-scale fading between a reference and an arbitrary terminal (dB)
$l_{\max}$	argument that maximizes the probability density function for large-scale fading (dB)
$\tilde{l}_0, \tilde{l}_L$	measures w.h.p. the lower and higher extremities of large-scale fading for an *L*-sized cell (dB)
$\tilde{l}_{L_1}, \tilde{l}_{L_2}$	measures w.h.p. the lower and higher extremities of large-scale fading for a circular ring lattice (dB)
$L_{dB}^{\max}$	maximum channel-loss threshold
$L_{PL}(r)_{dB}$	large-scale fading level
$\overline{L_{PL}(r)_{dB}}$	average path-loss decay
$m_{L_{PL}}, \sigma_{L_{PL}}$	mean and SD of the random variable for large-scale fading (dB)
n_{PL}	path-loss exponent
p_{out}	outage probability
p_S	sensing capability for an arbitrary sensor
P_D	detection capability
$P_{dBW}^{\min}$	minimum power tolerance at the receiver

P_{dBW}^{T}	emitted radiation from a target point
$P_{PL}(l)$	sub-function of the large-scale fading density that isolates and collects the l based components together
$P_{RX}(r)_{dBW}$	power intensity at the receiver with interspace $r \in \mathbb{R}_{+}^{*}$ from the transmitter
r_0	close-in distance for an omni-directional antenna (unit of length)
w_0, w_L	average channel-loss at the close-in distance and the cell border (dB)
w_{L_1}, w_{L_2}	average channel-loss at inner and outer cell radii of a circular network (dB)
$w(r)$	random variable for the average path-loss (dB)

Random Generation and Monte Carlo Estimation

$\delta_B(x), \delta_B(x, y)$	1D and 2D fundamental histogram bin positioned at the origin of a Cartesian coordinate system
$\delta_X(x)$	comparison probability density function of $f_X(x)$ used for the ARM algorithm
Δ_B	dimension of an equally spaced bivariate histogram grid (unit of length)
ε_A	percentage error of the spatial density among analysis and simulation
$\hat{\theta}$	randomly generated angular sample (rad)
$\mu_{\sigma_{\min}}, \mu_{\sigma_{\max}}$	minimum and maximum RCR values for the acceptance rate estimator variance
μ_I	RCR value at the intersection point between Cartesian and radial RNG acceptance rate
μ_{opt}	optimum RCR value for random generation
π_i^C	cumulative occurrence for the i-th bin
π_i^O	number of occurrence for the i-th bin
$\pi_b(x)$	arbitrary bounding function of $f_X(x)$ used for the ARM algorithm

$\hat{\psi}_j$	j-th random instance of shadowing (dB)
A	event that a random sample is accepted
$A \subseteq \Omega$	arbitrary event A in sample space Ω
A_{bin}	bin areal surface of a bivariate histogram (units^2/bin area)
cdf_i	estimated cumulative distribution function value measured at the i-th bin
D_i	domain for the i-th bin
$\tilde{f}_{L_{PL}}(l)$	numerical probability density estimation of $f_{L_{PL}}(l, \vec{\Lambda})$
$\tilde{f}_{XY}(x, y)$	numerical probability density estimation for spatial inhomogeneous deployment of $f_{XY}(x, y)$
$f_Z(z)$	representative density function used for estimation analysis
$\tilde{f}_Z(z)$	numerical probability density estimation of $f_Z(z)$
$\left(F_R^T\right)^{-1}(\hat{u})$	an experimentally generated instance of the interspace range (unit of length)
$(F_X)^{-1}(\hat{u})$	inverse cumulative distribution function that generates a random geometrical instance along the *x*-axis (unit of length)
$G(\hat{u}, r_0, L, \sigma_G)$	interdependence of elements for random generation of the internodal distance
$h_{(i,j)}$	number of occurrence for the (i, j)-th bin (no./bin area)
$h_{XY}^{\text{analytical}}, h_{XY}^{\text{simulation}}$	average bivariate histogram density obtained analytically and using MC simulation (no./bin area)
$H(x, y)$	spatial density histogram for a randomly deployed network
$H_{ASD}(x, y)$	spatial density histogram for heterogeneous ASD deployment
$k, k_{\min}$	constants that enlarge $\delta_X(x)$
l_i	center position of the i-th histogram bin for large-scale fading (dB)

$\hat{\bar{l}}_j, \hat{l}_j$	j-th random instance for the average path-loss and large-scale fading between a reference and an arbitrary node (dB)
$\hat{l}_L, \hat{l}_H$	lower and higher extremities of the argument for the estimated density of large-scale fading (dB)
Δl_B	width of each histogram bin for estimating the density of large-scale fading (dB)
$\hat{L}_{PL}$	random variable for the large-scale fading level associated with $\tilde{f}_{L_{PL}}(l)$ (dB)
$\tilde{m}_{L_{PL}}, \tilde{\sigma}_{L_{PL}}$	empirical mean and standard deviation of the random variable for large-scale fading computed from MC samples (dB)
m_{N_S}, σ_{N_S}	mean and standard deviation of random variable N_S
$m_{\tilde{p}_A}, \sigma_{\tilde{p}_A}$	mean and standard deviation of estimator $\tilde{p}_A$
$\tilde{m}_{\tilde{p}_A}, \tilde{\sigma}_{\tilde{p}_A}$	sample mean and standard deviation that estimates $m_{\tilde{p}_A}$ and $\sigma_{\tilde{p}_A}$
n_B	quantity of histogram bars considered for density estimation
n_{B-X}, n_{B-Y}	resolution of a bivariate histogram
$\hat{n}_j$	j-th random instance from a standard Gaussian density function
n_R	number of i.i.d. MC realizations used for estimating the statistics of $\tilde{p}_A$
n_S	amount of i.i.d. randomly generated: samples, or nodes geometrical positions.
n_{S-i}	number of accepted samples for the i-th instance out of n_R used for approximating the statistics of $\tilde{p}_A$
n_{XY}	amount of 2D bins over the deployment surface having a nonzero occurrence number
N_S	random variable representing the number of accepted samples
n_T	total number of randomly generated instances

$p_A = \Pr\{A \subset \Omega\}$	probability for accepting a randomly generated sample
$\tilde{p}_A$	MC estimator for the acceptance probability of samples
$\tilde{p}_{A-i}$	MC estimator of the acceptance probability for the i-th instance out of n_R used for approximating the statistics of $\tilde{p}_A$
pdf_i	estimated density function value measured numerically at the i-th bin
R	event that a random sample is rejected
$\hat{r}$	analytical notation for a sample of the interspace magnitude (unit of length)
$\hat{r}_j$	j-th random instance of the interspace between AP and a node (unit of length)
$\hat{u}, \hat{v}$	sample occurrence generated from a standard uniform distribution $\mathcal{U}(0,1)$
$\hat{u}_j$	j-th random instance of the cumulative distribution function
$(\hat{x}, \hat{y})$	geometrical occurrence generated from $f_X(x)$ and $f_{Y\|X=\hat{x}}(y)$ for the coordinate pair of a random node (unit of length)^2
(x_i, y_j)	center position of the (i, j)-th bivariate bin (unit of length)^2
$[x_L, x_H] \times [y_L, y_H]$	deployment surface (unit of length)^2
$\Delta x_B, \Delta y_B$	dimensions of a bivariate histogram bin (unit of length)^2
z_i	center position of the i-th bin
z_L, z_H	lower and higher extremities of the density domain
Δz_B	width of each histogram bin
$\vec{z}_S$	vector in $\mathbb{R}^{n_S}$ of i.i.d. randomly generated samples
$Z = Z(A) \in D$	random variable in D associated to an arbitrary event A

List of Acronyms

1D	one-dimensional line model
2D	two-dimensional surface model
3D	three-dimensional space model
4G	4^{th} generation mobile system
6LoWPAN	IPv6 over low-power WPAN
a.k.a.	also known as
AP	access point
ARM	acceptance rejection method
a.s.	almost surely
ASD	area-specific deployment
BPP	binomial point process
bps	bits per second
BS	base-station
CDF	cumulative distribution function
CDMA	code division multiple-access
CI	confidence interval
cm	centimeter
dB	decibels
DC	detection capability
E	electric field
EIRP	effective isotropic radiated power
EM	electromagnetic radiation
ERF	error function
ERFC	complementary error function
FR	frequency reuse
GHz	gigahertz
GLONASS	global navigation satellite system
GPS	global positioning system

GSM	global system for mobile communications
H	magnetic field
HA	horizontal asymptote
HART	highway addressable remote transducer protocol
HD	high definition
ICDF	inverse cumulative distribution function
IEEE	institute of electrical and electronics engineers
i.i.d.	independent and identically distributed random variables
inf	infimum
IP	internet protocol
IPv6	internet protocol version 6
ITM	inverse transformation method
kHz	kilohertz
LOS	line-of-sight
LR-UWB	low-rate UWB
LR-WPAN	low-rate WPAN
LSF	large-scale fading
LTE	long term evolution
LWN	large wireless network
MAC	media access control protocol
max.	maximum
MBWA	mobile broadband wireless access
MC	Monte Carlo
MCN	multi-cellular network
min.	minimum
MiWi	microchip wireless networking protocol
mm	millimeter band
mod	modulo operator
MS	mobile-station
MSC	mobile switching center
mW	milliwatts

NFC	near field communication
NLOS	non line-of-sight
OP	outage probability
OSI	open systems interconnection model
P2MP	point-to-multipoint
PC	power control
PDF	probability density function
PHY	physical layer protocol
PL	path-loss
PMF	probability mass function
PPP	Poisson point process
PR	pseudorandom number
QoS	quality of service
RCR	cellular radius to the close-in distance ratio
RF	radio frequency
RNG	random number generation
RPGM	reference point group mobility
RTT	round trip time
RV	random variable
Rx	receiver
SD	standard deviation
SINR	signal to interference plus noise ratio
SNR	signal to noise ratio
sup	supremum
Tx	transmitter
UCN	uni-cellular network
UMTS	universal mobile telecommunications system
UWB	ultra wideband
w.h.p.	with high probability
Wi-Fi	wireless fidelity over IEEE 802.11 WLAN standard
WiMAX	worldwide interoperability for microwave access

WirelessHART	wireless sensor network based on HART
WLAN	wireless local area network
WLOS	weak line-of-sight
WMAN	wireless metropolitan area network
WMN	wireless mesh network
WPAN	wireless personal area network
WSN	wireless sensor network
WWAN	wireless wide area network

Chapter 1

Introduction

1.1 – Motivation

In an effort to better gain comprehension of various pure and applied phenomena, it is quite conventional by theoreticians to mimic these realities through mathematical models. In fact, many of our surrounding scientific disciplines, although they may significantly differ in magnitude, have to a large extent comparable geometrical construct. And they are often reproduced in spatial coordinates by seemingly simple points or versatile-size orbs.

For instance, as manifested in Figure 1.1, these elements represent in chemistry atoms and molecules; in physics they model particles; in astrology they signify galaxies and stars; in material science they suggest pore bubbles; and in biology they denote cells; etc [1], [2]. Indeed, the broad common denominator in all these disciplines is the spatial modeling and analysis of geometrical structures where the point patterns will carry an exclusive connotation with distinctive characteristics for the targeted subject matter.

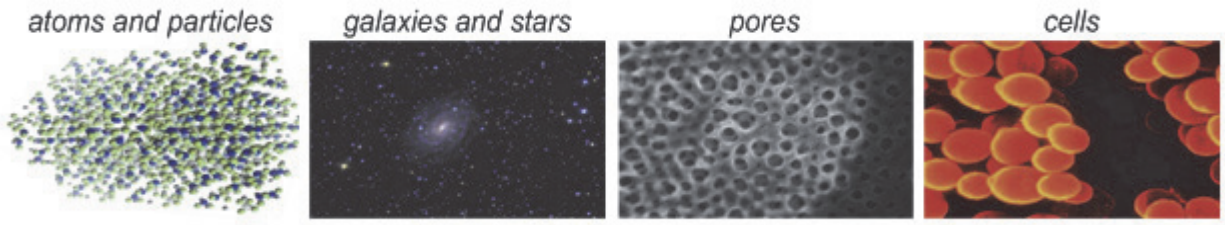

Figure 1.1 – Spatial geometry for modeling pure and applied phenomena

Analogously, this modeling approach may be extended to the concept of wireless information networks [3]. Namely, in telecommunications theory, these spatial dots indicate the physical location where a mobile-station (MS) or terminal is positioned. Thus, as visualized by Figure 1.2, the notion of spatial geometry is essential and practical for a number of professionals

including engineering designers and deployment planners modeling a host of network situations, ranging from: cellular network, relay network, wireless mesh network (WMN), wireless sensor network (WSN), femtocells, and all interoperable combinations of these realizations for setting-up heterogeneous internetworking. Furthermore, such practice should equally be of interest for any type of commercial radio communication purposes used to convey: audio telephony, data connectivity, mobile-IP, HD-video streaming, and interactive applications.

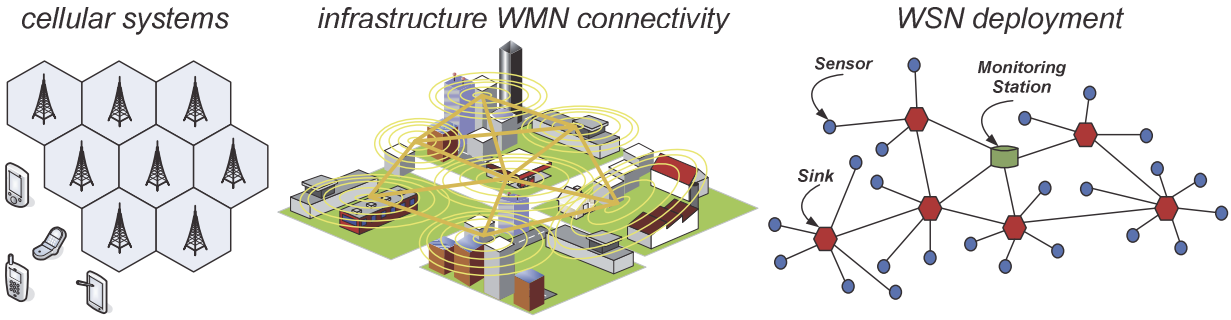

Figure 1.2 – Spatial geometry for modeling wireless network applications

Granted, there are so many wireless networking aspects, from diverse viewpoints, which are worthy of extensive investigation through modeling and analysis. However, above all it should be stressed that the geometry of wireless nodes is a topic that directly affects the lower levels of the open systems interconnection (OSI) model, and in particular the link layer of the network architecture. In fact, the principle of spatial distribution substantially impacts critical system parameters and communication factors, and is thus insightful for studying the various characteristics and performance of interacting nodes within a large wireless network (LWN) [4].

1.2 – Overview of Related Work

As of yet, we have briefly motivated the importance of terminals spatial location for radio communications. In this part, we want to discuss some of the necessary mechanisms and revelations surrounding feasible network replication. Therefore, related past work of relevance to spatial geometry will be reviewed.

Generally speaking, there are different ways for representing and modeling the spatial position of nodes. Indeed, widely available technology-assisted localization methods such as GPS, GALILEO and GLONASS are perhaps the best equipments for proving this sort of

observation [5], [6]. Despite the obvious benefit of instant data acquisition, these different positioning instruments introduce a number of noteworthy concerns:

- The added overhead and system complexity to the nodes will introduce further design challenges.
- The manufacturing cost of integrating the localization feature for large quantities of terminals will result in an expensive outcome.
- Incorporating this energy-hungry capability will accelerate the depletion of the power supply.
- The accuracy for civilian usage is still not to the level required for high-precision positioning.
- The satellite signal access is weak and non-reliable in regions such as: heavily buildup cities, forested land, canyons, etc [7].
- Although the above issues are true for all wireless items, yet they are even more significant for WSN due to the already limited size and life-expectancy of sensor points.

Next, in situations where handheld mobile devices are carried by users, human behavioral analysis through social patterns and inclinations is an interesting possibility for spatial prediction [8], [9]. In general, behavior is driven by physical conditions, emotional states, cognitive capabilities, and social status [10]. This is only an elementary description; fully understanding the population's conducts and preferences is rather complex for proper modeling. Moreover, social trends and tendencies require for the most part vast effort and resources due to the need for long and intense observations. Furthermore, the spatial realization obtained through this approach is exclusively valid in the area of study, and is generally unfeasible for replication to other network projects due to the non-generic nature of the method.

Because of technical intricacy, restricted resources, and high-cost for collecting empirical datasets, spatial modeling via analytical means has been considered as a widely practiced mechanism for inference. As a result, diverse models have been proposed for emulating the geometry of a network in order to explore its features.

Indeed, for the simplest case, it is possible to consider a deterministic deployment approach where the systems emplacement is known in advance [11], [12]. In fact, such preassigned nodal structure is mainly suitable for fixed antennas such as static sensor networks

for say habitat and environmental monitoring, and is unpractical for quasi-stationary nodes and fully mobile devices.

Additionally, a number of researchers have proposed various deployment algorithms that optimize a particular objective. For instance, the network could strategically be controlled or self-organized so as to meet a certain requirement, such as improved: coverage [13], detection capability [14], latency and energy consumption [15], to name a few. Of course, such spatial formation techniques are principally appropriate for WSNs, and are unfitting for a variety of handheld networks due to the unconstrained nature of users' position.

As a consequence, universal deployment procedures are needed for mobile-based spatial constellations so as to pragmatically emulate a network of portable units. For this purpose, stochastic modeling is convenient because it ensures impartiality and it introduces the prospect of likelihood during the generation of arbitrary positions. Accordingly, the outcome of this approach produce what is typically referred to as random networks. As a matter of fact, in this situation, the created random spatial models are analytically formulated. Specifically, some distribution functions are suggested based merely on conjectures [16], [17]. Although such stochastic techniques provide theoretical elucidations, these models may also be feasible, if they do indeed represent the spatial pattern of users.

Beyond this, the homogeneous distribution is perhaps the most commonly adopted technique for random emulation because of its unvarying nature and inherent canonical features [18]–[30]. From a practical outlook, such simplistic spatial model is generally realistic when the deployment surface has similar attributes, say in: surroundings, topographical landscape, atmospheric conditions, etc. If these physical properties are steady, then users' preference over certain regions of the overall deployment site will be eliminated, thus guaranteeing a uniform distribution. Evidently, in real-life situations, this particular scenario is rarely realized. Nonetheless, the random uniform network is still reasonable and tolerated for preliminary analysis especially when the geometrical construct is uncertain or completely unknown.

Apart from uniform generation, non-homogeneous modeling is also conducted as an interestingly appropriate approach for random deployment of mobile systems. In view of this, some investigators have applied the so-called principle of thinning, which depends on the location of neighboring terminals [31], [32]. Basically, an inhomogeneous spatial distribution is synthetically realized by deleting nodes from a uniformly deployed pattern.

Other contributions have focused on higher nodal concentration near the borders of a cell so as to examine edge related aspects of a contour [25]–[28], [33]–[35]. For such heterogeneous deployment, it is noteworthy to indicate that if multihop cellular communications is in effect, then the fewer mobile relay nodes that are closer to the base-station (BS) will have a higher traffic load than those near the margin of the cell border. This factor will then cause these center-based network nodes to rapidly drain their energy sources, thus lowering the already sparse volume of active terminals, which further exacerbates the bottleneck effect. In these situations, one possible avenue for mitigating this elevated traffic demand would be to apply load-balancing. Otherwise, to overcome this traffic surplus, a higher density of active nodes can be conceived in the vicinity surrounding the BS as opposed to the edges. In other words, a center-focused deployment can be considered using a particular distribution profile. Due to these potential aspects and the like, some spatial models have been theoretically adjusted to produce edge or center-focused deployments via a simple tunable variable [34], [35].

In addition to the above probabilistic emplacement techniques, the Gaussian geometry is distinctively an interesting heterogeneous model because both the geographical spread and the intensity of terminals position are flexible. Indeed, the dual purpose of this network deployment model can be controlled by its standard deviation (SD) [36]. Therefore, this random structure can be utilized for emulating various multi-pattern user-carried devices in a cellular architecture [24]–[26], [35]–[39]. Also, the Gaussian network has been considered in topology control of sensor networks [40], and for multihop connectivity [41].

Pursuing this further, besides cellular-based network usage, random geometry has been extensively considered for modeling airborne nodal deployment with practicality in rural monitoring, disaster areas such as earthquakes, and for mission critical networks. Indeed, it turns out, that in-flight node scattering is effectively emulated by the Gaussian probability density function (PDF) [42]–[45]. In other words, if a set of nodes are intended to be positioned about a specific location P (say a pre-deployed information processing point), once dropped, they are expected to be anywhere in a cloud around P due to factors such as: wind, speed, height, etc [42]. Hence, based on the central limit theorem the nodal constellation will follow a normal PDF [43].

So far, we noted a number of emulation directions taken to model the spatial position of wireless nodes. To be exact, these emplacement techniques are varied and their corresponding geometrical information can be acquired using different pathways which can range from:

technology, social and analytical means. We also pointed out, the drawbacks and limitations of each of these methods as compared to actual real-world deployments. For a quick recapitulation, Table 1.1 outlines a summary of the most prominent geometrical modeling approaches.

Table 1.1 – Notable techniques for geometrical representation and modeling of a network

methods	key advantages	drawbacks and limitations
technology-assisted localization	instant data acquisition	system overhead, manufacturing cost, resources, accuracy, access
social patterns	realistic positioning based on behavioral analysis	complexity of empirical observation, time-consuming, non-generic approach
deterministic modeling	*a priori* spatial allocation (i.e. no need for random generation)	valid for fixed/static systems and is unsuitable for portable units
strategic deployment	optimizes a particular performance metric	adequate for WSNs and is inappropriate for unconstrained networks
conjectured networks	analytically formulated for generating arbitrary positions	hypothesized models that do not necessarily echo users' spatial profile
random homogeneous	simplicity of setup, reasonable assumption when pattern is unknown	practically sound provided the deployment surface has similar physical attributes
Gaussian distribution	heterogeneous modeling, tunable geometry	valid for center-focused deployment and airborne nodal emulation

Overall, as it can be noticed from this survey, random emulation is generally preferred for analysis and for generating tractable results. And from previous contributions, we identified that the two commonly employed stochastic postulations are founded on the homogeneous structure and the Gaussian spatial pattern. As a consequence, this dissertation will in part focus and analyze in detail these two network models.

In light of this, in order to visualize the deployment principle, we demonstrate in Figure 1.3 different geometrical distribution models of 1,000 nodes. The first network follows a position-defined layout organized in an orderly fashion. It is important to note that the terminals need not be equally spaced as depicted in the image; this is only an example that further emphasizes the *a priori* nature of the deterministic assumption. The second network emplaces the same amount of nodes in a square grid based on the random uniform density. And the third utilizes the Gaussian distribution for the purpose of generating random coordinates over an equivalent deployment surface.

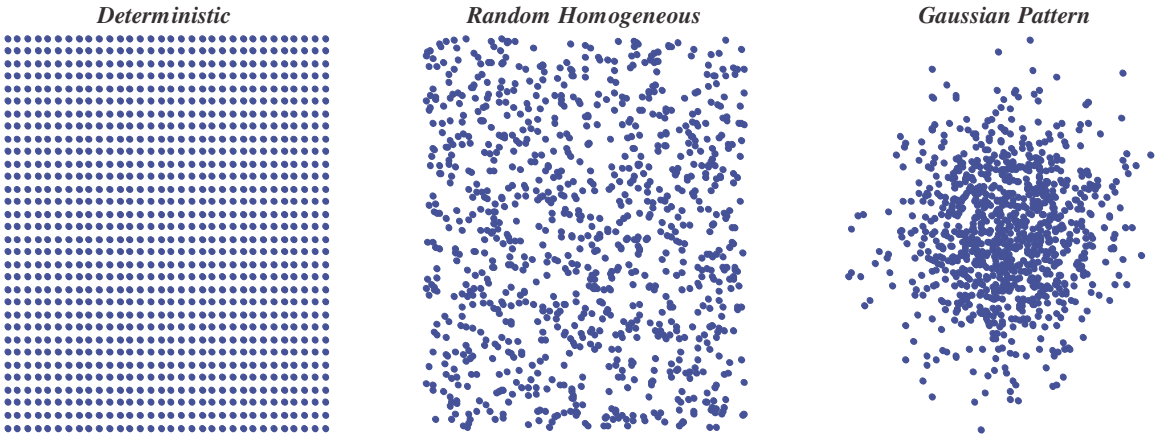

Figure 1.3 – Geometrical interpretation of several network deployment models

1.3 – Problem Statement and Objectives

Altogether, we may disaggregate the notion of random networks into three interconnected steps. The first step consists on spatially emulating a wireless network. Then, the objective of the second step is to extract valuable and interesting analytical observations from the realized network model. And the last step focuses on using and analyzing the deduced results to better comprehend the behavior and characteristics of the network. With these insights, the geometrical structure can then be planned and designed based on technical variations and appropriate parameter selections so as to improve the network performance and its quality of service (QoS).

Empowered with this high-level outlook, our central goal here is to develop and advance the understanding of LWNs by examining various unexplored fundamentals of communications and network modeling. Overall, as it will be articulated in the upcoming subsections, the major research results reported in this dissertation can be concentrated into four principal topics.

1.3.1 – Exact Expressions for Homogeneous Random Deployment

Before being able to identify interesting network properties, it is vitally necessary to reproduce the nodal graph. However, this task is far from being trivial and is rather quite involved. From the previous section, we recognized that there are typical approaches for terminal positioning based on location instruments and observational patterns. Given the fact that these methods are costly, complex and time-consuming, network designers have been inclined to consider

geometrical modeling as a rational substitute. Clearly, it should be emphasized that in order to generate a LWN it is natural to deploy arbitrarily located nodes in a terrain through the use of random network modeling. Indeed, randomly assigned positions ameliorate the model because it makes the network more real; thus, it is the preferred choice for geometrical emulation.

Specifically, homogeneous random networks are useful to theorize when no particular information about the deployment spatial pattern exits. In fact, over the past few decades, since the booming of wireless networking, many researchers have looked at the effect of such homogeneous spatial distribution [18]–[30]. However, despite the extensive use of this random model type, at its current state, the deployment approach raises a number of important concerns:

- There are no exact and definitive stochastic expressions for random generation in different lattice structures.

- The realized spatial models are incompatible for accurately deriving and analyzing the channel-loss distribution between a reference point and a randomly located node.

- The geometrical models are not flexible, and thus they cannot be used to produce random positions in various deployment surfaces without relying on heuristic workarounds, which are counterproductive because they are computationally inefficient, but more importantly they completely dissolve the wanted randomness.

Because of these critical reasons, analytical research work is required so as to explicitly derive appropriate and generic formulations for exact random deployment. Once derived, the adaptable results will ensure a more efficient random generation as opposed to synthetic sampling. In other words, because of unbiased randomness, every generated sample will be of use during the emulation process. In addition to emulation efficiency, the desired randomness will as well be preserved for the versatile networks. Also, the obtained results will have cascading benefits for channel-loss analysis, and for developing inhomogeneous deployment algorithms. Overall, to verify and demonstrate the validity and accuracy of the derivation for the different network cases, the theoretical findings will be accompanied by a number of stochastical simulations.

1.3.2 – Explicit Large-Scale Fading Distributions

Now that we have explained the necessity to obtain exact expressions for generating random networks, at this level, we are interested to look into the effect of such configurations on channel losses. In fact, in wireless communications, channel losses are an important contributor for weakening and corrupting the propagation of the information signal. Most notably, losses or fading measurements can be split into three complementary components: path-loss (PL), shadowing, and small-scale fading. The combination of PL and shadowing is commonly referred to as large-scale fading, and in some instances this dominant loss may simply be specified as PL.

Indeed, the physical gap among interacting wireless nodes straightforwardly influences the fidelity and quality of the communications. Above all, this is due to large-scale fading because it is essentially a measure that quantifies the power loss in the channel as the electromagnetic (EM) wave travels from the transmitter to the receiver. Therefore, there is a clear interdependence between the transmission geometry and PL. As a case in point, the Bluetooth technology uses the PL indicator in order to determine which among detectable devices is closer; namely, the nearby terminal that has the lowest PL value [46].

Moreover, having the large-scale fading element for a specific wireless channel during system analysis and design can directly lead us to other vital factors, along with: power consumption, connectivity, outage probability, detection capability, interference characterization, transmission capacity, energy-aware information routing, multihop access scheme, cooperative communications, localization techniques, etc. Altogether, we notice that Euclidian geometry affects PL, and knowing PL gives valuable information to the many items listed above. Thus, the channel access of a wireless network is a significant topic of research because of its impact to a host of metrics and applications. As a consequence, we want in this research contribution to focus on understanding the large-scale fading behavior for random-based LWNs.

Since the network geometry of wireless radios is spatially modeled based on stochastic configurations, then the practical approach for profiling the channel attenuation among communicating units would be to predict the PL by means of distribution functions. To be precise, for a given network model, we basically want to determine the PL density between a reference access point (AP) and an arbitrarily deployed unit for downlink applications. By and large, the only evident way to estimate the large-scale fading PDF for a random network relies on exhaustive computationally intense Monte Carlo (MC) simulations. Of course, this is an

unsophisticated method because during analysis and design, as parameters of the network or the propagation channel changes, then the entire random experimentation has to be repeated. Alternatively, this computational inefficiency can be replaced by the use of stochastic analysis in order to tractably characterize the channel behavior.

As a result, because of feasibility and efficiency concerns, the objective of this research is to analytically derive generic and exact closed-form distribution expressions for the large-scale fading over various random network models between a centrally excited cell and a mobile device. Granted, due to the random nature of shadowing, the distribution of the received power level or the PL has been previously shown for a deterministic separation from BS-to-MS as a prerequisite for quantifying the outage probability [47]–[51]. Because of the inevitability of random networks in real-life situations, the aim in this dissertation is to broaden and ameliorate this elementary model by overlaying the essential paradigm of stochastic geometry.

To be specific, we first intend to derive the large-scale fading PDF for a MCN layout. Basically, in this model, the geolocation of arbitrary units will be independent and identically distributed (i.i.d.) subject to the random homogeneous deployment. As for the cellular structure, it will be based on a modified version of the hexagonal lattice such that the impact of the far-field region is exclusively accounted for within the deployment surface. In fact, this geometrical accuracy will be executed for two important reasons:

1. It will ensure that the derived large-scale fading density function rigorously models the laws of EM propagation.

2. It will make the final density result more universal so that it can be applied for all types of MCN deployments ranging from: femtocells, picocells, microcells, and macrocells.

On the whole, the MCN formulation for the large-scale fading PDF will gather various network and channel properties. To be exact, it will by design consider: the lattice profile, users' geometry, the effect of the far-field phenomenon, the PL behavior, and the stochastic impact of channel scatterers. Because of this comprehensive approach, the anticipated distribution notation will precisely characterize the channel-loss while remaining fully generic and compatible for different network parameters and channel environments.

Furthermore, we also want to determine the exact closed-form large-scale fading density between a reference and a random node valid for all possible permutations of the UCN deployment. In fact, we aim to derive this predictive stochastical formulation as generic as analytically possible, such that once we have this result we can then personalize it not only for the particular technology and channel status, but also for flexibly versatile random network models. Actually, our expected result will profoundly generalize the analysis reported in [19], which basically found the PL density for uniformly deployed nodes in a fixed circular lattice. In other words, our analytical notation will support spatial adaptability for various disk-based surface regions, along with multi-width rings and circular sectors. Also, in the analysis of the probabilistic distribution, we will specifically include the necessary impact of the far-field, which was completely overlooked in the formerly noted contribution. Meanwhile, in order to gain greater insight into the channel-loss behavior, we also want to obtain statistical expressions that estimate the moments of the distribution function for the large-scale fading. After obtaining all these analytical findings, as a last step, we are also interested to study and observe the interplay among the diversity of the deployment regions on the PL density function.

In addition to homogeneous random networks, as motivated earlier, Gaussianly distributed nodes are regularly employed for emulating: cellular architectures [24]–[26], [35]–[39]; and airborne deployments [42]–[45]. Given the importance of propagation in general, and the specific relevance of this geometry for different deployment events, it then becomes instinctively natural to put these concepts together and attempt to characterize the behavior of the channel-loss for the entire random network. Thus, once again, the objective for this flexible network model would be to obtain an exact closed-form mathematical notation for the large-scale fading PDF in support of reusability purposes and analysis. In fact, we should emphasize that such result would be interesting to formulate because this convenient network model has the unique advantage of being tuned for the particular spatial deployment intensity and coverage by a simple modification to the SD variable of the Gaussian density function. Eventually, we aim at ensuring that the exact analytical result for the large-scale fading PDF remains completely generic and adaptable to the various channel conditions, and wireless technologies. But in particular, we also want to guarantee its suitability for the different spatial intensities of the Gaussian random pattern. Moreover, in the derivation we will add yet another degree of generalization by performing the analysis on a truncated Gaussian distribution. Namely, with this

change, the formula will explicitly incorporate the far-field region, and also it will confine the spatial deployment to a predefined cellular radius $L \in \mathbb{R}_{+}^{*}$, which adds to the leveraging appeal of the result during design. Furthermore, to better comprehend this distinct deployment model, we then intend to examine the impact of the PL density for a fix cellular size over variable spatial intensities.

Taken together, all the above exact and generic analytical derivations will be verified and their accuracy will be demonstrated by considering realistic operational parameters that characterize the channel. Even though parameters from any centralized networking technology can be used, nevertheless, we intend to carry out computational MC simulations using channel specifications from the relatively novel IEEE 802.20 protocol, also known as MBWA [52].

1.3.3 – Heterogeneous Spatial Deployment Algorithms

In general, we want to duplicate via models real-world wireless networks, and then draw important fundamentals from these characterizations in order to build smarter protocols. In fact, reliably emulating the network footprint is a very complicated task that requires extensive and often costly scrutiny. Indeed, some fairly acceptable conjectures have been adopted in literature to alleviate the burden of spatial emulation. Notably, the random homogeneous model is a conceivable assertion for stochastical inference, particularly when users' spatial pattern is lacking [18]–[30]. However, due to their social fabric, mobile carrying end-users tend to gather with a higher likelihood in some preferred locations as opposed to an equalized arrangement; thus implying the inevitability of heterogeneous distributions.

As a counter reaction for this need, various inhomogeneous spatial deployment models have been suggested. For instance, the principle of thinning can be applied as one possible approach [31], [32]. Another technique enables heterogeneity through different adaptation of edge or center-focused deployments [25]–[28], [33]–[35]. As an additional alternative, the Gaussian constellation is utilized for controlled non-homogeneous modeling so as to produce denser deployments around a reference point [24]–[26], [35]–[45]. Although, as noted before, these varied models are relevant in certain instances, on the whole, such methods do not necessarily echo the actual geometry of a network configuration over a particular deployment site. Hence, the indicated analytical heterogeneous emulations, and the like described in Table

1.1, will inaccurately reflect important technical issues of relevance to network planning and design.

As a consequence of the above, it becomes imperative to find new practices for inhomogeneous random deployment. Intrigued by this challenge, in this dissertation, we intend to contrive spatial mechanisms for constructing adaptable networks that can realistically map users' trends while still preserving the random character of deployments. Moreover, we want these bona fide heterogeneous models to require limited *a priori* input parameters from designers so as to ensure their ease of configuration for an array of network planning projects. To this end, while bearing in mind that reflective network emulation is usually very complex to realize, we nonetheless aim to specifically tackle this deployment objective by probing the essential underpinning of nodal clustering. As a matter of fact, users' spatial structures are mainly shaped and characterized by natural and manmade topographical land-cover features and environments. Thus, our solution to this complicated inhomogeneous undertaking would be to conceptualize a random deployment approach such that users tendency to cluster based on terrain limitations is exclusively taken into account.

To be precise, we will propose a simple inhomogeneous algorithm model known as area-specific deployment (ASD) for achieving targeted deployment. This devised spatial heterogeneity method is actually governed by the systematic principle of divide and conquer. Namely, instead of solving the entire task at once, we break it into smaller more manageable pieces, solve each separately, and then apply the superposition principle to aggregate the various results in order to formulate an explanation to the original challenging problem. In essence, for a specific deployment region of interest, the approach is based first on identifying various non-overlapping spatial clusters founded in part on landform features. In fact, each of these sub-regions will have a particular areal number density defined by the ratio of the enclosed nodal scale over its surface area. Then we consider geometrical analysis for selective deployment, where for every one of these cluster formations, we unbiasedly generate the desired quantity of arbitrary i.i.d. positions by means of the random homogeneous deployment. Finally, we synthesize the dismembered sectors in order to reconstruct a contiguous random network that has a more pragmatic heterogeneous spatial profile.

After providing a rigorous high-level understating of the ASD method, we then intend to apply it for various inhomogeneous deployment settings so as to be of practice during the quality

assessment of a network. Specifically, we first aim to develop a UCN algorithm for modeling a heterogeneous random deployment. In particular, the random homogeneous disk model has been considered for characterizing UCN cells and clusters. Motivated by this, as opposed to signifying BS radiation coverage, we will only consider a sector of an onion-like circular ring to represent the deployment surface terrain. Using this generically flexible region as a fundamental building block, we could then plan the overall footprint of a UCN as a combination of multiple circular-based sectors having each a specific: layer position, width, angular boundary, and nodal scale. In fact, the deployment plan can be stipulated based on minimal social observations of the project site, or by means of plausible assumptions founded as a function of the network: location, size, and purpose. Meanwhile, before assembling the algorithm together, we would have to derive the appropriate and generic expressions for exact random nodal generation in a circular ring sector. Based on the obtained results, we then coherently create a simulator tool that enables multi-density random deployment within each of the identified cluster formations in order to realize a non-homogeneous spatial distribution. Next, we will apply this conceptualized deployment method to multi-sector network examples to show how this technique achieves a more reflective inhomogeneous geometry with less effort, while maintaining users' arbitrary nature.

As explained above, for controlled deployment, the designer plans the network by specifying the quantity, size and position of sectors, in addition to the amount of nodes in every sub-region. However, there might be events where there is an interest to generate an inhomogeneous random structure without necessarily specifying the particulars of the network. For these uncontrolled arbitrary patterns, a feasible simulator tool should be created. Indeed, we have set proper design guidelines that we will attempt to put forward for this objective. Namely, once built, the emulation model should automatically generate a heterogeneous deployment in a simple manner, whilst exhibiting compatibility to multi-scale networks. Therefore, we intend to elaborate on the notion for formulating an uncontrolled UCN footprint, develop the corresponding algorithm, and analyze the performance of the inhomogeneous emulation. After deriving this sophisticated deployment algorithm, we intend to test and demonstrate its arbitrary behavior for small, medium, and large networks through MC realizations. In general, the anticipated uncontrolled algorithm will by itself do most of the network deployment decisions. Only few basic inputs will be required to initialize this procedure, such as: the cellular size and the network scale. Given that the set of *a priori* entries is way smaller than the controlled option;

it thus implies that if less information about the network is known, or if we are simply interested in generating an arbitrary structure, then this uncontrolled algorithm should be favored.

In addition to the above heterogeneous UCN algorithms, we are also interested to apply the ASD principle in order to formulate an approach for random MCN deployment. In fact, for modeling this MCN objective, tessellating grids would be needed to represent the EM coverage of the BS. Moreover, although the cause for UCN clustering will be based on terrain features; yet due to its geometrical nature, the source for MCN clustering will be founded as a function of BS positions and sectoring capability resulted by use of directional antennas. Thus, since the hexagonal lattice is the most suitable tessellating choice, we will hence need to provide a definitive framework for exact and unbiased random deployment in diverse unsectored and sectored hexagonal-based structures as primary elements for constructing an inhomogeneous MCN. Then, we aim at deriving the appropriate notations for geometrically navigating over a large honeycomb network grid. Next, these findings could be merged in order to create a modular subroutine that generically supports a complex heterogeneous MCN with varying: size, capacity, density, and sectoring capability. Furthermore, we will also demonstrate the inhomogeneous algorithm via stochastic simulation of a particular MCN deployment project. Practically speaking, this expected MCN deployment algorithm tool will generally be convenient for modeling a large urban-based mobile network. Also, this emulation mechanism will be informative in exploring various QoS metrics for the network performance of a complex MCN architecture.

For computational purposes, we further aim at formulating an explicit ASD-based expression for estimating the geometrical density relevant to the presented three spatial-level inhomogeneous algorithms, namely: controlled/uncontrolled UCN and MCN deployments.

1.4 – Main Research Contributions

In the previous section, we brought forth the improvements and needs essential in the area of network geometry, and we meticulously discussed the main purpose and objectives of our investigation. Overall, following careful, complex and extensive analysis, various genuine research results are reported in this dissertation, but among them the most prominent key contributions can specifically be summarized as follows:

- We first elaborated and formulated an optimal approach for stochastic position generation in a MCN layout tailored for channel-loss analysis. Then, we derived the corresponding exact closed-form large-scale fading PDF between a reference and a random node.
- We obtained an explicit stochastic expression for random deployment in a flexibly versatile UCN lattice and analyzed the results. We then generically derived the exact closed-form large-scale fading PDF for this adaptable random network model.
- We conceptualized a new approach for heterogeneous deployment identified as ASD. We then applied this principle to diverse emulation situations, and thus developed three inhomogeneous algorithms for: controlled/uncontrolled UCN and MCN deployments.
- We obtained an exact closed-form notation for the large-scale fading PDF for a generically truncated Gaussian random network model over a centralized communication. We then demonstrated various theoretical implications of the channel-loss densities.

It is important to highlight that the research formulated throughout this dissertation provides novel and generic fundamental results that are applicable to the concept of cellular-based networking while being independent of a particular technology. However, whenever relevant, we utilized specifications from the emerging IEEE 802.20 standard in order to demonstrate and verify the derived outcomes.

1.5 – Organization of the Dissertation

In Sections 1.3 and 1.4 we indicated the essence of this research; however, as we move forward in solving these technical objectives, a number of intermediary findings will be necessary, and hence will according be studied.

The rest of this dissertation is organized as follows. In Chapter 2, we will expand our insight into the essentials of cellular-based wireless networking by focusing on two fundamental aspects. First, we will provide a comprehensive overview for emulating the geometry of LWNs; then, we will specifically concentrate on the spatial modeling for UCN and MCN deployments. Second, we will explain the foundation for wireless propagation modeling, which will be a useful primer because an important portion of this treatment is devoted to the derivation of tractable channel-loss predictors. Moreover, main features of the MBWA standard will be discussed.

Next, in Chapter 3, we will lay the groundwork for the propagation analysis by fusing the fundamentals of spatial homogeneity and lattice geometry. This will be followed by a formulation for efficient random deployment personalized specifically for channel-loss analysis. After, the exact closed-form stochastical method for forecasting the large-scale fading between a reference and a random node over a MCN model will be detailed, and the practicality of the results will be demonstrated.

Thereafter, in Chapter 4, we will derive the expressions for a flexible UCN deployment, useful for producing various network realizations including the generation of random positions in an annulus, which is convenient for studying edge related aspects. Then, for this versatile random network, we will analytically derive the exact large-scale fading PDF, which is a predictor for the amount of power expected to be lost between a reference AP and a randomly deployed user. Next, given that different deployment techniques are not necessarily sound for modeling an inhomogeneous network, we will then describe the ASD principle, which is a novel emulation approach that takes into account users' clustering tendency. Using this approach, we will then derive systematic stochastic models for controlled and uncontrolled inhomogeneous deployment algorithms that can be utilized for UCN deployment projects to achieve a more realistic nodal distribution, whilst requiring basic information of users' patterns. After that, exact random homogeneous generation in unsectored and sectored MCN models will be deduced, and geometrical maneuvering tools will be derived. With these results, the ASD methodology is then applied in order to develop an additional heterogeneous algorithm for MCN deployment.

Pursuing this further, in Chapter 5, we will describe the properties of the Gaussian random network, which has various deployment implications, precisely for cellular systems, and for effectively modeling the emplacement of an airdropped network. Then, we will explicitly derive the large-scale fading distribution by an exact closed-form expression. In addition, we will show different ways the channel-loss PDFs derived in this chapter and the previous can be utilized for theoretically assessing various integrity measures.

Finally, in Chapter 6, we will conclude this dissertation by providing a synopsis of the major research highlights. We will also show how this type of research opens the door for diverse interesting extensions in order to further complement our presented scholarship.

Chapter 2

Essential Background of Cellular-Based Wireless Networking

2.1 – Introduction

2.1.1 – Objective

As it will be evident from subsequent chapters, this dissertation will mainly concentrate on the fundamentals of cellular communications by focusing our attention to two critical components; namely: the network geometry and the channel propagation. Thus, for context and foundation purposes, it becomes necessary to briefly review the essentials of:

- Network Modeling: Because it will serve as a background for emulating a stochastic spatial pattern aimed for different network deployment situations.
- Propagation Modeling: Because it will be useful as a basic primer for rigorously characterizing channel-loss predictors for random LWNs.

2.1.2 – Organization

The rest of this chapter is organized as follows. First, in order to expand our insight into wireless networking, we will begin in Section 2.2 by explaining a comprehensive approach for modeling the spatial geometry. This will be done by dissecting the spatial features of a LWN. Then, we will discuss and explicitly quantify the best approach for UCN and MCN deployment modeling. Afterward, in Section 2.3, we will provide an overview for characterizing the wireless propagation by describing: the causes for channel corruption, the various radiation boundaries, and channel-loss modeling. Next, in Section 2.4, we will briefly motivate the major highlights of the relatively recent MBWA standard, and identify its pertinent transmission models. Finally, Section 2.5 will close the chapter.

2.2 – Network Modeling

2.2.1 – Dissecting the Network Geometry

For the purpose of planning, designing and analyzing a LWN, geometrical network realization is fundamental. However, the underpinning of spatial network emulation is not unified, and so the purpose of this section is to briefly explain the different modalities of modeling in an interconnected complementary way.

Evidently, in order to constitute at once a complete wireless structure, it is more intuitive to breakdown the modeling task and gradually integrate the different components so as to tailor a particular network pattern. Hence, in Figure 2.1, we outline a coherent hierarchy for constructing a network. As it can be seen, the various peculiarities and specifications of spatial constellations are carefully and methodically organized so as to simplify the generation of a geometrical topology. Namely, the elements that will effectively express the essence of a network can broadly be dissected into a horizontally associated set of sub-branches designated by: spatial layouts, dimensions, lattice structures, internodal linkage, and mobility.

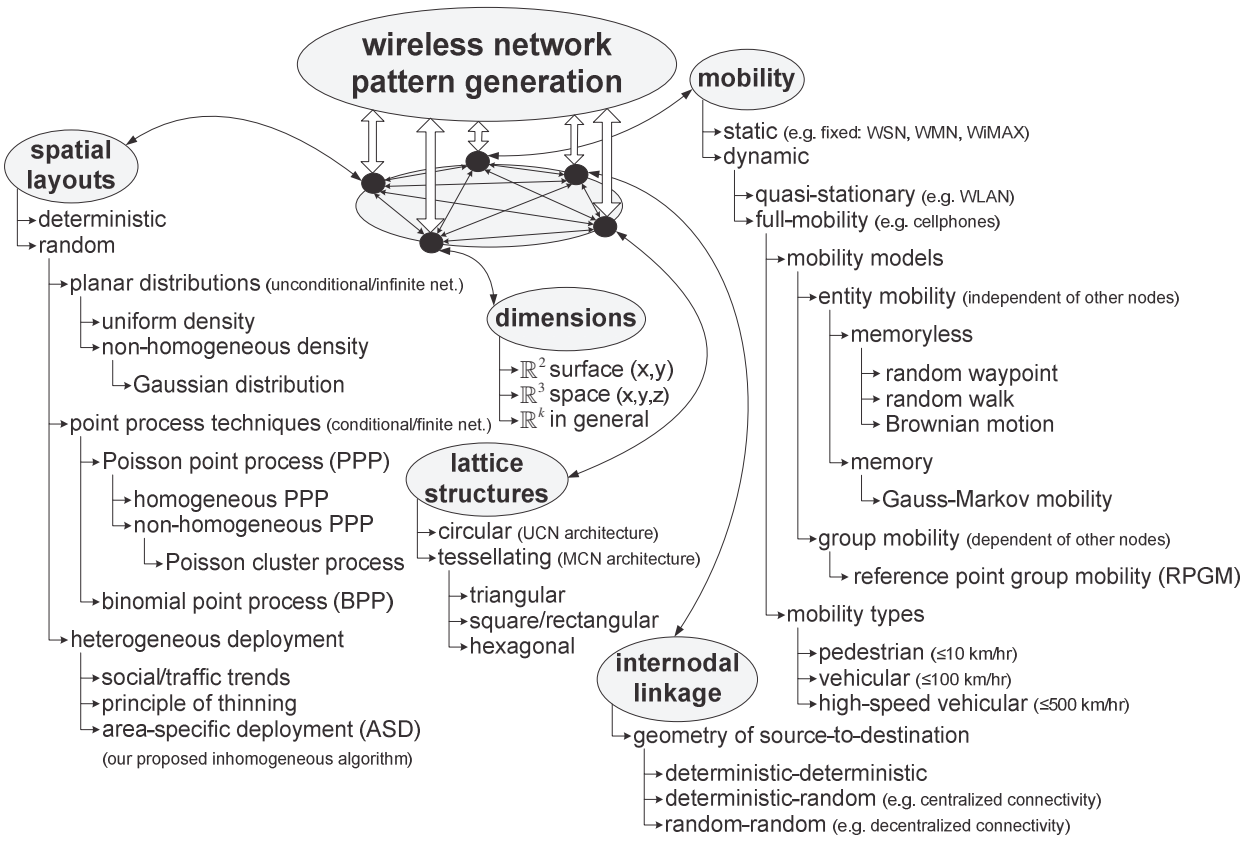

Figure 2.1 – Categorizing geometrical model features for network emulation

Granted, from this arrangement, we can clearly recognize that the diverse relations among these parameters are symbiotic. But indeed, this formation is double-sided, because on one hand, it suitably converges the items together, but on the other hand, it further deepens the emulation complexity.

Undoubtedly, among these attributes, the spatial layout is indeed the most decisive factor. And as discussed in the previous chapter, there are different geometry models. Yet, often the terminologies used to characterize a particular configuration vary from one source to the other. Thus, we find it necessary to classify and scrutinize the spatial distribution models as shown in the above taxonomy so as to remove this technical ambiguity and also to clarify the type of nodal deployment we intend to investigate in this contribution.

From this endeavor, we notice many possible categorizations, and most importantly are those rendered through stochastic emplacement. In fact, random networks can either be constructed using planar distribution functions [18]–[26], [35]–[45]; or through point process techniques [53]–[56]. In principle, these applied stochastic methods explore the same problem from different analytical references and frameworks. Technically speaking, discrete spatial coordinates can be generated from a continuous and differentiable planar density function that models the geometrical behavior of a network over the defined surface region. After, the desired number of independent samples can be extracted from this joint distribution. Alternatively, if the network scale is known beforehand, then point processes can be utilized to deploy these preset nodes over the designate metric space. So basically, the difference between the approaches is that on one hand, the network is unconditional because the nodal distribution is known irrespective of the scale; whereas on the other hand, the conditional emulation produces a finite structure.

As an example, a random configuration can be achieved based on independent uniform distribution, or by means of the homogeneous Poisson point process (PPP). Although the mathematical toolkit among the approaches is somewhat different, yet the final spatial rendering of the network for a specific amount of random nodes is indistinguishable. Thus, the term uniform and homogeneous may be used interchangeably without necessarily being associated with a particular stochastic approach.

Moreover, random inhomogeneous deployment may also be realized using other non-formulated means subject for instance to social and traffic trends. Besides these methods, spatial assortments founded on a particular deployment algorithm can be conceived.

Having pieced these different network deployments options together, we essentially can begin the modeling task by selecting the basic geometrical descriptions and properties, and progressively add features to it. For instance, the nodal positions can be distributed on a 2D Euclidian plane, or more realistically over a 3D space. For mathematical intrigue, the modeling may also be extended to higher $\mathbb{R}^k$ dimensional orders, e.g. [57]. Furthermore, as it will be explored and analyzed in the next subsections, the lattice structure of the network is also diverse and could take different geometrical shapes. Precisely, for a UCN, the grid over which the nodes superimpose can be modeled by a circular format. As for tessellating constructs, they are more appropriate for modeling large MCN architectures.

Additionally, in terms of the objects and building blocks of the network model, they can actually be used to signify different systems and platforms. Specifically, within a certain network cell, there are in general two fundamental elements: a reference point and multiple nodes. The reference could range on a case-by-case basis from BSs, to local aggregators or sinks; and spatially emplaced nodes could be MSs, sensor units, or even actuators[1]. Then, based on the particular connectivity scheme, these units either act as a transmitter, receiver, or a relay point. And the geometry of the internodal linkage from source-to-destination could vary from all possible combinations of fix and arbitrary locations. For instance, over a centralized connectivity, a randomly positioned node exchanges information data between a fixed cellular tower; and in an infrastructure-free network, ad hoc connectivity is enabled among arbitrarily deployed terminals.

Now that we have a holistic view for spatially generating a wireless network, we may further upgrade the model by including the mobility aspect. Certainly, this would add further realism to the emulation, but would in return intensify the difficulty of the analysis. For the simplest case, a motionless model may be assumed for a variety of fixed networks. It can for instance be of practice for centralized networks such as fixed WiMAX that provides broadband wireless connectivity to urban-based infrastructures ranging from: office buildings, residential areas, and other commercial properties. It may also characterize decentralized WSN and WMN networks assembled respectively by immovable sensors and rooftop mesh schemes.

---

[1] In this context, actuators are active nodes that perform mechanical operations after being triggered by onboard sensors (e.g. small robots).

Beyond these networks, some transportable units exhibit a quasi-stationary behavior. Indoor WLAN is a relevant case where equipments such as notebooks and tablets are typically active when subscribers are stationary in a particular location. For example, in a campus setting, during different times of the day, users could either be connected while in classes, library, cafeteria, etc. Although these information terminals are mobile, yet due to the nature of their connectivity, they could for analysis purposes be considered as immobile units.

As for fully movable devices, various mobility models can be used for mapping a network structure. The broad idea of these models is to change users' spatial pattern with time. One approach would be to consider deterministic motion in such a way that forces nodes to move in a predefined path. However, random direction and speed is generally more appropriate for representing the mobility of uncontrolled wireless terminals. Essentially, there are two forms of random motion, either group or entity mobility models [58]. For group mobility (e.g. RPGM), each cluster has a leader that determines the motional behavior for the entire group. On the other hand, in the case of entity mobility, the motion of a node is independent from other terminals within the network. In this scenario, there exist many models; most notably among them are random waypoint, random walk and Brownian motion. Specifically, random waypoint enables pause times between every change in direction and speed; and when the pause times are eliminated then the waypoint model transforms into the random walk mobility. Also, when the movement distances are relatively small, then the random walk mobility becomes similar to a Brownian motion. Overall, these different random mobility options are memoryless. In contrast, the so-called Gauss-Markov mobility is a memory model because at each interval the next position is calculated based on the current location [59].

On the whole, the larger context of Figure 2.1 aims at looking at each of the network attributes separately, and then the desired network can be customized by combining the specific characteristics. Thus, the categorization presented here will ultimately facilitate and help put into perspective the geometrical research reported in this dissertation, and hopefully it will also steer and incite future spatial-level research directions.

2.2.2 – UCN Spatial Modeling

There are various antennas available for the effective EM emission, where each has a distinct radiation pattern and coverage, serving a particular wireless application. When the radiation is

intended to radially propagate with a constant power in all-directions seen from a top-view on a surface away from the transmitter, it is then referred to as an omni-directional antenna. Otherwise, the antenna is directional, meaning that it radiates over a certain coverage space and not in others. For analytical convenience, the so-called isotropic antenna has been mathematically conceived to idealistically model an omni-directional emitter. Although the radiation of an isotropic antenna is realistically unachievable, theoretically it stretches outward in a perfect spherical way; whereas an omni-directional antenna has a toroidal-like shape with a small inner opening as illustrated in Figure 2.2.

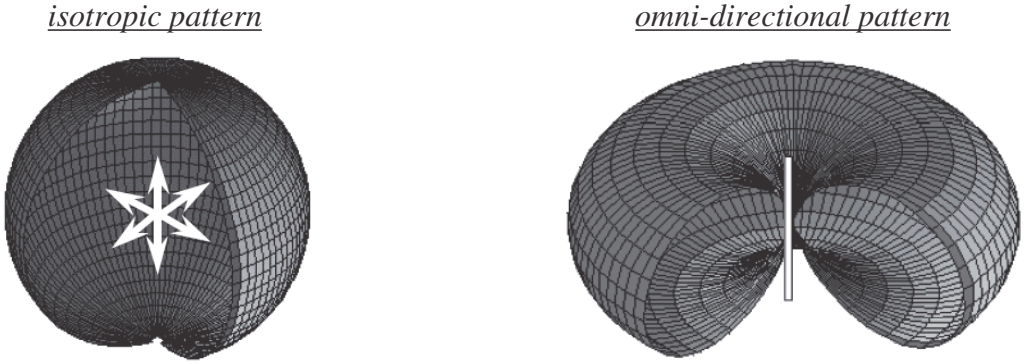

Figure 2.2 – All-direction antenna radiation models (3D) [49]

Irrespective of whether the model pattern is isotropic or omni-directional, when projected on a Euclidian plane, the extent of the EM propagation will result in a perfect circular contour where the BS is located at its centroid. However, practically speaking, the radiation shape will actually be irregular in format due to external agents such as channel losses caused by terrain features, manmade obstacles, and atmospheric attenuation [60].

Figure 2.3 visually depicts the actual and ideal radiation profile for an emitting tower station serving mobiles via centralized connectivity. As noted in the diagram, the power of the signal strength decays as the wave travels away from the BS. In principle, the cellular adjustment from the actual to the ideal is performed in order to facilitate various cellular-based technical analyses. Also, it will enable the spatial emulation of random networks. In other words, the geometrical construction of a network contained by an unpredictable lattice shape is mathematically demanding and likely inconceivable. On the other hand, spatially positioning an LWN in a well-defined cellular structure may analytically be realized via stochastical techniques.

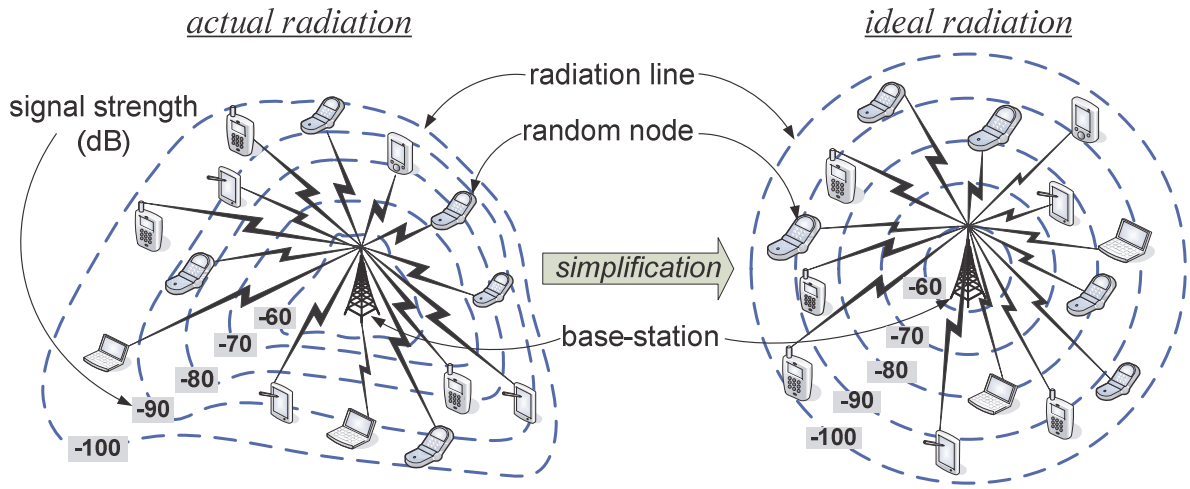

Figure 2.3 – Impact of channel features on EM radiation pattern (2D)

2.2.3 – MCN Spatial Modeling

From the previous part, we systematically recognized that despite the difference in radiation modeling and the impact of various channel deteriorations, the circular cell remains the most natural realization over a Euclidian surface. However, in the event where a wireless network is expected to supply connectivity service to a vast geographical territory that contains a high-density of subscribers, a single macrocellular choice will not yield the best experience for providers and users alike. As an alternative, smaller multi-cellular option known as microcells are preferred for a number of reasons, most notably because:

- Shrinking the cell size is an effective way for increasing the information throughput of bandwidth-demanding wireless users [48], [61].
- Mobile terminals will consume less transmission power given their closer proximity to the BS; thus ensure a longer system operation.
- PL level will be smaller, resulting in an MS with better fidelity due to a higher value of SNR/SINR.
- The notion of frequency reuse will be implementable following a tolerable spatial-separation; hence, additional mobile subscribers can be accommodated active connectivity.
- Although to a lesser degree, yet transmission latency will also diminish, which may prove to be a necessary delivery requirement especially for delay-sensitive multimedia applications.

- The electronic systems of the BSs will be more affordable given their demand for low-power emissions.

However, in addition to these benefits, there are several challenges that require exceptional attention when numerous microcells are considered; the most prominent elements are:

- The need for robust handoff capability in order to appropriately minimize the dropping rate probability.
- Dynamic network planning and management so as to ensure appropriate resource allocation and effective power control.
- Degradation due to intercellular interference.
- Infrastructure installation and maintenance cost of strategically distributed BSs.

Figure 2.4 illustrates the adaptation of a large UCN into smaller MCN. As shown in the depiction, the subnetworks will have smaller transmission radii that are managed by low-power BSs. For a particular geographical area, these cells are jointly handled by a nearby mobile switching center (MSC), where the data path that connects the subnetworks to the MSC backbone is known as the backhaul links. Specifically, there are three possible ways for implementing the backhaul connection, either via: radio, telephone line or fiber optics. In this organization, the MSC is the intermediary that routes back and forth a network interconnection with the rest of the world.

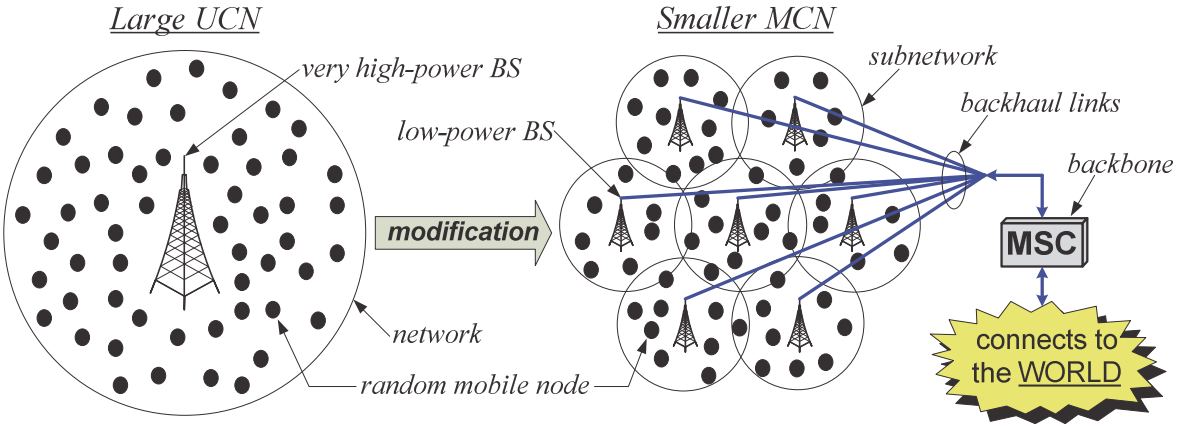

Figure 2.4 – A microcellular alternative for a large densely-populated macrocell network

In the model of Figure 2.4, the MCN realization produces an overlapping of subnetworks; thus complicating theoretical evaluation and analysis of such large access schemes. One way to overcome this burden would be to de-correlate the spatial overlap. However, this will occur at the expense of neglected surfaces. In Figure 2.5 we demonstrate the size of this gap as a function of adjacent cells, where $r_T \in \mathbb{R}_+^*$ is the constant power transmission radius of a BS, and $A_G \in \mathbb{R}_+^*$ is the marked area bounded by contiguously positioned cells. As suggested from the network models, the surface level of the created gap increases as the number of cells augments.

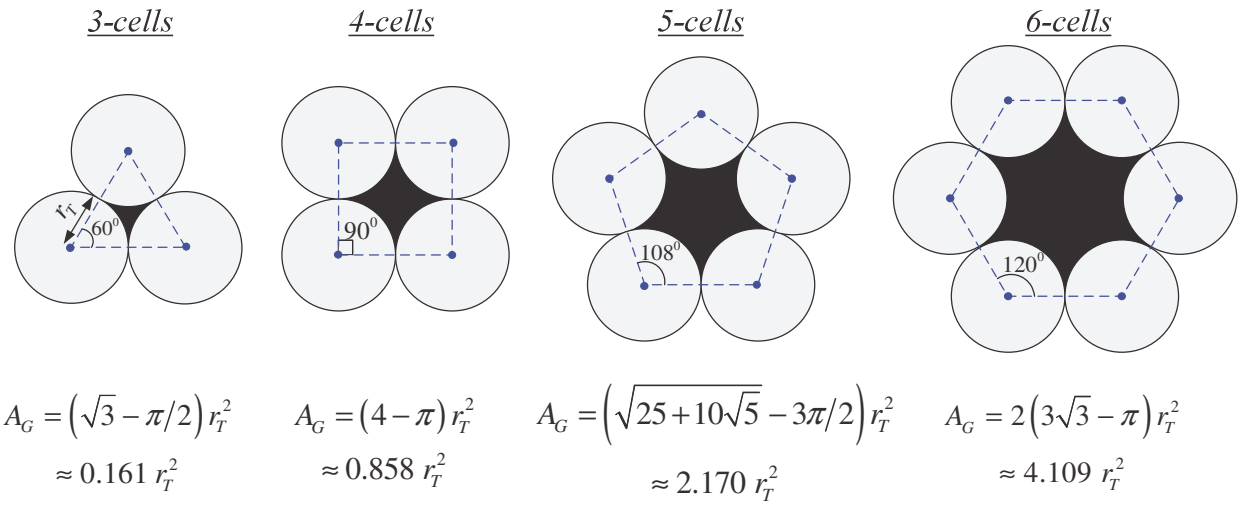

Figure 2.5 – Tendency of surface gaps among bordering cells

Indeed, having coverage holes in the model obviously defeats the notion of pervasive connectivity. Consequently, the better option for this architecture would be to consider non-intersecting structures. In effect, as exemplified by Figure 2.6, there are three possible models that exhibit tessellating traits which suit the purpose for MCN deployment.

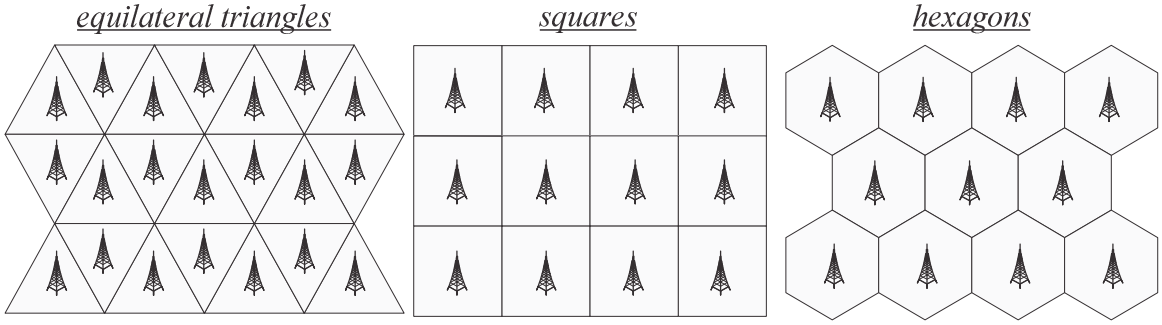

Figure 2.6 – MCN modeling by means of tessellating structures

Evidently, literatures in cellular theory have suitably argued the benefits of the hexagonal cell as the foremost tessellating form because of its closer resemblance to the circular contour. Though visually this observation is persuasive, yet we find it technically intriguing to quantify the actual extent of the hexagonal advantage. Following geometrical analysis for the identified tessellating forms, in Table 2.1, the definitive results to this concern are explicitly reported.

Table 2.1 – Quantitative comparative analysis of tessellating patterns

	equilateral triangle	square	hexagon
lattice structure	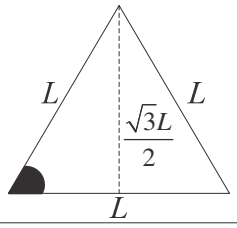	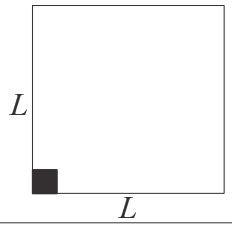	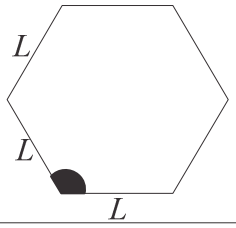
geometrical properties	•no. of edges = 3 •internal angle = 60^0 •perimeter = $3L$ •area = $\sqrt{3}L^2/4$	•no. of edges = 4 •internal angle = 90^0 •perimeter = $4L$ •area = L^2	•no. of edges = 6 •internal angle = 120^0 •perimeter = $6L$ •area = $3\sqrt{3}L^2/2$
circular reference	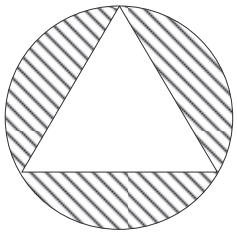	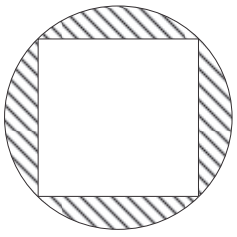	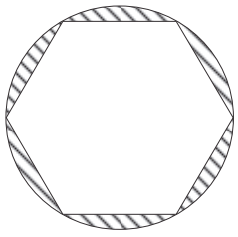
relative portion of selected area	$\left(1-3\sqrt{3}/4\pi\right)$ ~ 58.7%	$\left(1-2/\pi\right)$ ~ 36.3%	$\left(1-3\sqrt{3}/2\pi\right)$ ~ 17.3%
tessellating reference	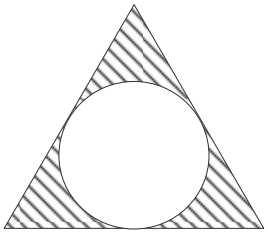	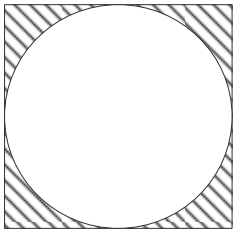	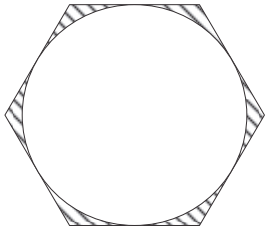
relative portion of selected area	$\left(1-\pi/3\sqrt{3}\right)$ ~ 39.5%	$\left(1-\pi/4\right)$ ~ 21.5%	$\left(1-\pi/2\sqrt{3}\right)$ ~ 9.3%

As it can be noticed form the above table, the numerical values of the dashed areas are congruent with their respective illustrations. In fact, the triangular geometry demonstrates the largest terrain margin when compared to the ideal constant power disk model. The second largest surface variance is exhibited by the square lattice. As for the hexagonal cell, it produces the smallest difference. Indeed from conventional wisdom, we know that the more a cellular shape has edges, the closer its resemblance to the circular cell. Meanwhile, we also interchanged the role of the reference structure for assessing the surface measure. Irrespective of the approach we scrutinize this problem; the hexagonal lattice remains the best possible tessellating choice by a comfortable margin; thus legitimizing it as the standard shape for MCN modeling and analysis.

Roughly speaking, as the lattice changes from a triangular profile, to a square, and subsequently to a hexagonal shape, the surface discrepancy drops by approximately $1/2$. Overall, this is a remark which may serve as a quick rule of thumb during network analysis.

2.3 – Propagation Modeling

2.3.1 – Sources for Channel Corruption

On the whole, information communicated between a transmitter and a receiver will be impacted by: the propagation channel, the Doppler shift due to mobility, the effect of interference, the additive white Gaussian noise, and the phase deviation due to synchronization issues.

Specifically, the behavior of the propagation channel is a key element for defining the attributes of a particular communication link. In wireless networking, the channel can actually be categorized for underwater access, terrestrial communications, and satellite transmission. In fact, for each of these cases the channel is faced with a certain drawback. For example, in the case of satellite broadcast, due to the large gap between an earthbound node and the outer-space orbit, the propagation delay will be high. As for terrestrial networking, fading is resulted because of the abundance of scatterers. And for underwater interconnection, it will combine the shortcomings of the other two cases, thus an elevated latency and poor channel quality will result.

2.3.2 – Modeling Wireless Radiation

For terrestrial communications, as the EM wave propagates form a radiating source, the behavior of the emitted energy will vary as a function of the distance away from the transmitting antenna.

Essentially, as shown in Figure 2.7, the radiation can be broken-down into multiple regions having exceptional characteristics [47], [50].

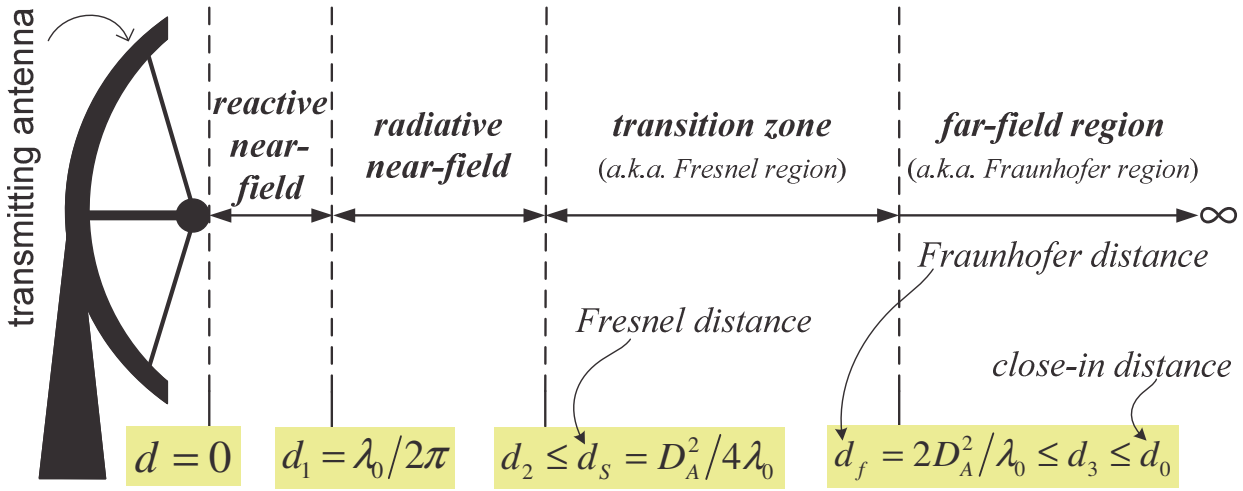

Figure 2.7 – EM radiation boundaries

Before describing the features of each of these regions, for context, it is valuable to comment on some aspects relating to the EM radiation model:

1. It is worth noting that although the illustration above shows a directional antenna, the principle is as well applicative with an omni-directional radiator, where these regions will surround the transmitter unit in a circular-ring layout.

2. It should be remarked that there is a lack of universal agreement for the radiation boundary values $d_1, d_2, d_3 \in \mathbb{R}_{+,*}^3$ in available literature. Therefore, diverse communication organizations and sources may define them differently.

3. Nonetheless, rough non-firm estimates of the boundaries have been conceived in order to facilitate analytical evaluation. Normally, the mathematical model of boundary values for these regions will depend on:
   - the operating frequency: $f_0 \in \mathbb{R}_+^*$.
   - the close-in distance of the emitter: $d_0 \in \mathbb{R}_+^*$.
   - the largest dimension of an antenna or its aperture width: $D_A \in \mathbb{R}_+^*$.

In what follows, we will briefly explain the most notable properties of the four regions shown in Figure 2.7:

- 1st Region – Reactive Near-Field: $0 \le d \le d_1$

  This region is extremely close to the antenna surface. Say, as premised throughout this dissertation, that the carrier frequency is set to $f_0 = 1.9$ GHz, then the associated wavelength is $\lambda_0 \approx 0.16$ m because $\lambda_0 = c/f_0$, where $c \approx 3\times10^8$ m/s is the speed of light in vacuum. This means that the span of the region is approximately 2.5 cm away from the antenna. Within this small gap, the relationship between the electric field (E) and the magnetic field (H) is too complex to predict; namely the EM fields are not orthogonal to each other.

- 2nd Region – Radiative Near-Field: $d_1 \le d \le d_2$

  In order to assess the amount of power decay in the channel of this region, we need to fully predict the behavior of the EM radiation and the polarization which describes the relationship among the E and H fields. In general, EM waves have four possible polarization types: horizontal, vertical, circular, and elliptical. Incidentally, in this interspace, all these polarizations can be present at once. Although more predictable than the reactive near-filed region, yet conceiving a channel-loss model under such conditions remains analytically demanding because the radiation pattern is significantly sporadic.

- 3rd Region – Transition Zone: $d_2 \le d \le d_3$

  In this Fresnel region, near-field and far-field characteristics are jointly manifested; thus challenges of mathematical formulation and tractability remains.

- 4th Region – Far-Field Region: $d_3 \le d < \infty$

  Evidently, in the Fraunhofer region, a unique polarization type is in effect, i.e. the EM fields are orthogonal to each other. As a result, the channel attenuation can be forecasted by analytical models as the wave energy is gradually propagated away from the antenna.

In any case, as a practical rule of thumb, the distinction between near-field and far-field can be made in a straightforward way by comparing the propagation distance d to the transmission wavelength:

$$\text{near-field region: } d \ll \lambda_0 \tag{2.1}$$

$$\text{far-field region: } d \gg \lambda_0 \tag{2.2}$$

On the whole, in this subsection, we demonstrated the unpredictability of the propagation channel extending from the antenna surface up until the far-field mark. Once the radiation wave reaches the close-in distance d_0, then feasible fading models may be utilized in order to adequately anticipate the power lost over the wireless medium.

2.3.3 – Modeling Channel Losses

Indeed, when the EM wave is emitted from source to destination, the transmitted information signal is deteriorated due to fading. In fact, the effect of fading can actually be split into a dominant and a weaker component. The dominant part is identified as large-scale fading, and it usually comprises of average PL and random shadowing[2]. As for the weaker part, it is known as small-scale fading, and it represents the multipath propagation.

In general, over a specific communication environment, the extent of the channel-loss can be measured empirically using a power-meter or a measuring-receiver through a gradual progression away from the transmitter about the beam-width of an antenna. For small-scale fading, shadowing, and PL, the probing interval accuracies are respectively somewhere in the vicinity of $\Delta \approx \lambda_0$, $40\lambda_0$, and $1000\lambda_0$ meters.

Ideally, analytical modeling for the propagation behavior should take into account all these channel losses together. However, in the larger scheme of things, the influence of small-scale multipath fluctuation is minor and at times negligible when compared to the overall energy loss. Thus, ignoring small-scale fading exclusively for power parameterization aspects is generally tolerated. Besides, removing this feature and considering only the more significant and

[2] Without loss of generality, large-scale fading and PL may be utilized interchangeably. In fact, when the PL terminology is used, though implicit, it often insinuates the inclusion of shadowing.

noticeable large-scale attenuation is expected to simplify the perplexed analysis anticipated in forthcoming chapters.

In general, whether for short-range picocell coverage or long-range macrocellular applications, the large-scale fading model will usually depend on a particular set of attributes as shown by:

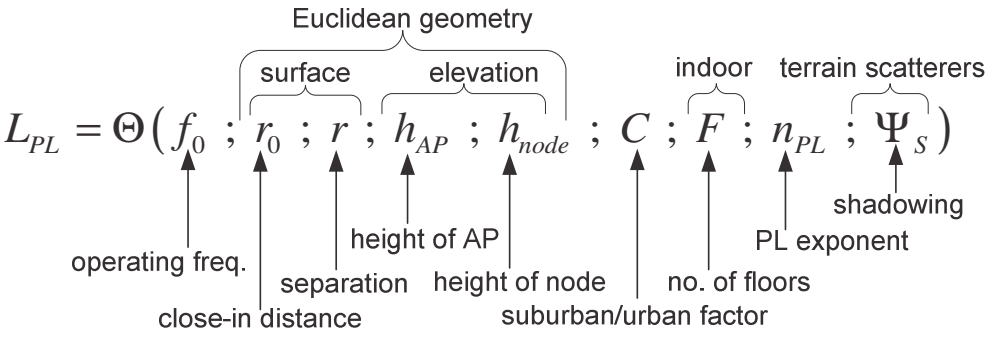

(2.3)

Of course, the actual model for each communication type will specifically be tailored to the particular application. This means that the model expression for the large-scale fading will behave in unique manner for the targeted channel. However, after entering some of the distinctive channel and geometry details, such as C and F, and provided the elevation values for the AP and node are set to some preassigned values, then no matter the model selected, it will typically reduce to a simple distance-dependency expression.

In fact, the received power between two interconnected nodes is given by $P_{RX}(r) = EIRP / L_{PL}(r)$ over $\mathbb{R}_+^* \mapsto \mathbb{R}_+^*$, $\forall EIRP \in \mathbb{R}_+^*$ radiated power, where the large-scale channel attenuation is expressed by $\exists L_{PL}(r) \in \mathbb{R}_+^* : L_{PL}(r) > 1$. Furthermore, it is shown (say [47]) that the large-scale fading for mobile cellular communications is modeled by:

$$L_{PL}(r) = \overline{L_{PL}(r)} \cdot \Psi_S = \overline{L_{PL}(r_0)} \cdot (r/r_0)^{n_{PL}} \cdot \Psi_S \tag{2.4}$$

where the average decay is given through $\exists \overline{L_{PL}(r_0)}, \overline{L_{PL}(r)} \in \mathbb{R}_{+,*}^2 : \overline{L_{PL}(r)} \geq \overline{L_{PL}(r_0)} > 1$ for $\forall r_0, r \in \mathbb{R}_{+,*}^2 : r_0 \leq r$ denoting respectively the close-in distance and the internodal gap;

$n_{PL} \in \mathbb{R}_+^* : n_{PL} > 1$ is the PL exponent; and $\Psi_S = 10^{\Psi_{S-dB}/10} \in \mathbb{R}_+^*$ is the shadowing element that analytically emulates in-field scatterers through a log-normal distribution: $\Psi_{S-dB} \sim \mathcal{N}_S\left(0, \sigma_\Psi^2\right)$, where $\sigma_\Psi \in \mathbb{R}_+^*$ is the associated SD in dB (and it is a.s. that $\sigma_\Psi > 1\,\text{dB}$). Alternatively, the model of (2.4) may be changed into decibel notation as follows:

$$\begin{aligned} L_{PL}(r)_{dB} &= \overline{L_{PL}(r)}_{dB} + \Psi_{S-dB} \qquad\qquad r \geq r_0 \\ &= \overline{L_{PL}(r_0)}_{dB} + 10 n_{PL} \log_{10}(r/r_0) + \Psi_{S-dB} \\ &= \overline{L_{PL}(r_0)}_{dB} - 10 n_{PL} \log_{10}(r_0) + 10 n_{PL} \log_{10}(r) + \Psi_{S-dB} \end{aligned} \tag{2.5}$$

The large-scale fading model of (2.5) can actually be reorganized and remapped to (2.6), where the close-in contribution along with its average channel-loss are included in α, and n_{PL} which depends on the propagation environment, such as the existence of line-of-sight (LOS) or otherwise, is integrated in β; and the PL dual (α, β) are elements in $\mathbb{R}_{+,*}^2$.

$$L_{PL}(r)_{dB} = \overline{L_{PL}(r)}_{dB} + \Psi_{S-dB} = \underbrace{\alpha + \beta \log_{10}(r)}_{\text{average PL}} + \underbrace{\Psi_{S-dB}}_{\text{shadowing}} \qquad r \geq r_0 \tag{2.6}$$

Therefore, whether for cellular communications or else, the large-scale fading may reliably be represented by the following simple formulation, where the particular propagation features are incorporated in α and β. Besides, mapping via simpler variables has the exceptional advantage for facilitating analytical manipulations. Overall, from the above model, we realize that:

- The dominant power loss between two nodes, which is centrally dependent on the interspace magnitude, is composed of PL and shadowing.
- The wireless channel attenuation among vertices adheres to an inverse power law.
- The shadowing component is interpreted by a log-normal distribution.
- Because of its negligible impact on the overall power loss, the small-scale fading fluctuation is relaxed.

2.4 – Overview of IEEE 802.20

Throughout the course of this dissertation, whenever needed for computational verifications, we will utilize actual parameters from IEEE 802.20. Thus, we find it necessary to briefly discuss some of the particulars of this relatively recent 4G standard.

Evidently, the cellular concept for mobile systems started few decades ago; however, its importance is even more significant as we migrate to next generation networks. In the time of this writing, such advanced technologies are mainly characterized by: LTE, WiMAX, and MBWA. In particular, as it can be seen by Figure 2.8, the MBWA standard is essentially the *missing link* between WMAN and WWAN networks. Namely, the unique fact that it combines the advantages of both topologies is the leading motive for this architecture.

Specifically, in June 2008, IEEE 802.20 or MBWA mobile technology was approved by the IEEE Standard Association Board. Soon after, in August 2008, the first active MBWA standard was published [62]. In essence, the aim of this protocol is to fill the current demand gap of increased mobility of up to 250 km/hr and a spectral efficiency of at least 1 bps/Hz/cell [63]. As for IEEE 802.16e-2005, it has a data rate that could practically reach 10 Mbps over 2 km under NLOS; but can only support radios with vehicular speed of 60+ km/h [64]. On the other hand, currently operable cellular systems, irrespective of whether they are founded on the global system for mobile communications (GSM) or code division multiple-access (CDMA), offer substantially higher mobility at the cost of low bandwidth. Therefore, it was natural to combine these advantages to form the essence of the IEEE 802.20 technology.

Additionally, when compared to other mobile systems, such as: EDGE, UMTS, CDMA2000 1xRTT and 1xEV; MBWA has the highest spectral efficiency [63]. And this criterion is needed because it will exploit the licensed channel BW more adequately; hence resulting in a cost-effective approach for providers and consumers alike.

Further, the IEEE 802.20 specification only defines the lower physical (PHY) and media access control (MAC) layers of the OSI model; thus granting vast compatibility with an array of systems through the upper network levels. Also, it has low latency with a frame round trip time (RTT) of at most 10 ms [63]. And in fact, there is a direct relation between latency and performance [65], which may be traded among each other to enhance the real-time experience and to satisfy the service delivery. Application wise, MBWA is specifically optimized for

mobile-IP connectivity. Furthermore, because the system has a short RTT, it may also be used for telephony purposes such as voice over IP (VoIP) exchanges.

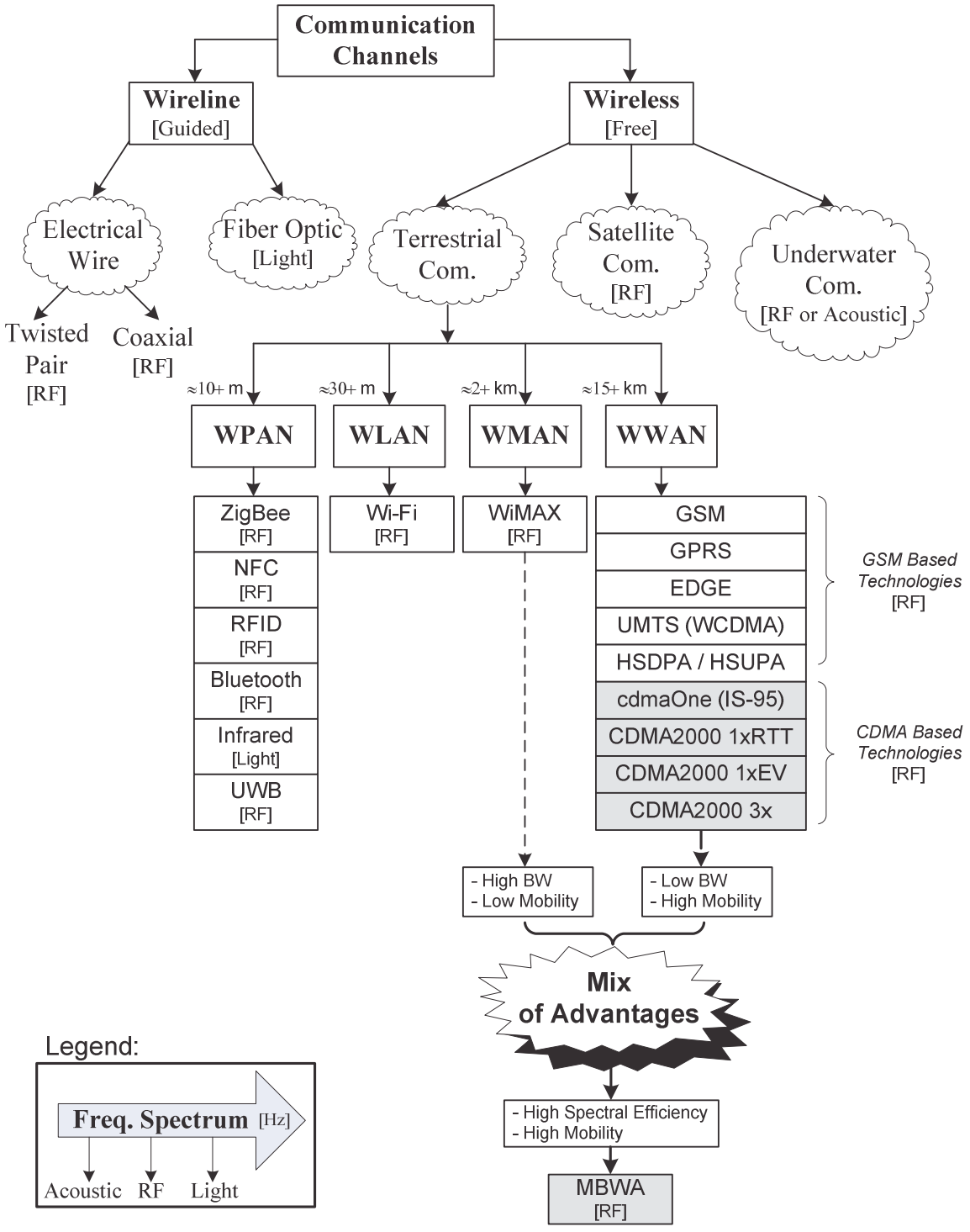

Figure 2.8 – Connecting and comparing the MBWA standard to other technologies

Overall, IEEE 802.20 is a technology that has many benefits; nonetheless, because it is a novel system, BS infrastructure cost is inevitable. Though, it is worth noting that in some circumstances, it may be possible to reuse existing cellular towers. In Table 2.2, a summary of the key MBWA properties is shown.

Meanwhile, the anticipated large-scale fading distribution functions that will be derived for MCN, UCN, and Gaussian random network models in subsequent chapters will be as generic as analytically possible. Nonetheless, to verify the veracity of these theoretical derivations, MC simulations will be applied. Thus, for these computational purposes, we will utilize channel specifications from the MBWA standard. Also, using actual channel parameters will further harmonize and connect fundamentally derived results to practice. In particular, the IEEE 802.20 technology supports three different channel environments, which will all be utilized during simulations; and they are as follows:

- Urban Macrocell based on the COST-231 Hata-Model – Tables 3.2
- Suburban Macrocell based on the COST-231 Hata-Model – Tables 4.2.
- Urban Microcell based on the COST-231 Walfisch-Ikegami-Model – Table 5.1.

As indicated, the particular parameters for each of these propagation models can be found by referring to the indicated tables found respectively in Chapters 3, 4, and 5.

Table 2.2 – Specifications of the MBWA technology

technology name	MBWA
date of approval	IEEE approval – Jun. 12, 2008
standard	IEEE 802.20
standard publication date	Aug. 29, 2008
industry consortium	iBurst Association
network type	WMAN
coverage range	~15 km [long-range]
terminal mobility	up to 250 km/hr [fast vehicle]
network topology	P2MP
network centralization	centralized cellular architecture
spectrum licensing	licensed band
ITU spectral band	UHF / SHF
frequency range	0.5 to 3.5 GHz
channel BW	2.5 to 20 MHz [FDD OFDMA] 5 to 40 MHz [TDD OFDMA] 625 kHz/carrier [TDD 625k-MC]

peak data-rate per user [or per carrier for 625k-MC]	1 to 4.5 Mbps [DL OFDMA] 0.3 to 2.25 Mbps [UL OFDMA] [values are only for the following BW: BW_{FDD} = 1.25 MHz | BW_{TDD} = 2.5 MHz for other BW use ratios of the values shown here] 1.493 Mbps [DL 625k-MC] 0.5712 Mbps [UL 625k-MC]
maximum EIRP	57 dBmW = 501.2 W [DL] 27 dBmW = 0.5 W [UL]
dominant fading p.d.f	Rayleigh fading [NLOS]
duplexing technique	FDD or TDD [OFDMA] TDD [625k-MC]
multiple-access and modulation	OFDMA / BPSK, QPSK, QAM HC-SDMA / 625k-MC [QAM]
key advantages	mobility, spectral-efficiency, low-latency, long-range
key disadvantage	cost of infrastructure
potential applications	mobile-IP, VoIP

2.5 – Conclusion

In this chapter we reviewed some of the essentials of network geometry and propagation modeling. In particular, we showed a coherent and comprehensive approach for building a spatial structure for a LWN pattern. Then, we focused specifically on the modeling approach aimed for UCN and MCN spatial deployments. Next, we discussed the main causes for channel corruption, the fundamentals of radio propagation, and the means for modeling transmission losses. We then provided the necessary details for analytically expressing the characteristics of the large-scale fading behavior for general wireless channels and cellular systems.

Finally, we briefly introduced the features of IEEE 802.20 cellular technology, where its commercialization is managed by the industry consortium known as iBurst Association. In fact, under their umbrella, the MBWA network has been successfully deployed in several countries around the globe. Precisely, this protocol has promising potentials for providers and subscribers because of mobility, spectral efficiency, low latency, long-range, and it is specifically optimized for mobile-IP connection and VoIP applications. In fact, we provided this overview because the channel features of this standard will regularly be utilized in subsequent chapters during computational analysis and verifications.

Overall, the discussed topics will be instrumental for modeling a random network and deriving fundamental results from it. Namely, the presented foundation of the network geometry will become handy during the derivations for exact random homogenous deployments, and for conceptualizing inhomogeneous spatial algorithms aimed for UCN and MCN models. Likewise, the primer for modeling the large-scale fading will be exploited in order to profile the expected amount of power loss between a reference AP and a random node over different network geometries.

Chapter 3

Homogeneous Network Modeling and Large-Scale Fading Analysis

3.1 – Introduction

3.1.1 – Objective

Many decades have passed since the conception of the cellular network; however, despite the years and accumulated experience, there still remain numerous technical facets that have not been investigated thoroughly. The most notable among them is the paradigm of spatial random networks. In principle, within this context, it is desired to overlay nodes geometrical position onto the traditional fundamentals and understanding of mobile systems, where the broad motive is to analytically extract critical network-based observations, such as the likelihood of coverage.

For wireless communications, large-scale fading is indeed the most overarching factor for ensuring connectivity between a BS and an MS. In fact, due to its prerequisite for a host of network metrics including outage probability, the density function for the PL or the received power level have been previously shown for a fixed predetermined separation between an MS and a BS [47]–[51]. The aim in this chapter is to reconsider this analytical problem by generalizing the channel-loss distribution between any homogeneously-based random positioned node and a reference BS. Evidently, this PDF can typically be obtained experimentally based on MC simulations. However there are two leading reasons why this approach is inconvenient:

1. Random simulation is an inefficient computationally expensive approach.
2. The obtained result is analytically intractable.

These factors are further testaments for the necessity to obtain an explicit, generic and rigorous theoretical derivation for the large-scale fading density.

3.1.2 – Organization

The rest of this chapter is organized as follows. In Section 3.2, we will set the stage for network analysis by jointly assimilating the fundamental characteristics of spatial homogeneity and lattice geometry. Then, in Section 3.3, the random network emulation geared specifically for MCN channel analysis will be detailed. Afterward, in Section 3.4, the large-scale fading PDF analysis will be developed, and the exact closed-form stochastic result will be verified using MC experimentations. Finally, Section 3.5 will close the chapter and a number of possible directions for using and extending the reported formulation will be mentioned.

3.2 – Characteristics of the Network Model

3.2.1 – Uniform Network Geometry

In order to understand the behavior of wireless networks, emulation by means of mathematical modeling is indispensible. Of course, there are various approaches and conjectures used for reconstructing a network constellation. Despite these techniques, the random homogeneous assumption has been considered extensively in analytical research, e.g. [18]–[30]. Essentially, the definition of a homogeneous network indicates a steady number density throughout the deployment field; i.e. the number of mobile terminals per unit of area is fixed.

As depicted in Figure 3.1, if we consider $A_0 \in \mathbb{R}_+^*$ to be the surface area of a particular network lattice, and $n_0 \in \mathbb{N}^*$ to represent the amount of random nodes or scale of the architecture, then the homogeneous areal density will be given by $\rho_0 \triangleq n_0 / A_0$.

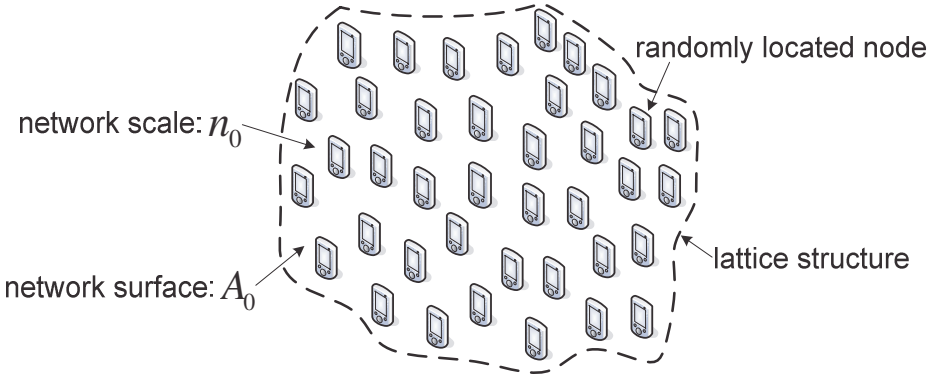

Figure 3.1 – Homogeneously deployed random network

When no major information about the considered network exists, then this spatial realization is simple, conceivable and quick to theorize and model. Only the surface structure and its size are needed for the analysis. As for the network scale, following analytical derivation, it could dynamically be determined by the deployment designer. This is one important convenience of planar distributions in contrast to point processes.

From a practical standpoint, this distribution model is accurate provided the terrain has no biases. In other words, the network surface must entirely be flat or equalized in format with no landforms or structures. Put differently, the land must have similar attributes, such as in: environment, topographical quality, temperature, etc. Whether in rural or urban setting, the occurrence of such a case for a LWN is for the most part uncommon. Nonetheless, the simplistic condition of the model enforces its analytical appeal and surpasses this drawback.

3.2.2 – Geometrical Alternative for Simplifying Channel Analysis

The major objective of this chapter is to obtain the large-scale fading distribution function between a homogeneously distributed random node and a reference service provider over a MCN model. In order to do this, the emulation of the random network must entirely be characterized. Exclusively in this subsection, we will discuss geometrical changes to the emulated network lattice so that the associated channel-loss derivation is simplified.

First of all, from visual inspection, it is clearly possible to dismember the hexagonal cell into smaller repetitive forms. The original cell could for instance be recreated by joining three rhombus lattices or six equilateral triangles. In fact, the equilateral triangle is the most elementary portion of this cell model. Thus, considering this sub-pattern for BS-to-MS internodal analysis will substantially alleviate the derivation complexity of the large-scale fading distribution. In fact, this is true because geometrically speaking the analysis only depends on the reference to mobile separation, and is unaffected by the sectors rotation angle.

Also, for so-called infinite networks, the planar distribution function is definitely the most essential component in contrast to the quantity of nodes. Yet regarding the number of nodes, for each emulation case, its value is set *a posteriori* to the analysis, where the spatial position of every node will accordingly be generated from the density function. In fact, this is the key difference between point process techniques and planar distributions, where the former conditionally require the quantity of points before deployment and the latter does not.

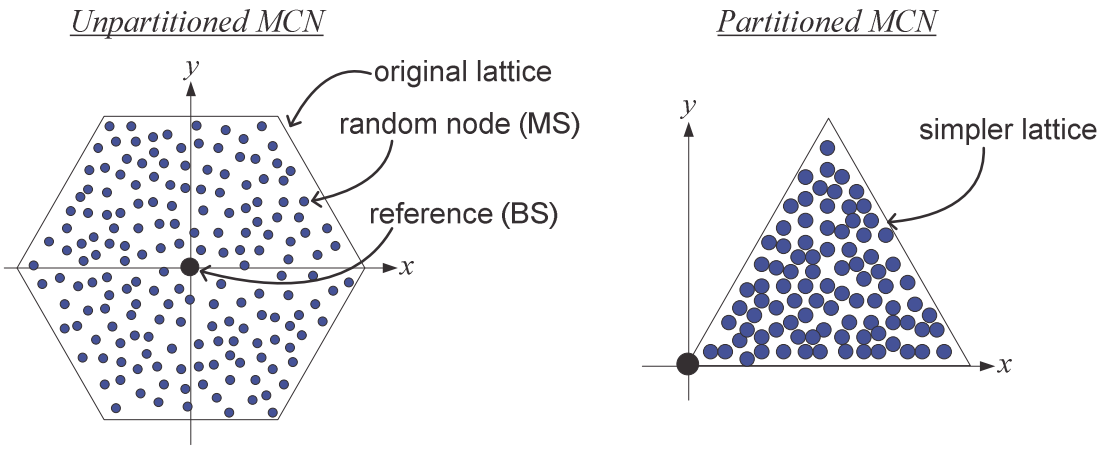

Figure 3.2 – Simplifying BS-to-MS channel analysis via geometrical partitioning

Overall, we want to highlight that for centralized channel-loss analysis, the partitioned random homogeneous network shown in Figure 3.2 will exhibit the same stochastic outcome as the original hexagonal structure at the benefit of a simpler derivation. Moreover, for uniform planar deployment, the areal density of the random network will not affect the channel analysis.

3.3 – Random Network Emulation for Channel Analysis

3.3.1 – Geometrical Analysis of the MCN Lattice

The characteristics described previously, namely: nodal homogeneity, lattice geometry, and far-field radiation phenomenon, must collectively be incorporated in the spatial properties of the random network. In principle, this integration has a dual purpose:

1. It will be used to stochastically model the random lattice and effectively derive the PL density function for the entire network between a reference and an arbitrary terminal.

2. It will be employed to emulate actual random pattern instances, and numerically verify by means of MC simulations the precision of the anticipated large-scale fading formulation.

To proceed, in Figure 3.3 the hexagonal cell is represented with the far-field region. In this surface model, the cellular size L and the far-field limit r_0 are the essential elements that define the entire geometry of the network structure.

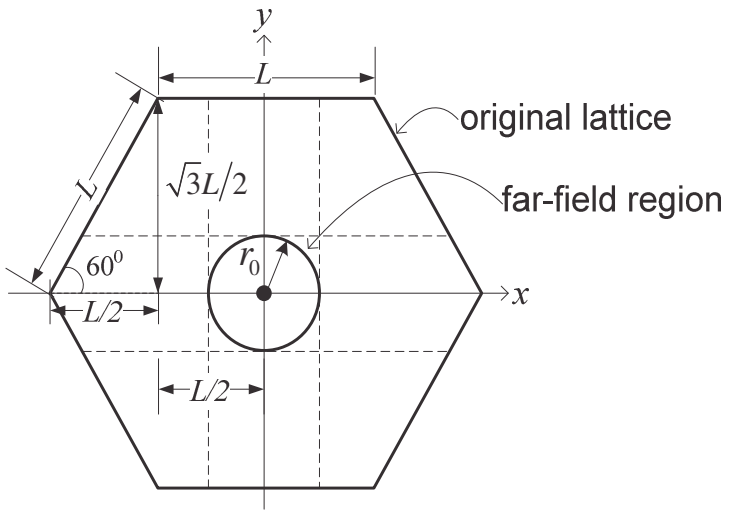

Figure 3.3 – Geometry of random network with far-field

For notational convenience, we will define a parameter for the cellular radius to the close-in distance ratio (RCR):

$$\forall L \in \mathbb{R}_+^* : \exists r_0 \in \mathbb{R}_+^* : \mu \triangleq L/r_0 \tag{3.1}$$

From the above rendering, we can determine the support range for the RCR indicator such that the layout of the lattice is preserved. In particular, values along the *x* and *y*-axes reveal that:

$$\{r_0 < L/2\} \cap \left\{r_0 < \sqrt{3}L/2\right\} = \{\mu > 2\} \cap \left\{\mu > 2/\sqrt{3}\right\} = \left\{\mu \in \mathbb{R}_+^* \middle| \mu > 2\right\} \tag{3.2}$$

Therefore, from (3.2) we notice that the geometry of Figure 3.3 holds provided the RCR is larger than two. But generally speaking, for mobile communications, the actual RCR is somewhere in the order of ten or greater, i.e. $\mu \gtrsim 10$.

Now, as motivated in Subsection 3.2.2, it is analytically rational to only look at a triangular sector for the analysis. Therefore, we decimate the cell model of Figure 3.3 into the subpart shown in Figure 3.4. Within this deployment surface, the various dimensions and variable relations of the lattice are accordingly displayed.

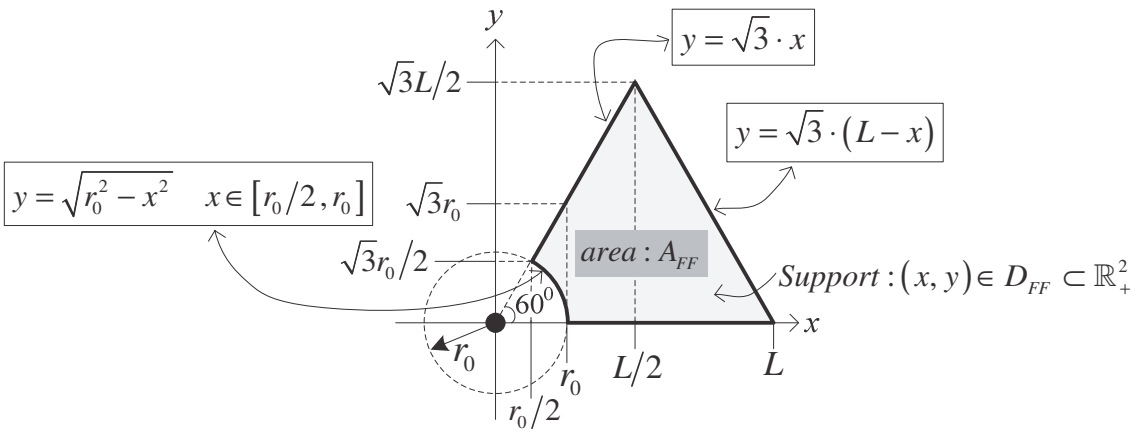

Figure 3.4 – Deployment surface for large-scale fading analysis

For homogeneous random positioning, the size of the deployment area is an integral part of the analysis. The surface with the effect of far-field is thus given by:

$$A_{FF}=\sqrt{3}L^2/4-\pi r_0^2/6=\left(3\sqrt{3}L^2-2\pi r_0^2\right)/12 \tag{3.3}$$

From (3.3), we obtain an expression in Cartesian coordinate notation for the spatial density function of a network cluster:

$$f_{XY}(x,y)=1/A_{FF}=12/\left(3\sqrt{3}L^2-2\pi r_0^2\right)=k_{FF}\quad (x,y)\in D_{FF}\subset\mathbb{R}_+^2 \tag{3.4}$$

Evidently, the homogeneous hypothesis has resulted in a steady distribution throughout the support area. For manipulation purposes, the intensity of the spatial density will be, as shown in (3.4), assigned to $k_{FF}\in\mathbb{R}_+^*$. As for the support domain of the deployment surface, with the impact of the Fraunhofer distance, it is given by:

$$D_{FF}=\left\{\begin{array}{c|c}(x,y)\in\mathbb{R}_+^2; & \sqrt{r_0^2-x^2}\le y\le\sqrt{3}x:\ x\in[r_0/2,r_0]\\ (r_0,L)\in\mathbb{R}_{+,*}^2: & y\le\sqrt{3}x:\ x\in[r_0,L/2];\\ r_0<L/2 & y\le\sqrt{3}(L-x):\ x\in[L/2,L]\end{array}\right\} \tag{3.5}$$

From (3.4) and (3.5), the marginal probability density for the nodal geometry along the *x*-axis can be determined by (3.6). The graphical representation of this PDF is accordingly displayed in Figure 3.5.

$$f_X(x)=\int_{(x,y)\in D_{FF}} f_{XY}(x,y)\,dy=k_{FF}\left\{\begin{array}{l}\left(\sqrt{3}x-\sqrt{r_0^2-x^2}\right)\cdot\mathbf{1}\left(r_0/2\le x\le r_0\right)\\ +\sqrt{3}x\cdot\mathbf{1}\left(r_0\le x\le L/2\right)+\sqrt{3}\left(L-x\right)\cdot\mathbf{1}\left(L/2\le x\le L\right)\end{array}\right\} \tag{3.6}$$

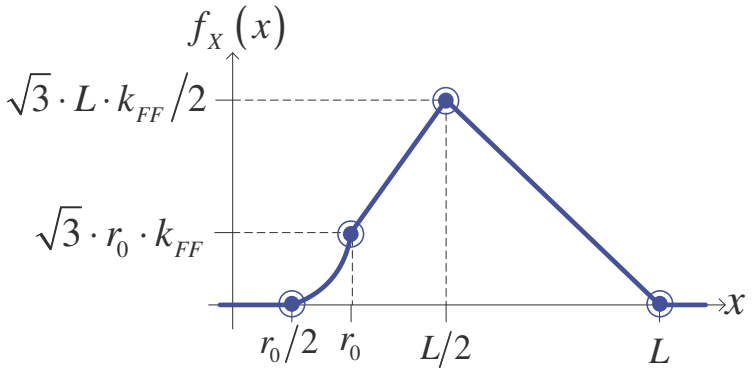

Figure 3.5 – Marginal PDF for spatial geometry along the *x*-axis

3.3.2 – Random Spatial Generation

At present, in order to efficiently generate random instances of *x*, the inverse CDF (ICDF) must be obtained; which consequently means that we first need to derive the CDF of (3.6). Following some analysis, we obtain:

$$\begin{aligned}F_X(x)&=\Pr\left(X\le x\right)=\int_{\tilde{x}=-\infty}^{x} f_X(\tilde{x})\,d\tilde{x}\\ &=k_{FF}\left\{\begin{array}{l}\left\{\sqrt{3}x^2/2-\left(x\sqrt{r_0^2-x^2}+r_0^2\arcsin\left(x/r_0\right)\right)\Big/2+\pi r_0^2/12\right\}\cdot\mathbf{1}\left(r_0/2\le x\le r_0\right)\\ \quad+\left\{\sqrt{3}x^2/2-\pi r_0^2/6\right\}\cdot\mathbf{1}\left(r_0\le x\le L/2\right)\\ \qquad+\left\{\sqrt{3}L\cdot x-\sqrt{3}x^2/2-\sqrt{3}L^2/4-\pi r_0^2/6\right\}\cdot\mathbf{1}\left(L/2\le x\le L\right)\end{array}\right\}\end{aligned} \tag{3.7}$$

In Figure 3.6 the derived marginal CDF is plotted, where each part is accordingly delineated. For completeness purposes, we also identified the CDF marks as a function of RCR.

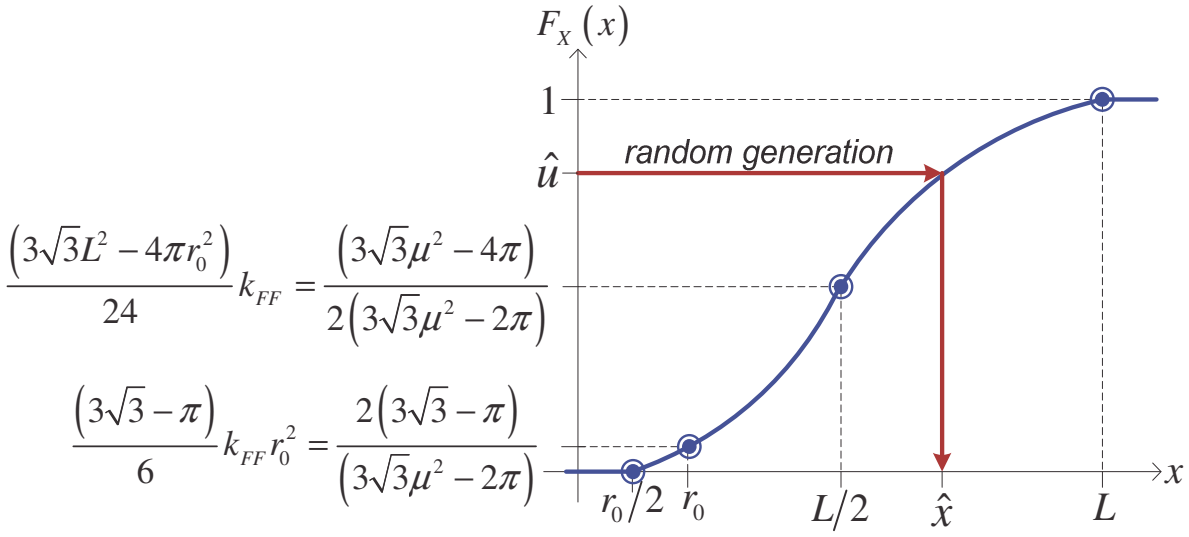

Figure 3.6 – Marginal CDF for spatial geometry along the *x*-axis

The most efficient way to randomly generate arbitrary instances would be to consider the inverse transformation method (ITM). As described in the arrows of Figure 3.6, the geometrical samples $\hat{x}$ are obtained through the ICDF. In particular, $(F_X)^{-1}(\hat{u})$ is computed by the use of random arbitrary samples generated from a standard uniform distribution. Altogether, random values are thus obtained by:

$$\hat{x}=\left\{(F_X)^{-1}\left(\hat{u}\sim\mathcal{U}(0,1)\right)\right\}\sim f_X(x) \tag{3.8}$$

In regard to the $\hat{u}$ in (3.8), it should be noted that most high-level computer simulation languages have a built-in pseudorandom (PR) sequence generated from a standard uniform distribution. Specifically, these values are obtained either through the multiplicative congruential algorithm or Marsaglia's generator. MATLAB® uses the latter with some modification to produce a very long PR sequence of length $2^{1492}\approx 1.370\times 10^{449}$ [66].

Although the method in (3.8) is the most efficient technique for random generation, the precondition in this approach requires the availability of the ICDF expression in closed-form notation. In the case of (3.7), it should be noticeable that it is in fact impossible to represent ICDF in an explicit way. As an alternative, the acceptance rejection method (ARM) can be used for random number generation (RNG) [67]. Granted, this iterative approach is suboptimal when compared to the ITM technique; nonetheless, in this section we will show an approach for modifying the ARM algorithm in order to maximize its performance.

Consider the distribution function $f_X(x): D_X \mapsto \mathbb{R}^+$, where the domain of the density is $D_X \triangleq \left[x_\alpha, x_\beta \right]$, and its associated extremities are given by:

$$x_\alpha \triangleq \min \chi \in \mathbb{R} \tag{3.9}$$

$$x_\beta \triangleq \max \chi \in \mathbb{R} \tag{3.10}$$

such that:

$$\chi \equiv \arg\left\{ \inf\left(f_X(x) > 0 \right) \right\} \subset \left(x \in \mathbb{R} \right) \tag{3.11}$$

Then, based on the ARM procedure, we would need to determine some continuous arbitrary bounding function, say $\pi_b(x): D_X \mapsto \mathbb{R}^+$, that covers the domain of $f_X(x)$, while $\pi_b(x) \geq f_X(x)$. Moreover, this bounding function is expected to be an augmented version to some valid comparison PDF $\delta_X(x): D_X \mapsto \mathbb{R}^+$. In fact, the most generic and simplest way would be to consider the uniform case for the comparison density, namely:

$$\delta_X(x) = \mathcal{U}_X\left(x_\alpha, x_\beta \right) \tag{3.12}$$

And thus, the bounding function can be realized by:

$$\pi_b(x) = k\delta_X(x) \quad \exists k \in \mathbb{R}_+^* : k \geq 1 \tag{3.13}$$

To further facilitate our understanding of these concepts, in Figure 3.7 we provided a graphical representation of the various functions needed for analyzing the ARM procedure. The likelihood for accepting a randomly generated sample is specified by the area below $f_X(x)$. In contrast, the remaining sector between $\pi_b(x)$ and $f_X(x)$ constitutes the rejection region of generated samples.

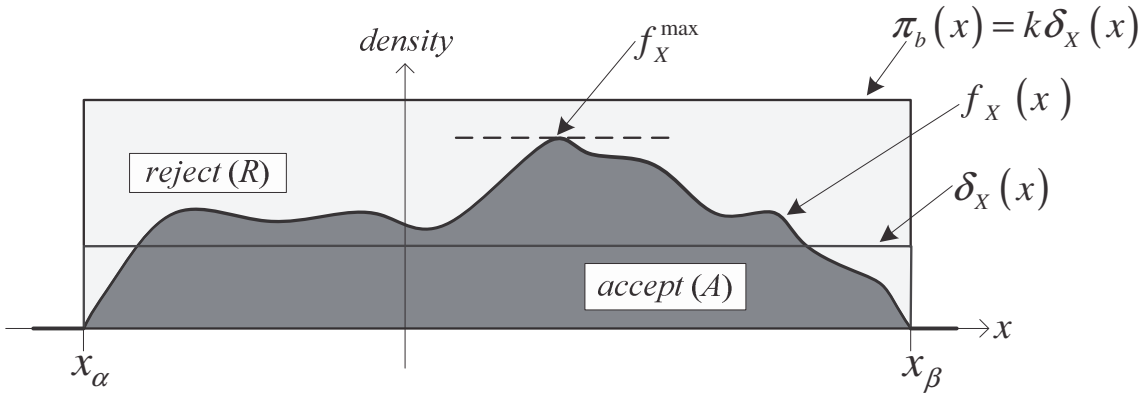

Figure 3.7 – Graphical interpretation of the related functions for the ARM algorithm

In order to maximize the rate for the acceptance of arbitrary samples, we could in essence minimize the rejection region shown in Figure 3.7. This could for instance be leveraged by adjusting the growth constant k to $k_{\min}$, such that $k > k_{\min} \geq 1$. To get this element, we need to identify the maximum value of the PDF:

$$f_X^{\max} \triangleq \max_{x \in \mathbb{R}} \{f_X(x)\} \in \mathbb{R}_+^* \tag{3.14}$$

Then, we perform the following association:

$$\inf_{k \in \mathbb{R}_+^*} \{\pi_b(x)\} = f_X^{\max} \tag{3.15}$$

From (3.15) we realize that:

$$k_{\min} = f_X^{\max} / \delta_X(x) = f_X^{\max} / \mathcal{U}_X(x_\alpha, x_\beta) = f_X^{\max}(x_\beta - x_\alpha) \tag{3.16}$$

In Figure 3.8, the general approach for random generation based on the ARM algorithm is according displayed. The performance of this quasi-optimum sampling method could be enhanced by combining the above analysis.

Algorithm 1 - Random Sampling based on the ARM Approach

1: Generate: $\hat{u} \sim \mathcal{U}(0,1)$ and $\hat{v} \sim \delta_X(x)$
2: **if** $\{\hat{u} < f_X(\hat{v})/\pi_b(\hat{v}) \leq 1\}$ **then**
3: $\hat{x} := \hat{v}$ (i.e. random sample is accepted)
4: Repeat the algorithm until the desired number of samples is obtained.

Figure 3.8 – ARM algorithm

In particular, $\hat{v} \sim \delta_X(x)$ is generated by the stochastic transformation of Figure 3.9. This outcome can in fact be proved by:

$$\delta_X(x) = \mathcal{U}_X(0,1) \Big/ \left| d\left\{x_\alpha + x\left(x_\beta - x_\alpha\right)\right\} \Big/ dx \right| = \mathcal{U}_X\left(x_\alpha, x_\beta\right) \quad \blacksquare \tag{3.17}$$

$$\hat{w} \sim \mathcal{U}_X(0,1) \xrightarrow{\text{transformation}} \boxed{x_\alpha + \hat{w}\left(x_\beta - x_\alpha\right)} \rightarrow \hat{v} \sim \delta_X(x)$$

Figure 3.9 – Uniform random generation

Now, as expressed in the above algorithm, a decision for the suitability of a sample depends on the $f_X(\hat{v})/\pi_b(\hat{v})$ ratio, which may further be elaborated by (3.12), (3.13), and (3.16):

$$\frac{f_X(\hat{v})}{\pi_b(\hat{v})} = \frac{f_X(\hat{v})}{k\delta_X(\hat{v})} < \frac{f_X(\hat{v})}{k_{\min}\delta_X(\hat{v})} = \frac{f_X(\hat{v})}{f_X^{\max}\left(x_\beta - x_\alpha\right)\mathcal{U}_X\left(x_\alpha, x_\beta\right)} = \frac{f_X(\hat{v})}{f_X^{\max}} \tag{3.18}$$

From (3.18), we therefore note that it is not necessary to verify the $f_X(\hat{v})/\pi_b(\hat{v}) \leq 1$ condition indicated in the algorithm of Figure 3.8, because $f_X(\hat{v}) \leq f_X^{\max}$ is always factual. If we apply (3.18) to the PDF of (3.6), we then get:

$$\frac{f_X(\hat{v})}{f_X^{\max}} = 2\left\{\begin{array}{l}\left(\hat{v}-\sqrt{\left(r_0^2-\hat{v}^2\right)/3}\right)\Big/ L\cdot\mathbf{1}\left(r_0/2\le\hat{v}\le r_0\right) \\ \quad +\hat{v}/L\cdot\mathbf{1}\left(r_0\le\hat{v}\le L/2\right)+\left(1-\hat{v}/L\right).\mathbf{1}\left(L/2\le\hat{v}\le L\right)\end{array}\right\} \tag{3.19}$$

After taking the analysis detailed above into account, we then obtain the RNG algorithm for $\hat{x} \sim f_X(x)$ in Figure 3.10 that ensures an efficient approach for generating n_S samples.

Algorithm 2 - Random Deployment with Far-Field Radiation along the *x*-axis

Require: $n_S \in \mathbb{N}^*$ $r_0 \in \mathbb{R}_+^*$ $L \in \mathbb{R}_+^*$
Initialize: $i = 0$ $n_T = 0$
while $\{i < n_S\}$ **do**
    $n_T := n_T + 1$
    Generate two i.i.d. RVs: $\{\hat{u}_0, \hat{u}_1\} \sim \mathcal{U}(0,1)$
    Compute: $\hat{v} = r_0/2 + \hat{u}_1(L - r_0/2) \sim \delta_X(x) = \mathcal{U}_X(r_0/2, L)$
    if $\{r_0/2 \le \hat{v} \le r_0\}$ **then**
        if $\left\{\hat{v} - \sqrt{\left(r_0^2 - \hat{v}^2\right)/3} > \hat{u}_0 L/2\right\}$ **then**
            $i := i + 1$
            Random sample is accepted: $\hat{x}_i := \hat{v} \sim f_X(x)$
        end if
    else if $\{r_0 \le \hat{v} \le L/2\}$ **then**
        if $\{\hat{v} > \hat{u}_0 L/2\}$ **then**
            $i := i + 1$
            Random sample is accepted: $\hat{x}_i := \hat{v} \sim f_X(x)$
        end if
    else if $\{L/2 \le \hat{v} \le L\}$ **then**
        if $\{\hat{v} < L(1 - \hat{u}_0/2)\}$ **then**
            $i := i + 1$
            Random sample is accepted: $\hat{x}_i := \hat{v} \sim f_X(x)$
        end if
    end if
end while
Return/Compute: $\{\hat{x}_i : i = 1, 2, \cdots, n_S$ $\tilde{p}_A = n_S/n_T$

Figure 3.10 – Pseudocode for efficient random generation

In Figure 3.11, the PDF along the *x*-axis is shown for two different values of RCR obtained by means of analysis and via MC simulation. The specifications for the simulation are as follows:

- For utilization in the density function, the cellular radius is normalized to 1 unit, and thus the close-in range is given by $r_0 = 1/\mu$.
- The random simulation is accomplished after getting $n_S = 15,000$ valid samples.
- Then, based on these samples an $n_B = 150$ bin histogram is constructed.
- Finally, the histogram is appropriately scaled to reflect the PDF.

We should also remark that as the amount of accepted samples increase, the fluctuation of the MC plot will lessen and will closely follow the theoretical relationship. However, as a consequence of this approach, the most evident drawback is a growth of the microprocessor average running time.

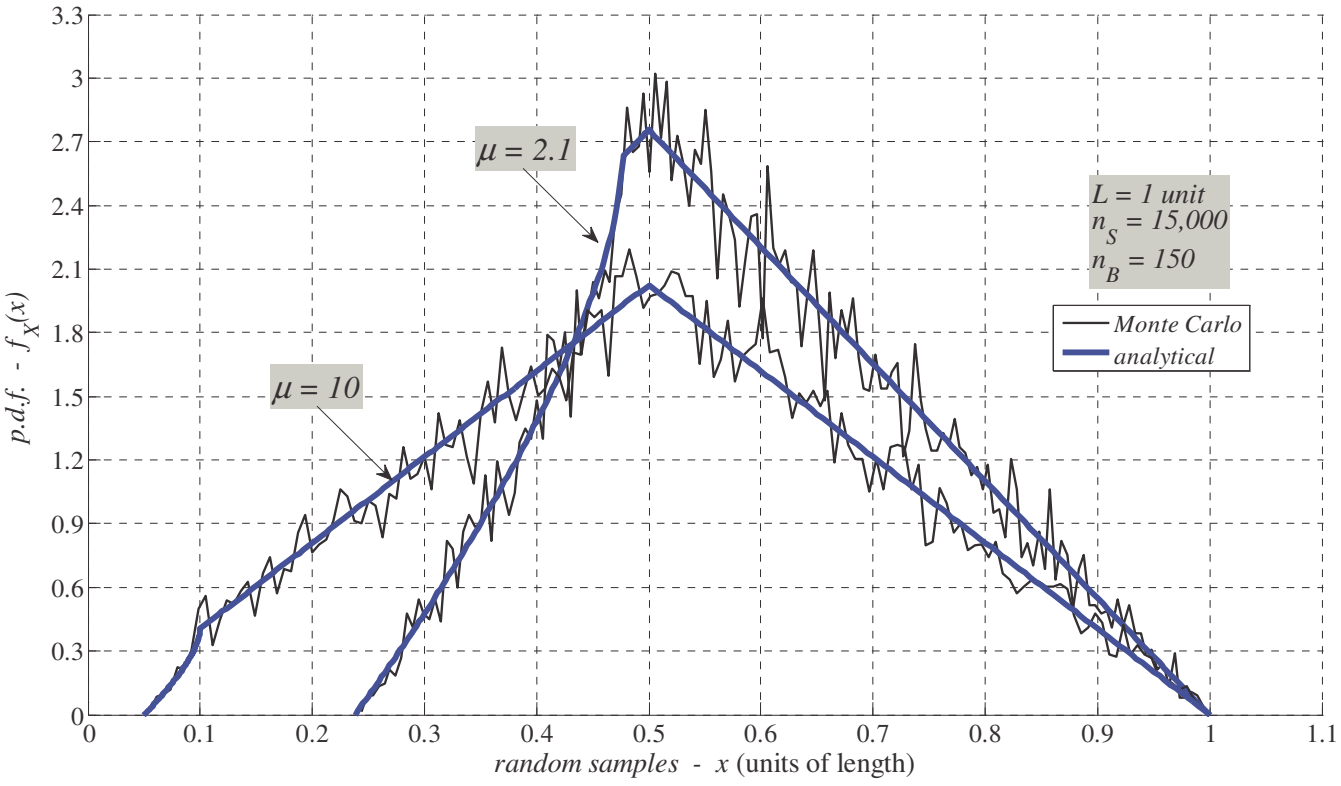

Figure 3.11 – Marginal density of nodal geometry by means of random simulation

3.3.3 – Measuring the Performance of Efficient Random Generation

In the previous subsection, we detailed an approach for efficient random generation. In this part, we are interested to quantify the performance of the obtained RNG. To begin, we want to determine an expression for the acceptance rate p_A of a randomly generated sample. In fact, this objective can be facilitated by the logic depicted in Figure 3.7, where the event of accepting a sample is a subset in the universal space $\Omega = \{A, R\}$. Consequently, the acceptance rate can be represented by:

$$\begin{aligned} p_A = \Pr\{A \subset \Omega\} &= \int_{x=-\infty}^{\infty} f_X(x)\,dx \Big/ \int_{x=-\infty}^{\infty} \pi_b(x)\,dx = 1 \Big/ \int_{x=-\infty}^{\infty} k\delta_X(x)\,dx \\ &= 1 \Big/ k_{\min} \int_{x=-\infty}^{\infty} \mathcal{U}_X(x_\alpha, x_\beta)\,dx = 1/k_{\min} \end{aligned} \tag{3.20}$$

Applying (3.16) to the PDF of (3.6) changes the acceptance rate to:

$$p_A = \frac{1}{f_X^{\max}(x_\beta - x_\alpha)} = \frac{2}{\sqrt{3}L \cdot k_{FF}(L - r_0/2)} = \frac{\left(3\sqrt{3}L^2 - 2\pi r_0^2\right)}{6\sqrt{3}L(L - r_0/2)} = \frac{\left(L^2 - 2\pi r_0^2/3\sqrt{3}\right)}{L(2L - r_0)} \tag{3.21}$$

Then, the result of (3.21) can be transformed as a function of the RCR:

$$p_A = p_A(\mu) = \frac{\left(L^2 - 2\pi r_0^2/3\sqrt{3}\right)/r_0^2}{L(2L - r_0)/r_0^2} = \frac{\left(\mu^2 - 2\pi/3\sqrt{3}\right)}{\mu(2\mu - 1)} \qquad \mu > 2 \tag{3.22}$$

We could at present scrutinize the validity of the above expression in different ways. First, from the denominator we note that $\mu \neq 0; 1/2$. Second, the probability measure is valid provided:

$$\forall A \subset \Omega : \exists p_A \in \mathbb{R}^+ : 0 \leq p_A = p_A(\mu) \leq 1 \qquad \mu > 2 \tag{3.23}$$

In other words, for $p_A \geq 0$, we get that $\mu^2 \geq 2\pi/3\sqrt{3}$, or that:

$$\left\{\mu \leq -\sqrt{2\pi/3\sqrt{3}}\right\} \cup \left\{\mu \geq \sqrt{2\pi/3\sqrt{3}}\right\} \tag{3.24}$$

Also, for $p_A \leq 1$, we remark that:

$$g(\mu) \triangleq \mu^2 - \mu + 2\pi/3\sqrt{3} \geq 0 \tag{3.25}$$

And the discriminant for this quadratic equation is given by:

$$\Delta_g = 1 - 8\pi/3\sqrt{3} \approx -3.84 \tag{3.26}$$

Because $\Delta_g < 0$, there are no possible roots in $\mathbb{R}$. Further, the vertex for the expression in (3.25) is positioned at the following coordinates:

$$\left(\mu_V \; ; \; g(\mu_V)\right) = \left(1/2 \; ; \; 2\pi/3\sqrt{3} - 1/4\right) \approx (0.5 \; ; \; 0.96) \tag{3.27}$$

This vertex is therefore in the first quadrant of the Cartesian coordinate system and $g(\mu)$ is concave upward, thus (3.25) holds for all $\mu \in \mathbb{R}$. Overall, all the identified support values are indeed coherent with the requirement that $\mu > 2$, which in part justifies the authenticity of (3.22). ■

In order to gain additional understanding of the acceptance rate behavior as a function of the RCR, in Figure 3.12 we show the corresponding theoretical and experimental plots. To be precise, the MC simulation is detailed as follows:

- The RCR is swept from $\mu = 2.1 \rightarrow 20$ in steps of 0.1, where for each μ value n_S accepted samples are sought.
- In this endeavor, the experimental acceptance rate $\tilde{p}_A$ for different RCR is numerically estimated and accordingly plotted. More on this estimation will be explained later on.
- We performed the simulation for $n_S = 1,000$ and $n_S = 10,000$ in order to show the impact of different sampling values on the acceptance rate accuracy. As n_S augments, MC obtained estimates closely envelope the theoretical plot.

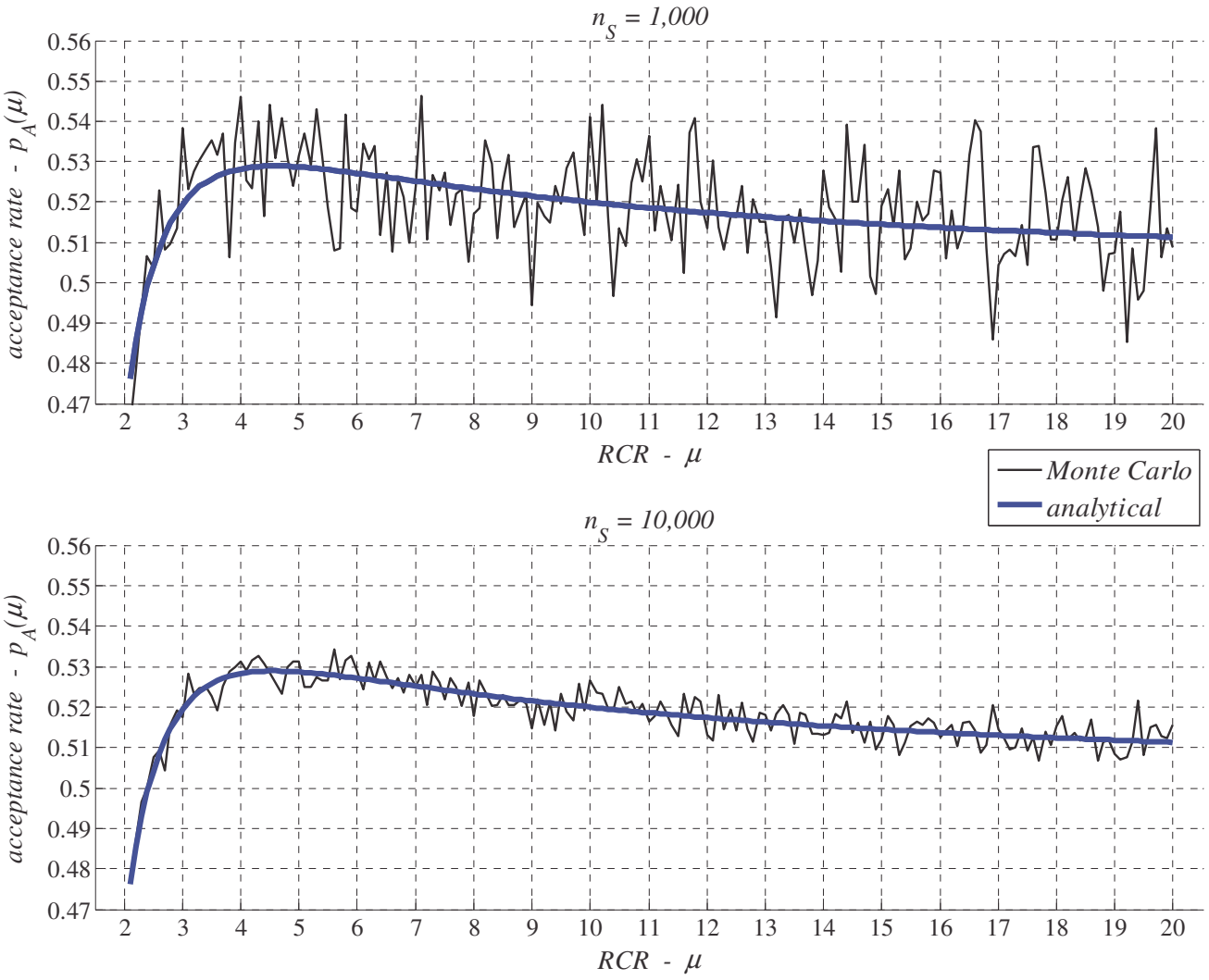

Figure 3.12 – Acceptance rate for efficient random generation versus RCR

At this point, the natural intrigue is to analytically obtain the optimum RCR value that maximizes $p_A(\mu)$. Therefore, we commence by taking the derivative of (3.22):

$$\frac{dp_A(\mu)}{d\mu} = \frac{d}{d\mu}\left\{\frac{\left(\mu^2 - 2\pi/3\sqrt{3}\right)}{\mu(2\mu-1)}\right\} \qquad \mu > 2$$
$$= \left(-\mu^2 + 8\pi\cdot\mu/3\sqrt{3} - 2\pi/3\sqrt{3}\right)\Big/\left\{\mu(2\mu-1)\right\}^2 \tag{3.28}$$

If we set (3.28) to zero, we then find:

$$-\mu_{opt}^2 + 8\pi\cdot\mu_{opt}/3\sqrt{3} - 2\pi/3\sqrt{3} = 0 \tag{3.29}$$

The discriminant of (3.29) is given by:

$$\Delta_{opt} = 8\pi\left(8\pi - 3\sqrt{3}\right)/27 \approx 18.56 > 0 \tag{3.30}$$

thus resulting in two real roots. However, one of these feasible solutions is outside $\mu > 2$; hence, the optimum RCR value for random generation is unique and given by:

$$\mu_{opt} = \frac{4\pi}{3\sqrt{3}} + \frac{\sqrt{\Delta_{opt}}}{2} = \frac{4\pi + \sqrt{2\pi\left(8\pi - 3\sqrt{3}\right)}}{3\sqrt{3}} \approx 4.57 \tag{3.31}$$

Conceptually, the efficient random generation approach is further improved when $\mu = \mu_{opt}$, which essentially ensures an acceptance rate of ~52.9%. This analytical quantification clearly agrees with the plots of Figure 3.12.

Pursuing this further, it is also worthwhile to characterize the acceptance rate as the RCR increases. This can be evaluated by:

$$\lim_{\mu\to\infty} p_A(\mu) = \lim_{\mu\to\infty} \left(\mu^2 - 2\pi/3\sqrt{3}\right)\Big/\mu(2\mu-1) = \lim_{\mu\to\infty} 2\mu/(4\mu-1) = 0.5 \tag{3.32}$$

In fact, $p_A = 0.5$ is a horizontal asymptote (HA) of the $p_A(\mu)$ relationship, because from long division we notice that:

$$p_A(\mu) = \frac{\left(\mu^2 - 2\pi/3\sqrt{3}\right)}{\mu(2\mu-1)} = \frac{1}{2} + \frac{\left(\mu - 4\pi/3\sqrt{3}\right)}{2\mu(2\mu-1)} \qquad \mu > 2 \tag{3.33}$$

Although this asymptote is not evident in Figure 3.12, but from (3.32) and (3.33) we explicitly recognize that the acceptance rate approaches ~50% as the RCR progressively increases. All things considered, we realize that the analytical RNG acceptance rate of the algorithm in Figure 3.10 is confined by:

$$0.47 < p_A(\mu) < 0.53 \qquad \mu \in (2,\infty) \tag{3.34}$$

In (3.22) we theoretically derived an expression for the acceptance rate. Conversely, we may also define a MC estimator for the acceptance probability of samples denoted by:

$$\exists \tilde{p}_A \in \mathbb{R}^+ : 0 \le \tilde{p}_A \le 1 \tag{3.35}$$

where this measure is numerically assessed by:

$$\tilde{p}_A = n_S / n_T \tag{3.36}$$

such that n_S represents the number of accepted samples and n_T is the total number of randomly generated instances for a particular simulation realization with values defined by:

$$\forall n_T \in \mathbb{N}^* : \exists n_S \in \mathbb{N} : n_S \leq n_T \tag{3.37}$$

The estimator of (3.36) can practically be utilized for MC simulations in two different ways. On one hand, n_S is preset before the beginning of the simulation as considered in the algorithm of Figure 3.10 and the results of Figure 3.12. On the other hand, n_T can be designated in advance, and as the MC simulation progresses, the amount of n_S is tracked for acceptance rate calculation.

For the sake of comparison, it is interesting to evaluate the computational complexity for estimating the acceptance rate based on these two different possible approaches. Specifically, if we assume that n_S is deterministic, then the while-loop of Figure 3.10 will be invoked n_T times. However, the algorithm growth rate must be a function of its input arguments; thus rationalizing the logic for the following manipulations:

$$\begin{aligned} O\left(T_{cost}\left(\mu, n_S\right)\right) &= O\left(c_0 + \sum_{i=1}^{n_T} \tilde{c}_0\right) = O\left(c_0 + \tilde{c}_0 n_T\right) \approx O\left(c_0 + \tilde{c}_0 n_S / p_A\left(\mu\right)\right) \\ &= O\left(c_0 + \tilde{c}_0 n_S \cdot \frac{\mu\left(2\mu - 1\right)}{\left(\mu^2 - 2\pi/3\sqrt{3}\right)}\right) = O\left(c_0 + \tilde{c}_0 n_S \cdot \left\{2 - \frac{\left(\mu - 4\pi/3\sqrt{3}\right)}{\left(\mu^2 - 2\pi/3\sqrt{3}\right)}\right\}\right) \\ &\sim \lim_{\mu \gg 2} O\left(T_{cost}\left(\mu, n_S\right)\right) = \lim_{\mu \gg 2} O\left(c_0 + \tilde{c}_0 n_S \cdot \left\{2 - 1/2\mu\right\}\right) \\ &= O\left(c_0 + 2\tilde{c}_0 n_S\right) \sim O\left(n_S\right) \end{aligned} \tag{3.38}$$

In contrast, if n_T is fixed, then the algorithm of Figure 3.10 is slightly modified. These changes can be summarized as follows:

- Line 1: instead of n_S , we rather require n_T as an input to the algorithm.
- Line 2: as a replacement for n_T , we initialize n_S to zero and we discard i .
- Line 3: the while-loop is changed to a for-loop over n_T values.
- Line 4: the update for n_T is completely removed.
- Lines 9, 14, 19: the code appearing on these lines is changed to $n_S := n_S + 1$.
- Lines 10, 15, 20: the index i should be changed to n_S .

Taking these changes into account alters the complexity of the algorithm to:

$$O\left(T_{cost}\left(\mu, n_T\right)\right) \sim O\left(n_T\right) \tag{3.39}$$

To facilitate the comparison amongst the estimations, in Table 3.1 we display the peculiarities for each of these methods. Granted, the 1st approach is more appropriate due to its failsafe nature for *a priori* setting of the desired number of accepted samples. Nonetheless, if we consider the 2nd option, further statistical examination of the estimator becomes simpler; this principle will be shown in the steps that follow.

Table 3.1 – Comparing estimation choices for the acceptance rate

estimation	n_S	n_T	stopping criterion	algorithm cost	key advantage
1st approach	deterministic	random	**while** $\{i < n_S\}$	$O\left(n_S\right)$	guaranteed RNG
2nd approach	random	deterministic	**for** $i = 1, 2, \cdots, n_T$	$O\left(n_T\right)$	simpler statistics

To emphasize, a randomly generated sample may either be accepted (A) or rejected (R). In other words, we only have two possible outcomes that are mutually exclusive events in $\Omega = \{A, R\}$, therefore:

$$p\left(A \cap R\right) = p\left(A \cap \bar{A}\right) = p\left(\varnothing\right) = 0 \tag{3.40}$$

Also, the probability for each related event is:

$$p(A) = p_A \tag{3.41}$$

$$p(R) = 1 - p_A \tag{3.42}$$

Assuming that the experiment is performed n_T times and the simulation trials are uncorrelated, then the binomial probability mass function (PMF) can be utilized such that N_S is a random variable (RV) representing the number of accepted samples:

$$N_S \sim Binomial(n_S, n_T, p_A) = \Pr(N_S = n_S) = \binom{n_T}{n_S} p_A^{n_S} (1 - p_A)^{n_T - n_S} \quad n_S = 0, 1, 2, \cdots, n_T \tag{3.43}$$

To be specific, the PMF in (3.43) is used for getting n_S successes in n_T trials, where each successful event has probability p_A. The important correspondence in this realization among the sample acceptance and the binomial distribution are as follows:

$$accepting\ a\ randomly\ generated\ sample \leftrightarrow success \leftrightarrow event\ A \leftrightarrow p_A \leftrightarrow N_S = n_S \tag{3.44}$$

The mean and variance of N_S are given by:

$$m_{N_S} = \mathrm{E}[N_S] = \sum_{n_S=0}^{n_T} n_S \ Binomial(n_S, n_T, p_A) = n_T p_A \tag{3.45}$$

$$\sigma_{N_S}^2 = \mathrm{E}\left[\left(N_S - m_{N_S}\right)^2\right] = \sum_{n_S=0}^{n_T} \left(n_S - m_{N_S}\right)^2 Binomial(n_S, n_T, p_A) = n_T p_A (1 - p_A) \tag{3.46}$$

The statistics for the estimator in (3.36) can be obtained as a function of (3.45) and (3.46). The result of these elaborations produces the following:

$$\begin{aligned} m_{\tilde{p}_A} &= \mathrm{E}\left[\tilde{p}_A\right] = \mathrm{E}\left[N_S / n_T\right] = \mathrm{E}\left[N_S\right] / n_T = m_{N_S} / n_T \\ &= n_T p_A / n_T = p_A \end{aligned} \tag{3.47}$$

$$\begin{aligned} \sigma^2_{\tilde{p}_A} &= \mathrm{E}\left[\left(\tilde{p}_A - m_{\tilde{p}_A}\right)^2\right] = \mathrm{E}\left[\left(N_S / n_T - m_{\tilde{p}_A}\right)^2\right] = \mathrm{E}\left[\left(N_S - n_T m_{\tilde{p}_A}\right)^2 / n_T^2\right] \\ &= \mathrm{E}\left[\left(N_S - n_T m_{\tilde{p}_A}\right)^2\right] / n_T^2 = \mathrm{E}\left[\left(N_S - m_{N_S}\right)^2\right] / n_T^2 = \sigma^2_{N_S} / n_T^2 \\ &= n_T p_A \left(1 - p_A\right) / n_T^2 = p_A \left(1 - p_A\right) / n_T \end{aligned} \tag{3.48}$$

In particular, the outcome of (3.47) indicates that the acceptance rate estimator is *unbiased*. Further, this estimator is *consistent* as:

$$\lim_{n_T \to \infty} \sigma^2_{\tilde{p}_A} = \lim_{n_T \to \infty} p_A \left(1 - p_A\right) / n_T = 0 \tag{3.49}$$

In other words, (3.49) implies that the estimation for p_A becomes more deterministic as the number of total samples increase; but by (3.39) this will intensify the running time complexity of the estimation. For completeness purposes, substituting (3.22) into the mean of (3.47) highlights the RCR dependence on this measure:

$$m_{\tilde{p}_A} = m_{\tilde{p}_A}(\mu) = p_A(\mu) \tag{3.50}$$

Likewise, as demonstrated by (3.51), the spread of the estimator in (3.48) is adjustable by two variables: the RCR and n_T . In fact, in order to facilitate its analysis, we wrote this second order statistical expression in different mathematical formats, such as: factorization, polynomials, long division, and for limit evaluation. From long division or its limit, we detect a HA at $\sigma^2_{\tilde{p}_A}(\infty, n_T) = 1/4\, n_T$.

$$\sigma^2_{\tilde{p}_A} = \sigma^2_{\tilde{p}_A}(\mu, n_T) = \left(\mu^2 - 2\pi/3\sqrt{3}\right)\left(\mu^2 - \mu + 2\pi/3\sqrt{3}\right)\Big/ \mu^2(2\mu-1)^2 n_T \qquad \mu > 2;\ n_T \in \mathbb{N}^*$$

$$= \left(\mu^4 - \mu^3 + 2\pi\mu/3\sqrt{3} - 4\pi^2/27\right)\Big/\left(4\mu^4 - 4\mu^3 + \mu^2\right) n_T$$

$$= \left\{1 - \left(\mu - 4\pi/3\sqrt{3}\right)^2 \Big/ \mu^2(2\mu-1)^2\right\}\Big/ 4n_T$$

$$= \left\{1 - \left(\left(1/\mu - 4\pi/3\sqrt{3}\mu^2\right)\Big/\left(2 - 1/\mu\right)\right)^2\right\}\Big/ 4n_T \tag{3.51}$$

In general, we want to minimize the variance of (3.51) as much as possible. In (3.49), we showed the effect of n_T on the variance. Now, we are interested to optimize this statistical value by understanding its impact on μ. To do this, we could locate the feasible stationary points of (3.51) via the following partial derivative:

$$\frac{\partial \sigma^2_{\tilde{p}_A}(\mu, n_T)}{\partial \mu} = \frac{\partial}{\partial \mu}\left[\frac{1}{4n_T}\left\{1 - \left(\frac{\left(\mu - 4\pi/3\sqrt{3}\right)}{\mu(2\mu-1)}\right)^2\right\}\right] = \frac{-\left(\mu - 4\pi/3\sqrt{3}\right)}{2n_T\mu(2\mu-1)}\left\{\frac{\left(\mu - 4\pi/3\sqrt{3}\right)}{\mu(2\mu-1)}\right\}'$$

$$= \frac{-\left(\mu - 4\pi/3\sqrt{3}\right)}{\mu^3(2\mu-1)^3 n_T}\left\{-\mu^2 + 8\pi\cdot\mu/3\sqrt{3} - 2\pi/3\sqrt{3}\right\} \tag{3.52}$$

Setting (3.52) to zero, we get the following stationary points:

$$\mu_{\sigma_{\max}} = 4\pi/3\sqrt{3} \approx 2.42 \tag{3.53}$$

$$\mu_{\sigma_{\min}} = \frac{4\pi + \sqrt{2\pi\left(8\pi - 3\sqrt{3}\right)}}{3\sqrt{3}} \approx 4.57 \tag{3.54}$$

In Figure 3.13, we plotted the estimator variance as a function of the RCR such that the effect of n_T is normalized. From this graph, the maximum and minimum of the curve are appropriately recognized. Clearly, our objective is to reduce the variance, thus the value of (3.54) is more relevant. It is interesting to mention from (3.31) and (3.54) that selecting $\mu \approx 4.57$ has a dual statistical advantage:

- It maximizes the acceptance rate of random sampling.
- It minimizes the acceptance rate estimator variance.

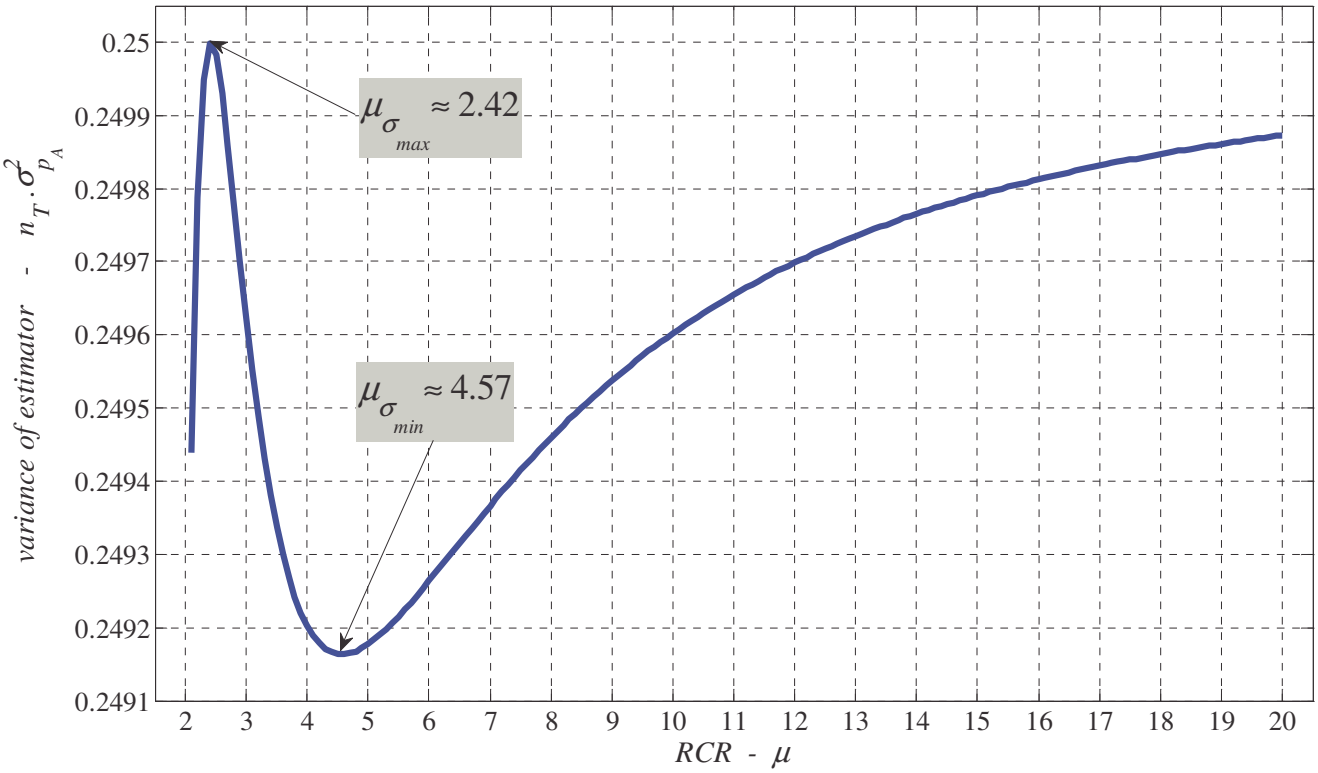

Figure 3.13 – Impact of RCR on the acceptance rate estimator variance

In (3.50) and (3.51) the first and second order statics of the acceptance rate estimator were analytically determined. These measures themselves may also be estimated by averaging it over $n_R \in \mathbb{N}^*$ MC realizations which results into:

$$\tilde{m}_{\tilde{p}_A} = \frac{1}{n_R}\sum_{i=1}^{n_R}\tilde{p}_{A-i} = \frac{1}{n_R n_T}\sum_{i=1}^{n_R} n_{S-i} \tag{3.55}$$

$$\tilde{\sigma}^2_{\tilde{p}_A} = \frac{1}{n_R}\sum_{i=1}^{n_R}\tilde{p}^2_{A-i} - \tilde{m}^2_{\tilde{p}_A} = \frac{1}{n_R n_T^2}\sum_{i=1}^{n_R} n^2_{S-i} - \frac{1}{n_R^2 n_T^2}\left(\sum_{i=1}^{n_R} n_{S-i}\right)^2 \tag{3.56}$$

such that $\tilde{p}_{A-i}$ and n_{S-i} are respectively the estimator of the acceptance probability and the number of accepted samples for the i-th instance. It is in fact expected that as the total number of random instances and the number of realizations per instance are jointly increased, then the sample statistics will converge to the analytical equivalents in (3.50) and (3.51); in other words:

$$m_{\tilde{p}_A} = \lim_{n_T\to\infty}\lim_{n_R\to\infty}\tilde{m}_{\tilde{p}_A} \tag{3.57}$$

$$\sigma^2_{\tilde{p}_A} = \lim_{n_T\to\infty}\lim_{n_R\to\infty}\tilde{\sigma}^2_{\tilde{p}_A} \tag{3.58}$$

To demonstrate this reality and to verify the analytical derivation, in Figure 3.14 the stochastic simulation was conducted. In particular, in order to understand the behavior of the MC estimator as a function of the total number of random instances, we performed the MC simulation by varying n_T from 1 to 500 samples. Then, for each n_T value, the experiment is repeated with $n_R = 50$ times to suitably approximate the statistics of the estimator. Further, to illustrate the interdependence of the RCR on the statistical measures, the simulation is reproduced for different μ values. Indeed, as n_T and n_R concurrently increase, the MC and analytical results are in close agreement. Also, the three variance plots seem relatively identical because the growth of n_T overshadows the impact of μ; but to be exact, $\mu \approx 4.57$ minimizes the variance more rapidly. Overall, the obtained graphical findings are indeed justifying the quality and accuracy of the estimator and the efficiency of random generation.

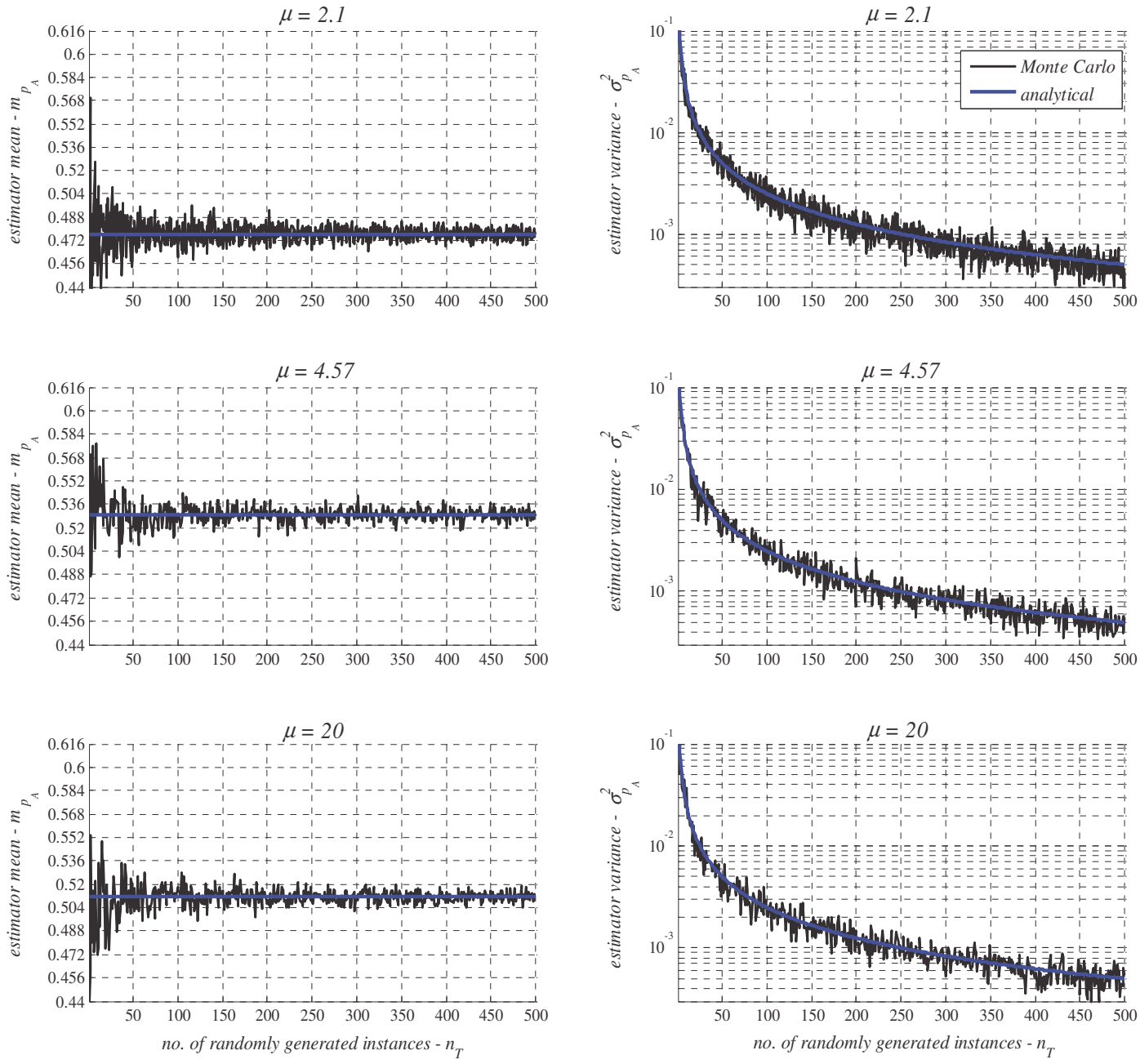

Figure 3.14 – Mean and variance of acceptance rate estimator over different RCR values

3.3.4 – Geometrical Deployment on the Euclidian Plane for Channel Analysis

Deployment along the *x*-axis was treated in the previous subsections. In this part, we will extend the derivation by analyzing the spatial emplacement along the *y*-axis in order to generate a random coordinate on the Euclidian plane. To do this, we require the conditional PDF which we obtain by:

$$f_{Y|X=\hat{x}}(y) = f_{XY}(\hat{x}, y) / f_X(\hat{x}) \tag{3.59}$$

Applying (3.4), (3.5), and (3.6) alongside the deployment support of Figure 3.4 to the PDF expression of (3.59) produces the notation in (3.60). In essence, depending on a particular range for $\hat{x}$, the related PDF is then considered in the expression of (3.60) for randomly emulating the *y*-component of an arbitrary node.

$$f_{Y|X=\hat{x}}(y) = \begin{cases} \mathcal{U}_Y\left(\sqrt{r_0^2 - \hat{x}^2}, \sqrt{3}\hat{x}\right) & r_0/2 \le \hat{x} \le r_0 \\ \mathcal{U}_Y\left(0, \sqrt{3}\hat{x}\right) & r_0 \le \hat{x} \le L/2 \\ \mathcal{U}_Y\left(0, \sqrt{3}(L - \hat{x})\right) & L/2 \le \hat{x} \le L \end{cases} \tag{3.60}$$

Based on this analysis, the spatial dispersion can at present be characterized by the algorithm of Figure 3.15.

Algorithm 3 - Random Deployment with Far-Field Radiation along the *y*-axis

Require: $n_S \in \mathbb{N}^* \quad r_0 \in \mathbb{R}_+^* \quad L \in \mathbb{R}_+^* \quad \{\hat{x}_i\} : i = 1, 2, \cdots, n_S$
for $i = 1, 2, \cdots, n_S$ **do**
    Generate a RV: $\hat{u} \sim \mathcal{U}(0,1)$
    if $\{r_0/2 \le \hat{x}_i \le r_0\}$ **then**
        Compute: $\hat{y}_i := \sqrt{r_0^2 - \hat{x}_i^2} + \left(\sqrt{3}\hat{x}_i - \sqrt{r_0^2 - \hat{x}_i^2}\right)\hat{u} \sim \mathcal{U}_Y\left(\sqrt{r_0^2 - \hat{x}_i^2}, \sqrt{3}\hat{x}_i\right)$
    else if $\{r_0 \le \hat{x}_i \le L/2\}$ **then**
        Compute: $\hat{y}_i := \sqrt{3}\hat{x}_i\hat{u} \sim \mathcal{U}_Y\left(0, \sqrt{3}\hat{x}_i\right)$
    else if $\{L/2 \le \hat{x}_i \le L\}$ **then**
        Compute: $\hat{y}_i := \sqrt{3}\left(L - \hat{x}_i\right)\hat{u} \sim \mathcal{U}_Y\left(0, \sqrt{3}\left(L - \hat{x}_i\right)\right)$
    end if
end for
Return: $\{\hat{y}_i\} : i = 1, 2, \cdots, n_S$

Figure 3.15 – Pseudocode for *y*-based random deployment

The deployment complexity for the optimum spatial random generation can be assessed by integrating the algorithms of Figure 3.10 and Figure 3.15 together:

$$O(n_S)+O(n_S)=O(n_S+n_S)=O(2n_S)\sim O(n_S) \tag{3.61}$$

From a geometrical dispersion point of view, the quantity of n_S in (3.61) translates into the amount of random nodes emplaced within the lattice structure. In other words, the deployment of n_S random terminals has a computational cost of $O(n_S)$ provided $\mu \gg 2$.

Finally, to demonstrate from a deployment perspective the analysis reported in this section, we simulated in Figure 3.16 the random geometry for different nodal capacity and RCR.

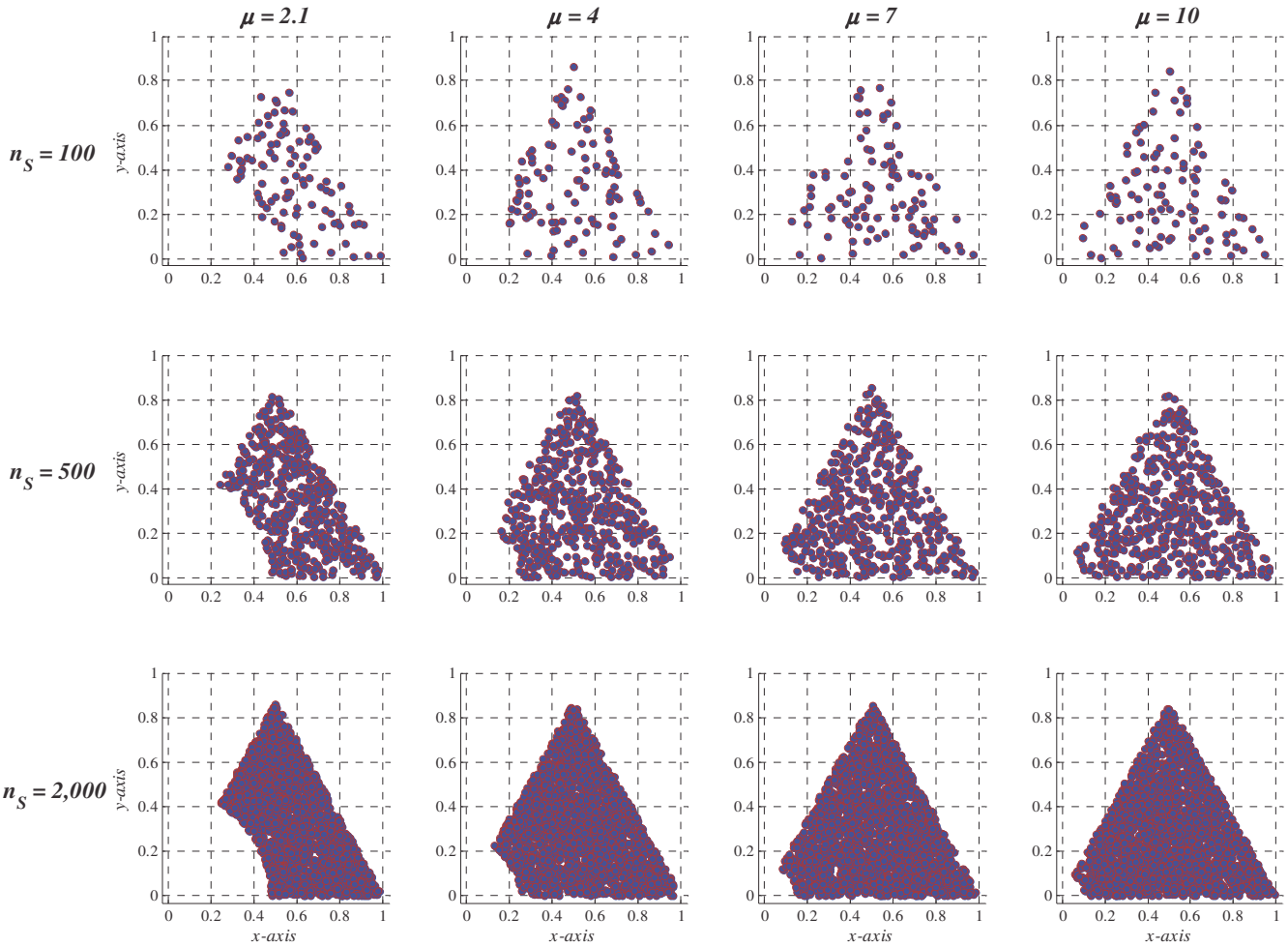

Figure 3.16 – Spatial random network emulation as a function of network scale and RCR

3.4 – Large-Scale Fading Distribution Analysis

3.4.1 – Spatial Density in Polar Notation

The spatial behavior was elaborated in the previous section. This was done as groundwork for: general network emulation, formulation of the large-scale fading density and to numerically verify the authenticity of the analysis. In this part, we are interested to move forward by describing the stochastic characteristics of the channel-loss between an arbitrary node and a reference located at the origin of the service area.

Given the nature of this problem, it is a wise option to perform the stochastic analysis in polar notation as opposed to the Cartesian coordinate format. That is, the joint density of (3.4) should be modified by the use of:

$$f_{R\theta}(r,\theta) = f_{XY}(x,y)\Big|_{\substack{x=r\cos\theta \\ y=r\sin\theta}} \cdot \left|J(r,\theta)\right| \qquad (r,\theta) \in D_{FF}^{P} \subset \mathbb{R}_{+}^{2} \tag{3.62}$$

where the Jacobian matrix is given by:

$$J(r,\theta) = \begin{vmatrix} \partial x/\partial r & \partial x/\partial \theta \\ \partial y/\partial r & \partial y/\partial \theta \end{vmatrix} = \begin{vmatrix} \cos\theta & -r\sin\theta \\ \sin\theta & r\cos\theta \end{vmatrix} = r \tag{3.63}$$

Consequently, the above alteration changes the geometrical PDF to:

$$f_{R\theta}(r,\theta) = \frac{12\cdot r}{\left(3\sqrt{3}L^2 - 2\pi r_0^2\right)} = k_{FF}\cdot r \qquad (r,\theta) \in D_{FF}^{P} \tag{3.64}$$

The challenge now is to explicitly identify the associated polar-based domain D_{FF}^{P}. This task can in fact be facilitated by the scrutiny of Figure 3.17. In this illustration, the marked blue triangle can be applied as an approach for expressing the radius of the coverage. From the law of sines we notice that:

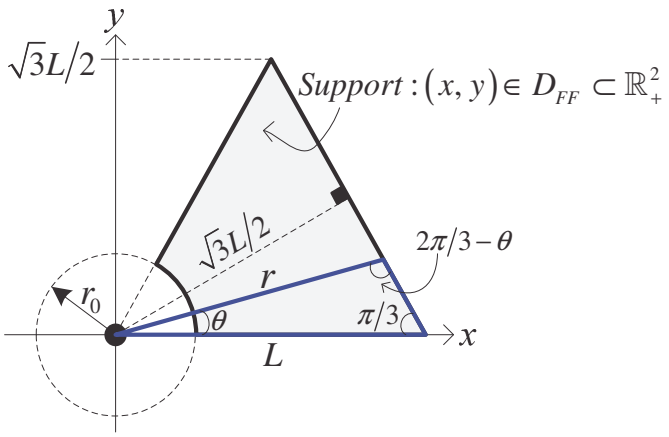

Figure 3.17 – Visual support for deriving the deployment region in polar format

$$\frac{r}{\sin(\pi/3)} = \frac{L}{\sin(2\pi/3-\theta)} \tag{3.65}$$

After arranging the terms of (3.65), we get the notation in (3.66) for the support surface. Its associated illustration is shown in Figure 3.18.

$$r_0 \le r \le r(\theta) = \sqrt{3}L/2\sin(2\pi/3-\theta) \qquad 0 \le \theta \le \pi/3 \tag{3.66}$$

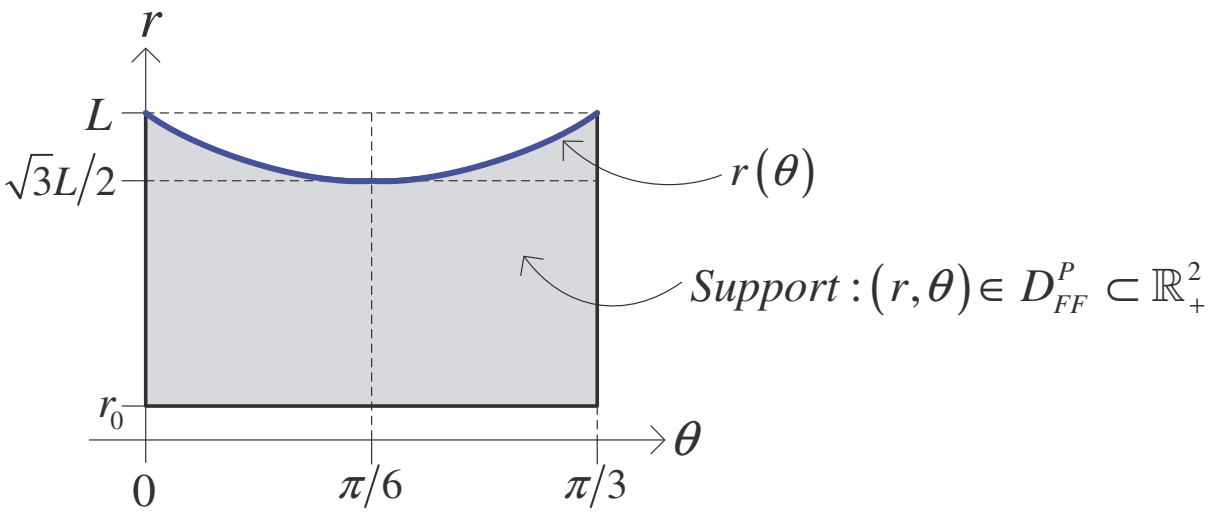

Figure 3.18 – Deployment surface in polar format with respect to the radius

If on the other hand we solve for the angle in (3.66), we then obtain the support region depicted in Figure 3.19. The mathematical equivalent of this figure is give by (3.67).

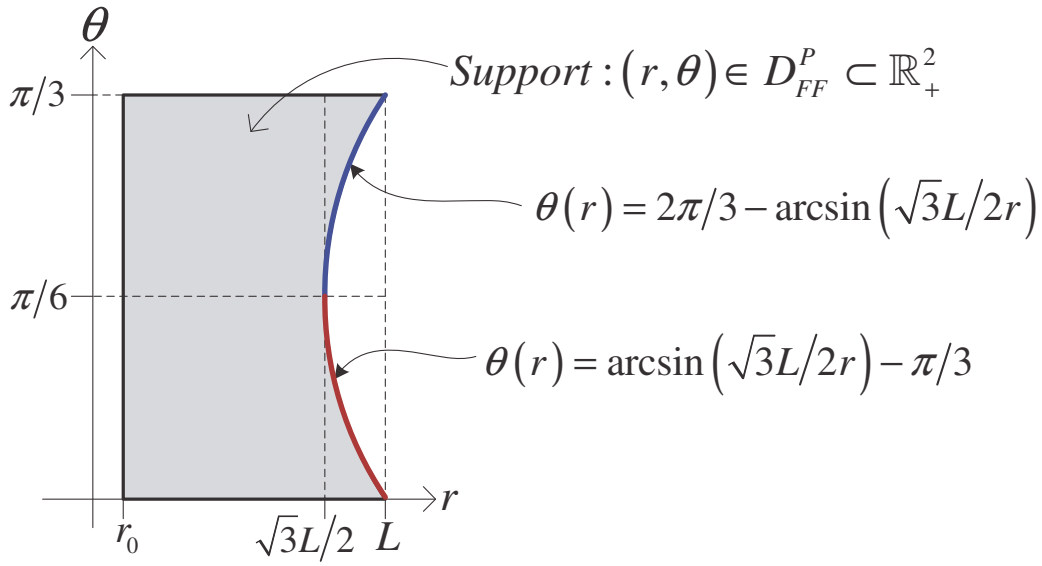

Figure 3.19 – Deployment surface in polar format with respect to the angle

$$D_{FF}^{P}=\left\{\begin{array}{l|l}(r,\theta)\in\mathbb{R}_{+}^{2}; & 0\le\theta\le\pi/3: r\in\left[r_0,\sqrt{3}L/2\right];\\ (r_0,L)\in\mathbb{R}_{+,*}^{2}: & 0\le\theta\le\arcsin\left(\sqrt{3}L/2r\right)-\pi/3: r\in\left[\sqrt{3}L/2,L\right];\\ r_0<L/2 & 2\pi/3-\arcsin\left(\sqrt{3}L/2r\right)\le\theta\le\pi/3: r\in\left[\sqrt{3}L/2,L\right]\end{array}\right\} \tag{3.67}$$

3.4.2 – Characterizing Radial Distribution

From (3.64) and (3.67), we could now derive the radial distribution:

$$\begin{aligned} f_R(r)&=\int_{(r,\theta)\in D_{FF}^{P}} f_{R\theta}(r,\theta)\,d\theta=\int_{(r,\theta)\in D_{FF}^{P}} k_{FF}\cdot r\,d\theta\\ &=\left\{4\pi r\Big/\left(3\sqrt{3}L^2-2\pi r_0^2\right)\right\}\cdot\mathbf{1}\left(r_0\le r\le\sqrt{3}L/2\right)\\ &\quad+\left\{8r\left\{3\arcsin\left(\sqrt{3}L/2r\right)-\pi\right\}\Big/\left(3\sqrt{3}L^2-2\pi r_0^2\right)\right\}\cdot\mathbf{1}\left(\sqrt{3}L/2\le r\le L\right)\end{aligned} \tag{3.68}$$

Furthermore, we find it intriguing to substantiate the radial PDF via MC experimentation. The simulation results are shown in Figure 3.20, where the theoretical plots for a unity cell are accordingly graphed over two RCR values. The outputs are also complemented through stochastic simulation of random samples. In principle, for a particular μ value, the spatial position of $n_S = 25,000$ random nodes is obtained in a manner similar to that carried in Figure 3.16. Then, the measure from the arbitrary node to the BS is computed by:

$$\hat{r}_i = \sqrt{\hat{x}_i^2 + \hat{y}_i^2} \qquad i = 1, 2, \cdots, n_S \tag{3.69}$$

Based on the obtained radial data, an $n_B = 250$ bin histogram is constructed. Finally, the histogram occurrence for each bin is scaled for the purpose of obtaining a PDF curve.

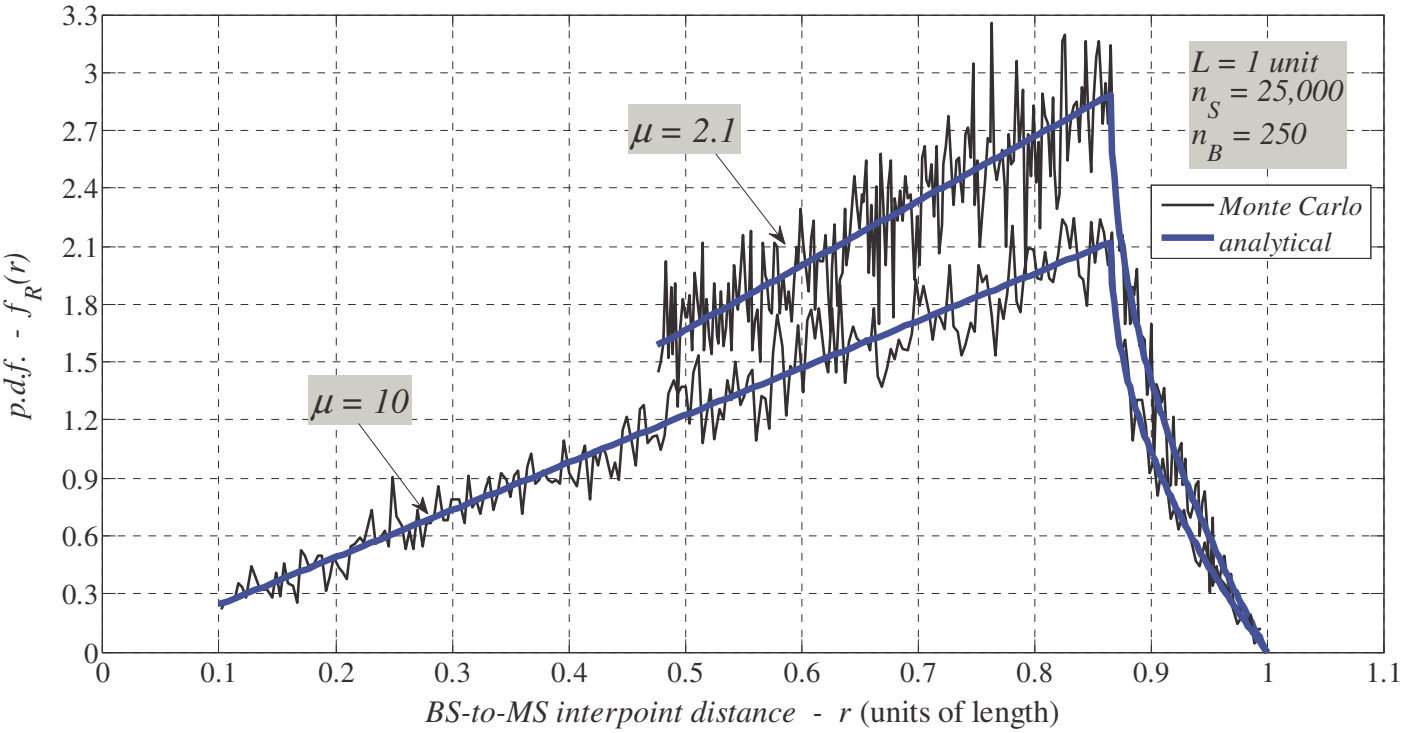

Figure 3.20 – Radial distribution for nodal geometry via stochastic simulation

3.4.3 – RNG based on Radial Distribution

Having $f_R(r)$ leads us to appropriately remark that in order to verify the anticipated analytical formulation for large-scale fading density, random MC data can also be generated straight from the radial distribution in addition to the Cartesian-based RNG analysis described in Section 3.3. To contrast the computational suitability of this generation option, we thus need to identify the RNG attributes of $f_R(r)$. For this reason, the CDF of (3.68) is required. Following some analysis, the expression for the CDF is obtained by:

$$F_R(r) = \Pr(R \le r) = \int_{\tilde{r}=-\infty}^{r} f_R(\tilde{r})\, d\tilde{r}$$

$$= \frac{2}{\left(3\sqrt{3}L^2 - 2\pi r_0^2\right)} \left\{ \begin{array}{l} \pi\left(r^2 - r_0^2\right) \cdot \mathbf{1}\left(r_0 \le r \le \sqrt{3}L/2\right) \\ + \left\{ \begin{array}{l} 3\sqrt{3}L \cdot \sqrt{r^2 - \left(\sqrt{3}L/2\right)^2} \\ + 6r^2 \arcsin\left(\sqrt{3}L/2r\right) - \pi\left(2r^2 + r_0^2\right) \end{array} \right\} \cdot \mathbf{1}\left(\sqrt{3}L/2 \le r \le L\right) \end{array} \right\}$$

(3.70)

From (3.70), we notice that the most efficient random generation founded on the ITM technique may not be applicable given that a closed-form ICDF is unattainable. As a workaround, despite being a suboptimal option for RNG, the modified version of the ARM procedure can still be considered for enhancing the generation performance of the radial probability distribution.

In particular, in (3.16) and (3.20) we characterized the utmost acceptance rate for the modified iterative algorithm. Applying this probability measure for the radial PDF of (3.68), we then determine that:

$$p_A(\mu) = 1 \Big/ f_R^{\max}\left(r_\beta - r_\alpha\right) = 1 \Big/ \max_{r \in \mathbb{R}}\left\{f_R(r)\right\} \cdot \left(L - r_0\right) \qquad \mu > 2$$

$$= \left(3\sqrt{3}L^2 - 2\pi r_0^2\right) \Big/ 2\sqrt{3}\pi L\left(L - r_0\right) = 3\left(\mu^2 - 2\pi/3\sqrt{3}\right) \Big/ 2\pi\mu\left(\mu - 1\right)$$

(3.71)

Furthermore, the HA of (3.71) can be developed by:

$$\lim_{\mu\to\infty} p_A(\mu) = \lim_{\mu\to\infty} 3\left(1-2\pi/3\sqrt{3}\mu^2\right)\Big/2\pi\left(1-1/\mu\right) = 3/2\pi \approx 0.48 \tag{3.72}$$

Additionally, it is insightful to find the intersection point for the RNG acceptance rate among the Cartesian and radial notations expressed accordingly in (3.22) and (3.71). In other words, if both statements are set equal to each other, then after solving for the RCR we get:

$$\mu_I = \left(2\pi-3\right)/2\left(\pi-3\right) \approx 11.59 \tag{3.73}$$

For comparison purposes, in Figure 3.21, we graph the acceptance rate for both of these random generation approaches. As shown, the acceptance rate for the radial distribution is monotonically decreasing, whereas the Cartesian alternative is not monotonic at all. Also from these plots, the intersection point μ_I can clearly be identified. Moreover, in (3.32) and (3.72), the acceptance rate for an RCR that tends to infinity was assessed; essentially, these results reveal that Cartesian-based RNG is more performant as μ extends beyond μ_I .

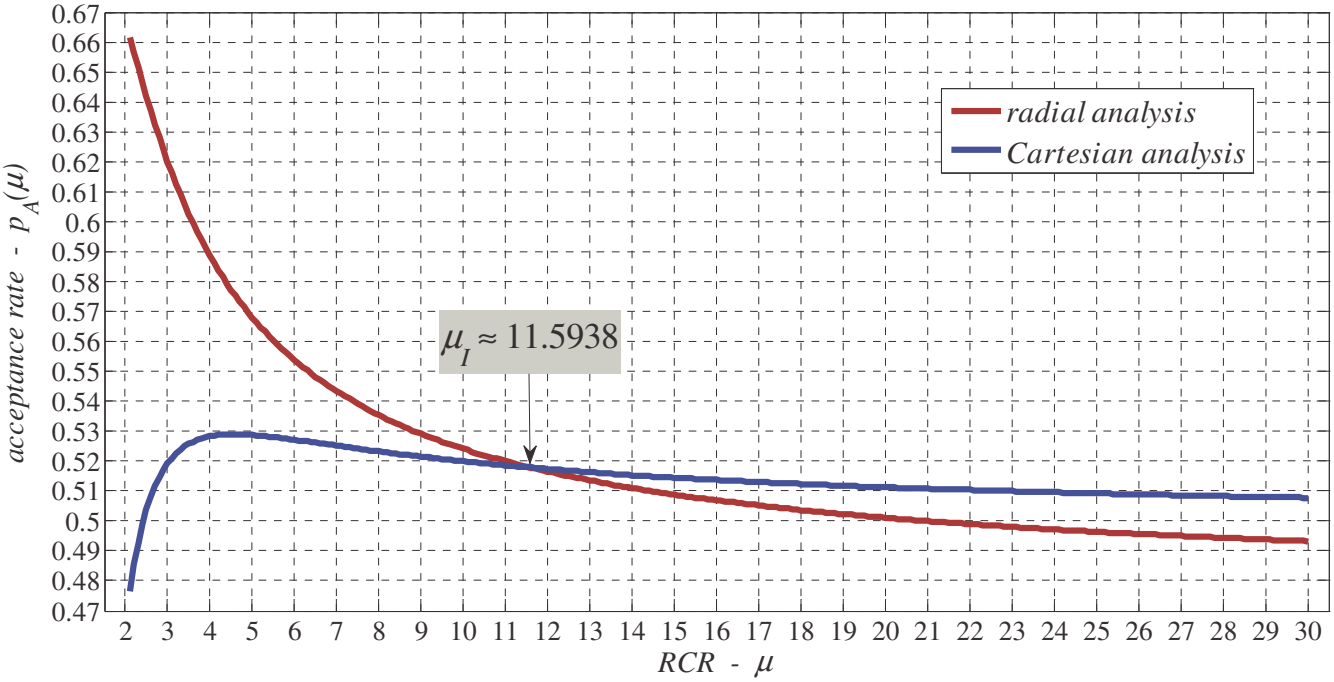

Figure 3.21 – Efficient RNG acceptance rate based on radial and Cartesian analysis

Empowered from Figure 3.21, the optimum RNG approach can thus be improved by partitioning the RCR range such that the $p_A(\mu)$ is maximized. Implementing this task, leads us to observe the following principle for efficient random generation:

$$\begin{aligned} 2 < \mu \le \mu_I \quad &\leftrightarrow \quad \textit{radial RNG} \\ \mu > \mu_I \quad &\leftrightarrow \quad \textit{Cartesian RNG} \end{aligned} \tag{3.74}$$

3.4.4 – Distribution of the Average Path-Loss

As discussed in Chapter 2, for analytical suitability, the channel-loss expression may be mapped to the simpler notation of (3.75), where the average PL for an L sized cellular network at a generic internodal gap is modeled by:

$$w(r) \equiv \overline{L_{PL}(r)}_{dB} = \alpha + \beta \log_{10}(r) \qquad 0 < r_0 \le r \le L \tag{3.75}$$

In fact, this function is described by $w(r):[r_0, L] \mapsto \{w_0 \le w \le w_L\} \subset \mathbb{R}_+^*$, such that the radial PDF of (3.68) has three breakpoints with extremities w_0, w_L and the intermediate value w_I, which can be associated with the following average channel measures:

$$\vec{r} = \begin{bmatrix} r_0 \\ \sqrt{3}L/2 \\ L \end{bmatrix} \Leftrightarrow \vec{w} = \begin{bmatrix} w_0 \\ w_I \\ w_L \end{bmatrix} = \begin{bmatrix} \alpha + \beta \log_{10}(r_0) \\ \alpha + \beta \log_{10}\left(\sqrt{3}L/2\right) \\ \alpha + \beta \log_{10}(L) \end{bmatrix} \in \mathbb{R}_{+,*}^3 \tag{3.76}$$

Furthermore, the inverse of (3.75), which will be required in upcoming parts, is provided by:

$$r(w) = 10^{(w-\alpha)/\beta} \qquad 0 < w_0 \le w \le w_L \tag{3.77}$$

Following the above explanation, the objective here is to characterize the distribution of the average PL overlaying the randomness of nodal geometry; in other words we want to obtain:

$$w = w\left(r \sim f_R\left(r\right)\right) \equiv \overline{L_{PL}\left(r\right)}_{dB} \sim f_W\left(w\right) \tag{3.78}$$

Thus, this stochastic transformation translates into these steps:

$$\begin{aligned} f_W\left(w\right) &= f_R\left(r = r\left(w\right)\right) \Big/ \left| dw\left(r\right)/dr \right|_{r=r(w)} = f_R\left(10^{(w-\alpha)/\beta}\right) \Big/ \left| \beta/\ln\left(10\right) r \right|_{r=10^{(w-\alpha)/\beta}} \\ &= \frac{\ln\left(10\right)}{\beta} \cdot 10^{(w-\alpha)/\beta} \left\{ \begin{array}{l} \dfrac{4\pi r}{\left(3\sqrt{3}L^2 - 2\pi r_0^2\right)} \cdot \mathbf{1}\left(r_0 \le r \le \sqrt{3}L/2\right) \\ + \dfrac{8r\left\{3\arcsin\left(\sqrt{3}L/2r\right) - \pi\right\}}{\left(3\sqrt{3}L^2 - 2\pi r_0^2\right)} \cdot \mathbf{1}\left(\sqrt{3}L/2 \le r \le L\right) \end{array} \right\}_{r=10^{(w-\alpha)/\beta}} \\ &= \frac{4 \cdot \ln\left(10\right)}{\beta\left(3\sqrt{3}L^2 - 2\pi r_0^2\right)} \cdot 10^{2(w-\alpha)/\beta} \left\{ \begin{array}{l} \pi \cdot \mathbf{1}\left(w_0 \le w \le w_I\right) \\ + \left\{6\arcsin\left(\sqrt{3}L/2 \cdot 10^{(w-\alpha)/\beta}\right) - 2\pi\right\} \cdot \mathbf{1}\left(w_I \le w \le w_L\right) \end{array} \right\} \end{aligned} \tag{3.79}$$

Although omitted here, yet, the veracity of the above density function can actually be demonstrated via a number of mathematical manipulations.

3.4.5 – Large-Scale Fading Distribution with Shadowing

In this part of the dissertation, we will supplement the PDF for the average power loss by introducing the impact of shadowing. In fact, this critical component stochastically characterizes the implication of scatterers in the propagation channel; thus, incorporating it in the PL model is of paramount importance.

Basically, shadowing is accounted for by merely adding a RV Ψ_{S-dB} that has a log-normal distribution to the average PL. It is imperative to note that the randomness of shadowing

and the average PL are statistically uncorrelated. Therefore, the overall large-scale fading PDF, namely $f_{L_{PL}}(l)$, is obtained by convolving the mentioned density functions; this is shown by:

$$L_{PL}(r)_{dB} = \left\{ \overline{L_{PL}(r)}_{dB} + \Psi_{S-dB} \right\} \cdot \mathbf{1}(r_0 \le r \le L) \sim f_{L_{PL}}(l) = (f_W * f_\Psi)(l) \tag{3.80}$$

Overall, the large-scale fading PDF of (3.80) that we seek to develop will jointly integrate various wireless networking fundamentals together; to be precise, these essential concepts are:

- Lattice structure of the network configuration.
- Users' nodal geometry.
- Effect of far-field phenomenon.
- Path-loss predictive behavior.
- Impact of shadowing due to channel scatterers.

As shown in (3.81), in order to facilitate the formulation process in later stages, the integrand of the convolution is denoted by $f_0(\tau)$:

$$f_{L_{PL}}(l) = \int_{\tau=-\infty}^{\infty} f_W(\tau) f_\Psi(l-\tau) d\tau \triangleq \int_{\tau=-\infty}^{\infty} f_0(\tau) d\tau \quad l \in \mathbb{R}_+^* \tag{3.81}$$

Specifically, the shadowing feature in (3.81) is designated by $f_\Psi(l-\tau)$, and this element can indeed be reorganized as follows:

$$f_\Psi(l-\tau) = f_\Psi(-(\tau - l)) \tag{3.82}$$

In other words, this expression can be solved in three successive steps:

1. Characterize: $f_\Psi(\tau)$
2. Obtain the reversal of the input: $A(\tau) \triangleq f_\Psi(-\tau)$

3. Perform a translation by l: $B(\tau) \triangleq A(\tau - l) = f_{\Psi}\left(-(\tau - l)\right) = f_{\Psi}(l - \tau)$

As remarked earlier, the shadowing entity is assessed by a zero-mean log-normal distribution with SD σ_{Ψ} measured in dB:

$$\Psi_{S-dB} \sim f_{\Psi}(\tau) = \mathcal{N}_S\left(0, \sigma_{\Psi}^2\right) \tag{3.83}$$

where $\mathcal{N}_X\left(m, \sigma^2\right)$ is a general Gaussian density function with mean $m \in \mathbb{R}$ and SD $\sigma \in \mathbb{R}_+^*$ defined as:

$$X \sim \mathcal{N}_X\left(m, \sigma^2\right) = \frac{1}{\sqrt{2\pi} \cdot \sigma} \exp\left\{-(x-m)^2 / 2\sigma^2\right\} \quad x \in \mathbb{R} \tag{3.84}$$

After applying (3.84) into (3.83), we obtain:

$$f_{\Psi}(\tau) = \frac{1}{\sqrt{2\pi} \cdot \sigma_{\Psi}} \exp\left\{-\tau^2 / 2\sigma_{\Psi}^2\right\} \quad \tau \in \mathbb{R} \tag{3.85}$$

The next step would be to perform a reversal of the input variable; however, this will not change the notation of (3.85) because:

$$f_{\Psi}(-\tau) = f_{\Psi}(\tau) \tag{3.86}$$

After, the expression in (3.86) is translated to the right by $l \in \mathbb{R}_+^*$:

$$f_{\Psi}(l - \tau) = \frac{1}{\sqrt{2\pi} \cdot \sigma_{\Psi}} \exp\left\{-(\tau - l)^2 / 2\sigma_{\Psi}^2\right\} \quad \tau \in \mathbb{R} \tag{3.87}$$

Alternatively, we may rewrite (3.87) more compactly as in (3.88). For further clarification, this result is also shown graphically in Figure 3.22.

$$f_{\Psi}\left(l-\tau\right)=\mathcal{N}_{S}\left(l,\sigma_{\Psi}^{2}\right)\quad \tau\in\mathbb{R},\ l\in\mathbb{R}_{+}^{*} \tag{3.88}$$

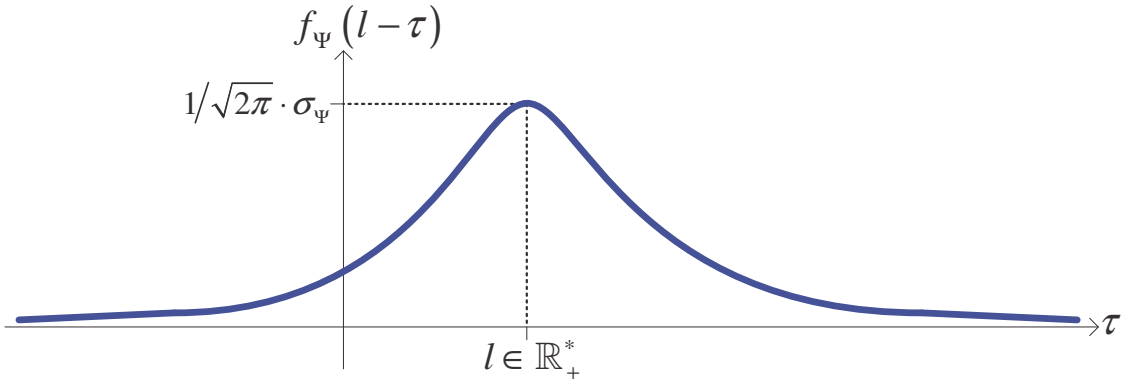

Figure 3.22 – Shadowing contribution for large-scale fading density analysis

In (3.81), the $f_{W}\left(\tau\right):\left[w_{0},w_{L}\right]\mapsto\mathbb{R}^{+}$ part can be attained by (3.79) following an exchange of w by τ ; for convenience this task is performed here as follows:

$$f_{W}\left(\tau\right)=\frac{4\cdot\ln\left(10\right)}{\beta\left(3\sqrt{3}L^{2}-2\pi r_{0}^{2}\right)}\cdot10^{2(\tau-\alpha)/\beta}\left\{\begin{array}{l}\pi\cdot\mathbf{1}\left(w_{0}\le\tau\le w_{I}\right)-2\pi\cdot\mathbf{1}\left(w_{I}\le\tau\le w_{L}\right)\\ +6\arcsin\left(\sqrt{3}L/2\cdot10^{(\tau-\alpha)/\beta}\right)\cdot\mathbf{1}\left(w_{I}\le\tau\le w_{L}\right)\end{array}\right\} \tag{3.89}$$

In view of the multiplication between (3.88) and (3.89), the integrand of the large-scale fading will have a domain which is limited by:

$$\left\{\tau\in\mathbb{R}\right\}\cap\left\{0<w_{0}\le\tau\le w_{L}\right\}=\left\{\tau\in\mathbb{R}_{+}^{*}\middle|\,w_{0}\le\tau\le w_{L}\right\} \tag{3.90}$$

As for the integrand, it is derived as follows:

$$
\begin{aligned}
f_0(\tau) &= f_W(\tau) f_\Psi(l-\tau) = f_W(\tau)\,\mathcal{N}_S\left(l,\sigma_\Psi^2\right) \\
&= \left\{\frac{2\sqrt{2}\ln(10)}{\sqrt{\pi}\left(3\sqrt{3}L^2-2\pi r_0^2\right)\beta\sigma_\Psi}\right\}\cdot 10^{2(\tau-\alpha)/\beta}\cdot\exp\left\{-(\tau-l)^2/2\sigma_\Psi^2\right\} \\
&\quad\times\left\{\begin{array}{l}\pi\cdot\mathbf{1}(w_0\le\tau\le w_I)-2\pi\cdot\mathbf{1}(w_I\le\tau\le w_L) \\ \qquad +6\arcsin\left(\sqrt{3}L/2\cdot 10^{(\tau-\alpha)/\beta}\right)\cdot\mathbf{1}(w_I\le\tau\le w_L)\end{array}\right\}
\end{aligned}
\tag{3.91}
$$

In (3.91), the base-10 part could be adjusted as follows:

$$
10^{2(\tau-\alpha)/\beta} = 10^{-2\alpha/\beta}10^{2\tau/\beta} = 10^{-2\alpha/\beta}\exp\left\{\ln\left(10^{2\tau/\beta}\right)\right\} = 10^{-2\alpha/\beta}\exp\left\{2\cdot\ln(10)\tau/\beta\right\} \tag{3.92}
$$

Now, we substitute (3.92) into (3.91) in order to merge the exponential parts that contain the τ variable together so as to obtain:

$$
\begin{aligned}
f_0(\tau) &= \left\{\frac{2\sqrt{2}\ln(10)\cdot 10^{-2\alpha/\beta}}{\sqrt{\pi}\left(3\sqrt{3}L^2-2\pi r_0^2\right)\beta\sigma_\Psi}\right\}\cdot\exp\overbrace{\left\{2\ln(10)\tau/\beta-(\tau-l)^2/2\sigma_\Psi^2\right\}}^{\triangleq q(\tau)} \\
&\quad\times\left\{\begin{array}{l}\pi\cdot\mathbf{1}(w_0\le\tau\le w_I)-2\pi\cdot\mathbf{1}(w_I\le\tau\le w_L) \\ \qquad +6\arcsin\left(\sqrt{3}L/2\cdot 10^{(\tau-\alpha)/\beta}\right)\cdot\mathbf{1}(w_I\le\tau\le w_L)\end{array}\right\}
\end{aligned}
\tag{3.93}
$$

Next, we could further arrange (3.93) by completing the square of the quadratic function $q(\tau)$ inside the exponential. Put differently, we want an equality of this form to hold:

$$
q(\tau) = a(\tau-h)^2 + k = a\tau^2 + b\tau + c \tag{3.94}
$$

If we work the details of (3.94), we then recognize that:

$$h = -b/2a \tag{3.95}$$

$$k = c - b^2/4a \tag{3.96}$$

In fact, the above (h,k) pair is actually the coordinates of the vertex for the parabola described in (3.94). To determine the equivalent parameters for (a,b,c) in (3.94), we need to expand the quadratic notation $q(\tau)$ inside the exponential of (3.93):

$$q(\tau) = 2\ln(10)\tau/\beta - (\tau - l)^2/2\sigma_\Psi^2 = \underbrace{\left(\frac{-1}{2\sigma_\Psi^2}\right)}_{a}\tau^2 + \underbrace{\left(\frac{2\ln(10)}{\beta} + \frac{l}{\sigma_\Psi^2}\right)}_{b}\tau + \underbrace{\left(\frac{-l^2}{2\sigma_\Psi^2}\right)}_{c} \tag{3.97}$$

The desired vertex coordinates can at present be computed by inserting the information identified in (3.97) into (3.95) and (3.96). Following some arithmetical manipulations, we get:

$$h = \left\{ l + \frac{2\ln(10)\sigma_\Psi^2}{\beta} \right\} \tag{3.98}$$

$$k = \left\{ \frac{2 \cdot l \cdot \ln(10)}{\beta} + \left(\frac{\sqrt{2}\ln(10)\sigma_\Psi}{\beta} \right)^2 \right\} \tag{3.99}$$

After, the exponential of (3.94) can be realized by:

$$\exp\{q(\tau)\} = \exp\left\{a(\tau - h)^2 + k\right\} = \exp\{k\} \cdot \exp\left\{a(\tau - h)^2\right\} \tag{3.100}$$

Inserting (3.99) into the first part of the outcome in (3.100), namely e^k component, and then simplifying the obtained expression develops into:

$$\exp\{k\} = \exp\left\{\frac{2\cdot l\cdot \ln(10)}{\beta} + \left(\frac{\sqrt{2}\ln(10)\sigma_{\Psi}}{\beta}\right)^2\right\}$$
$$= \exp\left\{\frac{2\cdot l\cdot \ln(10)}{\beta}\right\}\cdot \exp\left\{\left(\frac{\sqrt{2}\ln(10)\sigma_{\Psi}}{\beta}\right)^2\right\} = 10^{2\cdot l/\beta}\cdot \exp\left\{\left(\frac{\sqrt{2}\ln(10)\sigma_{\Psi}}{\beta}\right)^2\right\} \tag{3.101}$$

After, substituting from (3.97) the equivalent for a , the h from (3.98), and the result of (3.101) into (3.100), we obtain:

$$\exp\{q(\tau)\} = 10^{2\cdot l/\beta}\cdot \exp\left\{\left(\frac{\sqrt{2}\ln(10)\sigma_{\Psi}}{\beta}\right)^2\right\}\cdot \exp\left\{\frac{-1}{2\sigma_{\Psi}^2}\cdot\left(\tau - \left\{l + \frac{2\ln(10)\sigma_{\Psi}^2}{\beta}\right\}\right)^2\right\} \tag{3.102}$$

Going back to the integrand in (3.93) and plugging (3.102), we the find that:

$$f_0(\tau) = \left[\frac{2\sqrt{2}\ln(10)\cdot 10^{2(l-\alpha)/\beta}}{\sqrt{\pi}\left(3\sqrt{3}L^2 - 2\pi r_0^2\right)\beta\cdot\sigma_{\Psi}}\cdot \exp\left\{\left(\frac{\sqrt{2}\ln(10)\sigma_{\Psi}}{\beta}\right)^2\right\}\right]$$
$$\times \exp\left\{\frac{-1}{2\sigma_{\Psi}^2}\cdot\left(\tau - \left\{l + \frac{2\ln(10)\sigma_{\Psi}^2}{\beta}\right\}\right)^2\right\}$$
$$\times\left\{\begin{array}{l}\pi\cdot\mathbf{1}(w_0 \le \tau \le w_I) - 2\pi\cdot\mathbf{1}(w_I \le \tau \le w_L) \\ \quad + 6\arcsin\left(\sqrt{3}L/2\cdot 10^{(\tau-\alpha)/\beta}\right)\cdot\mathbf{1}(w_I \le \tau \le w_L)\end{array}\right\} \tag{3.103}$$

At present, the integrand of (3.103) is adequately ordered for the purpose of being integrated over the τ variable. To make the integration process more systematic, the τ independent expression, where for clarity purposes is contained by square brackets in (3.103), can be assigned to:

$$K = K\left(l, \alpha, \beta, \sigma_{\Psi}, r_0, L\right) \tag{3.104}$$

Pursuing this further, the τ dependent statement can be split into three parts. Taken together, (3.103) can now be arranged as follows:

$$f_0\left(\tau\right) = K\left\{\begin{array}{l} f_0^{(1)}\left(\tau\right)\cdot\mathbf{1}\left(w_0 \le \tau \le w_I\right) \\ \qquad + f_0^{(2)}\left(\tau\right)\cdot\mathbf{1}\left(w_I \le \tau \le w_L\right) \\ \qquad\qquad + f_0^{(3)}\left(\tau\right)\cdot\mathbf{1}\left(w_I \le \tau \le w_L\right) \end{array}\right\} \tag{3.105}$$

If we apply the integration of (3.81) to the notation in (3.105), we converge to (3.106). Moreover, as it can be noticed in (3.106), each large-scale fading density part is designated by a particular identifier.

$$\begin{aligned} f_{L_{PL}}\left(l\right) &= \int_{\tau=-\infty}^{\infty} f_0\left(\tau\right)d\tau \qquad l \in \mathbb{R}_+^* \\ &= K\underbrace{\left\{\underbrace{\int_{\tau=w_0}^{w_I} f_0^{(1)}\left(\tau\right)d\tau}_{\triangleq I_{LSF}^{(1)}(l)} + \underbrace{\int_{\tau=w_I}^{w_L} f_0^{(2)}\left(\tau\right)d\tau}_{\triangleq I_{LSF}^{(2)}(l)} + + \underbrace{\int_{\tau=w_I}^{w_L} f_0^{(3)}\left(\tau\right)d\tau}_{\triangleq I_{LSF}^{(3)}(l)}\right\}}_{\triangleq I_{LSF}(l)} \end{aligned} \tag{3.106}$$

After pursuing the first integration, we notice that:

$$I_{LSF}^{(1)}\left(l\right) = \int_{\tau=w_0}^{w_I} f_0^{(1)}\left(\tau\right)d\tau = \pi\int_{\tau=w_0}^{w_I} \exp\left\{-\left(\tau - \left\{l + 2\ln\left(10\right)\sigma_{\Psi}^2/\beta\right\}\right)^2 \Big/ 2\sigma_{\Psi}^2\right\}d\tau \tag{3.107}$$

We could change (3.107) to a simpler entry by using the following transformation:

$$z = z\left(\tau\right) = \frac{\left(\tau - \left\{l + 2\ln\left(10\right)\sigma_{\Psi}^2/\beta\right\}\right)}{\sigma_{\Psi}} \tag{3.108}$$

In fact, as it will be shown later on, we will use the transformation of (3.108) to the three integration components described in (3.106). Therefore, the limits of these integrations must be readjusted in order to reflect this modification. The association between the limits of τ and z are thus given by:

$$\vec{w}=\begin{bmatrix} w_0 \\ w_I \\ w_L \end{bmatrix} \Leftrightarrow \vec{z}=\begin{bmatrix} z_0 \\ z_I \\ z_L \end{bmatrix}=\begin{bmatrix} \left(w_0-\left\{l+2\ln(10)\sigma_\Psi^2/\beta\right\}\right)/\sigma_\Psi \\ \left(w_I-\left\{l+2\ln(10)\sigma_\Psi^2/\beta\right\}\right)/\sigma_\Psi \\ \left(w_L-\left\{l+2\ln(10)\sigma_\Psi^2/\beta\right\}\right)/\sigma_\Psi \end{bmatrix} \in \mathbb{R}^3 \tag{3.109}$$

Returning to (3.107), if we now solve for τ in (3.108), we notice that:

$$\tau=\tau(z)=\sigma_\Psi z+l+2\ln(10)\sigma_\Psi^2/\beta \tag{3.110}$$

and the derivative of (3.110) is obviously $d\tau=\sigma_\Psi dz$. Inserting (3.110), its derivative, and the related limits from (3.109) into the formulation of (3.107) becomes:

$$I_{LSF}^{(1)}(l)=\pi\cdot\sigma_\Psi\int_{z=z_0}^{z_I}\exp\left(-z^2/2\right)dz \tag{3.111}$$

To further simplify and represent (3.111) in an elegant manner, we need to define the so-called Q-function, $Q(x):\mathbb{R}\mapsto[0,1]$, such that:

$$Q(x)=\int_{z=x}^{\infty}\mathcal{N}(0,1)\,dz=\frac{1}{\sqrt{2\pi}}\int_{z=x}^{\infty}\exp\left(-z^2/2\right)dz \tag{3.112}$$

In fact, it can be shown that the Q-function is related to the error function (ERF) and the complementary error function (ERFC) by the following relationship:

$$Q(x)=erfc\left(x/\sqrt{2}\right)/2=\left\{1-erf\left(x/\sqrt{2}\right)\right\}/2 \tag{3.113}$$

Granted, the integration in (3.112) is performed over the $\left\{z\in\mathbb{R}\,\middle|\,x\le z<\infty\right\}$ set; if on the other hand the set is limited between two fixed values, say $\left\{x\in\mathbb{R}\,\middle|\,x_1\le x\le x_2\right\}$, then we observe that:

$$\begin{aligned}\int_{x=x_1}^{x_2}\mathcal{N}(0,1)\,dx&=\int_{x=x_1}^{\infty}\mathcal{N}(0,1)\,dx-\int_{x=x_2}^{\infty}\mathcal{N}(0,1)\,dx\\&=Q(x_1)-Q(x_2)=\left\{Q(x)\right\}_{x=x_2}^{x_1}=-\left\{Q(x)\right\}_{x=x_1}^{x_2}\end{aligned} \tag{3.114}$$

or we could rewrite (3.114) as:

$$\int_{x=x_1}^{x_2}\exp\left(-x^2/2\right)dx=-\sqrt{2\pi}\left\{Q(x)\right\}_{x=x_1}^{x_2} \tag{3.115}$$

Coming back to (3.111), we could specify the result via the use of (3.115) by:

$$I_{LSF}^{(1)}(l)=-\pi\sqrt{2\pi}\cdot\sigma_{\Psi}\cdot\left\{Q(z)\right\}_{z=z_0}^{z_I} \tag{3.116}$$

Moving to the second integration of (3.106), we can readily solve it because by (3.103) it is similar to $I_{LSF}^{(1)}(l)$ shown in (3.111), except π should be changed to -2π and the limits of integration ought to be within $\left[z_I\,,\,z_L\right]$; thus after doing these alterations we obtain:

$$I_{LSF}^{(2)}(l)=2\pi\sqrt{2\pi}\cdot\sigma_{\Psi}\cdot\left\{Q(z)\right\}_{z=z_I}^{z_L} \tag{3.117}$$

At this point, we could get an intermediate result by adding (3.116) and (3.117) together:

$$
\begin{aligned}
I_{LSF}^{(1)}(l)+I_{LSF}^{(2)}(l) &= -\pi\sqrt{2\pi}\cdot\sigma_{\Psi}\cdot\left\{Q(z)\right\}_{z=z_0}^{z_I}+2\pi\sqrt{2\pi}\cdot\sigma_{\Psi}\cdot\left\{Q(z)\right\}_{z=z_I}^{z_L} \\
&= \pi\sqrt{2\pi}\cdot\sigma_{\Psi}\left\{2\left\{Q(z)\right\}_{z=z_I}^{z_L}-\left\{Q(z)\right\}_{z=z_0}^{z_I}\right\} \\
&= \pi\sqrt{2\pi}\cdot\sigma_{\Psi}\left\{2\left\{Q(z_L)-Q(z_I)\right\}-\left\{Q(z_I)-Q(z_0)\right\}\right\} \\
&= \pi\sqrt{2\pi}\cdot\sigma_{\Psi}\left\{Q(z_0)-3Q(z_I)+2Q(z_L)\right\}
\end{aligned}
\tag{3.118}
$$

Finally, moving to the third large-scale fading density integration defined in (3.106), it is manifested by:

$$
\begin{aligned}
I_{LSF}^{(3)}(l) &= \int_{\tau=w_I}^{w_L} f_0^{(3)}(\tau)\,d\tau \\
&= 6\int_{\tau=w_I}^{w_L}\exp\left\{\frac{-1}{2\sigma_{\Psi}^2}\cdot\left(\tau-\left\{l+\frac{2\ln(10)\sigma_{\Psi}^2}{\beta}\right\}\right)^2\right\}\cdot\arcsin\left(\frac{\sqrt{3}L}{2\cdot 10^{(\tau-\alpha)/\beta}}\right)d\tau
\end{aligned}
\tag{3.119}
$$

If we start by applying the transformation of (3.110) to the base-10 entity inside the arcsine of (3.119), we find that:

$$
\begin{aligned}
\left[1/10^{(\tau-\alpha)/\beta}\right]_{\tau=\sigma_{\Psi}z+l+2\ln(10)\sigma_{\Psi}^2/\beta} &= 1/10^{\left(\sigma_{\Psi}z+l+2\ln(10)\sigma_{\Psi}^2/\beta-\alpha\right)/\beta} = 1/10^{\sigma_{\Psi}z/\beta}\cdot 10^{\left(\beta\cdot l-\beta\cdot\alpha+2\ln(10)\sigma_{\Psi}^2\right)/\beta^2} \\
&= 10^{-\sigma_{\Psi}z/\beta}/10^{\left\{\beta(l-\alpha)+2\ln(10)\sigma_{\Psi}^2\right\}/\beta^2}
\end{aligned}
\tag{3.120}
$$

Overall, with the help of (3.120), the transformation of (3.110) changes (3.119) to:

$$
I_{LSF}^{(3)}(l) = 6\cdot\sigma_{\Psi}\int_{z=z_I}^{z_L}\exp\left(-z^2/2\right)\cdot\arcsin\left(\frac{\sqrt{3}L}{2\cdot 10^{\left\{\beta(l-\alpha)+2\ln(10)\sigma_{\Psi}^2\right\}/\beta^2}}\cdot 10^{-\sigma_{\Psi}z/\beta}\right)dz \tag{3.121}
$$

If we combine the intermediate result of (3.118) and (3.121) together, we then get:

$$I_{LSF}(l)=\sigma_{\Psi}\left\{\begin{array}{l}\pi\sqrt{2\pi}\cdot\left\{Q(z_0)-3Q(z_I)+2Q(z_L)\right\}\\ +6\int_{z=z_I}^{z_L}\exp\left(-z^2/2\right)\cdot\arcsin\left(\dfrac{\sqrt{3}L\cdot 10^{-\sigma_{\Psi}z/\beta}}{2\cdot 10^{\left\{\beta(l-\alpha)+2\ln(10)\sigma_{\Psi}^2\right\}/\beta^2}}\right)dz\end{array}\right\} \tag{3.122}$$

In the expression of (3.122), the utilized variables $\{z_0, z_I, z_L\}$ were defined in (3.109) as a function of $\{w_0, w_I, w_L\}$. Likewise, the w parameters were identified in (3.76). Ideally, these two cascading transformations can be merged together in a compact arrangement:

$$\begin{aligned}z_{0,I,L}=z_{0,I,L}(l)&=\left(\tilde{w}-\left\{l+2\ln(10)\sigma_{\Psi}^2/\beta\right\}\right)\Big/\sigma_{\Psi}\quad\leftrightarrow\quad\tilde{w}=w_0,w_I,w_L\\&=\left(\alpha+\beta\log_{10}(\tilde{r})-\left\{l+2\ln(10)\sigma_{\Psi}^2/\beta\right\}\right)\Big/\sigma_{\Psi}\quad\leftrightarrow\quad\tilde{r}=r_0,\sqrt{3}L/2,L\\&=\frac{1}{\sigma_{\Psi}}\left\{\alpha-l+\beta\log_{10}(\tilde{r})-\frac{2\sigma_{\Psi}^2}{\beta}\ln(10)\right\}\\&=\frac{1}{\sigma_{\Psi}}\left\{\alpha-l+\frac{\beta}{\ln(10)}\ln(\tilde{r})-\frac{2\sigma_{\Psi}^2}{\beta}\ln(10)\right\}\\&=\frac{1}{\sigma_{\Psi}}\left\{\alpha-l+\ln\left(\tilde{r}^{\beta/\ln(10)}\right)-\ln\left(10^{2\sigma_{\Psi}^2/\beta}\right)\right\}\\&=\frac{1}{\sigma_{\Psi}}\left\{\alpha-l+\ln\left(\tilde{r}^{\beta/\ln(10)}\Big/10^{2\sigma_{\Psi}^2/\beta}\right)\right\}\end{aligned} \tag{3.123}$$

If we observe all the items that constitute the PDF of the large-scale fading, namely: (3.104), (3.122) and (3.123), we remark that these mathematical statements are fundamentally dependent on $\{l,\vec{\Lambda}\}\in\mathbb{R}_{+,*}^{6}$, such that:

$$\vec{\Lambda}=\{\alpha,\beta,\sigma_{\Psi},r_0,L\}\in\mathbb{R}_{+,*}^{5} \tag{3.124}$$

is an array of parameters that demonstrates the generic nature of the analytical derivation.

Moreover, as a reminder from (3.80), the l entry represents a random sample of the large-scale fading between a reference and an arbitrary terminal. Indeed, due to the log-normal nature of shadowing, this variable is expected to be in $\mathbb{R}$; yet from a practical standpoint it is a.s. element in $\mathbb{R}_{+}^{*}$. For further precision, the range for this RV can additionally be narrowed-down. Again, from (3.80), we know that large-scale fading is composed of the average PL and shadowing:

$$L_{PL}\left(r\right)_{dB} = \overline{L_{PL}\left(r\right)}_{dB} + \Psi_{S-dB} \tag{3.125}$$

The lower extremity of (3.125) is analyzed in (3.126). As noticeable, the optimization of the large-scale fading level is split because the contribution from the average PL and shadowing are independent of each other, where their characteristics are respectively provided in (3.75) and (3.83).

$$\begin{aligned} l_0 &\triangleq \min_{(r,\sigma_\Psi)\in\mathbb{R}_{+,*}^{2}} \left\{L_{PL}\left(r\right)_{dB}\right\} = \min_{(r,\sigma_\Psi)\in\mathbb{R}_{+,*}^{2}} \left\{\overline{L_{PL}\left(r\right)}_{dB} + \Psi_{S-dB}\right\} \\ &= \min_{r\in\mathbb{R}_{+}^{*}}\left\{\overline{L_{PL}\left(r\right)}_{dB}\right\} + \min_{\sigma_\Psi\in\mathbb{R}_{+}^{*}}\left\{\Psi_{S-dB}\right\} \\ &= \min_{r\in\mathbb{R}_{+}^{*}}\left\{\alpha+\beta\log_{10}\left(r\right)\right\} + \min_{\sigma_\Psi\in\mathbb{R}_{+}^{*}}\left\{\Psi_{S-dB}\right\} \\ &= \alpha+\beta\log_{10}\left(r_0\right) + \min_{\sigma_\Psi\in\mathbb{R}_{+}^{*}}\left\{\Psi_{S-dB}\sim\mathcal{N}_S\left(0,\sigma_\Psi^2\right)\right\} \end{aligned} \tag{3.126}$$

By the same token, the higher extremity of the large-scale measure for an L size cellular network model is obtained through:

$$l_L \triangleq \max_{(r,\sigma_\Psi)\in\mathbb{R}_{+,*}^{2}} \left\{L_{PL}\left(r\right)_{dB}\right\} = \alpha+\beta\log_{10}\left(L\right) + \max_{\sigma_\Psi\in\mathbb{R}_{+}^{*}}\left\{\Psi_{S-dB}\sim\mathcal{N}_S\left(0,\sigma_\Psi^2\right)\right\} \tag{3.127}$$

In particular, the optimization for the shadowing entity, which is modeled by a zero-mean Gaussian distribution, is still needed in order to complete the results of (3.126) and (3.127). To do this, we will stochastically emulate the impact of shadowing. However, for this purpose we

need to elaborate on the approach for generating values from a general $\mathcal{N}\left(m,\sigma^2\right)$ distribution function.

Indeed, several software packages, including MATLAB®, are capable based on the ziggurat algorithm to generate random values from the standard normal distribution. Then, these standard samples could be changed to the desired Gaussian density function $\mathcal{N}_X\left(m,\sigma^2\right)$, such that:

$$\forall x\in\mathbb{R}:\exists m\in\mathbb{R}:\exists\sigma\in\mathbb{R}_+^*\mapsto\left[0,1/\sqrt{2\pi}\sigma\right] \tag{3.128}$$

In fact, this stochastic modification could be achieved using the transformation shown in the block diagram of Figure 3.23.

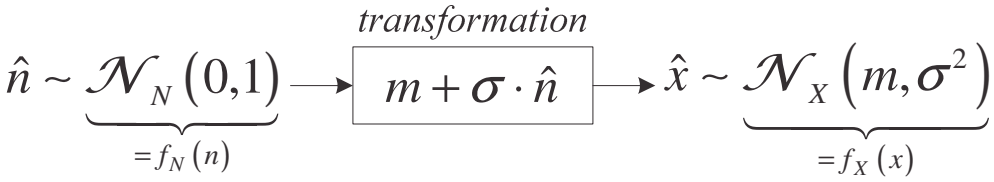

Figure 3.23 – Gaussian random generation

Empowered with the above, we could now randomly generate shadowing instances using the simple algorithm of Figure 3.24.

Algorithm 4 - RNG of Channel Shadowing

1: Require: $n_S\in\mathbb{N}^*\quad\sigma_\Psi\in\mathbb{R}_+^*$
2: **for** $i=1,2,\cdots,n_S$ **do**
3: Generate a RV: $\hat{n}_i\sim\mathcal{N}\left(0,1\right)$
4: Compute: $\hat{\psi}_i=\sigma_\Psi\hat{n}_i\sim\mathcal{N}_S\left(0,\sigma_\Psi^2\right)$
5: **end for**
6: Return: $\left\{i;\ \hat{\psi}_i\right\}:i=1,2,\cdots,n_S$

Figure 3.24 – Pseudocode for the generation of shadowing

Say, we generate some $n_S = 5,000$ random samples of shadowing having an SD of 10 dB, which is typically considered for the channel environments of IEEE 802.20 [52]. When we plot the shadowing levels as random realization of dots on a graph against indices of instances, we then obtain the output of Figure 3.25. As manifested in the simulation result, the shadowing is partitioned into different layers via multiples of SD:

$$\left|\Psi_{S-dB}\right| = j \cdot \sigma_{\Psi} \qquad j = 1, 2, \cdots \tag{3.129}$$

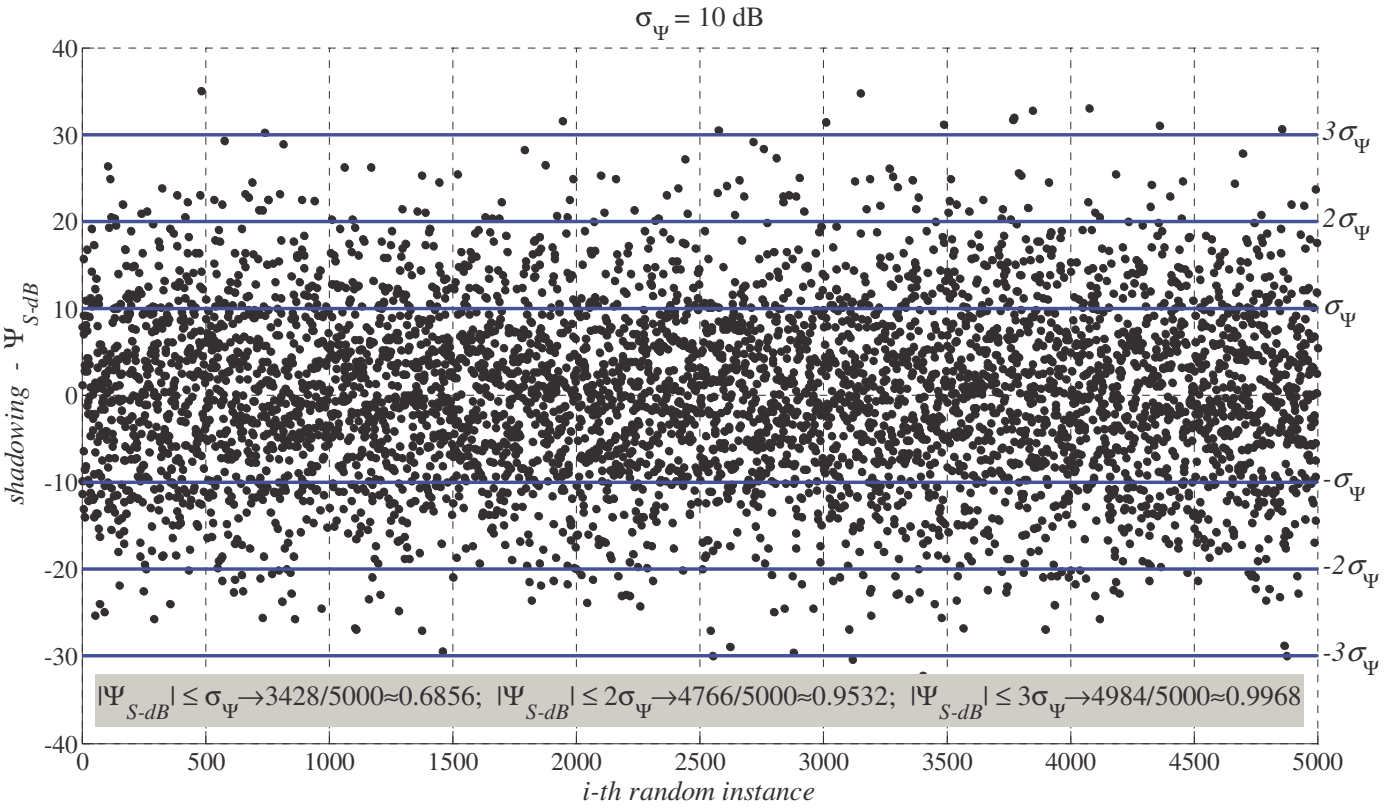

Figure 3.25 – Generating 5,000 random realizations of channel shadowing

In the above MC experiment, the probabilities for random samples contained in a particular interval were estimated. From this example, the most significant observation stem from the fact that a negligible of only 16 out of 5,000 random samples were located outside three SDs. Statistically speaking, a more precise estimation of these probabilities for the associated confidence intervals (CI) reveal that:

$$\begin{aligned} \left|\Psi_{S-dB}\right| &\le \sigma_{\Psi} \quad \rightarrow \quad \sim 68.2690\% \\ \left|\Psi_{S-dB}\right| &\le 2\sigma_{\Psi} \quad \rightarrow \quad \sim 95.4500\% \\ \left|\Psi_{S-dB}\right| &\le 3\sigma_{\Psi} \quad \rightarrow \quad \sim 99.7300\% \end{aligned} \tag{3.130}$$

Thus, from this analysis, we realize that within three SDs most randomly generated samples will be accounted for with high probability (w.h.p.). As a result, the extent of shadowing can be estimated by:

$$\min_{\sigma_{\Psi}\in\mathbb{R}_{+}^{*}} \left\{ \Psi_{S-dB} \sim \mathcal{N}_{S}\left(0,\sigma_{\Psi}^{2}\right) \right\} \approx -3\sigma_{\Psi} \tag{3.131}$$

$$\max_{\sigma_{\Psi}\in\mathbb{R}_{+}^{*}} \left\{ \Psi_{S-dB} \sim \mathcal{N}_{S}\left(0,\sigma_{\Psi}^{2}\right) \right\} \approx 3\sigma_{\Psi} \tag{3.132}$$

Substituting (3.131) and (3.132) into (3.126) and (3.127) will respectively provide w.h.p. an approximation for the lower and higher extremities of the large-scale fading:

$$l_0 \approx \tilde{l}_0 = \alpha + \beta \log_{10}\left(r_0\right) - 3\sigma_{\Psi} \tag{3.133}$$

$$l_L \approx \tilde{l}_L = \alpha + \beta \log_{10}\left(L\right) + 3\sigma_{\Psi} \tag{3.134}$$

Hence, a tighter support values for l is given by:

$$\left\{ l \in \mathbb{R}_{+}^{*} \middle| 0 < \tilde{l}_0 \lesssim l \lesssim \tilde{l}_L < \infty \right\} \tag{3.135}$$

Having characterized the extent of the large-scale fading, we now find it interesting to graphically demonstrate in Figure 3.26 the average PL and the deviation from it caused by shadowing. In the illustration, an approximately all-inclusive CI for large-scale fading is obviously represented by:

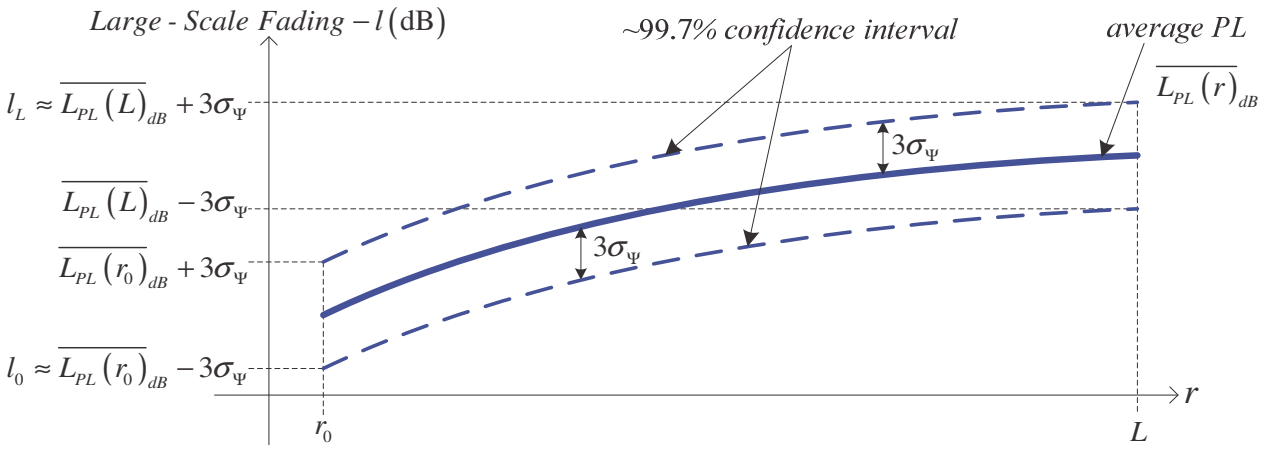

Figure 3.26 – Interpreting the confidence interval and extent of large-scale fading

$$\Pr\left\{\left|l - \overline{L_{PL}(r)}_{dB}\right| \le 3\sigma_\Psi\right\} \approx 0.997300 \tag{3.136}$$

Indeed, estimates for the lower and higher extremities of the large-scale fading measures are recognizable and are accordingly indicated in the above visual representation. As we can easily observe, the analyzed results are indeed congruent with the graphical extent shown in Figure 3.26.

At this moment, we have all the necessary features to analytically assemble the PDF of the channel-loss. To be precise, from (3.106), we recognize that the density function is composed of two parts. The first part, which is identified and described in (3.103) and (3.104), is designated by K . The second part, namely $I_{LSF}(l)$, was obtained in (3.122) with Q-function in (3.113); and its associated variables were solved in (3.123). Overall, the derived density result is generic due to the changeable parameters specified in (3.124). Further, the domain of the density function was detailed in (3.135), where the related boundaries were assessed in (3.133) and (3.134). The final, exact and closed-form stochastic statement for the probability distribution of the large-scale fading between a randomly positioned MS and a reference BS over a MCN model is elegantly ordered and explicitly shown in (3.137).

$$f_{L_{PL}}\left(l,\vec{\Lambda}\right)=\frac{4\cdot\ln(10)\cdot 10^{2(l-\alpha)/\beta}}{\beta\left(3\sqrt{3}L^2-2\pi r_0^2\right)}\cdot\exp\left\{\left(\sqrt{2}\ln(10)\sigma_\Psi/\beta\right)^2\right\}$$
$$\times\left\{\begin{array}{l}\pi\cdot\left\{Q\left(z_0(l)\right)-3\cdot Q\left(z_I(l)\right)+2\cdot Q\left(z_L(l)\right)\right\}\\ \quad+3\sqrt{2/\pi}\cdot\int_{z=z_I(l)}^{z_L(l)}\exp\left(-z^2/2\right)\cdot\arcsin\left(\dfrac{\sqrt{3}L\cdot 10^{-\sigma_\Psi z/\beta}}{2\cdot 10^{\left\{\beta(l-\alpha)+2\cdot\ln(10)\sigma_\Psi^2\right\}/\beta^2}}\right)dz\end{array}\right\}$$

$$0<\tilde{l}_0\lesssim l\lesssim\tilde{l}_L<\infty$$

- $\vec{\Lambda}=\{\alpha,\beta,\sigma_\Psi,r_0,L\}\in\mathbb{R}^5_{+,*}$
- $Q(z)=erfc\left(z/\sqrt{2}\right)/2=\left\{1-erf\left(z/\sqrt{2}\right)\right\}/2$
- $z_0(l)=\left\{\alpha-l+\ln\left(r_0^{\beta/\ln(10)}/10^{2\sigma_\Psi^2/\beta}\right)\right\}/\sigma_\Psi$
- $z_I(l)=\left\{\alpha-l+\ln\left(\left(\sqrt{3}L/2\right)^{\beta/\ln(10)}/10^{2\sigma_\Psi^2/\beta}\right)\right\}/\sigma_\Psi$
- $z_L(l)=\left\{\alpha-l+\ln\left(L^{\beta/\ln(10)}/10^{2\sigma_\Psi^2/\beta}\right)\right\}/\sigma_\Psi$
- $\tilde{l}_0=\alpha+\beta\log_{10}(r_0)-3\sigma_\Psi$
- $\tilde{l}_L=\alpha+\beta\log_{10}(L)+3\sigma_\Psi$

■

(3.137)

3.4.6 – Experimental Validation by MC Simulations

Here, we will authenticate the expression for the large-scale fading PDF of (3.137) by means of stochastic simulations. Generally speaking, the approach for the validation process is broken-down into three major steps:

1. For a given lattice structure and dimensions, the random network geometry of wireless nodes is emulated via MC approach.
2. The large-scale fading density for a particular channel environment is numerically estimated using the emulated spatial samples.
3. The analytically derived PDF is plotted and then compared with the scholastic estimation.

It is imperative to emphasize that the tractable expression of (3.137) is fully generic and thus can be adaptable for any cellular application and wireless technology, as long as user's spatial geometry is assumed to be random and homogeneous over a MCN. Although the obtained result is generic in nature, yet to examine its correctness, we will exclusively consider the channel parameters of IEEE 802.20 [52] for an urban macrocell as specified in Table 3.2.

Table 3.2 – MBWA channel model for urban macrocell

IEEE 802.20 Propagation Parameters	
Propagation Model :	*COST*-231 *Hata-Model*
Operating Frequency :	1.9 GHz
Support Range :	$r_0 = 35 \text{ m} \le r \le L$ $600 \le L \le 3,500 \text{ m}$
Channel - Loss :	$\alpha = 34.5 \text{ dB}$ $\beta = 35 \text{ dB}$
Shadowing :	$\sigma_\Psi = 10 \text{ dB}$

In this situation, the actual details for the MC simulations are as follows:

- In Table 3.2, the transmission radius L can take different values. We will however consider a cellular size of 600 m, which translates into an RCR of ~ 17.14. Given this RCR value, we therefore realize from (3.74) that Cartesian-based RNG is more efficient.
- An $n_S = 10,000$ random samples for nodes 2D spatial position is required. In fact, the set of $\hat{x}_i : i = 1, 2, \cdots, n_S$ components are generated from the Cartesian algorithm of Figure 3.10. After, based on these values, the $\hat{y}_i$ counterparts are obtained using the approach described in Figure 3.15.
- Next, the distance $\hat{r}_i$ between the reference BS and random nodes is calculated using the simple Pythagorean notation of (3.69).
- After that, the average PL for each of the n_S random samples is computed by:

$$\hat{\overline{l}}_i \triangleq \overline{L_{PL}(\hat{r}_i)}_{dB} = \alpha + \beta \log_{10}(\hat{r}_i) \qquad i = 1, 2, \cdots, n_S \tag{3.138}$$

- Using the emulation method detailed in Figure 3.24, values for shadowing are generated in order to get instances of large-scale fading as expressed by:

$$\hat{l}_i \triangleq L_{PL}(\hat{r}_i)_{dB} = \hat{\overline{l}}_i + \hat{\psi}_i \qquad i = 1, 2, \cdots, n_S \tag{3.139}$$

- The uppermost plot of Figure 3.27 shows a scatter diagram for the large-scale fading as a function of the BS-to-MS interpoint range. Specifically, each of the 10,000 instances is represented by a random point. For perspective to this MC realization, three deterministic plots, namely: $\overline{L_{PL}(r)}_{dB}$, $\overline{L_{PL}(r)}_{dB} - 3\sigma_\Psi$, and $\overline{L_{PL}(r)}_{dB} + 3\sigma_\Psi$ over $r \in [r_0, L]$ are also shown so as to characterize the average PL and the $\sim 99.7\%$ CI of large-scale fading caused by shadowing. Indeed, as noticeable from the figure, only a negligible of $\sim 0.3\%$ quantity of samples can be found outside the delineation of the CI.
- Then, based on the described scatter plot, a histogram for the large-scale fading measure is constructed. In this simulation, an $n_B = 100$ bin histogram is considered with equal width designated by $\Delta l_B \in \mathbb{R}_+^*$. Precisely, the bars of the histogram are positioned next to each other with no spacing among them. As for the quantity of occurrence per bar, they are accordingly scaled to reflect an estimate of the PDF; i.e. the occurrence is divided by the amount of random samples and the bin width[3]. Once scaling is performed, we obtain the PDF estimation at discrete points, namely: $pdf_j : j = 1, 2, \cdots, n_B$.
- Also, the CDF of the large-scale fading measure for randomly positioned nodes is approximated by the following recursive relationship:

$$\begin{aligned} cdf_1 &= pdf_1 \cdot \Delta l_B \\ cdf_j &= cdf_{j-1} + pdf_j \cdot \Delta l_B \qquad j = 2, 3, \cdots, n_B \end{aligned} \tag{3.140}$$

[3] A more rigorous analysis for PDF estimation is available in Chapter 5 of this dissertation.

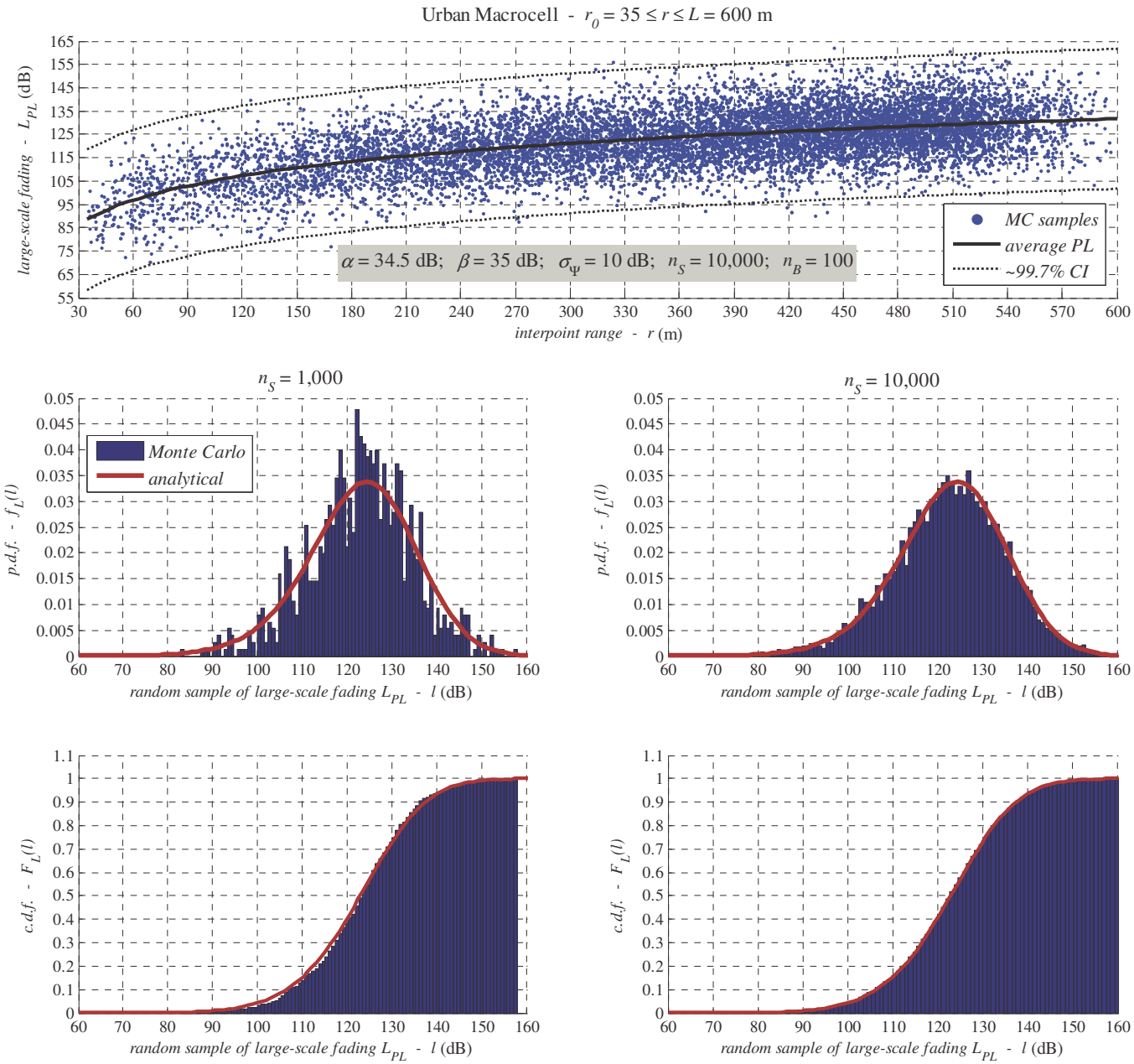

Figure 3.27 – Verifying the analytically derived formulation for large-scale fading PDF

- As shown in Figure 3.27, the PDF estimation is performed over two values of n_S . As expected, an increase of random samples produces a better estimate that appropriately matches the theoretically derived density function of the large-scale fading.
- As remarked earlier in Table 3.2, the cellular size varies from $L = 600 \rightarrow 3,500$ m . Therefore, we find it intriguing to randomly simulate the large-scale PDF as L changes.

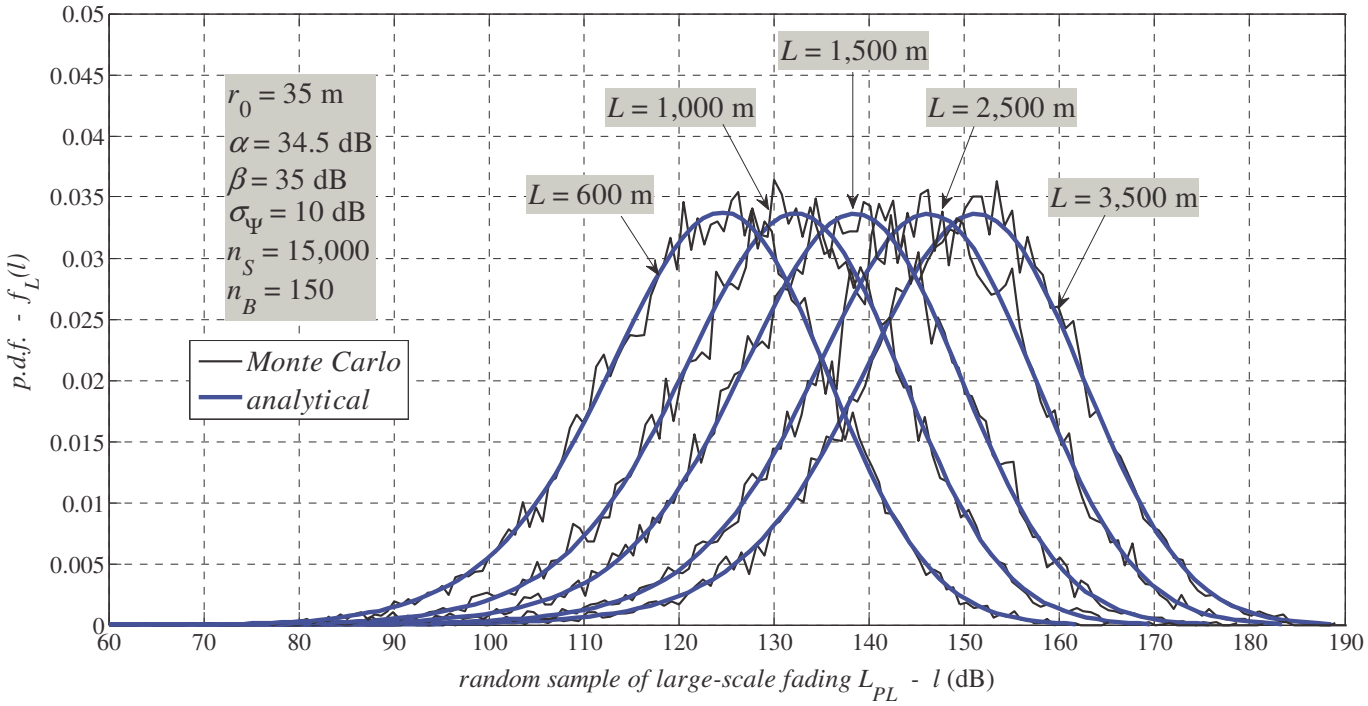

Figure 3.28 – Large-scale fading PDF for BS-to-MS over different cellular sizes

The result of this undertaking is shown in Figure 3.28. It is worth noting from the simulation that an increase in the cellular dimension raises the channel-loss interval, and as a result the first-moment of the PDF is further shifted to the right. Also, it is obvious that the analytical derivation of the PDF and the estimation are properly congruent to each other. In fact, as n_S and n_B increase, the PDF estimation of the large-scale fading is further improved.

3.5 – Conclusion

The main objective of this chapter was to describe the channel-loss density for a random LWN with respect to its service provider. In fact, such density can be obtained numerically using MC simulations. However this approach is computationally expensive, and also it does not produce a tractable and universal stochastic statement useful for analysis and interplay of input/output parameters. Consequently, in order to mathematically characterize with great precision the manifestation of the channel decay, we progressed into various technical steps.

In particular, we first had to explain the essential groundwork for the derivation of large-scale fading density by specifying and combining the analytical features of spatial homogeneity, and the geometrical attributes of the MCN lattice.

Next, we developed an efficient approach for emulating the geometry of the random MCN geared specifically for channel attenuation analysis. This was done as a preliminary step in deriving the large-scale fading PDF and also for verifying the authenticity of the derivation via actual spatial deployment. We also measured the performance of the RNG, and its stochastic features were theoretically formulated and experimentally evaluated.

Equipped with all the necessary steps, we then analytically derived the exact and closed-form expression for the large-scale fading density function between a reference BS and a randomly positioned node; and we performed various MC simulations in order to ensure and confirm the veracity of the result. To be precise, in this derivation we took into account a number of fundamentally important elements, namely: the cellular structure of the architecture, the nodal spatial emplacement, the far-field effect of the reference antenna, the PL behavior, and the impact of channel scatterers.

In fact, the final and overall stochastic expression of the large-scale fading PDF expressed in (3.137), is entirely generic and can directly be adjusted to any cellular size L, close-in distance r_0, PL parameters α and β, and shadowing features described by its SD σ_Ψ. That is to say that the stochastic formulation was attained in such a way that it could be applied to numerous MCN applications and technologies having a unique scale, coverage size, and channel features. In other words, as shown in Figure 3.29, the reported predictive result is indeed adaptable via the insertion of related variables to the different network planning architectures such as: femtocell, picocell, microcell, and macrocell systems [68].

Also, given the diversity of the transmission coverage for each of the listed network realizations, it is thus evident to recognize the variability of the RCR. Notably, for mobile applications that operate with microcell or macrocell networks, the RCR is in generally in the order of ten or greater. As for femtocell and picocell communications, the RCR is typically smaller than this value. Therefore, when the RCR has a slighter level, the significance of the BS far-field radiation is more prominent. On the other hand, a superior RCR is marginally impacted by the far-field region. Nonetheless, this EM propagation phenomenon was explicitly considered

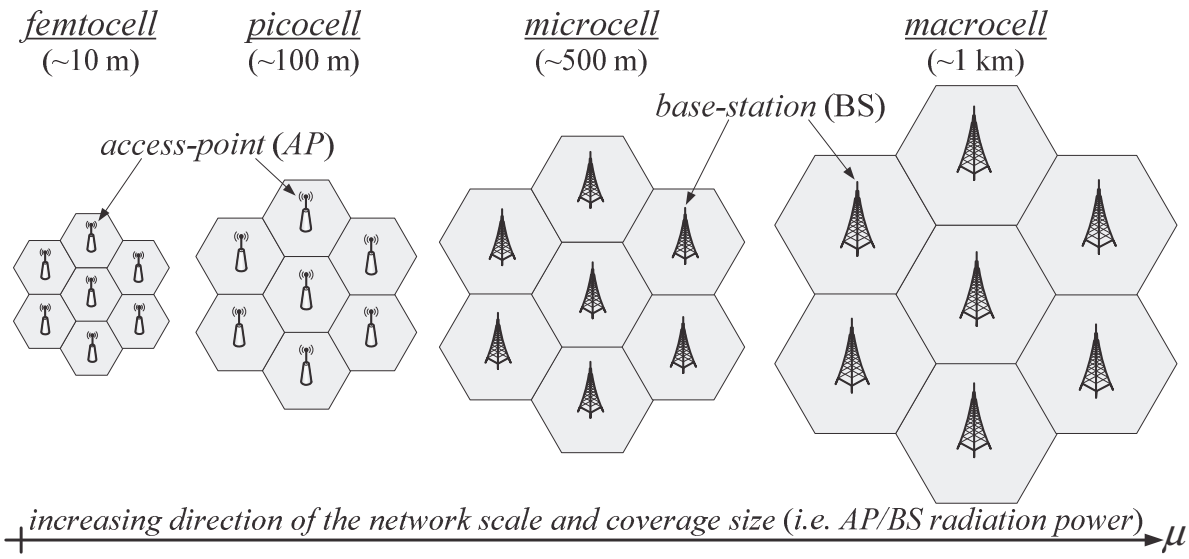

Figure 3.29 – MCN model feasible for various deployment applications and purposes

in the derived density of the large-scale fading model in order to characterize the laws of communications in a rigorous manner; and also to ensure the soundness of the stochastic expression for all type of cellular systems, irrespective of the network scheme.

Furthermore, it is worthwhile to remark that the closed-form analytical expression of the compiled channel-loss PDF will still be applicative for cellular network cases that are partitioned into three or six sectors. In fact, this premise was remarked in Section 3.2. More on this topic will further be elaborated in the next chapter.

For future work, the reported analytical result can be utilized by theoretically deriving the outage probability as a feasible integrity measure for the quality of the random network. Ideally, this formulation can be determined by an exact result; but to remain pragmatic, the derivation is likely to be founded on tight approximation bounds.

Chapter 4

Emulating Heterogeneous Deployment via Geometrical Stochastic Modeling

4.1 – Introduction

4.1.1 – Objective

Emulation is a powerful approach that assists applied scientists to better appreciate the system under investigation. Indeed, once adequately conceptualized, this technique develops into an indispensible analysis mechanism because the method for reengineering and modeling the network architecture can be shown to be:

- Cost and time efficient.
- Straightforwardly adjustable by simple parameter modifications.
- Informative in understanding the attributes of a complex platform.

As a result, having the capability to emulate the footprint of a LWN is fundamentally important for effective network design and planning during both pre- and post-deployment. Of course, some work has been initiated in spatial modeling of the network, but on the whole there are various research aspects in this subject matter that require extensive ameliorations or alternatives. In this chapter, our genuine contribution is based on a threefold objective:

1. Deriving exact stochastic expressions for random spatial deployment over a flexible UCN model. The anticipated findings will also serve as intermediate steps for the subsequent channel-loss and inhomogeneity objectives.

2. Obtaining a tractable closed-form stochastic notation for the large-scale fading PDF over a geometrically versatile random UCN deployment.

3. Proposing novel geometrical deployment algorithms for achieving spatial heterogeneity such that users clustering tendencies are accounted for UCN and MCN structures.

After formulation, the above analytical undertakings will be supplemented by the demonstration of various random networks generated from MC realizations. Altogether, the obtained results are expected to deliver a practical toolkit that will be instrumental in researching the facets of radio networks related to connectivity and service quality.

4.1.2 – Organization

The rest of this chapter is organized as follows. In Section 4.2, we will explicitly formulate and analyze the geometrical characteristics of a flexibly versatile random UCN model. Under such network configuration, in Section 4.3, we will then derive a predictive model for the large-scale fading density function that exhibits adaptable and tractable properties. After, in Section 4.4, we will reveal the ASD algorithm for the purpose of emulating spatial inhomogeneity. Next, we will utilize this proposed algorithm to develop a heterogeneous mechanism for controlled UCN deployment. We will also conceive a technique for automatically generating an arbitrary geometrical structure with least amount of inputs. Afterward, in Section 4.5, we will develop an additional algorithm for spatially modeling a large MCN founded in part on antenna sectoring. Finally, Section 4.6 will conclude the chapter.

4.2 – Stochastical Characteristics of a Versatile UCN Model

4.2.1 – Exact Geometrical Expressions for Spatial Deployment

As noted in Chapter 2, the BS coverage of a cellular network is influenced by multiple factors, such as: antenna radiation, atmospheric attenuation, channel deteriorations due to terrain features and manmade obstacles. Considering these items simultaneously will result in an unpredictable lattice contour. As a result, random nodal deployment in this irregular lattice model will be highly intricate and likely inconceivable. Fortunately, for cellular networks, it is customary to model the extent of the transmission coverage by an ideal disk-shaped circular geometry. The key rational for considering a well-defined cellular structure is done so as to facilitate the theoretical analysis and stochastically enable the spatial emulation of a LWN.

For various mobile communication purposes the circular random network model has been presumed, among others, in [18]–[25]. Despite the availability of this spatial model, in its current state it does not offer any deployment versatility in dealing with sectored layers and edge related aspects. Clearly, the needed geometrical adaptability could be created synthetically through heuristic means. However, besides being an inefficient generation approach, such workarounds alters the wanted randomness; thus defeating the main principle of stochastic networks. As a consequence, we will in this subsection derive the exact and appropriate expressions needed for random nodal emplacement.

To begin, instead of making the cell shape represents the BS radiation coverage, we rather make it correspond to the surface area of some terrain. For the sake of the argument, let us assume that the surface region of interest has circular ring sector geometry. And, for the simplest and possibly most intuitive case for spatial deployment, we may postulate that nodes are uniformly distributed within this geographical strip. As a result, the joint spatial PDF for nodes 2D position will have the form depicted in Figure 4.1, where the inner and outer cellular radii of the ring sector are identified in (4.1), and the angular limits are given by (4.2).

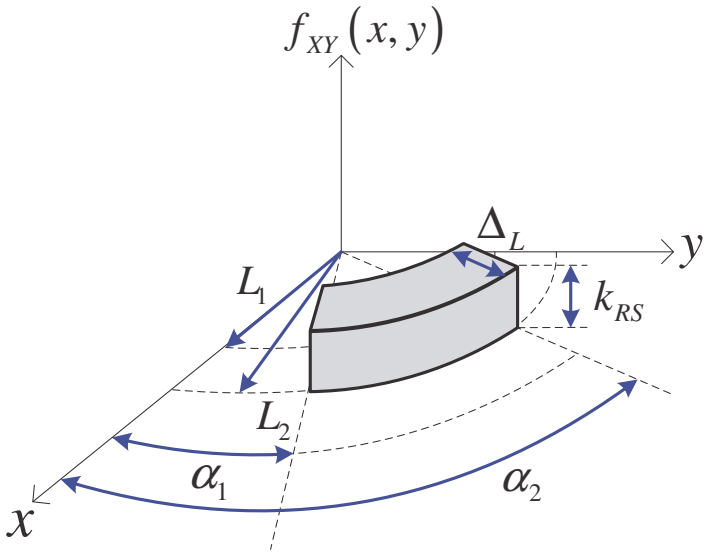

Figure 4.1 – Spatial density function over a circular ring sector in Cartesian coordinates

$$\exists L_1, L_2 \in \mathbb{R}_+^2 : 0 \le L_1 < L_2 \tag{4.1}$$

$$\exists \alpha_1, \alpha_2 \in \mathbb{R}_+^2 : 0 \le \alpha_1 < \alpha_2 \le 2\pi \tag{4.2}$$

As for the region shown in Figure 4.1, it can be assessed over the surface domain by simply integrating an infinitesimal area element which is represented in Cartesian and polar notations by:

$$dA = \underbrace{dx \cdot dy}_{Cartesian} = \underbrace{r \cdot dr \cdot d\theta}_{polar} \tag{4.3}$$

Pursuing this task produces:

$$A_{RS} = \iint_{(x,y)\in D_{RS}\subset\mathbb{R}^2} dA = \left(L_2^2 - L_1^2\right)\left(\alpha_2 - \alpha_1\right)\Big/2 \tag{4.4}$$

such that $A_{RS} \in \mathbb{R}_+^*$ is the corresponding deployment area of the network cluster for the ring sector, D_{RS} is the support domain in Cartesian format, and D_{RS}^P is the equivalent domain in polar notation. From (4.4), the spatial density can then be formulated by its reciprocal as follows:

$$f_{XY}(x,y) = 1/A_{RS} = 2\Big/\left(L_2^2 - L_1^2\right)\left(\alpha_2 - \alpha_1\right) = k_{RS} \quad (x,y) \in D_{RS} \subset \mathbb{R}^2 \tag{4.5}$$

Also, the magnitude of this spatial density function is constant and set by $k_{RS} \in \mathbb{R}_+^*$.

For generation purposes, the next step demands that we determine the marginal density along each axis. It turns out that if we continue with the rectangular coordinates, the analysis will become longer and more complicated to solve. Specifically, RVs X and Y are correlated; thus a generic and compact stochastic model for diverse cellular parameters will not be possible, rather derivation will be needed for different subsets of the values. Further, under these conditions, efficient random generation is unfeasible because the marginal ICDF is not expressible in an explicit format; thus requiring the use of the iterative suboptimal ARM procedure detailed in the former chapter. Also due to the variables interdependence, serial processing during the RNG step will be necessary as opposed to time-efficient parallel computation. In light of these observations, we will need to determine a stochastical conversion procedure in order to simplify these important challenges.

Given the character of the network cluster being modeled, it is evident that the best transformation ought to depend on the polar coordinate system. In other words, the spatial density of (4.5) is stochastically converted to:

$$\begin{aligned} f_{R\theta}(r,\theta) &= f_{XY}(x,y)\big|_{\substack{x=r\cos\theta \\ y=r\sin\theta}} \cdot \left|J(r,\theta)\right| \qquad (r,\theta)\in D_{RS}^{P}\subset\mathbb{R}_{+}^{2} \\ &= 2\cdot r\Big/\left(L_2^2-L_1^2\right)\left(\alpha_2-\alpha_1\right) \end{aligned} \tag{4.6}$$

where its support surface is described by:

$$D_{RS}^{P}=\left\{\begin{array}{c|c} (r,\theta)\in\mathbb{R}_{+}^{2} & 0\le L_1\le r\le L_2 \\ (L_1,L_2,\alpha_1,\alpha_2)\in\mathbb{R}_{+}^{4} & 0\le\alpha_1\le\theta\le\alpha_2\le 2\pi \end{array}\right\} \tag{4.7}$$

The portrayal of this distribution function is accordingly shown in Figure 4.2.

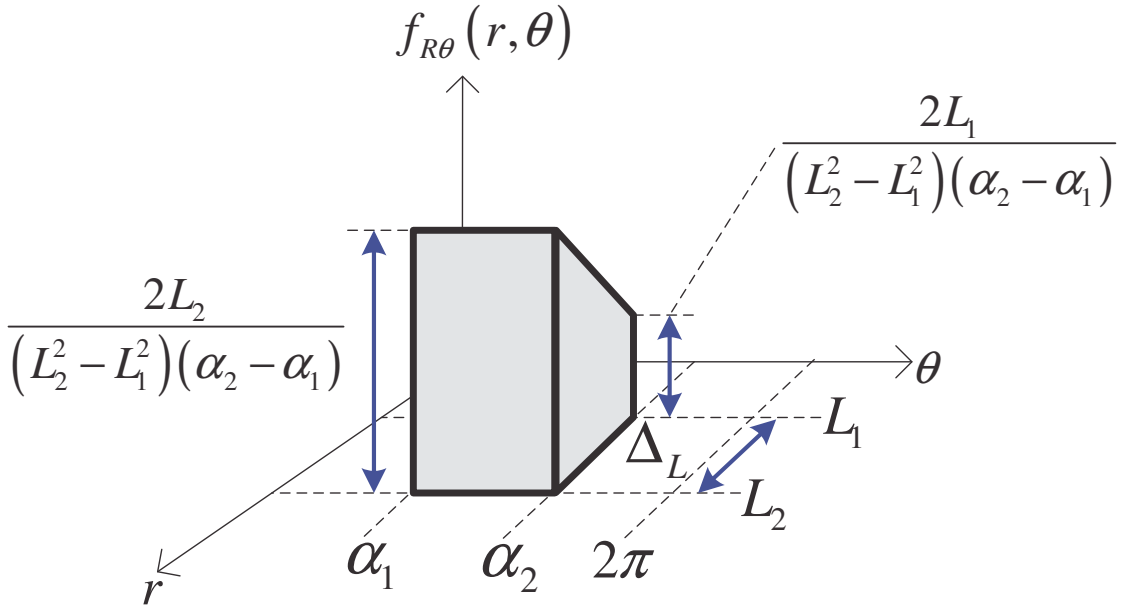

Figure 4.2 – Spatial density function over a circular ring sector in polar coordinates

Using the results of (4.6) and (4.7), we could at present express the marginal probability densities for the radial and angular components:

$$f_R(r) = \int_{(r,\theta)\in D_{RS}^P} f_{R\theta}(r,\theta)\,d\theta = \int_{\theta=\alpha_1}^{\alpha_2} 2\cdot r\; d\theta \Big/ \left(L_2^2 - L_1^2\right)(\alpha_2 - \alpha_1)$$
$$= \left\{2r \Big/ \left(L_2^2 - L_1^2\right)\right\} \cdot \mathbf{1}(L_1 \le r \le L_2) \tag{4.8}$$

$$f_\theta(\theta) = \int_{(r,\theta)\in D_{RS}^P} f_{R\theta}(r,\theta)\,dr = \int_{r=L_1}^{L_2} 2\cdot r\; dr \Big/ \left(L_2^2 - L_1^2\right)(\alpha_2 - \alpha_1)$$
$$= \mathcal{U}_\theta(\alpha_1,\alpha_2) \quad 0 \le \alpha_1 \le \theta \le \alpha_2 \le 2\pi \tag{4.9}$$

From (4.8) and (4.9), we could readily show that RVs R and θ are indeed independent because:

$$f_{R\theta}(r,\theta) = f_R(r)\cdot f_\theta(\theta) \tag{4.10}$$

Pursuing this further, the radial CDF $F_R(r) : \mathbb{R}^+ \mapsto [0,1]$ is also determined:

$$F_R(r) = \Pr(R \le r) = \int_{\tilde{r}=-\infty}^{r} f_R(\tilde{r})\,d\tilde{r} = \left\{\left(r^2 - L_1^2\right) \Big/ \left(L_2^2 - L_1^2\right)\right\} \cdot \mathbf{1}(L_1 \le r \le L_2) \tag{4.11}$$

Now, if we set the CDF of (4.11) to an arbitrary sample occurrence $\hat{u}$ generated from a standard uniform distribution, namely $F_R(\hat{r}) = \hat{u}$, then the related ICDF should enable perfect emulation of random instances:

$$\hat{r} = \left\{\left(F_R\right)^{-1}\left(\hat{u} \sim \mathcal{U}(0,1)\right)\right\} \sim f_R(r) \tag{4.12}$$

After solving the expression in (4.12), we notice that the radial samples will be generated from a function specified by:

$$\hat{r} = \hat{r}(\hat{u}, L_1, L_2) = \sqrt{L_1^2 + \hat{u}\left(L_2^2 - L_1^2\right)} : \left\{\exists \hat{u} \in \mathbb{R}_+^* : 0 < \hat{u} < 1\right\} \mapsto (L_1, L_2) \tag{4.13}$$

As for the angular component, its random samples can be produced using the transformation of Figure 3.9; and therefore we get:

$$\hat{\theta} = \hat{\theta}\left(\hat{v}, \alpha_1, \alpha_2\right) = \left\{\alpha_1 + \hat{v}\left(\alpha_2 - \alpha_1\right)\right\} \sim f_\theta\left(\theta\right) \tag{4.14}$$

where $\hat{u}$ and $\hat{v}$ are uncorrelated random i.i.d. samples, or $\langle \hat{u} \cdot \hat{v} \rangle = \langle \hat{u} \rangle \cdot \langle \hat{v} \rangle$. Overall, due to the $(x, y) \to (r, \theta)$ transformation, we have changed inconveniences into advantages. Namely, R and θ are statistically independent, a unique model is valid for all supported parameter values, and the ITM approach can be used as the efficient RNG of choice.

To verify the generation accuracy of the radial density, we performed in Figure 4.3 a set of random simulations. Specifically, the outer radius of the network ring was fixed at one unit, whereas the inner radius varied for different values. For each network case, the simulation was performed based on 10,000 random samples with a histogram resolution of 100. As obvious from the outputs, the radial PDF based on theoretical analysis and MC measures are in agreement.

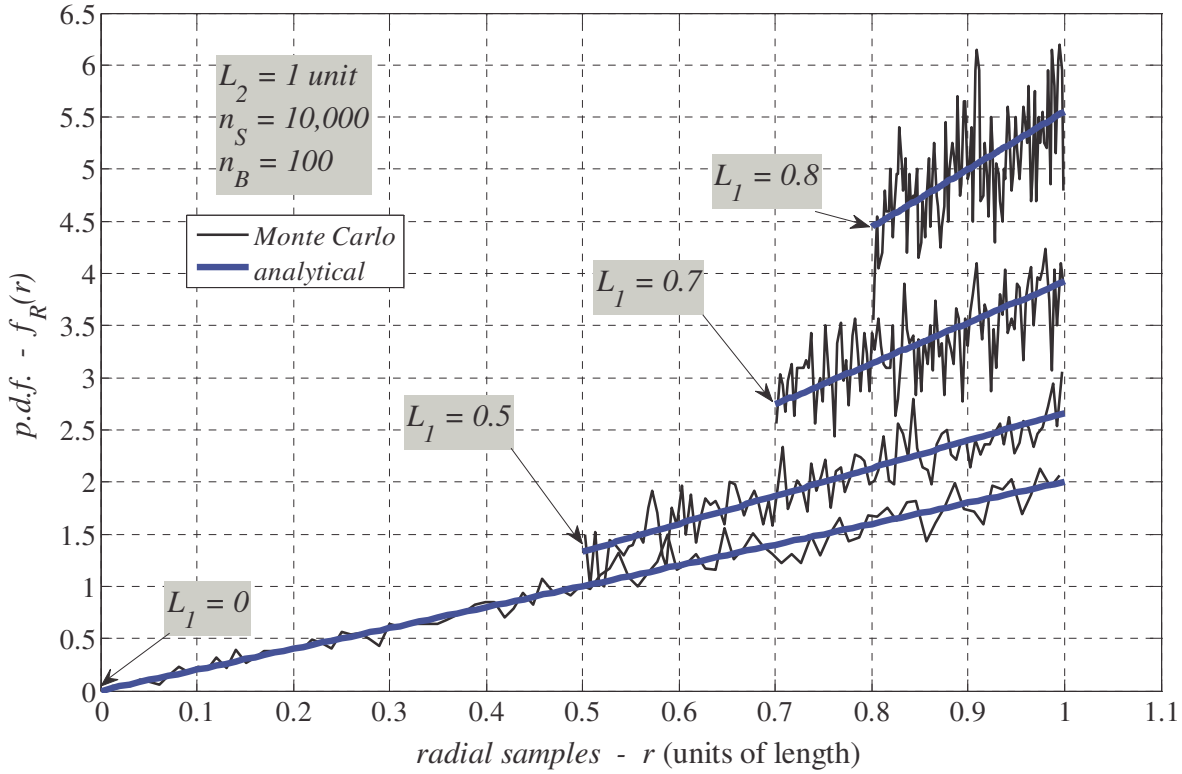

Figure 4.3 – Radial density by means of MC simulations for UCN deployment

As for spatially modeling the versatility of UCN random deployment, using the above exact analysis, we show in Figure 4.4, a $O\left(n_S\right)$ pseudocode for this objective.

Algorithm 5 - Random Deployment for a Circular Network

Require: $n_S \in \mathbb{N}^* \quad (L_1, L_2) \in \mathbb{R}_+^2 \quad (\alpha_1, \alpha_2) \in \mathbb{R}_+^2$
for $i = 1, 2, \cdots, n_S$ **do**
  Generate two i.i.d. RVs: $\{\hat{u}_0, \hat{u}_1\} \sim \mathcal{U}(0,1)$
  Compute: $\hat{r}_i := \sqrt{L_1^2 + \hat{u}_0\left(L_2^2 - L_1^2\right)} \sim f_R(r)$
  Compute: $\hat{\theta}_i := \left\{\alpha_1 + \hat{u}_1(\alpha_2 - \alpha_1)\right\} \sim f_\theta(\theta)$
  Compute: $\{\hat{x}_i;\ \hat{y}_i\} = \left\{\hat{r}_i \cos\left(\hat{\theta}_i\right);\ \hat{r}_i \sin\left(\hat{\theta}_i\right)\right\} \sim f_{XY}(x, y)$
end for
Return: $\{\hat{x}_i, \hat{y}_i\} : i = 1, 2, \cdots, n_S$

Figure 4.4 – Pseudocode for random UCN spatial deployment

Furthermore, to demonstrate the flexibility and the generic nature of the UCN model just derived, we obtained through random MC simulation the results of Figure 4.5 for different parameter values and nodal densities assessed by ρ_A. The six unique random network examples of these random networks were realized by two type of inputs to the algorithm; namely the geometrical attributes of the random cluster: $L_1, L_2, \alpha_1, \alpha_2$, and the scale of the network: n_S. As visually manifest in Figure 4.5, the 2D deployments and the spatial densities match the anticipated footprint of the network.

4.2.2 – Experimental Analysis of the Spatial Density

In this subsection, we intend to further probe in the estimation of spatial density between theoretically predicted formulation and randomly simulated results. Precisely, once the random 2D deployment is realized, we then consider these arbitrary geometrical samples in order to represent a bivariate histogram that approximates the Euclidian distribution of the deployment.

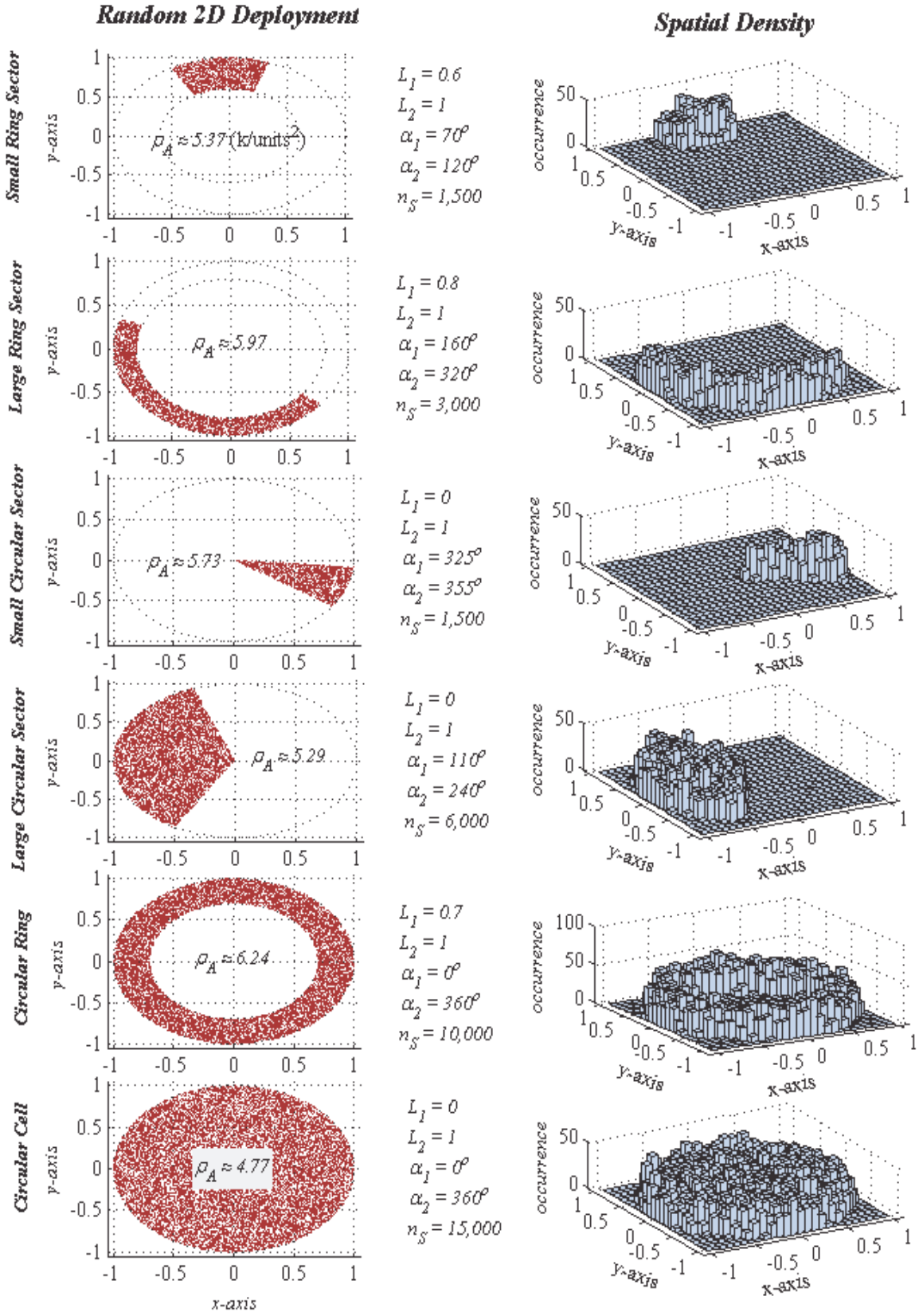

Figure 4.5 – Versatility of UCN random network models

For this purpose, as illustrated in Figure 4.6, we start by considering the approximation of a general 2D probability function by its histogram equivalent.

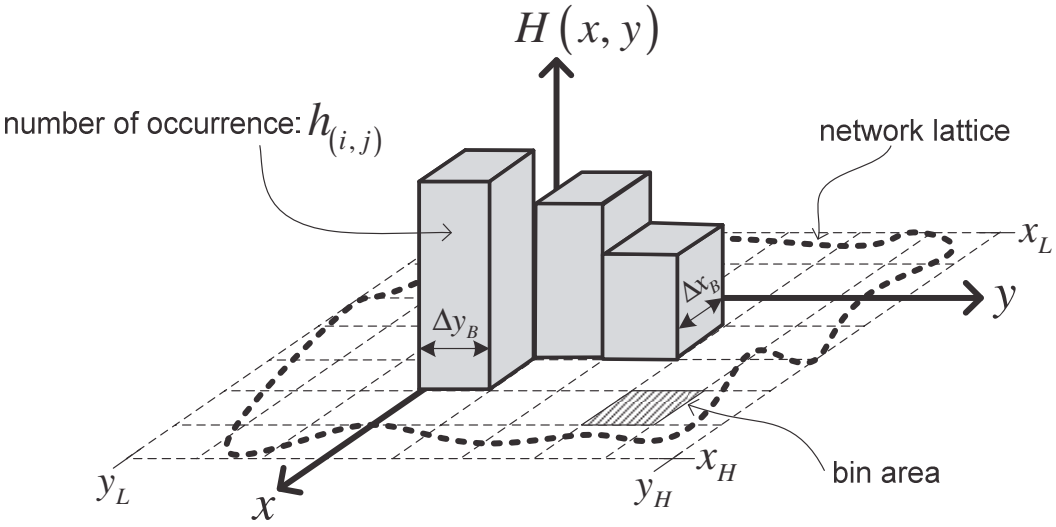

Figure 4.6 – A general bivariate histogram realization

To analytically characterize this estimation, the bivariate fundamental histogram bin positioned at the origin of a Cartesian coordinate system is assigned to:

$$\delta_B(x, y) = \mathbf{1}\left(|x| \le \Delta x_B/2;\ |y| \le \Delta y_B/2\right) \tag{4.15}$$

such that $\mathbf{1}_A(x, y)$ is a 2D indicator function over $(x, y) \in A \subseteq \mathbb{R}^2$, and $(\Delta x_B, \Delta y_B) \in \mathbb{R}^2_{+,*}$ are the dimensions of each histogram bin. In fact, these dimensions can be computed by:

$$\Delta x_B = (x_H - x_L)/n_{B-X} \tag{4.16}$$

$$\Delta y_B = (y_H - y_L)/n_{B-Y} \tag{4.17}$$

where $[x_L, x_H] \times [y_L, y_H]$ identifies the deployment surface of the network, and (n_{B-X}, n_{B-Y}) represents the resolution of the bivariate histogram. Furthermore, the number of occurrence for the (i, j)-th bin is defined by:

$$h_{(i,j)} : \left\{ (i,j) \in \mathbb{N}_*^2;\ (n_{B-X}, n_{B-Y}) \in \mathbb{N}_*^2 \middle|\ 1 \le i \le n_{B-X};\ 1 \le j \le n_{B-Y} \right\} \mapsto \mathbb{N} \tag{4.18}$$

Using the above definitions and assignments, we could therefore express the overall spatial density histogram $H(x, y) : \mathbb{R}^2 \mapsto \mathbb{N}$ for a randomly deployed network by:

$$H(x,y) = \sum_{j=1}^{n_{B-Y}} \sum_{i=1}^{n_{B-X}} h_{(i,j)} \cdot \delta_B (x - x_i, y - y_j) \tag{4.19}$$

having bin center positions $(x_i, y_j) \in \mathbb{R}^2$ parameterized by:

$$x_i = x_L + (i - 1/2)\Delta x_B \quad i = 1, 2, \cdots, n_{B-X} \tag{4.20}$$

$$y_j = y_L + (j - 1/2)\Delta y_B \quad j = 1, 2, \cdots, n_{B-Y} \tag{4.21}$$

At this point, we could analytically obtain the average bivariate histogram density as follows:

$$h_{XY}^{\text{analytical}} = \langle h_{XY} \rangle = \rho_A \cdot A_{bin} \tag{4.22}$$

such that $\rho_A \in \mathbb{R}_+^*$ is the number density of the spatial network, and $A_{bin} \in \mathbb{R}_+^*$ represents the surface area of the bivariate bin. As a consequence, we could rewrite (4.22) in generic terms by:

$$h_{XY}^{\text{analytical}} = n_S \cdot A_{bin} / A_N = n_S \cdot \Delta x_B \cdot \Delta y_B / A_N \tag{4.23}$$

where $n_S \in \mathbb{N}^*$ is the number of randomly generated position samples, and $A_N \in \mathbb{R}_+^*$ is the surface area of the network lattice.

Specifically, if we want to estimate the histogram density for the circular network case, we could consider the spatial footprint depicted in Figure 4.7. As illustrated, the histogram grid is based on equally-spaced bin regions of $\Delta_B \in \mathbb{R}_+^*$ dimensions. For precisions purposes, it is

worth noting that although the figure portrays a 10×10 grid, in our generic derivation we will assume a 2D resolution of n_B^2 .

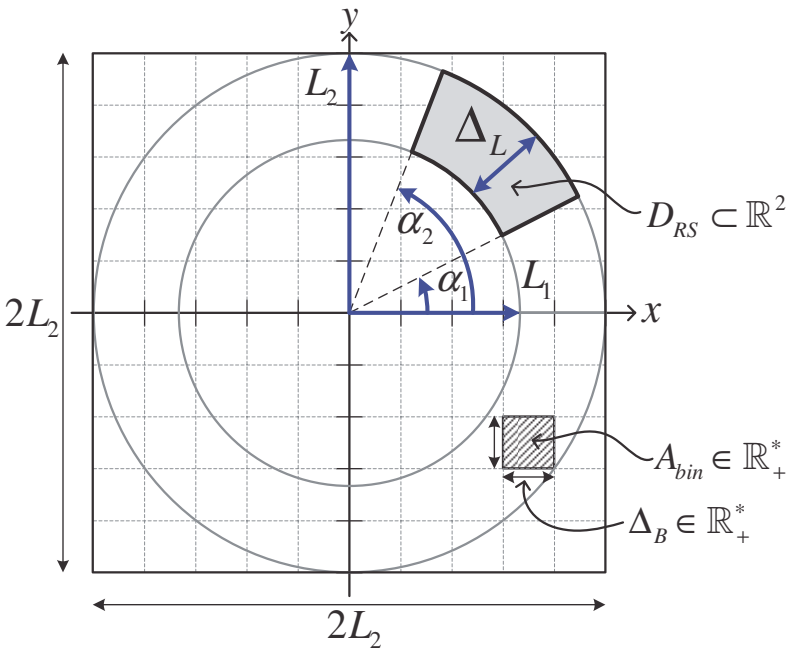

Figure 4.7 – Footprint of a UCN model for spatial density estimation

The dimension of the bin area is therefore obtained by:

$$\Delta_B = \Delta x_B = \Delta y_B = 2L_2 / n_B \tag{4.24}$$

Substituting (4.24) and (4.4) into (4.23), we then find that:

$$h_{XY}^{\text{analytical}} = n_S \cdot \Delta_B^2 / A_{RS} = 8 \cdot n_S \Big/ n_B^2 \cdot (\alpha_2 - \alpha_1) \cdot \left\{1 - (L_1/L_2)^2\right\} \tag{4.25}$$

The histogram density may also be computed from experimental MC data points through its empirical mean, which is defined in its general format by:

$$h_{XY}^{\text{simulation}} = \left\langle \hat{h}_{XY} \right\rangle = \frac{1}{n_{XY}} \sum_{j=1}^{n_{B-Y}} \sum_{i=1}^{n_{B-X}} h_{(i,j)} \tag{4.26}$$

where $n_{XY} \in \mathbb{N}^*$ is the amount of bins over the deployment surface having a nonzero occurrence number. To be accurate, this value is in fact bounded by:

$$0 < n_{XY} \leq n_{B-X} \cdot n_{B-Y} \tag{4.27}$$

For explicit computational purposes, the expression of (4.26) can be evaluated by means of the simple algorithm outlined in Figure 4.8.

Algorithm 6 - Computing the Empirical Mean of the Histogram Density

```
Require: (n_{B-X}, n_{B-Y}) ∈ ℕ*_2   {h_{(i,j)} ∈ ℕ} : i = 1,2,⋯,n_{B-X} ; j = 1,2,⋯,n_{B-Y}
Initialize: h_sum = 0   n_XY = 0
for i = 1,2,⋯,n_{B-X} do
    for j = 1,2,⋯,n_{B-Y} do
        if {h_{(i,j)} ≠ 0} then
            h_sum := h_sum + h_{(i,j)}
            n_XY := n_XY + 1
        end if
    end for
end for
Return/Compute: h_XY^simulation = h_sum / n_XY
```

Figure 4.8 – Pseudocode for evaluating the average simulated histogram density

In order to verify the statistical metrics developed above, we performed a number of MC simulations for various permutations of the randomly modeled network. In essence, we considered the same network geometries as those described in Figure 4.5; except, random instances of the nodal position samples were augmented in order to produce a reliable approximation of the spatial density. As for the estimation step, the quantity of subdivisions along the *x* and *y* axes were equal and set to $n_B = 500$ for all cases.

Table 4.1 presents a contrast of the spatial density estimation between theoretical prediction and simulated data. It should be clear from the table that although both bivariate histogram density measures of (4.25) and (4.26) have units of no. per bin area, they will not be integer values, rather each will be in $\mathbb{R}_{+}^{*}$ because they represent average quantities. The percentage error of the spatial density among analysis and simulation were quantified using (4.28). Given the slight value of the error, we can straightforwardly conclude the validity of the statistical estimation analysis formulated.

$$\varepsilon_A = \frac{\left| h_{XY}^{\text{simulation}} - h_{XY}^{\text{analytical}} \right|}{h_{XY}^{\text{analytical}}} \times 100 \tag{4.28}$$

Table 4.1 – Contrasting spatial density estimation among theoretical and empirical values

random network models	A_{RS} (units^2)	n_S (no.)	ρ_A $(\text{k/units})^2$	n_B (no.)	$h_{XY}^{\text{analytical}}$ (no./bin area)	$h_{XY}^{\text{simulation}}$ (no./bin area)	ε_A (%)
small ring sector	0.2793	10^6	3.5810	500	57.2958	56.4602	1.46
large ring sector	0.5027	10^6	1.9894	500	31.8310	31.2297	1.89
small circular sector	0.2618	10^6	3.8197	500	61.1155	59.9434	1.92
large circular sector	1.1345	10^6	0.8815	500	14.1036	14.0280	0.54
circular ring	1.6022	10^6	0.6241	500	9.9862	9.9137	0.73
circular cell	3.1416	10^7	3.1831	500	50.9296	50.7354	0.38

Overall, in this section, we demonstrated and analyzed the approach for spatial flexibility in random deployment because we derived exact and generic stochastic expressions based on efficient random generation. As it will be shown in the next section, the described geometrical model will also be useful as a steppingstone for obtaining a tractable channel-loss distribution, because the impact of far-field will inherently be accounted for in the network model. Also, it will enable a more focused study of the large-scale fading behavior in the vicinity of the cellular border in order to study edge related aspects. Moreover, the versatile circular network model will as well be instrumental for deriving both controlled and uncontrolled algorithms for achieving network inhomogeneity.

4.3 – Channel-Loss Predictor for an Adaptable UCN Model

4.3.1 – PDF of the Path-Loss

Being able to model and predict the probability density of PL is always essential in wireless communications due to its insight for a range of network quality indicators. As a sophisticated substitute to intense and exhaustive MC simulations for each network geometry and channel environments, the channel-loss PDF can stochastically be obtained in a generic and tractable format. In this section, this mentioned purpose will constitute the central challenge to be solved.

Notably, for the spatial model characterized in Section 4.2, we need to find a corresponding PL density function that preserves the adaptable attributes of the random network. That is, we aim to derive the propagation loss between a cellular tower or AP positioned at the origin of the Euclidian plane and any arbitrarily located node in the deployment surface $D_{RS} \subset \mathbb{R}^2$ of a circular ring sector.

A generic model for the average PL is expressed in (4.29). As we notice, the PL model is only valid and defined for interpoint distances between a random node and a reference that extends beyond the close-in range $r_0 \in \mathbb{R}_+^*$ of the transmitting antenna. In other words, for channel analysis, the inner cellular radius of the ring sector during deployment has an additional requirement, constraining it by $L_1 \geq r_0 > 0$ as opposed to the support surface stipulated earlier in (4.7), which only specifies that $L_1 \geq 0$.

$$w(r) \equiv \overline{L_{PL}(r)}_{dB} = \alpha + \beta \log_{10}(r) \qquad 0 < r_0 \leq L_1 \leq r \leq L_2 \tag{4.29}$$

In (4.30), the PL parameters $(\alpha, \beta) \in \mathbb{R}_{+,*}^2$ are deterministic values, and the BS-to-MS spatial gap $r \in \mathbb{R}_+^*$ is a RV specified by the radial PDF of (4.8). Empowered with this information, at present, we want to determine the density of the average PL which we define by:

$$\overline{L_{PL}(r)}_{dB} \sim f_W(w) : \left\{ w \in \mathbb{R}_+^*;\ (w_0, w_{L_1}, w_{L_2}) \in \mathbb{R}_{+,*}^3 \,\middle|\, w_0 \leq w_{L_1} \leq w \leq w_{L_2} \right\} \mapsto \mathbb{R}^+ \tag{4.30}$$

where w_0, w_{L_1} and w_{L_2} are respectively the average channel-loss at the close-in distance, inner and outer radii of a circular network. From stochastic theory, and using the statements of (4.8), (4.29) and (4.30), we analytically compute the average PL density:

$$\begin{aligned} f_W(w) &= f_R\left(r=r(w)\right)\Big/\left|dw(r)/dr\right|_{r=r(w)} \\ &= f_R\left(10^{(w-\alpha)/\beta}\right)\Big/\left|\beta/\ln(10)\,r\right|_{r=10^{(w-\alpha)/\beta}} = \frac{\ln(10)}{\beta}\cdot 10^{(w-\alpha)/\beta}\cdot f_R\left(10^{(w-\alpha)/\beta}\right) \\ &= \left\{2\cdot\ln(10)\cdot 10^{2(w-\alpha)/\beta}\Big/\beta\left(L_2^2-L_1^2\right)\right\}\cdot\mathbf{1}\left(w_{L_1}\le w\le w_{L_2}\right) \end{aligned} \tag{4.31}$$

4.3.2 – PDF of the Large-Scale Fading

Superimposing the random impact of in-field scatterers to the PL will further enhance the large-scale fading model. In other words, we want to obtain the probability density of the following analytical upgrade:

$$L_{PL}(r)_{dB} = \overline{L_{PL}(r)}_{dB} + \Psi_{S-dB} \sim f_{L_{PL}}(l) : \mathbb{R}_+^* \mapsto \mathbb{R}^+ \tag{4.32}$$

It is paramount to remember that indeed the average PL which depends on nodal geometry and channel shadowing are stochastically disconnected, namely:

$$f_{W\Psi}(w,\psi) = \underbrace{f_W(w)}_{\text{average PL}} \times \underbrace{f_\Psi(\psi)}_{\text{shadowing}} \tag{4.33}$$

Thus, the large-scale fading PDF of (4.32) will be based on the convolution of these independent stochastic components:

$$\begin{aligned} f_{L_{PL}}(l) = f_W(l) * f_\Psi(l) &= \int_{|\tau|<\infty} f_W(\tau)\cdot f_\Psi(l-\tau)\,d\tau \qquad \sigma_\Psi\in\mathbb{R}_+^*,\ l\in\mathbb{R}_+^* \\ &= \int_{|\tau|<\infty} f_W(\tau)\cdot\mathcal{N}_S\left(l,\sigma_\Psi^2\right)d\tau \end{aligned} \tag{4.34}$$

Working the details of (4.34) produces:

$$f_{L_{PL}}(l)=\sqrt{\frac{2}{\pi}}\frac{\ln(10)}{\beta\cdot\sigma_{\Psi}\left(L_2^2-L_1^2\right)}\int_{\tau=w_{L_1}}^{w_{L_2}}10^{2(\tau-\alpha)/\beta}\cdot\exp\left\{-(\tau-l)^2/2\sigma_{\Psi}^2\right\}d\tau$$
$$=\sqrt{\frac{2}{\pi}}\frac{\ln(10)\cdot10^{-2\alpha/\beta}}{\beta\cdot\sigma_{\Psi}\left(L_2^2-L_1^2\right)}\int_{\tau=w_{L_1}}^{w_{L_2}}10^{2\tau/\beta}\cdot\exp\left\{-(\tau-l)^2/2\sigma_{\Psi}^2\right\}d\tau$$
$$=\sqrt{\frac{2}{\pi}}\frac{\ln(10)\cdot10^{-2\alpha/\beta}}{\beta\cdot\sigma_{\Psi}\left(L_2^2-L_1^2\right)}\int_{\tau=w_{L_1}}^{w_{L_2}}\exp\left\{2\cdot\ln(10)\tau/\beta-(\tau-l)^2/2\sigma_{\Psi}^2\right\}d\tau \tag{4.35}$$

An alternate expression for the integrand of (4.35) was previously found in (3.102); after inserting it in the above notation, we get:

$$f_{L_{PL}}(l)=\sqrt{\frac{2}{\pi}}\frac{\ln(10)\cdot10^{2(l-\alpha)/\beta}}{\beta\cdot\sigma_{\Psi}\left(L_2^2-L_1^2\right)}\cdot\exp\left\{\left(\sqrt{2}\ln(10)\sigma_{\Psi}/\beta\right)^2\right\}$$
$$\times\int_{\tau=w_{L_1}}^{w_{L_2}}\exp\left\{-\left(\tau-\left\{l+2\ln(10)\sigma_{\Psi}^2/\beta\right\}\right)^2/2\sigma_{\Psi}^2\right\}d\tau \tag{4.36}$$

If we transform the τ variable of (4.36) by:

$$z=z(\tau)=\left(\tau-\left\{l+2\ln(10)\sigma_{\Psi}^2/\beta\right\}\right)/\sigma_{\Psi} \tag{4.37}$$

we then obtain the following outcome:

$$f_{L_{PL}}(l)=\sqrt{\frac{2}{\pi}}\frac{\ln(10)\cdot10^{2(l-\alpha)/\beta}}{\beta\left(L_2^2-L_1^2\right)}\cdot\exp\left\{\left(\sqrt{2}\ln(10)\sigma_{\Psi}/\beta\right)^2\right\}\times\int_{z=z_{L_1}}^{z_{L_2}}\exp\left(-z^2/2\right)dz \tag{4.38}$$

such that $z_{L_1} = z\left(\tau = w_{L_1}\right)$ and $z_{L_2} = z\left(\tau = w_{L_2}\right)$. In (3.115), we showed an approach for expressing the integration of (4.38) using the Q-function; after exercising this we get:

$$f_{L_{PL}}(l) = \frac{2 \cdot \ln(10) \cdot 10^{2(l-\alpha)/\beta}}{\beta\left(L_2^2 - L_1^2\right)} \cdot \exp\left\{\left(\sqrt{2}\ln(10)\sigma_\Psi/\beta\right)^2\right\} \cdot \left\{Q\left(z_{L_1}\right) - Q\left(z_{L_2}\right)\right\} \tag{4.39}$$

As noted above, $z = z(\tau)$, but τ is a variable that characterizes the average PL; hence:

$$z = z\left(\tau = \overline{L_{PL}(r)}_{dB}\right) = z\left(\alpha + \beta\log_{10}(r)\right) = z(r) \tag{4.40}$$

and so, (4.37) will change to:

$$z = z(r) = \left\{\alpha + \beta\log_{10}(r) - l - 2\ln(10)\sigma_\Psi^2/\beta\right\}/\sigma_\Psi = \left\{\alpha - l + \ln\left(r^{\beta/\ln(10)}/10^{2\sigma_\Psi^2/\beta}\right)\right\}/\sigma_\Psi \tag{4.41}$$

From (4.41), we therefore can solve for $z_{L_1} = z\left(r = L_1\right)$ and $z_{L_2} = z\left(r = L_2\right)$ utilized in (4.39).

Before putting the final expression together, for the sake of mathematical elegance, we can attempt to represent the limits of the Q-function in (4.39) in a coherent fashion. Specifically, say we assign the $Q(z)$ part of (4.39) to:

$$I_{LSF} \triangleq \left\{Q\left(z_{L_1}\right) - Q\left(z_{L_2}\right)\right\} = \left\{Q(z)\right\}_{z=z_{L_2}}^{z_{L_1}} \tag{4.42}$$

From probability theory, we know that:

$$Q(z) = 1 - Q(-z) \tag{4.43}$$

Plugging (4.43) into (4.42), we then deduce that:

$$I_{LSF}=\left\{Q(z)\right\}_{z=z_{L_2}}^{z_{L_1}}=\left\{1-Q(-z)\right\}_{z=z_{L_2}}^{z_{L_1}}=Q\left(-z_{L_2}\right)-Q\left(-z_{L_1}\right)=\left\{Q(-z)\right\}_{z=z_{L_1}}^{z_{L_2}} \tag{4.44}$$

If we insert the z of (4.41) into (4.44), we obtain:

$$\begin{aligned} I_{LSF}=\left\{Q(-z)\right\}_{z=z_{L_1}}^{z_{L_2}} &=\left\{Q\left(-\left\{\alpha-l+\ln\left(r^{\beta/\ln(10)}\Big/10^{2\sigma_\Psi^2/\beta}\right)\right\}\Big/\sigma_\Psi\right)\right\}_{r=L_1}^{L_2} \\ &=\left\{Q\left(\left\{l-\alpha+\ln\left(10^{2\sigma_\Psi^2/\beta}\Big/r^{\beta/\ln(10)}\right)\right\}\Big/\sigma_\Psi\right)\right\}_{r=L_1}^{L_2} \end{aligned} \tag{4.45}$$

Last, substituting (4.45) into (4.39), we then obtain in (4.46) the final PDF notation for the large-scale fading between a reference BS and an arbitrary random terminal located in a UCN ring sector. Overall, as emphasized by $\vec{\Lambda}$, the derived stochastic statement exhibits generic and adaptable traits for a particular channel behavior characterized by its distinctive propagation parameters, and for a flexibly variable random geometry over a UCN.

$$\begin{aligned} f_{L_{PL}}\left(l,\vec{\Lambda}\right)=\frac{2\cdot\ln(10)\cdot10^{2(l-\alpha)/\beta}}{\beta\left(L_2^2-L_1^2\right)}\cdot\exp\left\{\left(\sqrt{2}\ln(10)\sigma_\Psi/\beta\right)^2\right\} \\ \times\left\{\ Q\left(\left\{l-\alpha+\ln\left(10^{2\sigma_\Psi^2/\beta}\Big/r^{\beta/\ln(10)}\right)\right\}\Big/\sigma_\Psi\right)\ \right\}_{r=L_1}^{L_2} \end{aligned}$$

- $\vec{\Lambda}=\{\alpha,\beta,\sigma_\Psi,r_0,L_1,L_2\}\in\mathbb{R}_{+,*}^6$ $\qquad 0<\tilde{l}_{L_1}\lesssim l\lesssim\tilde{l}_{L_2}<\infty$
- $Q(z)=erfc\left(z/\sqrt{2}\right)/2=\left\{1-erf\left(z/\sqrt{2}\right)\right\}/2$ $\qquad 0<r_0\le L_1\le r\le L_2$
- $\tilde{l}_{L_1}=\alpha+\beta\log_{10}(L_1)-3\sigma_\Psi$
- $\tilde{l}_{L_2}=\alpha+\beta\log_{10}(L_2)+3\sigma_\Psi$ ■

(4.46)

4.3.3 – Analyzing the Domain and Range of the Large-Scale Fading PDF

Having derived the exact closed-form formulation for the large-scale fading density, at present, it is informative to further scrutinize and identify the properties of this function. In particular, the domain gap and range of this distribution function can be useful to characterize its behavior.

Admittedly, as demonstrated in the previous chapter, it is w.h.p. (i.e. ~99.7% CI) possible to model and compute the extremities of large-scale fading. Indeed, in (4.46) these lower and higher measures were shown for all possible UCN deployments. In view of this, the span of the domain $\Delta_{PL} \in \mathbb{R}_{+}^{*}$ can be determined by:

$$\begin{aligned}\Delta_{PL} = \tilde{l}_{L_2} - \tilde{l}_{L_1} &= \alpha + \beta \log_{10}\left(L_2\right) + 3\sigma_{\Psi} - \left\{\alpha + \beta \log_{10}\left(L_1\right) - 3\sigma_{\Psi}\right\} \\ &= \beta \log_{10}\left(L_2 / L_1\right) + 6\sigma_{\Psi}\end{aligned} \tag{4.47}$$

Next, it is enlightening to describe the extent of the range, which basically can be evaluated by the maximum value of the large-scale fading PDF:

$$f_{L_{PL}}^{\max} \triangleq \max_{l \in \mathbb{R}_{+}^{*}} \left\{ f_{L_{PL}}\left(l, \vec{\Lambda}\right) \right\} \in \mathbb{R}_{+}^{*} \tag{4.48}$$

To analytically solve (4.48), we first rewrite (4.46) as shown in (4.49), such that $A_1 < A_2$ because $L_1 < L_2$.

$$\begin{aligned} f_{L_{PL}}\left(l, \vec{\Lambda}\right) = \frac{2 \cdot \ln(10) \cdot 10^{-2\alpha/\beta}}{\beta\left(L_2^2 - L_1^2\right)} \cdot \exp\left\{\left(\sqrt{2}\ln(10)\sigma_{\Psi}/\beta\right)^2\right\} \qquad l \in \mathbb{R}_{+}^{*} \\ \times \underbrace{10^{2l/\beta} \cdot \left\{Q\left(\left(l - A_2\right)/\sigma_{\Psi}\right) - Q\left(\left(l - A_1\right)/\sigma_{\Psi}\right)\right\}}_{\triangleq P_{PL}(l)} \end{aligned} \tag{4.49}$$

- $A_1 = \alpha + \ln\left(L_1^{\beta/\ln(10)} \Big/ 10^{2\sigma_{\Psi}^2/\beta}\right)$
- $A_2 = \alpha + \ln\left(L_2^{\beta/\ln(10)} \Big/ 10^{2\sigma_{\Psi}^2/\beta}\right)$

For analytical convenience, in the above (4.49) expression, we define the function $P_{PL}(l):\mathbb{R}_{+}^{*}\mapsto\mathbb{R}^{+}$ that isolates and collects the l based components together. This is actually done because the optimization of (4.48) is only dependent on this variable.

Next, we need to find the derivative of $P_{PL}(l)$, which in part requires the differentiation of a Q-function in the form of $Q\left((x-A)/B\right)$, where A and B are some arbitrary constants. Equipped with the elegant result derived in Appendix-A, at this level, we could proceed with the optimization problem by carrying out the following derivative:

$$\begin{aligned}\frac{\partial P_{PL}\left(l,\vec{\Lambda}\right)}{\partial l}&=\frac{\partial}{\partial l}\left[10^{2\cdot l/\beta}\cdot\left\{Q\left((l-A_2)/\sigma_{\Psi}\right)-Q\left((l-A_1)/\sigma_{\Psi}\right)\right\}\right]\\&=\frac{2\cdot\ln(10)}{\beta}\cdot10^{2\cdot l/\beta}\left\{Q\left((l-A_2)/\sigma_{\Psi}\right)-Q\left((l-A_1)/\sigma_{\Psi}\right)\right\}\\&\quad+10^{2\cdot l/\beta}\left\{\mathcal{N}_{L_{PL}}\left(A_1,\sigma_{\Psi}^2\right)-\mathcal{N}_{L_{PL}}\left(A_2,\sigma_{\Psi}^2\right)\right\}\end{aligned}\tag{4.50}$$

After replacing the Q-function in (4.50) by its equivalent integration format shown in (3.112), we then obtain:

$$\begin{aligned}\frac{\partial P_{PL}\left(l,\vec{\Lambda}\right)}{\partial l}&=\frac{2\cdot\ln(10)}{\sqrt{2\pi}\cdot\beta}\cdot10^{2\cdot l/\beta}\cdot\int_{t=(l-A_2)/\sigma_{\Psi}}^{(l-A_1)/\sigma_{\Psi}}\exp\left(-t^2/2\right)dt\\&\quad-\frac{10^{2\cdot l/\beta}}{\sqrt{2\pi}\cdot\sigma_{\Psi}}\cdot\left[\exp\left\{-(l-A)^2/2\sigma_{\Psi}^2\right\}\right]_{A=A_1}^{A_2}\end{aligned}\tag{4.51}$$

Finally, as demonstrated by (4.52), we set the above result to zero so as to solve for the optimum value of l which we designate by $l_{\max}\in\mathbb{R}_{+}^{*}$. To be precise, this variable is the argument that maximizes the density function of the large-scale fading indicator.

$$\int_{-(l_{\max}-A_2)/\sigma_\Psi}^{(l_{\max}-A_1)/\sigma_\Psi} \exp\left(-t^2/2\right) dt = \frac{\beta}{2\cdot\ln(10)\,\sigma_\Psi} \cdot \left[\exp\left\{-\left(l_{\max}-A\right)^2/2\sigma_\Psi^2\right\}\right]_{A=A_1}^{A_2} \tag{4.52}$$

From the equality in (4.52), it should be clear that there is no explicit way to solve for $l_{\max}$ without the utilization of numerical techniques. Once an approximation for this parameter is realized, then the optimization problem of (4.48) leads us to:

$$f_{L_{PL}}^{\max} = \max_{l\in\mathbb{R}_+^*}\left\{f_{L_{PL}}\left(l,\vec{\Lambda}\right)\right\} \approx f_{L_{PL}}\left(l=\tilde{l}_{\max},\vec{\Lambda}\right) \tag{4.53}$$

In this subsection, the theoretical characteristics of the domain and range for the large-scale fading distribution were determined. In the simulation part, these parameters will be evaluated for a number of network examples, and remarks on the obtained results will be made.

4.3.4 – Analyzing and Estimating the Moments of the Large-Scale Fading PDF

Specifically, the moments of the distribution, and in particular the first and second moments of the density function, are instrumental in understanding the behavior of the large-scale fading for a given random network. As a matter of fact, the first moment can analytically be evaluated by:

$$m_{L_{PL}} = \mathrm{E}\left[L_{PL}\left(r\right)_{dB}\right] = \mathrm{E}\left[L_{PL}\right] = \int_{l\in\mathbb{R}_+^*} l\cdot f_{L_{PL}}\left(l,\vec{\Lambda}\right) dl \tag{4.54}$$

where $m_{L_{PL}} \in \mathbb{R}_+^*$ is a pointer for the mean of the RV for large-scale fading. Given the convoluted nature of the above analysis, this measure can alternatively be estimated from MC samples of the simulation. In essence, because the randomly generated data instances have unequal contribution, the approximation should be performed based on the weighted sample mean, which is formulated by:

$$\tilde{m}_{L_{PL}} = \left\langle \hat{L}_{PL} \right\rangle = \sum_{i=1}^{n_B} l_i \cdot \Pr\left(\hat{L}_{PL} = l_i\right) \tag{4.55}$$

such that $\tilde{m}_{L_{PL}} \in \mathbb{R}_+^*$ is the empirical mean computed from MC samples, and $\hat{L}_{PL} \in \mathbb{R}_+^*$ is a RV for the large-scale fading level associated with $\tilde{f}_{L_{PL}}(l): \mathbb{R}_+^* \mapsto \mathbb{R}^+$, which is basically the numerical PDF estimation of $f_{L_{PL}}(l, \vec{\Lambda})$. For further clarification, we could loosely think of $\hat{L}_{PL}$ as a RV of a PMF because the estimated density is only available at discrete points. And these discrete points are labeled by $l_i \in \mathbb{R}_+^*$, which is essentially the center position of the i-th histogram bin with values determined by:

$$l_i = \hat{l}_L + (i - 1/2)\Delta l_B \qquad i = 1, 2, \cdots, n_B \tag{4.56}$$

where $\Delta l_B \in \mathbb{R}_+^*$ is the width for each histogram bar calculated by:

$$\Delta l_B = \left(\hat{l}_H - \hat{l}_L\right) \Big/ n_B \tag{4.57}$$

such that $\left(\hat{l}_L, \hat{l}_H\right) \in \mathbb{R}_{+,*}^2$ are the lower and higher extremities of the argument for the estimated large-scale fading density. To be Precise, for each simulation run, these extremities are found from the set of randomly generated instances by:

$$\hat{l}_L = \min_{j=1,2,\cdots,n_S} \left\{\hat{l}_j\right\} \tag{4.58}$$

$$\hat{l}_H = \max_{j=1,2,\cdots,n_S} \left\{\hat{l}_j\right\} \tag{4.59}$$

where the set of large-scale fading samples $\hat{l}_j \in \mathbb{R}_+^*$ are generated from:

$$\hat{l}_j = \alpha + \beta \log_{10}\left(\hat{r}_j \sim f_R(r)\right) + \left\{\hat{\psi}_j \sim \mathcal{N}_S\left(0, \sigma_\Psi^2\right)\right\} \qquad j = 1, 2, \cdots, n_S \tag{4.60}$$

The notation of (4.55) is shown in terms of a probability measure; however, it could equally be represented by the estimation of the large-scale fading density. We could therefore adjust this mathematical statement by expressing it in terms of the empirical PDF using the fact that:

$$\Pr\left(\hat{L}_{PL}=l_i\right)=\pi_i^O/n_S=pdf_i\cdot\Delta l_B \qquad i=1,2,\cdots,n_B \tag{4.61}$$

where $\pi_i^O\in\mathbb{N}^*$ is the number of occurrence for the i-th bin, and $pdf_i\in\mathbb{R}_+^*$ is the corresponding approximated density. After inserting (4.61) into (4.55), we find that:

$$\tilde{m}_{L_{PL}}=\Delta l_B\cdot\sum_{i=1}^{n_B}l_i\cdot pdf_i \tag{4.62}$$

As for the second moment of the PDF, it is theoretically obtained by:

$$\sigma_{L_{PL}}^2=\mathrm{E}\left[\left(L_{PL}(r)_{dB}-m_{L_{PL}}\right)^2\right]=\mathrm{E}\left[\left(L_{PL}-m_{L_{PL}}\right)^2\right]=\int_{l\in\mathbb{R}_+^*}\left(l-m_{L_{PL}}\right)^2\cdot f_{L_{PL}}\left(l,\vec{\Lambda}\right)dl \tag{4.63}$$

where $\sigma_{L_{PL}}^2\in\mathbb{R}_+^*$ is an indicator for the variance of the RV for large-scale fading. Similar to the argument made for the first moment of (4.54), this measure can rather be quantified via random estimation based on the weighted sample variance:

$$\tilde{\sigma}_{L_{PL}}^2=\left\langle\left(\hat{L}_{PL}-\tilde{m}_{L_{PL}}\right)^2\right\rangle=\sum_{i=1}^{n_B}\left(l_i-\tilde{m}_{L_{PL}}\right)^2\cdot\Pr\left(\hat{L}_{PL}=l_i\right) \tag{4.64}$$

such that $\tilde{\sigma}_{L_{PL}}^2\in\mathbb{R}_+^*$ is the empirical variance of the channel-loss computed from MC samples. In fact, $\tilde{m}_{L_{PL}}$ is a deterministic value, and so the expression inside the averaging operator of (4.64) can be simplified by:

$$\tilde{\sigma}_{L_{PL}}^2=\left\langle\left(\hat{L}_{PL}-\tilde{m}_{L_{PL}}\right)^2\right\rangle=\left\langle\hat{L}_{PL}^2-2\cdot\tilde{m}_{L_{PL}}\cdot\hat{L}_{PL}+\tilde{m}_{L_{PL}}^2\right\rangle=\left\langle\hat{L}_{PL}^2\right\rangle-\tilde{m}_{L_{PL}}^2 \tag{4.65}$$

With the insight of (4.65), the expression of (4.64) can be written as:

$$\tilde{\sigma}^2_{L_{PL}} = \left\{ \sum_{i=1}^{n_B} l_i^2 \cdot \Pr\left(\hat{L}_{PL} = l_i \right) \right\} - \tilde{m}^2_{L_{PL}} \tag{4.66}$$

Next, if we substitute (4.61) and (4.62) into the result of (4.66), we at last obtain:

$$\tilde{\sigma}^2_{L_{PL}} = \Delta l_B \cdot \left(\sum_{i=1}^{n_B} l_i^2 \cdot pdf_i \right) - \Delta l_B^2 \cdot \left(\sum_{i=1}^{n_B} l_i \cdot pdf_i \right)^2 \tag{4.67}$$

To recap, as a consequence of the above statistical analysis, we have derived in (4.62) and (4.67) explicit formulas for practically estimating the first and second moments of the large-scale fading PDF obtained via random MC samples. These measures will be evaluated in the subsequent simulation section so as to gain further knowledge of the channel-loss behavior as the geometrical structure of the random network changes.

4.3.5 – MC Simulations and Discussions for the Channel-Loss PDF

In this subsection, we in part aim to confirm the veracity of the analytical expression derived in (4.46), and also assess the statistical characteristics of the distribution. The analysis and MC simulation will be based on the IEEE 802.20 channel parameters for a suburban macrocellular model [52]. Table 4.2 provides a list for the necessary propagation values considered in this radiation environment.

Table 4.2 – MBWA channel model for suburban macrocell

IEEE 802.20 Propagation Parameters	
Propagation Model :	*COST*-231 *Hata-Model*
Operating Frequency :	1.9 GHz
Support Range :	$r_0 = 35 \text{ m} \le r \le L$ $600 \le L = L_2 \le 3,500 \text{ m}$
Channel - Loss :	$\alpha = 31.5 \text{ dB}$ $\beta = 35 \text{ dB}$
Shadowing :	$\sigma_\Psi = 10 \text{ dB}$

In the simulation of Figure 4.9, we assumed a random network in a circular ring delineated between $L_1 = 1.5$ km and $L_2 = 2.5$ km. As for the spatial random samples, they were founded on the analysis conducted in Section 4.2. Once random instances of the interpoint between a reference host and an arbitrarily positioned mobile were generated, we then assembled an $n_B = 100$ histogram for the PDF and CDF of the corresponding large-scale fading level. Further, for the interest of exemplifying the empirical PDF of the large-scale fading as a function of the amount of random samples, we simulated the same exact channel and network with $n_S = 1{,}000$ and $n_S = 10{,}000$. As palpable from the graphical results, an increase in the volume of MC samples appropriately enhances the consistency with the analytically derived density.

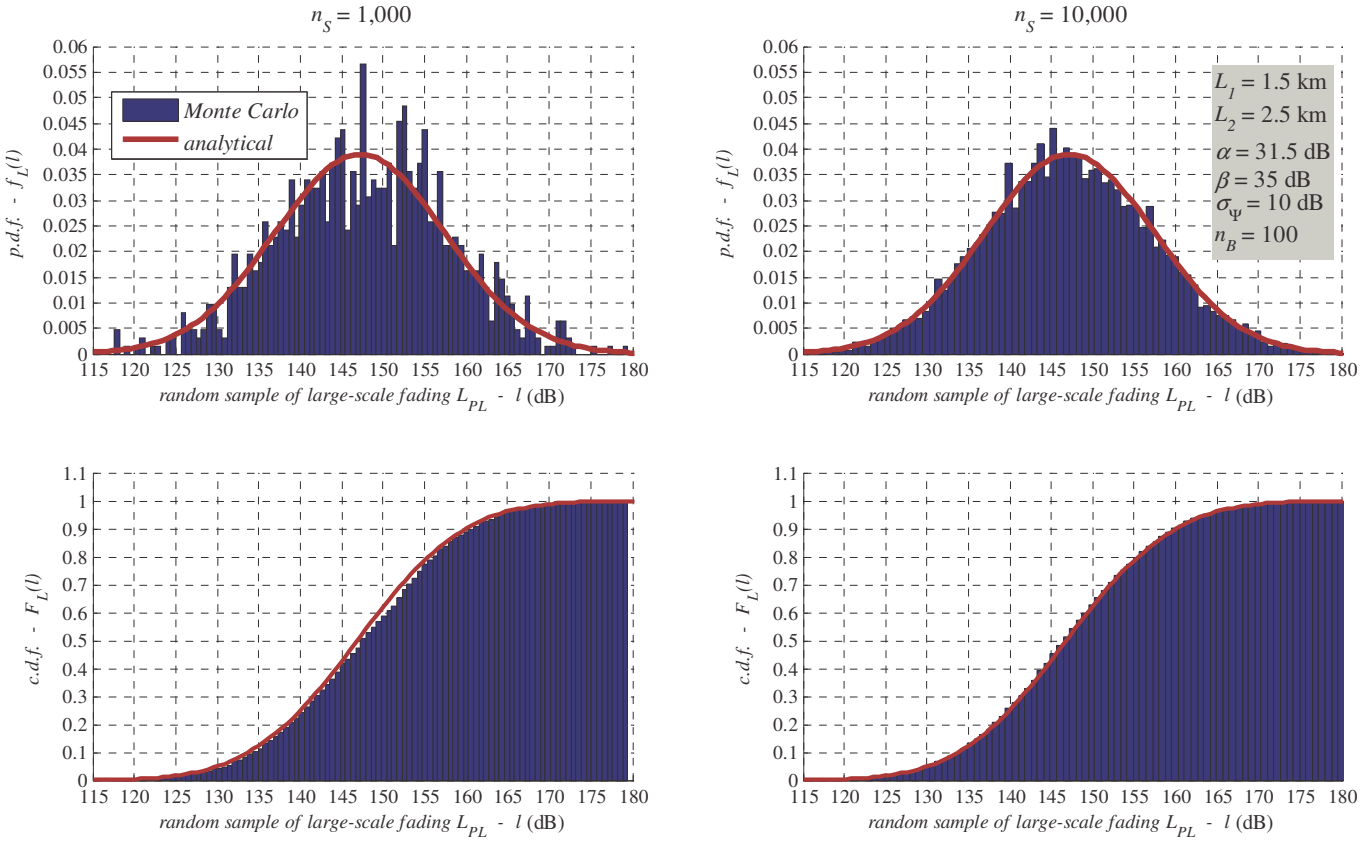

Figure 4.9 – Authenticating the large-scale fading density analysis for a random UCN

Moreover, we ran three simulations for different spatial networks; however, the channel parameters, the quantity of MC samples, and the histogram resolution were held fix for all of these cases. In particular, the diversity of the network was setup by a variation of $\Delta_L \in \mathbb{R}_+^*$,

which represents the width of a circular ring. To be precise, we kept the outer radius constant and we modified the inner radius of the lattice, that is:

$$\Delta_L = L_2 - L_1 = L_2 - L_1^{(j)} \qquad j = 1,2,3 \tag{4.68}$$

such that $L_1^{(j)} \in [r_0, L_2)$, where the values of r_0 and L_2 are specified in Table 4.2. On balance, we could have varied Δ_L by fixing L_1 and changing L_2. Yet, from a design point of view, it is technically more practical to preset the size of the BS transmission coverage, and study the channel-loss as users' concentration gradually shifts towards the cellular border. In the case at hand, we in fact set L_2 to $2.5\ \text{km}$ and L_1 was assigned: to the close-in distance, to $1\,\text{km}$, and $2\,\text{km}$. To put these values into perspective, we visually depicted in Figure 4.10 the associated deployment surfaces for the planned spatial networks.

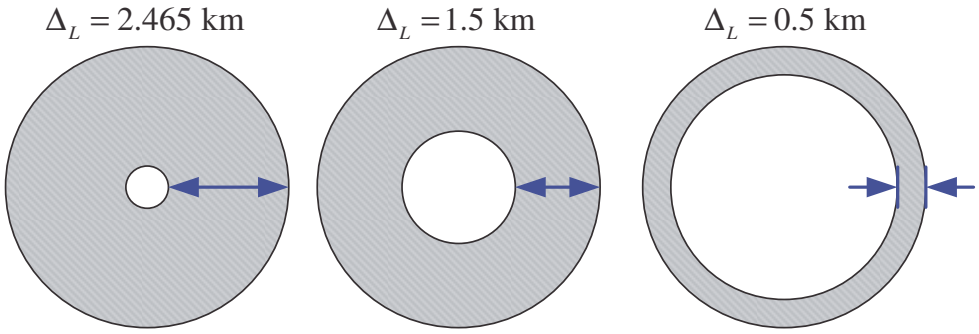

Figure 4.10 – Deployment surfaces for the spatial networks used in the simulations

Overall, Figure 4.11 plots the density result of the simulations, where the MC estimation was based on $n_S = 15{,}000$ random samples, and $n_B = 150$ bins. Again, as expected, simulation and theory produces matching results for all of the considered network cases.

Pursuing this further, we could compare and contrast several key parameters that are fundamental in exploring the attributes of the large-scale fading density curve as the deployment surface of the random network changes. In particular, we are interested to study the effect on the shape of the density function, and what these changes correspond in terms of statistical properties.

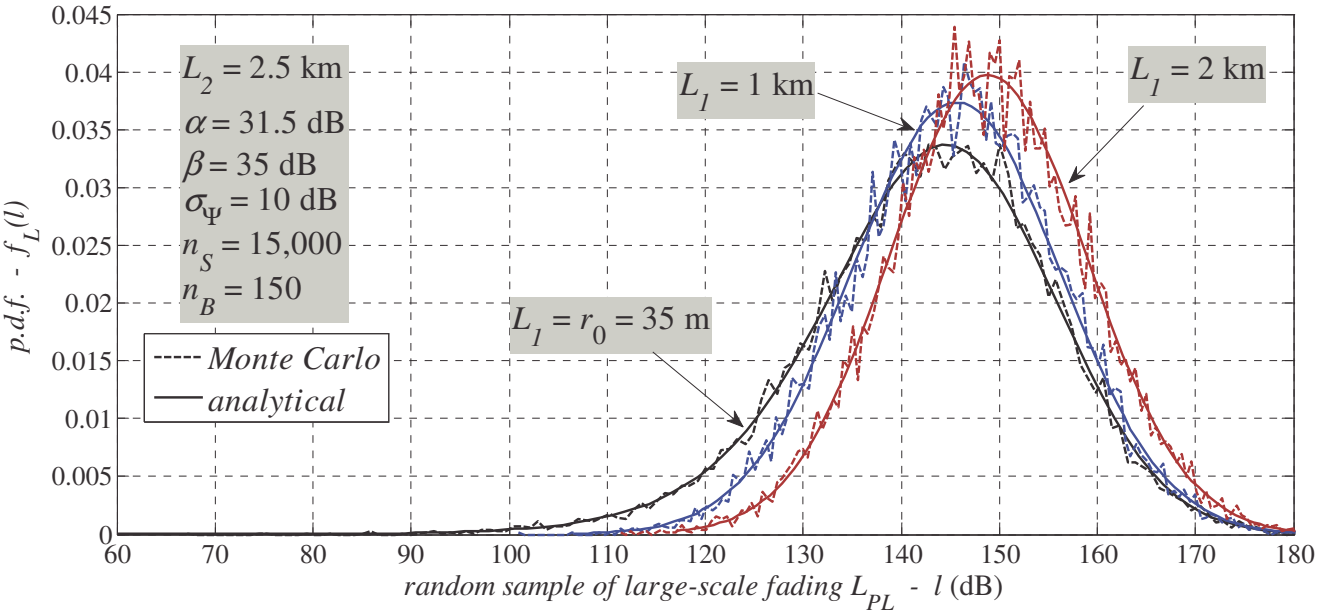

Figure 4.11 – Large-scale fading PDF over different widths of a circular ring

To this end, in Table 4.3, we numerically quantified the domain gap, the extent of the range, the first moment, and the second moment for each density result associated to a particular random network.

Table 4.3 – Contrasting the statistical attributes associated with a random network

network lattice		large-scale fading		lattice width	domain gap	range	empirical mean	empirical SD
L_1 (km)	L_2 (km)	$\tilde{l}_{L_1}$ (dB)	$\tilde{l}_{L_2}$ (dB)	Δ_L (km)	Δ_{PL} (dB)	$f_{L_{PL}}^{\max}$	$\tilde{m}_{L_{PL}}$ (dB)	$\tilde{\sigma}_{L_{PL}}$ (dB)
0.035	2.5	55.54	180.43	2.465	124.89	0.0337	142.7545	12.4490
1.0	2.5	106.50	180.43	1.5	73.93	0.0374	145.5134	10.5374
2.0	2.5	117.04	180.43	0.5	63.39	0.0397	149.0484	10.0509

As shown in the table, the lower extremity of the channel-loss has a unique value for each spatial network. As for the higher extremity of the PDF, given that L_2 has a fixed value, it therefore has a singular outcome for all the network scenarios. Thus, the span of the domain is evaluated w.h.p. by:

$$\Delta_{PL}^{(i)} = \beta \log_{10}\left(L_2 / L_1^{(i)}\right) + 6\sigma_\Psi \qquad i = 1,2,3 \tag{4.69}$$

And as discussed earlier, the extent of the range is numerically realized for each simulation run. Also, the mean and variance of the distribution function were accordingly estimated from the MC samples using the statistical expressions derived in the previous subsection. From the values presented in Table 4.3, we can remark several noteworthy observations:

1. As Δ_L decreases, the span of the PDF domain shrinks.
2. And because the area under the PDF curve has to remain unchanged, then as Δ_L reduces, the extent of the range is expanded.
3. For an edge-focused spatial network, i.e. when L_1 moves closer to the cellular border, the first moment is further shifted to the right of the large-scale fading axis. Likewise, it is safe to consider that if the inner radius was fixed, then as L_2 moves inward towards L_1, the mean of the density will progress to the left of the axis.
4. Further, as Δ_L drops, the second moment of the distribution function lessens. In other words, the RV for the large-scale fading becomes more predictable (i.e. less random).

Overall, in this section, we analytically derived the exact large-scale fading density between a BS and a randomly deployed node situated inside a flexible UCN. We also derived various statistical expressions useful to characterize the unique attributes of the large-scale fading density associated with a certain UCN lattice. We then verified through MC experimentations the accuracy of the analysis. Also, we investigated through simulations the interplay between the random network and its impact on the channel-loss behavior. Moreover, we should affirm that the formulated closed-form large-scale fading density has generic inputs. That is, it can be tuned for a particular channel environment, and also the determined expression is valid for all permutations of a UCN random pattern.

While on the subject, it is worth noting that although the analysis began from the circular ring sector defined in Figure 4.1; yet the derived large-scale fading PDF is independent of the lattice angular limits. This outcome is to be expected given that the propagation loss for centralized communications is dependent of the interspace between a random node and a tower station; which implies that the radial component is the necessary parameter. Having said that, we should stress that the reported density result is still applicable for all type of UCN deployments, including those contained in a ring sector delineated by angular boundaries.

4.4 – Deployment Strategy for Spatial Inhomogeneity

4.4.1 – Motivation and Background

The principle of random geometry is necessary for mimicking the wireless architecture because it adds an element of realism to the spatial network. In fact, due of its well-behaved stochastic features, the homogeneous random network has been extensively considered in academic scholarship [18]–[30]. However, such oversimplification may not necessarily yield accurate spatial models that are reflective of actual scenarios. This is especially true during instances where the deployment terrain has topographical features; thus causing mobile carrying users to cluster in certain locations and not in others [34], [37]. Precisely, we can recognize that what mainly cause a set of wireless nodes to cluster are in fact natural features, such as: mountains, valleys, irregular hills, densely forested lands, rivers, lakes, etc; and manmade infrastructures, among other: ports, building structures, roads and highways.

Given that these earthbound items are indeed the major driving force for users' spatial preferences, effective modeling techniques for non-homogeneous deployment are needed. In particular, several emulation methods have been proposed for achieving a heterogeneous network[4]. The most notable among them is the Gaussian spatial network [24]–[26], [35]–[45]. Specifically, the key advantage of this scheme is the geometrical flexibility obtained by tuning its spatial intensity $\sigma_G \in \mathbb{R}_+^*$. That is, by this variable the deployment terrain can either expand or shrink. In other words, the random network is elastic, where the amount of nodes need not change but the concentration of the network about a reference point is the varying component. In this dissertation, Chapter 5 is entirely devoted to the analysis of this random network type.

Besides the Gaussian architecture, other non-homogeneous networks were obtained by adopting a distribution index $\beta_d \in \mathbb{R}$ into the spatial density as a modifying agent to either produce a centric or edge-focused deployment [34], [35]. Further, some investigators have also shown an approach for inhomogeneity using the so-called principle of thinning which is dependent on the position of neighboring nodes [31], [32].

---

[4] From a semantic point of view, it is important to note that the term *heterogeneous* may have different connotations in wireless networking. For instance, it may refer to the paradigm of seamless and ubiquitous interoperability between various multi-coverage protocols. Otherwise, it may refer to the non-uniform spatial distribution of users. From the context expressed in this chapter, it should be obvious that the latter meaning is always insinuated.

Although the above efforts are important alternatives for the idealized homogeneous model, yet they still remain unfeasible for emulating and investigating the site of a geographically-specific network. Therefore, there is a demand to find better emulation algorithms that give greater control to network designers while preserving users' stochastic characteristics. Notably, the model should principally attempt to take into account clustering tendencies due to terrain features. Also, the anticipated mechanism is desired to be generic, coherent, straightforward, and easily configured through software subroutines so as to be used for all type of cellular systems; namely: small, medium, and large-scale networks.

4.4.2 – ASD Technique for Generating Random Heterogeneous Networks

Basically, we need to construct a randomly tunable algorithm that takes into consideration the fundamental ingredients of spatial deployment. From a visceral observation, it becomes natural to give precise attention to the following criteria:

1. Geography of the Network: This constitutes the general location and setting of the network. For instance, is the spatial emulation intended for a rural, or rather a built-up urban region?
2. Topography of the Network: This part looks into the details of the terrain and its distinctive landforms and features.
3. Demography of the Network: Here, the scale and distribution of the users are important. Namely, is the network densely or sparsely populated, and how does this composition change over time?

Overall, it is desired to conceive an easily controlled and configured algorithm with least amount of inputs while overlaying the above three aspects in order to closely reflect the terrain specifications and limitations of a specific site. These are all diametrically opposing requirements, and so reconciling them simultaneously is rather difficult to solve. Despite being quite involved, it is still possible to undertake this complex objective by contriving a framework that adheres to the notion of *divide and conquer*. In other words, the conundrum of spatial deployment can be tackled by gradually breaking down this nontrivial challenge into smaller algorithmically solvable parts, and then synthesizing the results.

In particular, this is done by proposing a superposition-based algorithm which we refer to as area-specific deployment (ASD). As shown in the arbitrary example of Figure 4.12, the general abstraction of the ASD approach can be described gradually in a systematic manner. Essentially, for a particular project site, the deployment designer will identify various likely clusters such that the overall network scale and surface is selectively split among these smaller sub-regions. As a matter of fact, each of the compiled non-overlapping clusters is uniquely specified by its:

- lattice shape or support domain $D_i \subseteq \mathbb{R}^2$
- surface area $A_i \in \mathbb{R}_+^*$
- quantity of randomly positioned nodes $n_i \in \mathbb{N}^*$
- and corresponding number density $\rho_i \in \mathbb{R}_+^*$

Moreover, the areal size and nodal volume of the original lattice are respectively given by:

$$A_N = \sum\nolimits_{i=1}^{n_{\text{sec-total}}} A_i \tag{4.70}$$

$$n_S = \sum\nolimits_{i=1}^{n_{\text{sec-total}}} n_i \tag{4.71}$$

such that $n_{\text{sec-total}} \in \mathbb{N}^*$ is the overall amount of sectors. Once the planning of the network footmark is set, we then focus on the sub-regions in a standalone way so as to stochastically generate the desired volume of Euclidian positions. Precisely, random uniform deployment is presumed over the specified sectors as expressed by the particular spatial density function of the sub-regions:

$$f_{XY}(x, y) = 1/A_i \cdot \mathbf{1}_{D_i \subseteq \mathbb{R}^2}(x, y) \qquad i = 1, 2, \cdots, n_{\text{sec-total}} \tag{4.72}$$

However, since the cluster envelopes have different 2D lattice shapes; probabilistic analysis has to carefully be drafted for random generation in a specific location, with a particular geometrical contour, coverage size, and nodal scale. Following the analysis step, the various subnetworks are then reassembled in a puzzle-like format. Thus, as a consequence of network synthesis, heterogeneous spatial distribution emerges over the deployment field.

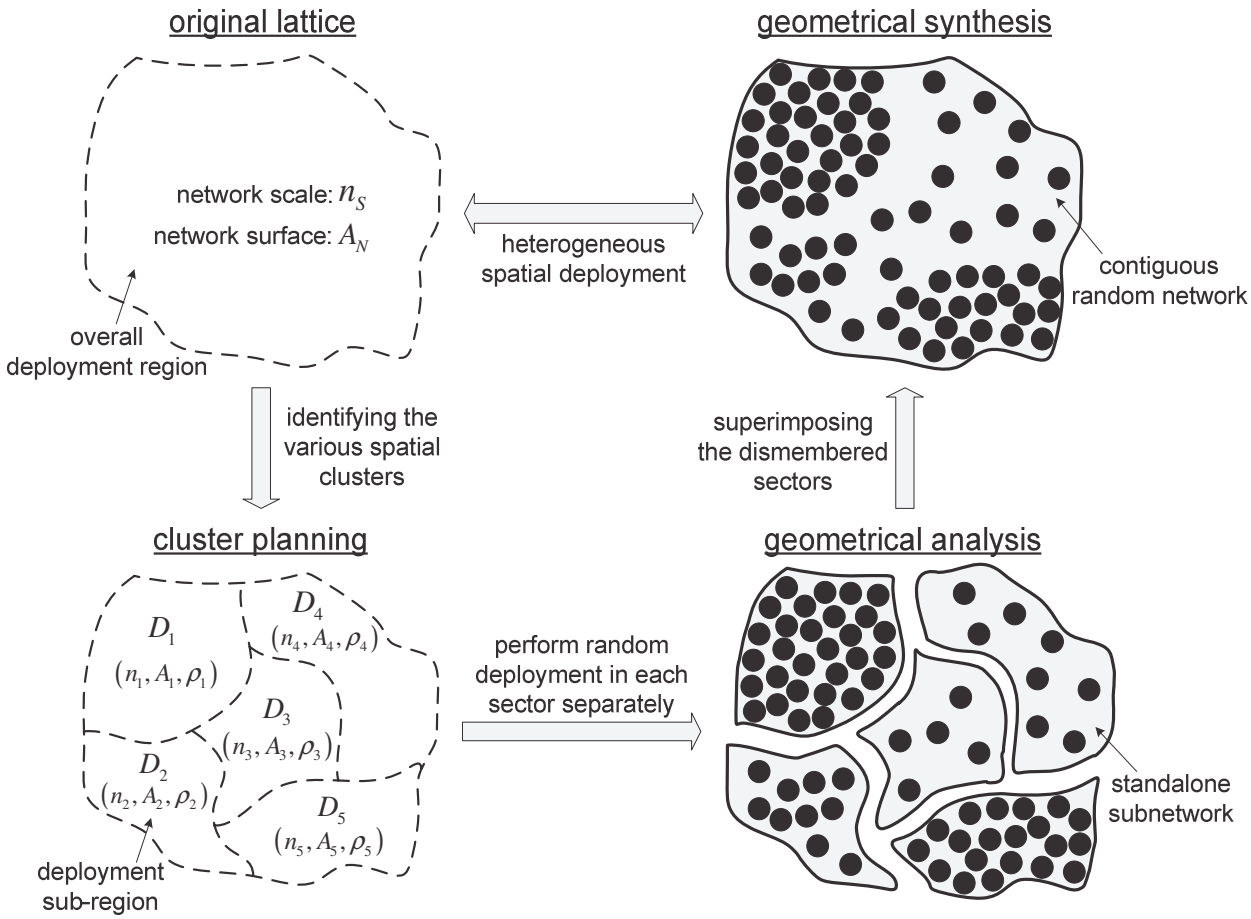

Figure 4.12 – Characterizing ASD by an arbitrary network model

Evidently, the ASD technique gives the necessary leverage to designers to tailor and plan the spatial architecture when *a priori* knowledge of the network is asserted while still preserving the geometrical randomness of the users. Such attributes will hence ensure greater emulation flexibility and attain spatial heterogeneity so as to evaluate a host of network-based QoS factors.

4.4.3 – UCN Algorithm for Heterogeneous Random Deployment

In the previous section, we provided a high-level view for attaining inhomogeneity. In this part of the dissertation, we apply the proposed ASD method in order to conceive a UCN approach for generating spatial heterogeneity. But before beginning, we ought to remark that when the aim is to explore a UCN, then it is a natural choice to consider a disk-shaped circular lattice model. In fact, such network layout is mainly feasible for designing and analyzing a sparse cellular structure commonly encountered in rural settings.

As a visual aid in deriving the non-uniform algorithm, we consider the canonical network model of Figure 4.13. From the display, it should be evident that the approach for partitioning the cell is in part inspired by the various layer formations apparent in the cross-section of an onion. Clearly, there are no sectors in the onion-layer arrangements; yet to add another level of deployment versatility to the conceptualized spatial model, we enable the possibility of incorporating sector strips in each layer of the network plan. This modification will in essence augment and enhance the inhomogeneous capability of the UCN model.

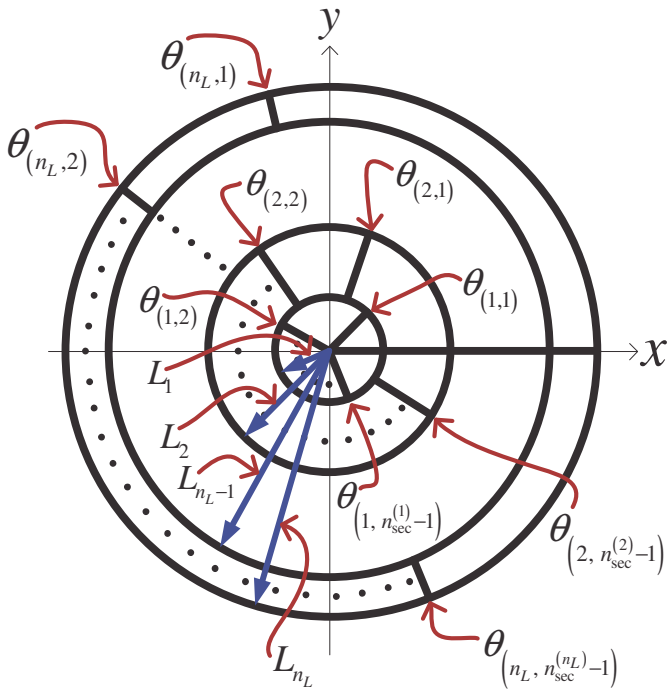

Figure 4.13 – Modeling the network plan of a heterogeneous UCN

In the above model, we recognize that the circular cell is split into $n_L \in \mathbb{N}^*$ layers. And, each layer contains $n_{\text{sec}}^{(i)} \in \mathbb{N}^*$ sectors, such that $i = 1, 2, \cdots, n_L$. Therefore, the total number of sectors in the UCN inhomogeneous model of Figure 4.13 can be computed by:

$$n_{\text{sec-total}} = \sum_{i=1}^{n_L} n_{\text{sec}}^{(i)} \tag{4.73}$$

In principle, the more terrain strips we consider during the planning stage of a particular project site, the more network clusters will be resulted, and thus $n_{\text{sec-total}}$ will raise. And as the total number of sectors with varying densities increase, it will consequently impact the geometrical inhomogeneity level of the wireless nodes. In other words, the size of $n_{\text{sec-total}}$ is an indicator for the details and precision of the deployment plan, which is in fact left to the discretion of the network architect.

Furthermore, each cluster sector is indeed bounded within two radii and two angular limits. The layers radii for heterogeneous random deployment are collectively contained by the $\mathbf{R} \in \mathbb{R}_{+,*}^{n_L}$ vector, which is specified by:

$$\underset{n_L \times 1}{\mathbf{R}} = \begin{bmatrix} r_1 & r_2 & \cdots & r_{n_L} \end{bmatrix}^T = \left[r_i \in \mathbb{R}_+^* \right]_{i=1,2,\cdots,n_L} \tag{4.74}$$

such that $r_{i-1} < r_i : i = 2,3,\cdots,n_L$. As for the sectors angular information, they are identified by their higher values within the $\boldsymbol{\Theta} \in \mathbb{R}_+^{n_L \times (\gamma-1)}$ matrix:

$$\underset{n_L \times (\gamma-1)}{\boldsymbol{\Theta}} = \begin{bmatrix} \theta_{(1,1)} & \theta_{(1,2)} & \cdots & \theta_{\left(1,\, n_{\text{sec}}^{(1)}-1\right)} & 0 & \cdots & 0 \\ \theta_{(2,1)} & \theta_{(2,2)} & \cdots & \theta_{\left(2,\, n_{\text{sec}}^{(2)}-1\right)} & 0 & \cdots & 0 \\ \vdots & \vdots & \vdots & \vdots & \vdots & \vdots & \vdots \\ \theta_{(k_L,1)} & \theta_{(k_L,2)} & \cdots & \cdots & \cdots & \cdots & \theta_{\left(k_L,\, n_{\text{sec}}^{(k_L)}-1\right)} = \theta_{(k_L,\, \gamma-1)} \\ \vdots & \vdots & \vdots & \vdots & \vdots & \vdots & \vdots \\ \theta_{(n_L,1)} & \theta_{(n_L,2)} & \cdots & \theta_{\left(n_L,\, n_{\text{sec}}^{(n_L)}-1\right)} & 0 & \cdots & 0 \end{bmatrix} = \left[\theta_{(i,j)} \in \mathbb{R}_+^* \right]_{\substack{i=1,2,\cdots,n_L \\ j=1,2,\cdots,n_{\text{sec}}^{(i)}-1}} \tag{4.75}$$

However, since the last sector of any layer is always set to 2π, then there is no need to enter this reoccurring measure in the matrix. In fact, the various angular values for each layer are bordered by:

$$0 < \theta_{(i,1)} < \theta_{(i,2)} < \cdots < \theta_{\left(i,\, n_{\text{sec}}^{(i)}-1\right)} < 2\pi \qquad i = 1,2,\cdots,n_L \tag{4.76}$$

Also, in (4.75) the $\gamma \in \mathbb{N}^*$ represents the largest number of sectors in a particular UCN layer, which is quantified by:

$$\gamma \triangleq \max_{i=1,2,\cdots,n_L} \left\{ n_{\text{sec}}^{(i)} \right\} = n_{\text{sec}}^{(k_L)} \tag{4.77}$$

such that $\left\{ k_L \in \mathbb{N}^* \middle| 1 \le k_L \le n_L \right\}$ is the UCN layer that has the greatest number of sectors. It is worth noting that this value is not necessarily unique because there might be multiple layers that have the similar maximum number of sectors.

Pursuing this further, the $\mathbf{N} \in \mathbb{N}^{n_L \times \gamma}$ matrix of (4.78) holds the amount of randomly positioned nodes deployed in each sector. This means that the spatial topology is tunable by simply modifying the quantity of nodes in the cluster strips of the network plan.

$$\underset{n_L \times \gamma}{\mathbf{N}} = \begin{bmatrix} n_{(1,1)} & n_{(1,2)} & \cdots & n_{\left(1,\, n_{\text{sec}}^{(1)}\right)} & 0 & \cdots & 0 \\ n_{(2,1)} & n_{(2,2)} & \cdots & n_{\left(2,\, n_{\text{sec}}^{(2)}\right)} & 0 & \cdots & 0 \\ \vdots & \vdots & \vdots & \vdots & \vdots & \vdots & \vdots \\ n_{(k_L,1)} & n_{(k_L,2)} & \cdots & \cdots & \cdots & \cdots & n_{\left(k_L,\, n_{\text{sec}}^{(k_L)}\right)} = n_{(k_L,\gamma)} \\ \vdots & \vdots & \vdots & \vdots & \vdots & \vdots & \vdots \\ n_{(n_L,1)} & n_{(n_L,2)} & \cdots & n_{\left(n_L,\, n_{\text{sec}}^{(n_L)}\right)} & 0 & \cdots & 0 \end{bmatrix} = \left[n_{(i,j)} \in \mathbb{N}^* \right]_{\substack{i=1,2,\cdots,n_L \\ j=1,2,\cdots,n_{\text{sec}}^{(i)}}} \tag{4.78}$$

For the convenience of manipulations, the radial, angular and nodal entries respectively expressed in (4.74), (4.75), and (4.78) can be assembled together by the network plan matrix $\mathbf{P} \in \mathbb{R}_+^{n_L \times 2\gamma}$, which is defined as:

$$\underset{n_L \times 2\gamma}{\mathbf{P}} = \left[\underset{n_L \times 1}{\mathbf{R}} \;\middle|\; \underset{n_L \times (\gamma-1)}{\mathbf{\Theta}} \;\middle|\; \underset{n_L \times \gamma}{\mathbf{N}} \right] = \left[p_{(i,j)} \in \mathbb{R}^+ \right]_{\substack{i=1,2,\cdots,n_L \\ j=1,2,\cdots,2\gamma}} \tag{4.79}$$

Overall, within the expression of (4.79), the following essential deployment parameters are inscribed:

- the number of deployment layers
- the width of each layer
- the number of sectors in each layer
- the extent of the angular boundary for each cluster
- the nodal scale randomly located in each sector

At this level, we may harness the above descriptions by creating a generically flexible algorithm that enables controlled inhomogeneous random geometry. To emphasize, this method gives the necessary freedom to a cellular analyst or designer to selectively deploy random nodes in desired locations in order to form clusters. Once cluster-based random deployment is complete, the superposition principle can be applied to get the overall inhomogeneous spatial distribution of the cell.

All the required steps to accomplish the described ASD algorithm over a UCN model for the purpose of spatial inhomogeneity are provided in the pseudocode of Figure 4.14. As evident by the nested for-loop, the algorithm is in part based on the foundation formulated for unbiased and exact random generation inside a flexibly versatile ring sector model derived and analyzed in earlier parts of this chapter.

On the whole, the conceptualized algorithm is a simple emulation tool useful for modeling a non-homogeneous network in instances when some elementary knowledge about a cell site is known or hypothesized. In fact, the treated inhomogeneous approach has the benefit of preserving full spatial randomness without relying on synthetic workarounds.

Now that we have the above pseudocode, it is noteworthy to determine by (4.80) the algorithm cost for executing this operation, where $n_S \in \mathbb{N}^*$ is the overall number of randomly deployed nodes within the UCN model.

$$O\left(\sum_{i=1}^{n_L}\sum_{j=1}^{n_{\text{sec}}^{(i)}} p_{(i,\,j+\gamma)}\right) = O\left(\sum_{i=1}^{n_L}\sum_{j=1}^{n_{\text{sec}}^{(i)}} n_{(i,j)}\right) = O\left(n_S\right) \tag{4.80}$$

Algorithm 7 - Emulating an Inhomogeneous Random Network - Controlled Footprint

Require: $n_L \in \mathbb{N}^*$ $\left\{n_{\text{sec}}^{(i)} \in \mathbb{N}^*\right\} : i = 1, 2, \cdots, n_L$ $\mathbf{P} = \left[\, p_{(i,j)} \in \mathbb{R}^+ \,\right]_{\substack{i=1,2,\cdots,n_L \\ j=1,2,\cdots,2\gamma}}$

Compute: $\gamma = \max\limits_{i=1,2,\cdots,n_L} \left\{n_{\text{sec}}^{(i)}\right\}$

Initialize: $n_S = 0$

for $i = 1, 2, \cdots, n_L$ **do**

  if $\{i \neq 1\}$ **then** $L_1 \coloneqq p_{(i-1,\ 1)}$ **else** $L_1 \coloneqq 0$ **end if**

  $L_2 \coloneqq p_{(i,1)}$

  for $j = 1, 2, \cdots, n_{\text{sec}}^{(i)}$ **do**

    if $\{j \neq 1\}$ **then** $\alpha_1 \coloneqq p_{(i,\ j)}$ **else** $\alpha_1 \coloneqq 0$ **end if**

    if $\left\{j \neq n_{\text{sec}}^{(i)}\right\}$ **then** $\alpha_2 \coloneqq p_{(i,\ j+1)}$ **else** $\alpha_2 \coloneqq 2\pi$ **end if**

    $n_0 \coloneqq p_{(i,\ j+\gamma)}$

    for $m = 1, 2, \cdots, n_0$ **do**

      Generate two i.i.d. RVs: $\{\hat{u}_0, \hat{u}_1\} \sim \mathcal{U}(0,1)$

      Compute: $\hat{r}_m \coloneqq \sqrt{L_1^2 + \hat{u}_0\left(L_2^2 - L_1^2\right)} \sim f_R(r)$

      Compute: $\hat{\theta}_m \coloneqq \left\{\alpha_1 + \hat{u}_1(\alpha_2 - \alpha_1)\right\} \sim f_\theta(\theta)$

      Compute: $\left\{\hat{x}_{n_S+m};\ \hat{y}_{n_S+m}\right\} = \left\{\hat{r}_m \cos\left(\hat{\theta}_m\right);\ \hat{r}_m \sin\left(\hat{\theta}_m\right)\right\} \sim f_{XY}(x, y)$

    end for

    $n_S \coloneqq n_S + n_0$

  end for

end for

Return: $\{\hat{x}_t, \hat{y}_t\} : t = 1, 2, \cdots, n_S$

Figure 4.14 – Pseudocode for heterogeneous spatial deployment of controlled UCN plan

In Figure 4.15, an example of a possible 3-layer network plan is shown. From the illustration, we identify that $n_{\text{sec-total}} = 6$ where the inner and outer layers have each a singular sector, and the middle layer is split into four clusters. Also, in each of these zones, the amount of random nodes to be deployed is accordingly mapped. Although the derived inhomogeneous algorithm is scalable, in this UCN example we consider an $n_S = 3{,}300$ nodes.

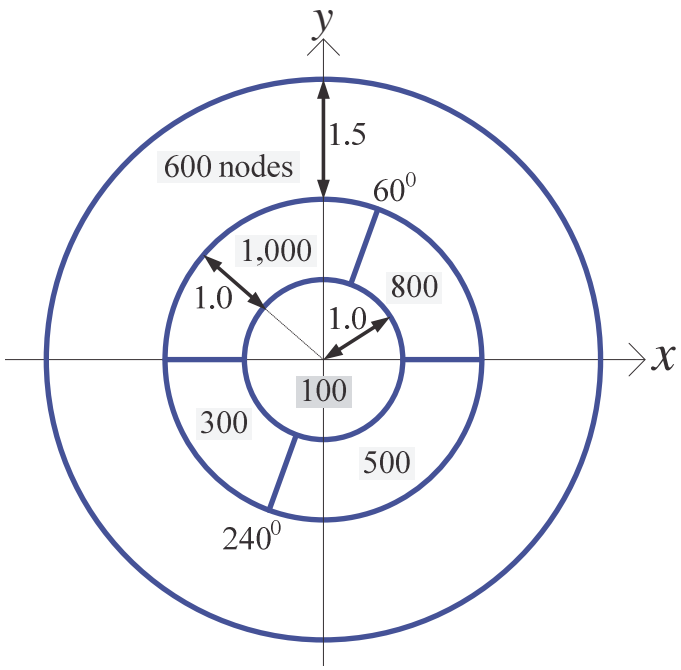

Figure 4.15 – Example of a 6-sector network footprint

The network plan of Figure 4.15 can equivalently be transformed into matrix format as follows:

$$\underset{3\times 8}{\mathbf{P}} = \left[\underset{3\times 1}{\mathbf{R}} \;\middle|\; \underset{3\times 3}{\Theta} \;\middle|\; \underset{3\times 4}{\mathbf{N}}\right] = \left[\begin{array}{c|ccc|cccc} r_1 & 0 & 0 & 0 & n_{(1,1)} & 0 & 0 & 0 \\ r_2 & \theta_{(2,1)} & \theta_{(2,2)} & \theta_{(2,3)} & n_{(2,1)} & n_{(2,2)} & n_{(2,3)} & n_{(2,4)} \\ r_3 & 0 & 0 & 0 & n_{(3,1)} & 0 & 0 & 0 \end{array}\right]$$

$$= \left[\begin{array}{c|ccc|cccc} 1.0 & 0 & 0 & 0 & 100 & 0 & 0 & 0 \\ 2.0 & \pi/3 & \pi & 4\pi/3 & 800 & 1{,}000 & 300 & 500 \\ 3.5 & 0 & 0 & 0 & 600 & 0 & 0 & 0 \end{array}\right] \tag{4.81}$$

Figure 4.16 shows the MC simulation result for the non-homogeneous network of (4.81). The generated structure is clearly a random network, i.e. this outcome is one of infinitely many random realizations of users' Euclidian geometry. This means that at every simulation run, the characterized network plan produces a unique inhomogeneous spatial emplacement. As for the corresponding spatial density shown in the figure, it was estimated based on 25×25 grid.

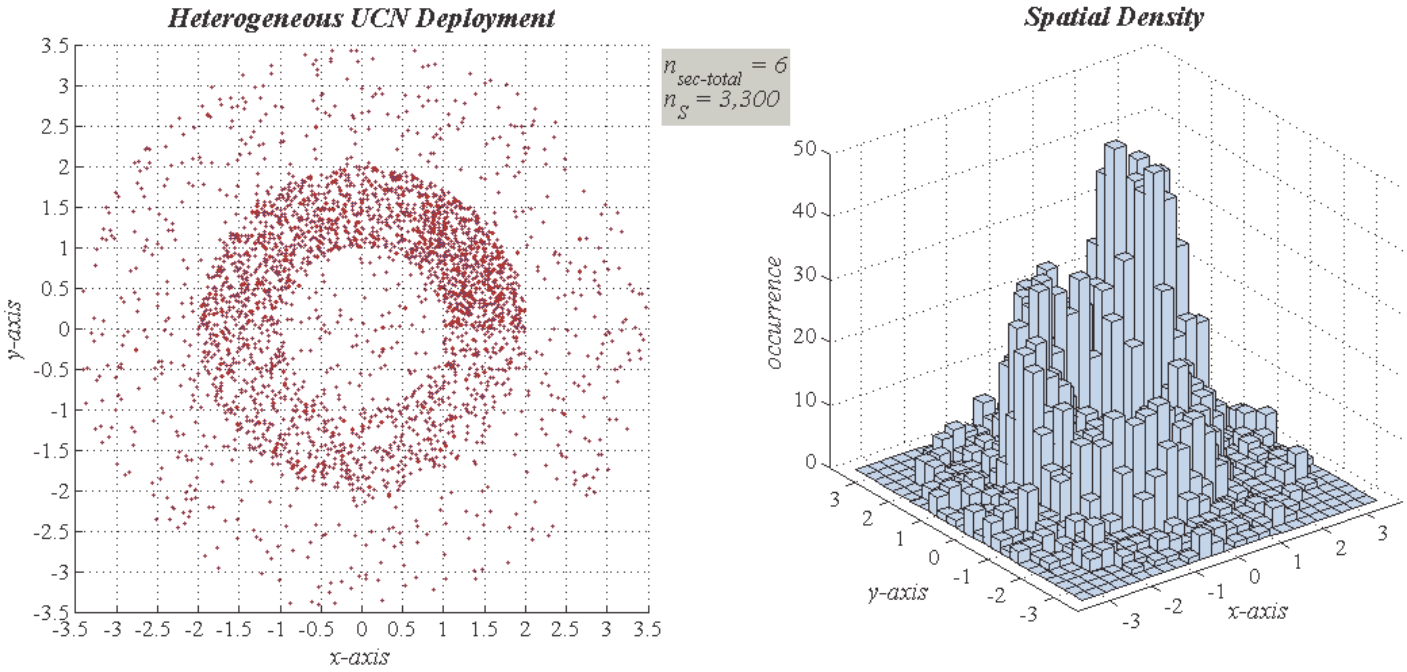

Figure 4.16 – Heterogeneous spatial deployment and density for a 6-sector UCN example

To further display the conceptualized inhomogeneous algorithm of Figure 4.14, we designed another cellular deployment with $n_S = 3{,}300$ nodes. This time however, the UCN is composed of 4-layers with $n_{\text{sec-total}} = 10$ sectors. The considered network footprint is depicted in Figure 4.17, and its matrix equivalent is given in (4.82).

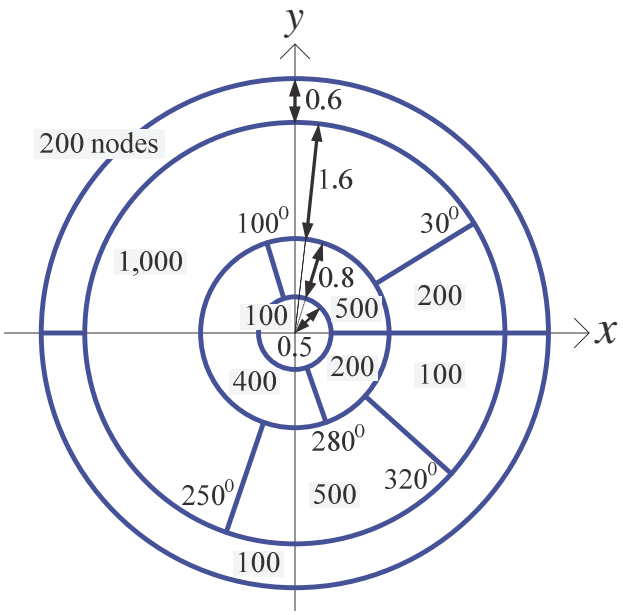

Figure 4.17 – Example of a 10-sector network footprint

$$\underset{4\times 8}{\mathbf{P}} = \left[\underset{4\times 1}{\mathbf{R}} \;\middle|\; \underset{4\times 3}{\boldsymbol{\Theta}} \;\middle|\; \underset{4\times 4}{\mathbf{N}}\right] = \left[\begin{array}{c|ccc|cccc} r_1 & 0 & 0 & 0 & n_{(1,1)} & 0 & 0 & 0 \\ r_2 & \theta_{(2,1)} & \theta_{(2,2)} & 0 & n_{(2,1)} & n_{(2,2)} & n_{(2,3)} & 0 \\ r_3 & \theta_{(3,1)} & \theta_{(3,2)} & \theta_{(3,3)} & n_{(3,1)} & n_{(3,2)} & n_{(3,3)} & n_{(3,4)} \\ r_4 & \theta_{(4,1)} & 0 & 0 & n_{(4,1)} & n_{(4,2)} & 0 & 0 \end{array}\right]$$

$$= \left[\begin{array}{c|ccc|cccc} 0.5 & 0 & 0 & 0 & 100 & 0 & 0 & 0 \\ 1.3 & 5\pi/9 & 14\pi/9 & 0 & 500 & 400 & 200 & 0 \\ 2.9 & \pi/6 & 25\pi/18 & 16\pi/9 & 200 & 1{,}000 & 500 & 100 \\ 3.5 & \pi & 0 & 0 & 200 & 100 & 0 & 0 \end{array}\right] \tag{4.82}$$

As a consequence of simulating this network, we obtain in Figure 4.18 one of many possible random instances of the result.

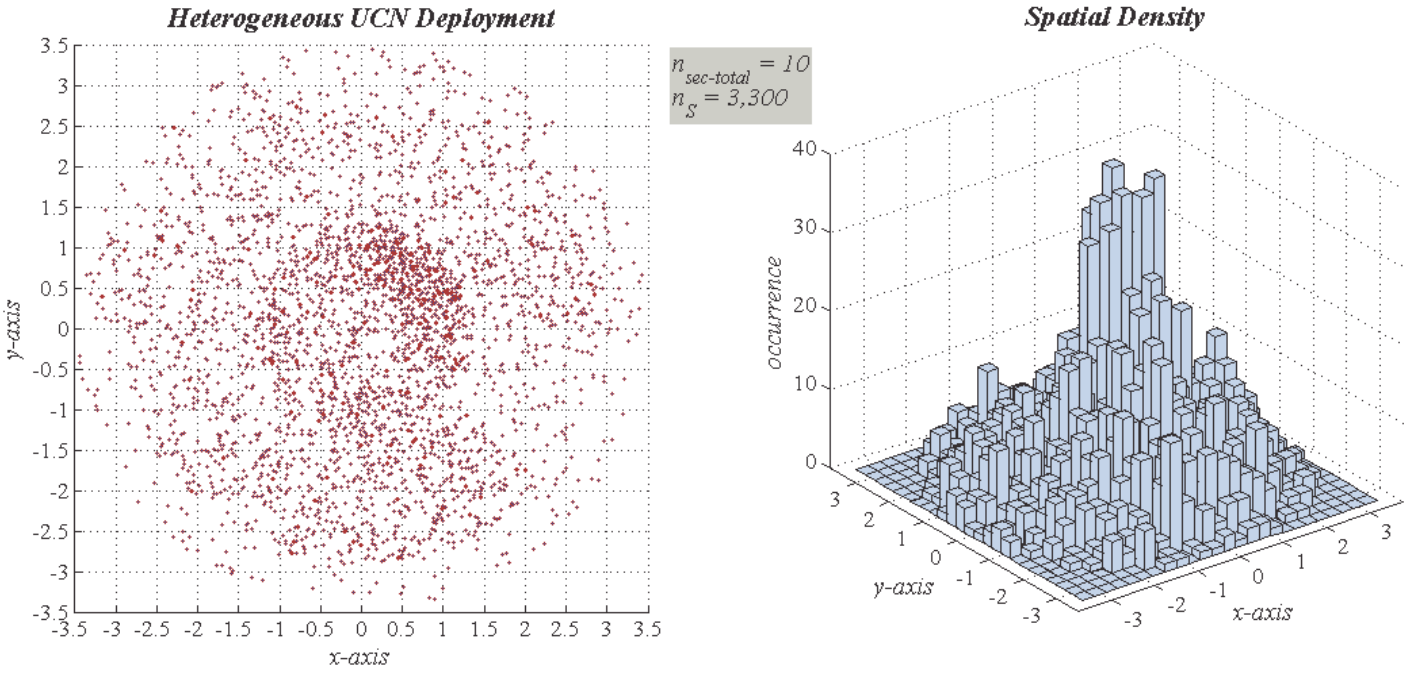

Figure 4.18 – Heterogeneous spatial deployment and density for a 10-sector UCN example

When we compare the network plans of (4.82) with (4.81), we obviously notice that it has more entries, which in essence means that the associated spatial design is more elaborate than the previous one. In fact, the major elaboration of the network plan for a particular site is

characterized by the $\mathbf{R}$ and Θ components as a function of terrain features. Then, we could study and verify various QoS measures as the number of nodes in each sector is altered by a simple modification of the values in the $\mathbf{N}$ matrix.

Evidently, this approach may become handy when we couple to the described spatial model a temporal element in order to further improve the modeling of users clustering tendency. That is, users' gathering inclinations in a particular sector due to topographical biases will in fact change with time. In other words, during a certain point a particular geometrical density is in effect and perhaps at another timeframe terminals concentration shifts to different locations. For instance during business hours mobile subscribers' activity is expected in commercial areas; while after hours, users' spatial pattern relocates to residential areas [37].

Thus, the aim here is to highlight the fact that the position density is indeed dependent on the correlation of both the spatial landscape and the temporal component of users' communications activity. And so, the nodal information of the network plan can accordingly be adjusted to reflect the changeable nature of users' geometry. In fact, these values could be conjectured based on plausible situations, or they could be compiled from simple statistical data gathering of a site as opposed to socially-intensive trend studies. Then, the ASD method for UCN can effortlessly be triggered to emulate a random spatial model which can assist in bridging the gap between reality and modeling.

Before closing this subsection, we should acknowledge the main shortcoming for emulating an inhomogeneous random network. In particular, the model of the derived algorithm considers circular-based deployment strips. However, the various cluster sectors need not necessarily be of this form. Thus, the random deployment may not be appropriate at all times in an accurate way. Nonetheless, it could still be instrumental as an approximately more realistic deployment approach than the typical homogeneous alternative.

4.4.4 – Automatic Emulation of Heterogeneous Random Networks

From the above discussion, it should be obvious by now that the occurrence of clustering is inevitable in most real-life scenarios. As a result, the spatial distribution of nodes for a given deployment project will likely be non-homogeneous. For this reason, in the previous section we developed a practical spatial-level simulator tool for inhomogeneous random nodal deployment based on controlled network planning. While the approach is adequate, in particular cases,

various modeling accommodations and extensions could be incorporated to this mechanism so that the emulation experience becomes more lucid for network designers. This endeavor will actually be the primary intention of the treatment that follows.

Specifically, we want to provide greater emulation leverage by conceptualizing another algorithm that can achieve heterogeneity with very limited planning information to the network subroutine. Thus, in contrast to the controlled approach of Subsection 4.4.3, the aim here is to construct an inhomogeneous random network in an uncontrolled or arbitrary manner. This could be done by redesigning the algorithm of Figure 4.14 such that it maintains similar attributes while requiring less input parameters in order to produce a simpler process for generating a heterogeneous spatial network.

From the ASD principle in Subsection 4.4.2, we explained a strategy for inhomogeneity by having different areal number densities in each of the deployment sub-regions. In fact, the density for the sectors is obtained by:

$$\forall A_i \in \mathbb{R}_+^* : \exists n_i \in \mathbb{N}^* : \rho_i \triangleq n_i / A_i \qquad i = 1, 2, \cdots, n_{\text{sec-total}} \tag{4.83}$$

From (4.83), we clearly notice that the densities can be made unique in one of three ways:

1. change n_i , and keep A_i fixed.
2. change A_i , and keep n_i fixed.
3. change simultaneously n_i and A_i .

In deriving the desired inhomogeneous algorithm, we find that actually the second approach is more suitable; thus, (4.83) becomes:

$$\rho_i = n_0 / A_i \qquad i = 1, 2, \cdots, n_{\text{sec-total}} \tag{4.84}$$

In order to obtain different sub-regions, we will consider $n_L \in \mathbb{N}^*$ onion-like layers; therefore, for this layout $n_{\text{sec-total}} = n_L$. In fact, for the purpose of uncontrolled inhomogeneity, the number of layers will randomly be chosen from a predefined integer range. Therefore, this task will necessitate the formulation of a generic technique for randomly producing discrete values.

Say, we want to generate a random integer bounded by $[n_1, n_2]$ in such a way that these values have equal contribution. That is, we desire to obtain a generic method for discrete RNG from a PMF. In Figure 4.19, we visually show the stem plot for the $n_2 - n_1 + 1$ discrete data sequence distribution. Analytically speaking, this PMF is defined by:

$$\Pr\{X = x\} : \forall x \in \mathbb{Z} : \exists n_1, n_2 \in \mathbb{Z}^2 : [n_1, n_2] \mapsto 1/(n_2 - n_1 + 1) \tag{4.85}$$

To randomly generate discrete points from this PMF, we could consider a workaround that depends on the corresponding continuous uniform distribution, namely:

$$f_X(x) = \mathcal{U}_X(n_1 - 1/2, n_2 + 1/2) \qquad (n_1, n_2) \in \mathbb{Z}^2 : n_1 \le n_2 \tag{4.86}$$

This density function is also graphed in Figure 4.19. Once a continuous sample from the PDF of (4.86) is randomly generated, we then assign it to the nearby discrete value of the PMF.

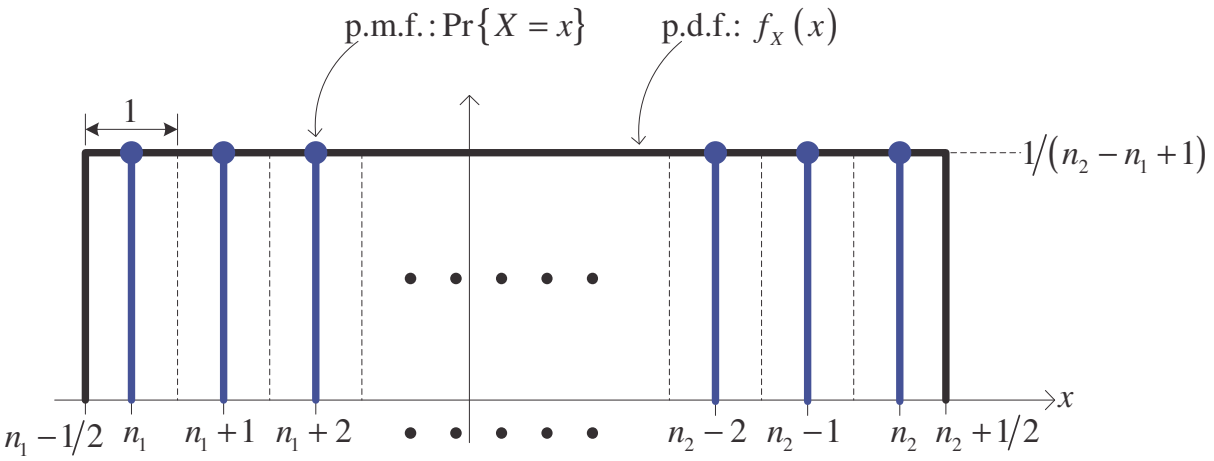

Figure 4.19 – Uniform PMF and its corresponding PDF

As a shorthand notation to a discrete uniform distribution, we rather utilize this statement:

$$\Pr\{X = x\} = \mathcal{U}_D(n_1, n_2) \qquad (n_1, n_2) \in \mathbb{Z}^2 : n_1 \le n_2 \tag{4.87}$$

Equipped with the above rationalization, we can then write a simple pseudocode for generating n_S random samples from the PMF of (4.87). The generic solution is expressed in the algorithm of Figure 4.20. As for the cost of this algorithm, it can be measured by the worst case computational complexity assessed by:

$$O\left(T_{cost}\left(n_1, n_2, n_S\right)\right) = O\left(n_S\left(n_2 - n_1 + 1\right)\right) \tag{4.88}$$

Algorithm 8 - Generic method for uniform random integer generation

Require: $n_S \in \mathbb{N}^* \quad (n_1, n_2) \in \mathbb{Z}^2 : n_1 \le n_2$
for $i = 1, 2, \cdots, n_S$ **do**
  Generate a RV: $\hat{u}_i \sim \mathcal{U}(0,1)$
  Compute: $\hat{v}_i := \left\{n_1 + \hat{u}_i\left(n_2 - n_1 + 1\right) - 1/2\right\} \sim \mathcal{U}_X\left(n_1 - 1/2, n_2 + 1/2\right)$
  for $j = n_1, n_1 + 1, \cdots, n_2 - 1, n_2$ **do**
    if $\left\{\left|\hat{v}_i - j\right| \le 1/2\right\}$ **then**
      $\hat{x}_i := j \sim \Pr\{X = x\} = \mathcal{U}_D\left(n_1, n_2\right)$ **break for**
    end if
  end for
end for
Return: $\left\{\hat{x}_i\right\} : i = 1, 2, \cdots, n_S$

Figure 4.20 – RNG from discrete uniform distribution

To ascertain the effectiveness of the determined algorithm for random integer generation, we performed in Figure 4.21 a set of MC simulations for a particular amount of n_S values from the discrete set bounded by say $[-4, 9]$. In the figures, the estimated PMF is represented by bars; also, for the sake of comparison in each case we plotted the corresponding theoretical PDF.

First, irrespective of the simulation case, when we add the likelihood for each of the discrete samples, it always sums up to unity; which is in accordance with the fundamentals of probability theory. Second, from the obtained results, we can evidently notice that as the number of samples increases, the PMF estimation gets closer to the theoretical baseline. Overall, the simulation reveals that the random generation approach produces the expected distribution.

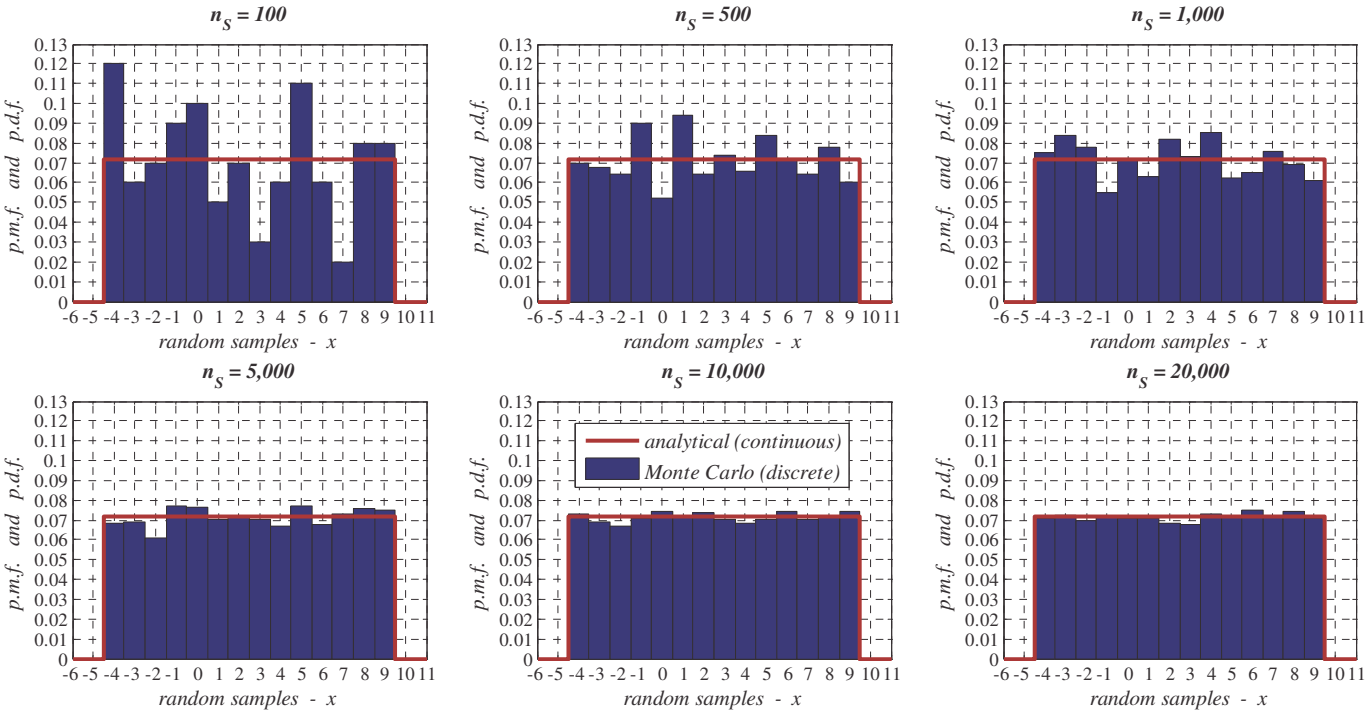

Figure 4.21 – Substantiating experimentally the random generation of discrete samples

Returning back to the main problem, using the above derivation, we aim to randomly generate n_L from a range delimited by $n_{L-\max}$, which essentially refers to the maximum arbitrary number of deployment layers possible for achieving spatial inhomogeneity. This value will actually be preset by the UCN designer at the start of the automatic emulation process. Therefore, the number of layers at a simulation instance will be a discrete RV specified by:

$$n_L \sim \mathcal{U}_D\left(2, n_{L-\max}\right) \qquad n_{L-\max} \in \mathbb{N}^* : n_{L-\max} > 1 \tag{4.89}$$

From (4.89), we notice that the sampling range begins at $n_1 = 2$ because from the ASD principle, we at least need 2-layers for attaining inhomogeneity. In other words, if we would have started with $n_1 = 1$, and by discrete RNG n_L is randomly set to this value, then we will simply obtain a homogeneous random network; this will actually be the antithesis to the wanted objective of spatial heterogeneity. Meanwhile, it is worth adding that in the rare but possible case where $n_{L-\max}$ is set to 2, then from (4.89) the number of layers will deterministically be assigned at all times to this value.

Now that we have framed an approach for randomly obtaining the number of layers, as explained in (4.84), the next step requires us to equally split the number of nodes among these sub-regions. By design, the overall amount of nodes $n_S \in \mathbb{N}^*$ planned for random deployment is supplied by the network architect. Since n_S and n_L need not necessarily be multiples of each other, then the number of nodes per layer must be arranged in a careful way. In particular, the amount of random nodes deployed in the innermost layer of an automatically emulated inhomogeneous UCN is designated by $n_{in} \in \mathbb{N}^*$. As for the outer layers, each of these sub-regions will contain $n_{out} \in \mathbb{N}^*$ nodes computed by:

$$\forall n_S \in \mathbb{N}^* : \exists n_L \in \mathbb{N}^* : n_{out} \triangleq \lfloor n_S / n_L \rfloor \tag{4.90}$$

Knowing the volume of nodes in the outer layers, then it should be evident that the rest of the overall nodal quantity will constitute the amount of terminals in the innermost sub-region of the cell. Therefore, this measure can be calculated as follows:

$$n_{in} \triangleq n_S - (n_L - 1) \cdot n_{out} = n_S - (n_L - 1) \cdot \lfloor n_S / n_L \rfloor \tag{4.91}$$

So far, we have determined the number of layers and the amount of nodes in each sector. At present, we want to vary the areal size of each sub-region. This task can be done by randomly deciding on the geometrical position of the layers. That is, we want the width or thickness $\Delta_i \in \mathbb{R}_+^*$ of the various deployment layers to be different. In fact, this value corresponds to:

$$\Delta_i = r_i - r_{i-1} \qquad i = 2, 3, \cdots, n_L \tag{4.92}$$

such that $\Delta_1 = r_1$ is the radius measured from the origin of the Cartesian coordinate system to the first layer, and $r_i \in \mathbb{R}_+^*$ is the particular radius for all the other deployment layers. In this situation, the procedure to generate diverse widths of the deployment sub-regions can be realized by randomly producing radial values for the layers; this can be accomplished by:

$$r_i \sim \mathcal{U}_R(0, L) \qquad i = 1, 2, \cdots, n_L - 1 \tag{4.93}$$

From (4.93), it should be clear that we only generate random radial values for the first $n_L - 1$ layers since r_{n_L} will always be equal to the preassigned size of the cellular radius, namely $L \in \mathbb{R}_+^*$.

Following the generation of these radial distances, it then becomes necessary to sort them in ascending order, i.e.:

$$\vec{r}_{sorted} = \text{sort}\left(\vec{r} \in \mathbb{R}_{+,*}^{n_L - 1}\right) = \text{sort}\left(\left[r_i\right]_{i=1,2,\cdots,n_L-1}\right) \tag{4.94}$$

There are many techniques available for implementing the sorting operator of (4.94); some of the most notable among them are: quicksort, heapsort, and mergesort. Specifically, quicksort has been established as one of the fastest algorithms for ordering an array of numbers. Thus, MATLAB® uses this approach for its **sort** function.

Next, as discussed in Section 4.2, we will stochastically deploy in each of the formed random sized sub-regions the corresponding amount of nodes. Then, we superimpose these multi-density sectors together and look at the network as a holistic entity, which results into a heterogeneous outcome that has a random characteristic.

With the above conceptualization, we have progressively developed an automatic mechanism for randomly constructing the network plan so as to produce an inhomogeneous spatial structure. To be precise, the geometrical randomness is achieved due to the arbitrary nature of:

- the number of deployment layers: n_L
- the size of the layers: Δ_i
- the position of nodes within each layer: $\{\hat{x}_i, \hat{y}_i\}$

Consequently, the amalgamation of the above factors will result into a heterogeneous random network. For the sake of completeness, these attributes are graphically depicted in the geometrical model of Figure 4.22 used for automatically producing a random UCN footprint.

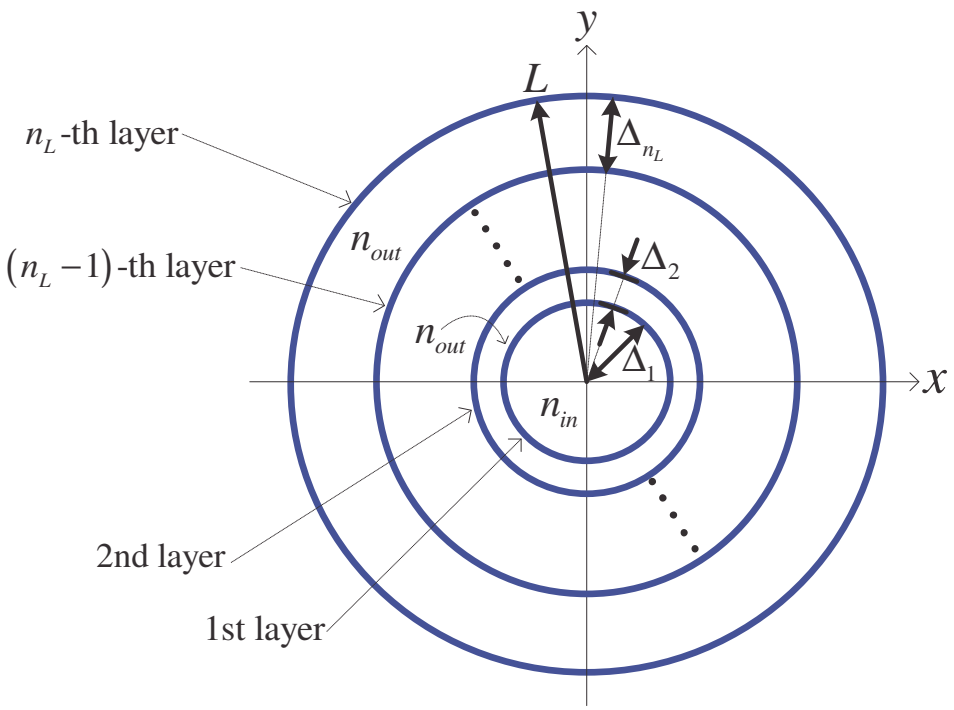

Figure 4.22 – Geometrical details for uncontrolled random realization of the UCN footprint

Overall, the culmination of the above explanations and analysis enables us to derive the uncontrolled inhomogeneous algorithm of Figure 4.23. From this algorithm, it can vividly be observed that a deployment designer will only require entering three essential inputs:

- the size of the cellular network: L
- the maximum number of deployment layers: $n_{L-\max}$
- the quantity of nodes to be deployed: n_S

Given that the formulated method only demands few entries, it then means that the heterogeneous algorithm of Figure 4.23 will basically do most of the network decisions automatically in a stochastic way. In fact, when compared to the set of required parameters for the network footprint of the controlled deployment option detailed in Figure 4.14, the discrepancy of the inputs among these inhomogeneous random network algorithms is considerable. In light of this reality, we can therefore remark that if less *a priori* information about the network project site is known or hypothesized, then the automatic inhomogeneous alternative for spatial emulation should be favored as opposed to the controlled algorithm.

Algorithm 9 - Emulating an Inhomogeneous Random Network - Uncontrolled Footprint

Require: $n_S \in \mathbb{N}^* \quad L \in \mathbb{R}_+^* \quad \left\{ n_{L-\max} \in \mathbb{N}^* \middle| n_{L-\max} > 1 \right\}$
Generate a RV: $\hat{u}_0 \sim \mathcal{U}(0,1)$
Compute: $\hat{v}_0 := \left\{ 3/2 + \hat{u}_0 \left(n_{L-\max} - 1 \right) \right\} \sim \mathcal{U}_V \left(3/2, n_{L-\max} + 1/2 \right)$
for $i = 2, 3, \cdots, n_{L-\max}$ **do**
    if $\left\{ \left| \hat{v}_0 - i \right| \le 1/2 \right\}$ **then**
        $n_L := i \sim \mathcal{U}_D \left(2, n_{L-\max} \right)$ **break for**
    end if
end for
Compute: $n_{in} := n_S - \left(n_L - 1 \right) \cdot \lfloor n_S / n_L \rfloor \quad n_{out} := \lfloor n_S / n_L \rfloor$
for $j = 1, 2, \cdots, n_L - 1$ **do**
    Generate a RV: $\hat{u}_1 \sim \mathcal{U}(0,1)$
    Compute: $\hat{r}_j := \hat{u}_1 L \sim \mathcal{U}_R (0, L)$
end for
Sort in ascending order: $\left\{ \hat{r}_j \right\} := \text{sort} \left(\hat{r}_j \right) \quad j = 1, 2, \cdots, n_L - 1$
Initialize: $t = 0$
for $j = 1, 2, \cdots, n_L$ **do**
    if $\left\{ j \ne 1 \right\}$ **then**
        $L_1 := \hat{r}_{j-1} \quad n_0 := n_{out}$
    else
        $L_1 := 0 \quad n_0 := n_{in}$
    end if
    if $\left\{ j \ne n_L \right\}$ **then** $L_2 := \hat{r}_j$ **else** $L_2 := L$ **end if**
    for $m = 1, 2, \cdots, n_0$ **do**
        Generate two i.i.d. RVs: $\left\{ \hat{u}_2, \hat{u}_3 \right\} \sim \mathcal{U}(0,1)$
        Compute: $\hat{r}_m := \sqrt{L_1^2 + \hat{u}_2 \left(L_2^2 - L_1^2 \right)} \sim f_R(r)$
        Compute: $\hat{\theta}_m := 2\pi \hat{u}_3 \sim f_\theta(\theta)$
        Compute: $\left\{ \hat{x}_{t+m};\ \hat{y}_{t+m} \right\} = \left\{ \hat{r}_m \cos\left(\hat{\theta}_m \right);\ \hat{r}_m \sin\left(\hat{\theta}_m \right) \right\} \sim f_{XY}(x, y)$
    end for
    $t := t + n_0$
end for
Return: $\left\{ \hat{x}_i, \hat{y}_i \right\} : i = 1, 2, \cdots, n_S$

Figure 4.23 – Pseudocode for heterogeneous spatial deployment of uncontrolled UCN plan

In order to comprehend the time performance of the above algorithm, we therefore find it necessary to evaluate in (4.95) its overall computational complexity. We should note that in this cost analysis, we considered $n_L = n_{L-\max}$ so as to reflect the worst computational scenario.

$$
\begin{aligned}
O\left(T_{\cos t}\left(L, n_{L-\max}, n_S\right)\right) &= O(1) + O\overbrace{\left(n_{L-\max} - 1\right)}^{\triangleq m} + O\left(n_{L-\max} - 1\right) \\
&\quad + O\left(\left(n_{L-\max} - 1\right) \cdot \log_2\left(n_{L-\max} - 1\right)\right) + O\left(n_S\right) \\
&= O(1) + O\left(n_S\right) + 2 \cdot O\left(m\right) + O\left(m \cdot \log_2 m\right) \sim O\left(n_S\right) + O\left(m\right) + O\left(m \cdot \log_2 m\right) \\
&= O\left(n_S\right) + O\left(m + m \cdot \log_2 m\right) = O\left(n_S\right) + O\left(m \cdot \left(1 + \log_2 m\right)\right) \\
&\sim O\left(n_S\right) + O\left(m \cdot \log_2 m\right) = O\left(n_S + m \cdot \log_2 m\right) \\
&= O\left(n_S + \left(n_{L-\max} - 1\right) \cdot \log_2\left(n_{L-\max} - 1\right)\right) \sim O\left(n_S + n_{L-\max} \cdot \log_2 n_{L-\max}\right)
\end{aligned}
\tag{4.95}
$$

At this level, it is interesting to highlight that the derived inhomogeneous algorithm of Figure 4.23 can be used to automatically emulate a host of wireless network applications contained within a disk-shaped lattice. In particular, it could be appropriate for stochastically mapping the spatial configuration of: WSN, WMN, or cellular networks. Indeed, each of these networks has a particular purpose and application focus. For instance, WSN is considered for low-power remote sensing; WMN is rather a multihop topology used for range extension or as a backup connectivity route; and cellular networks are aimed for ubiquitous long-range mobile communications [70]. In Table 4.4, the distinctive characteristics of these networks are accordingly outlined.

Furthermore, these featured wireless networks are generally composed of variable-sized scale. For example, the volume of nodes in a WSN is for the most part way lager than a WMN because point sensors are typically cheaper to fabricate. Specifically, the scale of a WSN is somewhere in the order of hundreds up to thousands, and could in extreme cases reach millions of nodes [42], [71]. Irrespective of the quantity of nodes to be deployed, the formulated inhomogeneous random network algorithm is scalable for the emulation scenario under study. Given that the algorithm supports diverse spatial geometries, we will therefore demonstrate the scalability aspect by generating various heterogeneous random realizations of the network.

Table 4.4 – On the specifications and characteristics of different wireless networks

network applications	communication range	P2MP network topology	examples of technologies	principal feature
WSN	meters	LR-WPAN	ZigBee, 6LoWPAN WirelessHART MiWi, LR-UWB	low-power sensor commuications
WMN	meters	WPAN WLAN	UWB, Bluetooth Wi-Fi	high-speed commuications
cellular network	kilometers	WMAN WWAN	MBWA, WiMAX LTE	long-range commuications

In Figure 4.24, we show four random instances of a small-scale heterogeneous random deployment. Within these results, in addition to the actual spatial deployment, the network plan is separately graphed so as to emphasize its arbitrary nature. In other words, the planning of the network, which is assembled by the number of layer, the deployment size, and the geometry of nodes, is randomly obtained in an automatic way at every simulation run.

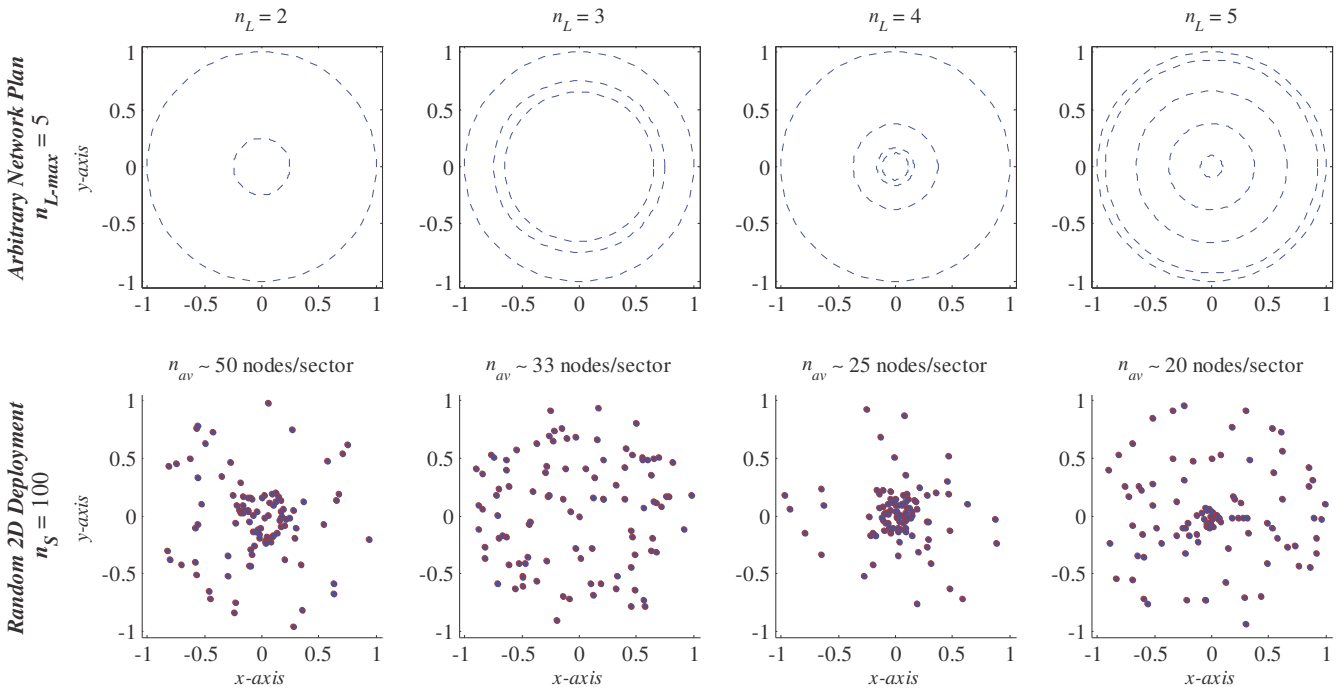

Figure 4.24 – Random instances of small-scale heterogeneous network deployment

Similarly, in Figure 4.25, we demonstrate another set of examples for a medium-scale network. Again, each run of the simulation produces a unique inhomogeneous random spatial realization.

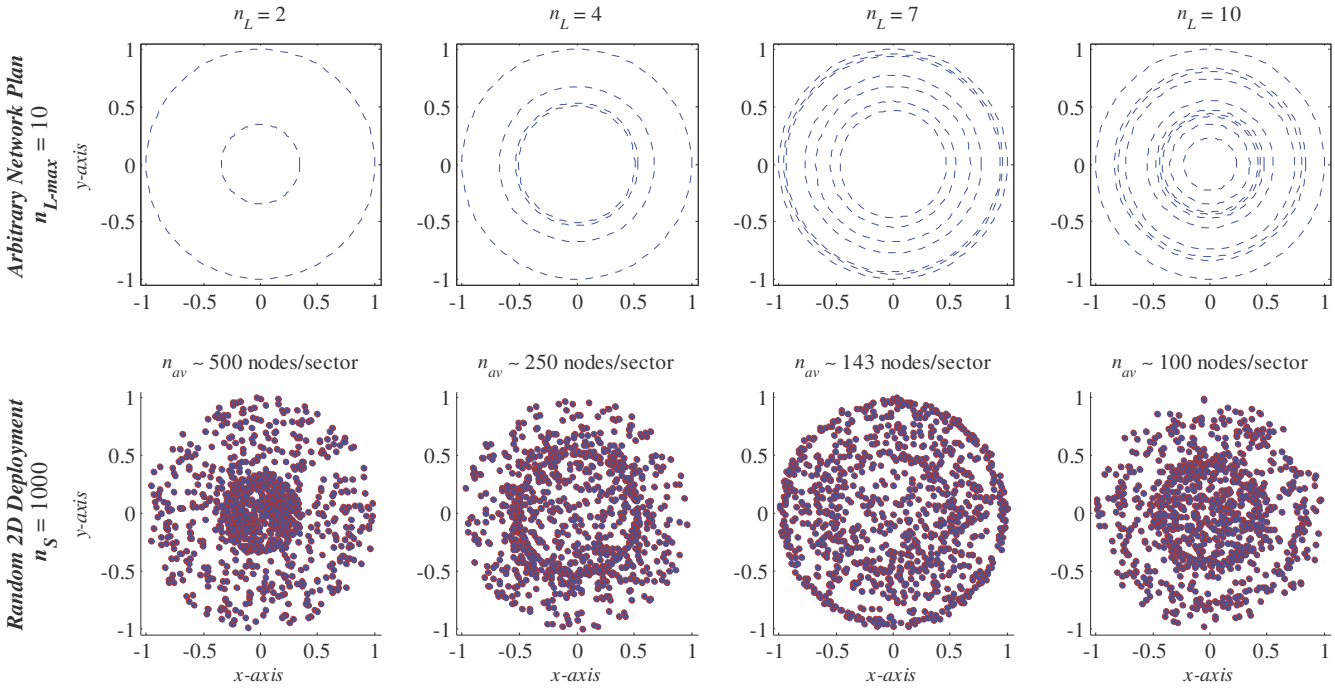

Figure 4.25 – Random instances of medium-scale heterogeneous network deployment

As a final representative example, a large-scale model for the network is emulated in Figure 4.26. Because the scale is relatively elevated when compared to the other two cases, as illustrated by this MC simulation, the geometrical resolution of each node is reduced.

It is valuable to note that in emulating an uncontrolled inhomogeneous architecture, there is no particular interconnection, linear or otherwise, between the inputted maximum number of deployment layers and the network scale; unless such relation is intentionally assumed by the designer. From Table 4.5, which essentially summarizes the considered inputs to the network instances generated in Figures 4.24, 4.25 and 4.26, we in fact hypothesized such correlation between the supplied variables. That is, for the three network cases, as $n_{L-\max}$ increased, by design the network scale n_S also rose.

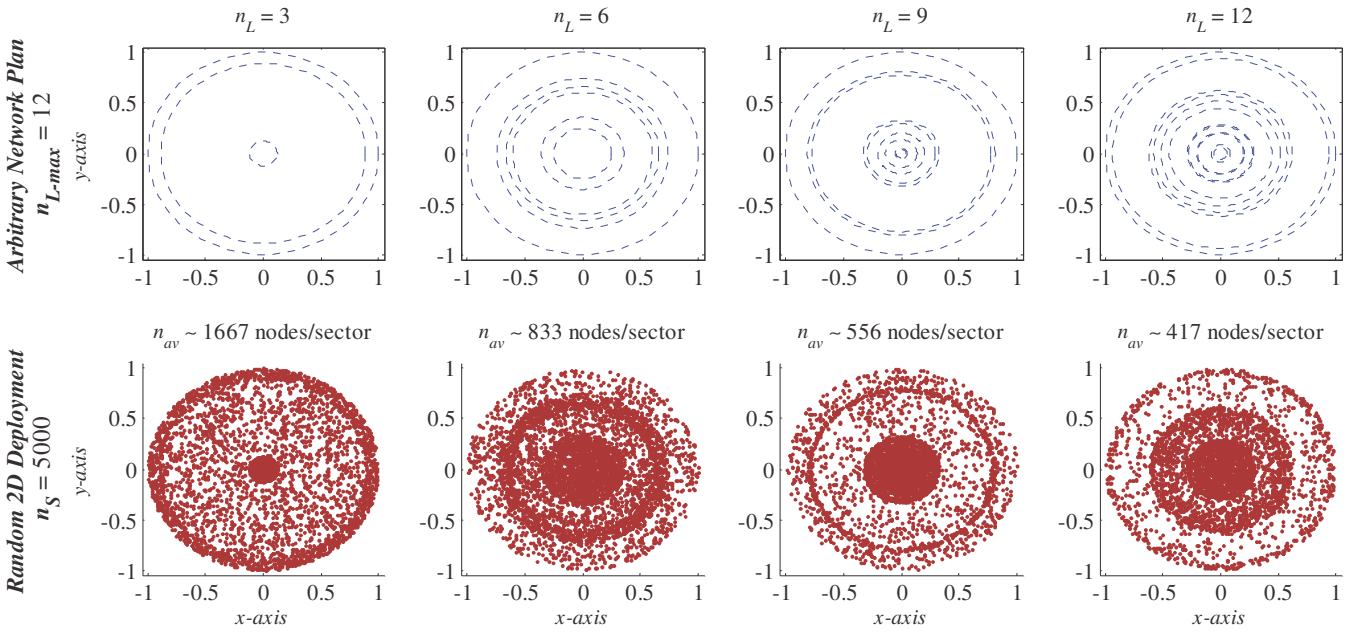

Figure 4.26 – Random instances of large-scale heterogeneous network deployment

Although there is no explicit association among $n_{L-\max}$ and n_S; yet on the other hand, we notice a symbiotic relationship between $n_{L-\max}$ and the degree of network inhomogeneity that requires some carefully calculated scrutiny. To be precise, the direct interdependence with $n_{L-\max}$ and the random number of layers is indicated in (4.89). And, as n_L increases, the amount of random sized sub-regions will straightforwardly augment. Assuming from (4.84) that the number of nodes per sector remains steady; consequently, the quantity of layers with unique densities will also rise. Thus, for all practical purposes, it is projected that $n_{L-\max}$ affects the inhomogeneity of a random network constellation. However, more research work is required in order to describe the interplay between $n_{L-\max}$ and its significance on the geometrical heterogeneity of a random graph.

Table 4.5 – Simulation inputs used for generating a random inhomogeneous UCN

network models	L (unit)	$n_{L-\max}$ (no.)	n_S (no.)
small-scale	1	5	100
medium-scale	1	10	1,000
large-scale	1	12	5,000

4.5 – Modeling a Large Multi-Cellular Spatial Network

4.5.1 – Motivation and Background

In earlier parts, it was noted that the actual BS coverage has an irregular contour due to antenna radiation and channel impairments. To overcome this unpredictability of the cellular geometrical structure, it was asserted that the ideal disk-shaped circular profile is a feasible and instinctive model for the purpose of UCN analysis and spatial emulation. Indeed, this configuration is mainly relevant for mapping scarcely distributed mobile users that are typically set in a suburban environment.

In the event that it is desired to supply wireless network service for a broad urban-based geographical region containing a high-density of users, then a large UCN will be inappropriate. As a practical substitute, a MCN assembled by a number of contiguously positioned smaller cells is rather preferred[5]. In order to put together such MCN architecture, tessellating cells are needed; thus implying that the circular model will be unsuitable due to its noncompliant layout. Therefore, as premised and quantified in Table 2.1, the hexagonal shape is rationally the leading cellular model of choice because it closely resembles the circular lattice while still remaining compatible for the MCN objective.

In fact, various research works have considered spatial deployment in a hexagonal cell model under a homogeneous profile, e.g. [26]–[30]. However, to the best of our knowledge, the random generation approach was not explicitly and thoroughly specified in any of these or other contributions; thus leading us to believe that perhaps a heuristic method was applied to artificially produce a random network pattern. In other words, emulation used for analysis of complex mobile systems is not obtained from accurate stochastical models, but is rather realized synthetically via selective sampling. And certainly, such simplification measures completely dissolve and defeat the true randomness and purpose sought by the MC simulation process.

In light of this revelation, we thus clearly perceive the technical effort needed for improving and advancing the emulation of these network models. Namely, even though the cellular concept has tangibly existed for over thirty years, and despite the wide use and practicality of probabilistic emplacement, it is astonishing to note that no detailed algorithm is available in literature for unbiased random nodal deployment in hexagon-based models. As a

[5] Some of the key advantages and challenges of such configuration were noted in Chapter 2 of this dissertation.

consequence, in this section, we aim to meticulously derive from first principle the exact stochastic expressions necessary for emulating random network models enclosed by diverse tessellating geometries for non-sectored and sectored hexagonal lattices. These analytical statements will then be modulated into algorithm format so as to be used for the anticipated heterogeneous random deployment of mobile nodes.

To emphasize, the outcomes to be obtained from rigorous analysis for random dispersion in a honeycomb grid, as well as its sectored counterparts, will serve as essential building blocks for formulating the spatial inhomogeneity of a MCN. In fact, this heterogeneous generation approach is founded on the ASD principle, which is literally based on dividing the deployment surface into smaller sub-regions, analyzing each separately, and then synthesizing the results. Overall, the spatial emulator to be developed in this section is expected to serve as a useful modeling mechanism for exploring the various QoS metrics of a random MCN.

4.5.2 – Exact Stochastic Generation in a Hexagonal Lattice

The aim of this part is to stochastically derive an approach for distributing random nodes inside a hexagonal cell. One possibility to perform this duty would be to consider arbitrary deployment in a circular cell by the use of the analysis conducted in Section 4.2. However, this process will specifically produce an unfair nodal density at the edges of the non-circular contour. Therefore to adjust this aspect, a simple heuristic rule can be integrated in the simulation code in order to take into account the geometrical profile of the border. Nonetheless, this technical rectification method used to handle the edges of the tessellating cell will actually corrupt the wanted randomness of the generation. For this reason, we will here derive the exact RNG technique required for nodes spatial deployment inside a hexagonal cell.

For the sake of analysis, and perhaps from an intuitive modeling perspective, we assume that randomly located users are homogeneously spread over the coverage area $A_H \in \mathbb{R}_+^*$ of a hexagonal lattice with side length $L \in \mathbb{R}_+^*$ depicted in Figure 4.27. This surface area is in fact determined by:

$$A_H = \iint_{(x,y)\in D_H \subset \mathbb{R}^2} dA = 3\sqrt{3}L^2/2 \approx 2.598L^2 \tag{4.96}$$

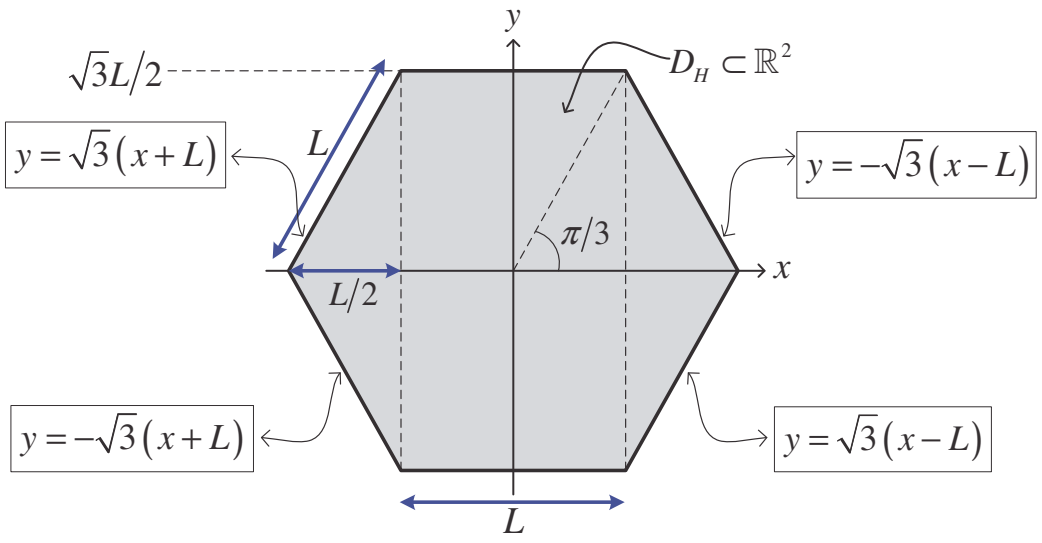

Figure 4.27 – Deployment surface of the hexagonal lattice

such that D_H is the corresponding deployment domain which can compactly be represented by:

$$D_H = \left\{ \begin{matrix} (x,y)\in\mathbb{R}^2; \\ L\in\mathbb{R}_+^* \end{matrix} \middle| \begin{matrix} |y|\le\sqrt{3}\left(L-|x|\right):\ L/2\le|x|\le L \\ |y|\le\sqrt{3}L/2:\ |x|\le L/2 \end{matrix} \right\} \tag{4.97}$$

From (4.96) and (4.97), the homogeneous spatial density can readily be obtained as follows:

$$f_{XY}(x,y) = 1/A_H = 2/3\sqrt{3}L^2 \quad (x,y)\in D_H \subset \mathbb{R}^2 \tag{4.98}$$

Next, using (4.98), we can derive the marginal PDF along the *x*-axis by:

$$\begin{aligned} f_X(x) &= \int_{(x,y)\in D_H} f_{XY}(x,y)\,dy \\ &= \frac{2}{3\sqrt{3}L^2}\left\{ \begin{matrix} [y]_{|y|\le\sqrt{3}(x+L)}\cdot\mathbf{1}(-L\le x\le -L/2) \\ +[y]_{|y|\le\sqrt{3}L/2}\cdot\mathbf{1}(|x|\le L/2)+[y]_{|y|\le\sqrt{3}(L-x)}\cdot\mathbf{1}(L/2\le x\le L) \end{matrix} \right\} \\ &= \{2/3L\}\cdot\mathbf{1}(|x|\le L/2)+\{4(L-|x|)/3L^2\}\cdot\mathbf{1}(L/2\le|x|\le L) \end{aligned} \tag{4.99}$$

Also, via the use of (4.99), and following several manipulations, the marginal CDF is derived:

$$\begin{aligned} F_X(x) &= \Pr(X \le x) = \int_{\tilde{x}=-\infty}^{x} f_X(\tilde{x})\, d\tilde{x} \\ &= \left\{2(1+x/L)^2/3\right\} \cdot \mathbf{1}(-L \le x \le -L/2) \\ &\quad + \left\{2x/3L + 1/2\right\} \cdot \mathbf{1}(|x| \le L/2) + \left\{1-2(1-x/L)^2/3\right\} \cdot \mathbf{1}(L/2 \le x \le L) \end{aligned} \tag{4.100}$$

In Figure 4.28, we provide a generic plot for the CDF of (4.100). Also, this graph demonstrates the approach for random generation, provided the ICDF is explicitly reachable by the fact that:

$$\hat{x} = \left\{(F_X)^{-1}(\hat{u} \sim \mathcal{U}(0,1))\right\} \sim f_X(x) \tag{4.101}$$

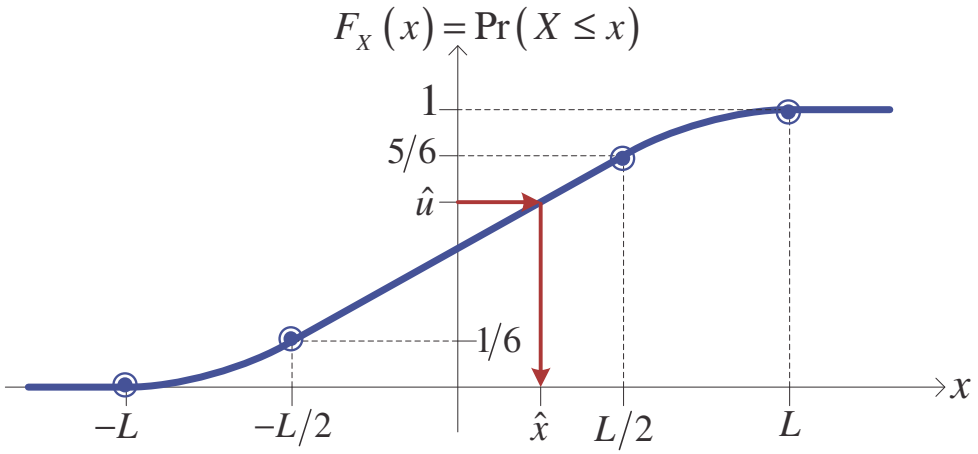

Figure 4.28 – Marginal CDF for hexagonal random network geometry along the *x*-axis

The ICDF is indeed invertible and is equal to:

$$\begin{aligned} \hat{x} = \hat{x}(\hat{u}, L) &= \left\{L\left(\sqrt{3\hat{u}/2} - 1\right)\right\} \cdot \mathbf{1}(0 \le \hat{u} \le 1/6) + \left\{3L(2\hat{u}-1)/4\right\} \cdot \mathbf{1}(1/6 \le \hat{u} \le 5/6) \\ &\quad + \left\{L\left(1 - \sqrt{3(1-\hat{u})/2}\right)\right\} \cdot \mathbf{1}(5/6 \le \hat{u} \le 1) \end{aligned} \tag{4.102}$$

To verify the accuracy and effectiveness of this random generator, we performed MC experimentation based on $n_S = 15{,}000$ samples for different cellular sizes. As shown in Figure 4.29, the theoretical and the randomly generated PDF estimation with $n_B = 150$ are in agreement; thus implying the correctness of the above analysis.

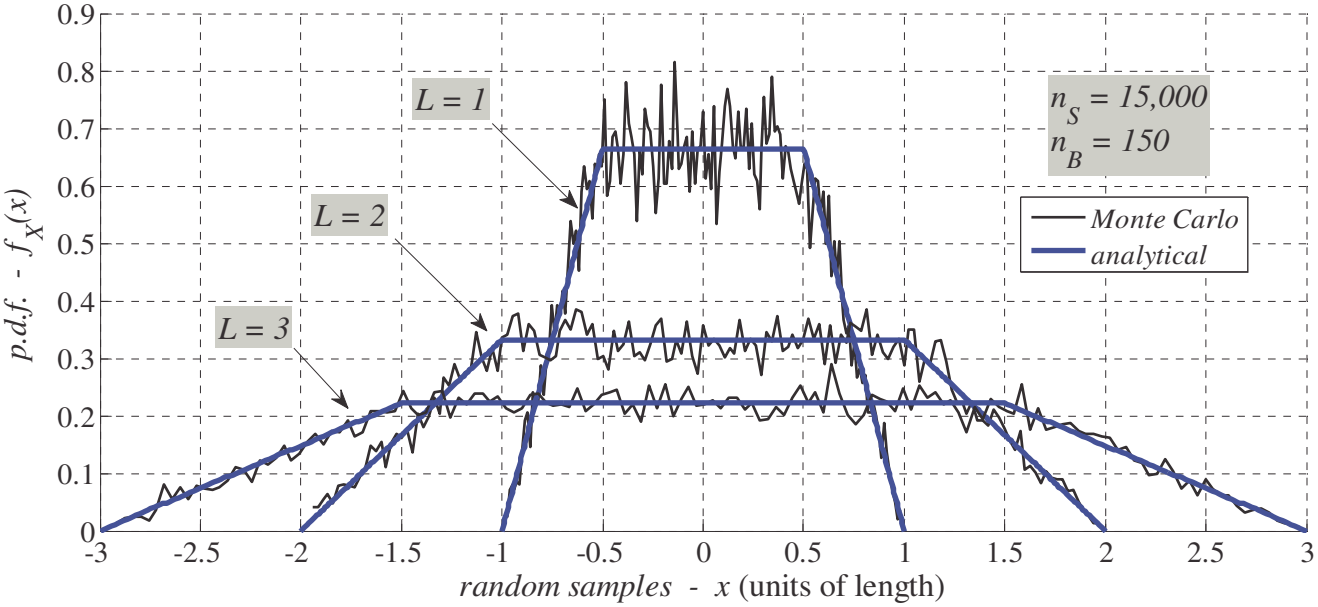

Figure 4.29 – Marginal PDF of nodal geometry for a hexagonal network along the *x*-axis

At this level, we could also determine the marginal PDF along the *y*-axis. To facilitate this task, we should first change the deployment domain of (4.97) as a function of the *x*-variable. After several careful manipulations, we get the elegant notation of (4.103). Although this expression appears simpler, yet we should underscore that both (4.97) and (4.103) refer to the same exact Euclidian domain; except each is seen from a different vantage point.

$$D_H = \left\{ (x,y) \in \mathbb{R}^2 ; L \in \mathbb{R}_+^* \;\middle|\; |x| \le L - |y|/\sqrt{3} :\; 0 \le |y| \le \sqrt{3}L/2 \right\} \tag{4.103}$$

With the direction of (4.103), we can now compute the desired marginal density function:

$$f_Y(y) = \int_{(x,y)\in D_H} f_{XY}(x,y)\,dx = \frac{4}{3\sqrt{3}L^2}\left(L - |y|/\sqrt{3}\right)\cdot \mathbf{1}\left(0 \le |y| \le \sqrt{3}L/2\right) \tag{4.104}$$

Clearly, the stochastic correlation between the random coordinates of a deployed node is expected due to the nature of the honeycomb structure. Nonetheless, we can analytically establish this interconnectedness by applying the stochastical test $f_{XY}(x,y) \neq f_X(x) \cdot f_Y(y)$ while considering the geometrical densities of (4.98), (4.99) and (4.104).

Evidently, in comparison to the random disk model explored in Section 4.2, analysis for the hexagonal spatial deployment is relatively involved. In essence, the inherent advantage of the UCN model is due to the fact that the radial and angular PDFs are statistically disconnected; thus facilitating the geometrical generation. On the other hand, as mentioned earlier, an important drawback of this postulation for MCN emulation is related to its non-tessellating geometry.

In view of the interdependence among the RVs for a hexagonal network, and assuming that we begin by randomly generating $\hat{x}$ from (4.102), then the following step requires us to characterize the conditional PDF along the *y*-axis as follows:

$$f_Y(y|x) = f_{XY}(x,y) / f_X(x) = f_{Y|X=\hat{x}}(y) = f_{XY}(\hat{x},y) / f_X(\hat{x}) \tag{4.105}$$

After carefully inserting (4.98) and (4.99) into the expression of (4.105), we then obtain:

$$\begin{aligned} f_{Y|X=\hat{x}}(y) = {} & \frac{1}{\sqrt{3}L} \cdot \mathbf{1}\left(|\hat{x}| \le L/2;\ |y| \le \sqrt{3}L/2\right) \\ & + \frac{1}{2\sqrt{3}\left(L - |\hat{x}|\right)} \cdot \mathbf{1}\left(L/2 \le |\hat{x}| \le L;\ |y| \le \sqrt{3}\left(L - |\hat{x}|\right)\right) \\ & = \mathcal{U}_Y\left(-\sqrt{3}L/2, \sqrt{3}L/2\right) \cdot \mathbf{1}\left(|\hat{x}| \le L/2\right) \\ & \quad + \mathcal{U}_Y\left(-\sqrt{3}\left(L - |\hat{x}|\right), \sqrt{3}\left(L - |\hat{x}|\right)\right) \cdot \mathbf{1}\left(L/2 \le |\hat{x}| \le L\right) \end{aligned} \tag{4.106}$$

The overall approach for exact random spatial generation inside a hexagonal cell is specified in the algorithm of Figure 4.30. The spatial interpretation of this non-synthetic formulation is manifested in Figure 4.31 over different network scales. For these random networks, it is interesting to notice how perfectly the cell boundaries are respected.

Algorithm 10 - Random Deployment for a Hexagonal Network

Require: $n_S \in \mathbb{N}^* \quad L \in \mathbb{R}_+^*$
for $i = 1, 2, \cdots, n_S$ **do**
  Generate two i.i.d. RVs: $\{\hat{u}_0, \hat{u}_1\} \sim \mathcal{U}(0,1)$
  if $\{0 \le \hat{u}_0 \le 1/6\}$ **then**
    Compute: $\hat{x}_i \coloneqq L\left(\sqrt{3\hat{u}_0/2} - 1\right) \sim f_X(x)$
  else if $\{1/6 \le \hat{u}_0 \le 5/6\}$ **then**
    Compute: $\hat{x}_i \coloneqq 3L\left(2\hat{u}_0 - 1\right)/4 \sim f_X(x)$
  else if $\{5/6 \le \hat{u}_0 \le 1\}$ **then**
    Compute: $\hat{x}_i \coloneqq L\left(1 - \sqrt{3(1-\hat{u}_0)/2}\right) \sim f_X(x)$
  end if
  if $\{|\hat{x}_i| \le L/2\}$ **then**
    Compute: $\hat{y}_i \coloneqq \sqrt{3}L\left(\hat{u}_1 - 1/2\right) \sim \mathcal{U}_Y\left(-\sqrt{3}L/2, \sqrt{3}L/2\right)$
  else if $\{L/2 \le |\hat{x}_i| \le L\}$ **then**
    Compute: $\hat{y}_i \coloneqq \sqrt{3}\left(L - |\hat{x}_i|\right)\left(2\hat{u}_1 - 1\right) \sim \mathcal{U}_Y\left(-\sqrt{3}\left(L - |\hat{x}_i|\right), \sqrt{3}\left(L - |\hat{x}_i|\right)\right)$
  end if
end for
Return: $\{\hat{x}_i, \hat{y}_i\} : i = 1, 2, \cdots, n_S$

Figure 4.30 – Pseudocode for spatial random deployment within a hexagonal lattice

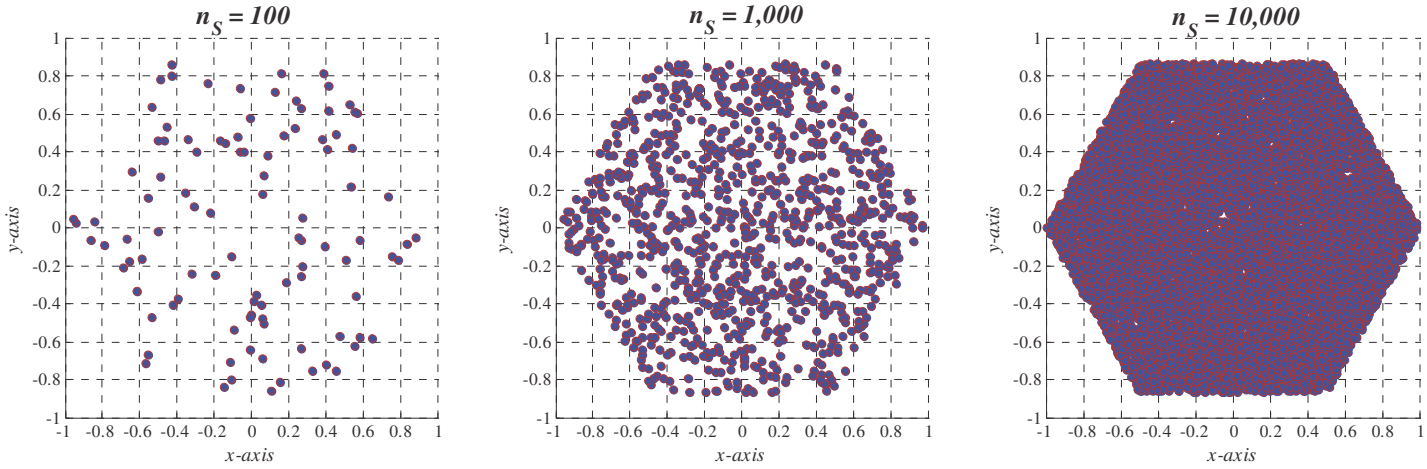

Figure 4.31 – Random hexagonal networks

4.5.3 – Exact Random Nodal Dispersion in Sectored Cells

At this level, we are interested to derive the method for random deployment in sectored regions of a cell. But before carrying on this RNG analysis, we find it necessary to promptly revisit and discuss the major technical implications of cellular sectoring. Fundamentally, cellular sectoring by the use of directional antennas is frequently implemented in mobile networking in order to mitigate the distorting impact of co-channel interference [47]–[49]. However, this crucial benefit is obtained at the expense of a number of challenges, among them:

- Traffic Intensity per Sector: Sectoring lowers the traffic intensity, thus accommodating less channel-demanding active users. Precisely, 60˚ are worse than 120˚ sectors since the portion of frequency channels per sector is lessened. Yet, because of the frequency reuse (FR) principle, the deployment coverage will have a wider reach. Hence, the overall number of users throughout the MCN will still rise without the need of extra spectrum.
- Handover Capability: As the number of sectoring increases, the need for sophisticated handoff capability becomes more important for MSs that travel among these regions.
- Infrastructure Cost: cellular sectoring is achieved by means of directional antennas, which are generally more expensive to design and manufacture than omni-directional emitters. Also, sectoring requires more antennas per cell, thus increasing the overall cost.

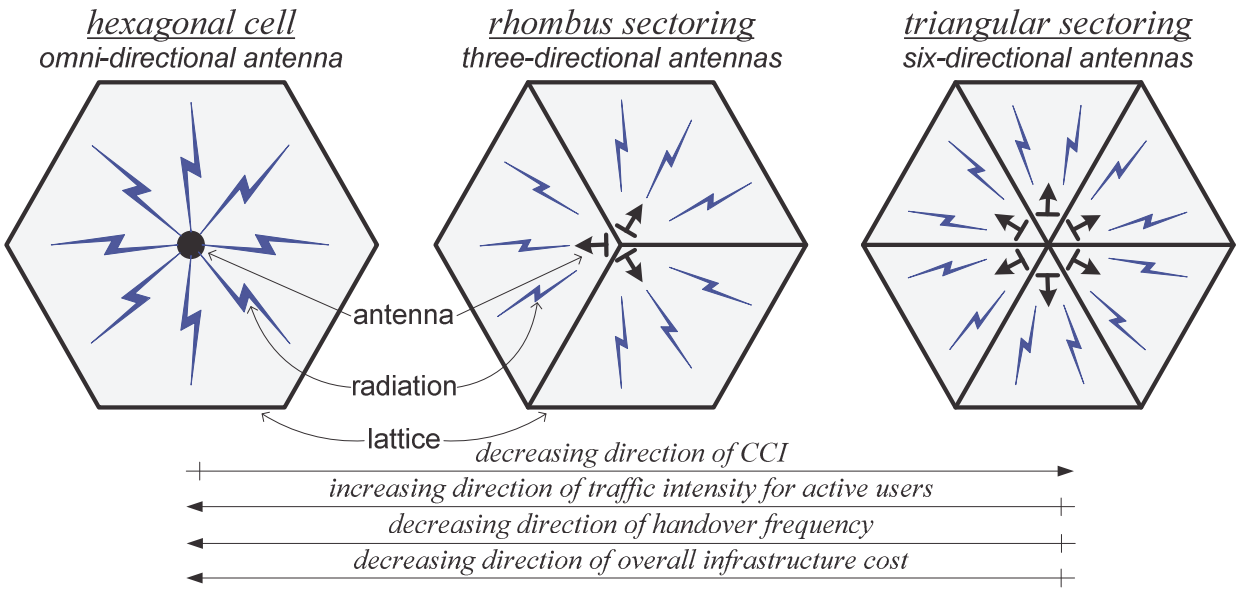

Figure 4.32 – Antenna radiation for unsectored and sectored cells

In Figure 4.32, we illustrated the radiation features for unsectored and sectored cells. Also, as shown by the arrows which point to the preferred direction, we visualized the conflicting engineering requirements for a host of network attributes. As a result, tradeoff analysis during the design process is required for each particular network deployment case.

In the previous subsection, the exact MC simulation approach for random position generation within the boundaries of a hexagonal cell was found. In this part, we will supplement this uncovering by deriving the precise random generation in rhombus and triangular sectors.

To describe the stochastical interpretation for random homogeneous spatial density over a rhombus region, we will consider the deployment surface of Figure 4.33.

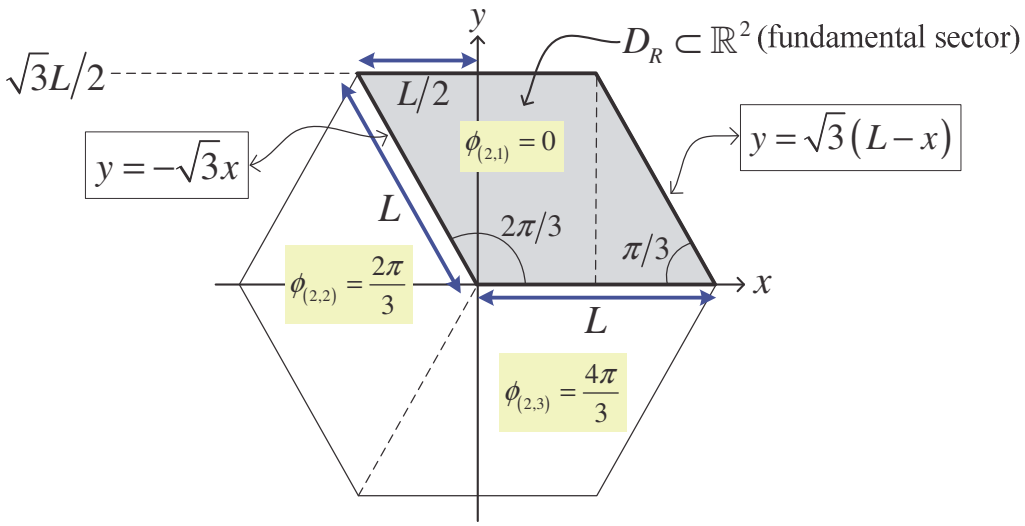

Figure 4.33 – Deployment surface of the rhombus lattice

The marked area is given by:

$$A_R = \iint_{(x,y)\in D_R \subset \mathbb{R}^2} dA = \sqrt{3}L^2/2 \approx 0.866L^2 \tag{4.107}$$

such that:

$$D_R = \left\{ \begin{matrix} (x,y)\in \mathbb{R}^2; \\ L\in \mathbb{R}_+^* \end{matrix} \middle| \begin{matrix} -\sqrt{3}x \le y \le \sqrt{3}L/2:\ -L/2 \le x \le 0 \\ 0 \le y \le \sqrt{3}L/2:\ 0 \le x \le L/2 \\ 0 \le y \le \sqrt{3}(L-x):\ L/2 \le x \le L \end{matrix} \right\} \tag{4.108}$$

From (4.107) and (4.108), we get the following spatial density:

$$f_{XY}(x,y) = 1/A_R = 2/\sqrt{3}L^2 \quad (x,y) \in D_R \subset \mathbb{R}^2 \tag{4.109}$$

Next, from (4.109), the marginal PDF can be computed:

$$\begin{aligned} f_X(x) = \int_{(x,y)\in D_R} f_{XY}(x,y)\,dy = &\left\{(2x+L)/L^2\right\}\cdot \mathbf{1}(-L/2 \le x \le 0) + \left\{1/L\right\}\cdot \mathbf{1}(0 \le x \le L/2) \\ &+ \left\{2(L-x)/L^2\right\}\cdot \mathbf{1}(L/2 \le x \le L) \end{aligned} \tag{4.110}$$

Then after, the marginal CDF of (4.110) is obtained:

$$\begin{aligned} F_X(x) = \Pr(X \le x) &= \int_{\tilde{x}=-\infty}^{x} f_X(\tilde{x})\,d\tilde{x} \\ &= \left\{(x/L+1/2)^2\right\}\cdot \mathbf{1}(-L/2 \le x \le 0) \\ &\quad + \left\{x/L+1/4\right\}\cdot \mathbf{1}(0 \le x \le L/2) + \left\{1-(x/L-1)^2\right\}\cdot \mathbf{1}(L/2 \le x \le L) \end{aligned} \tag{4.111}$$

From (4.111), we solve for the ICDF:

$$\begin{aligned} \hat{x} = \hat{x}(\hat{u},L) = &\left\{L\left(\sqrt{\hat{u}} - 1/2\right)\right\}\cdot \mathbf{1}(0 \le \hat{u} \le 1/4) \\ &+ \left\{L(\hat{u}-1/4)\right\}\cdot \mathbf{1}(1/4 \le \hat{u} \le 3/4) + \left\{L\left(1-\sqrt{1-\hat{u}}\right)\right\}\cdot \mathbf{1}(3/4 \le \hat{u} \le 1) \end{aligned} \tag{4.112}$$

If we simulate the above random generation, we obtain the PDF estimation result of Figure 4.34. Clearly the generated samples produce outcomes that are consistent with the analytical expression; thus ascertaining the correctness of the derivation.

At this stage, by (4.108), (4.109) and (4.110), we determine the conditional density along the y-axis:

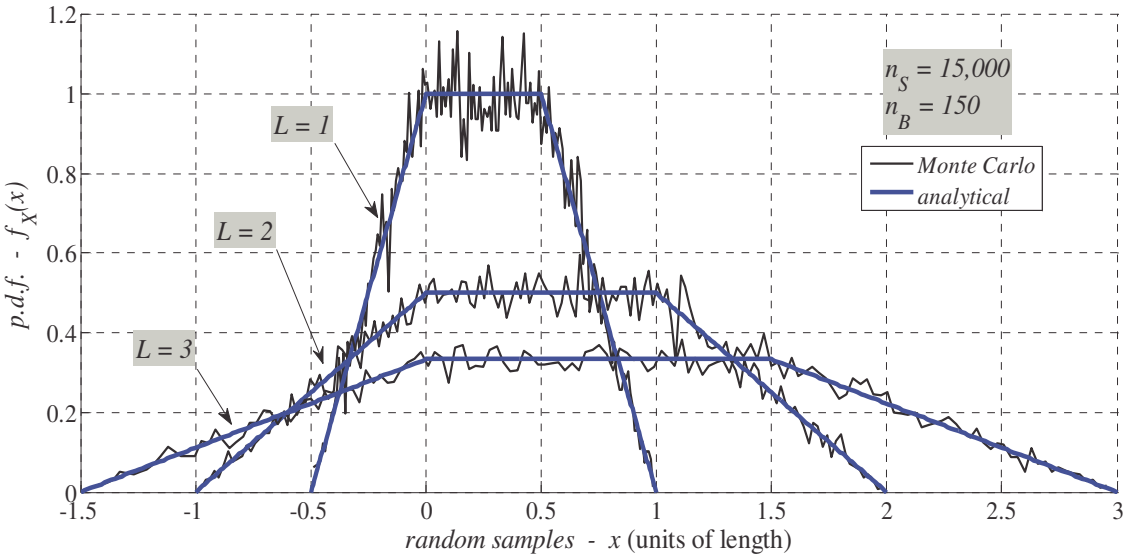

Figure 4.34 – Marginal PDF of nodal geometry for a rhombus network along the *x*-axis

$$f_{Y|X=\hat{x}}(y) = \mathcal{U}_Y\left(-\sqrt{3}\hat{x}, \sqrt{3}L/2\right)\cdot\mathbf{1}\left(-L/2 \le \hat{x} \le 0\right) + \mathcal{U}_Y\left(0, \sqrt{3}L/2\right)\cdot\mathbf{1}\left(0 \le \hat{x} \le L/2\right) + \mathcal{U}_Y\left(0, \sqrt{3}\left(L-\hat{x}\right)\right)\cdot\mathbf{1}\left(L/2 \le \hat{x} \le L\right) \quad (4.113)$$

In Figure 4.35, we randomly generated the nodal geometry for various network scales of the rhombus lattice. In fact, this graph was obtained by utilizing the outlined algorithm of Figure 4.36, which is actually based on the merger of the above formulated expressions. As it can be noted, the algorithm only requires two inputs, namely the size of the cell and the scale of the network. Similar to the observation made for hexagonal model, here too the MC results are within the delineation of the lattice.

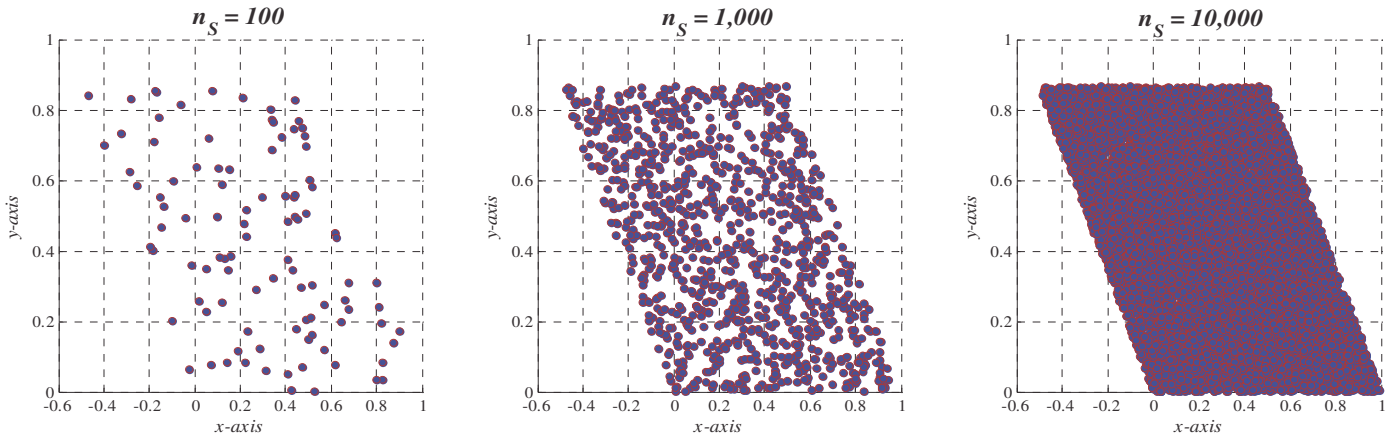

Figure 4.35 – Random rhombus networks

Algorithm 11 - Random Deployment for a Rhombus Network

Require: $n_S \in \mathbb{N}^* \quad L \in \mathbb{R}_+^*$
for $i = 1, 2, \cdots, n_S$ **do**
  Generate two i.i.d. RVs: $\{\hat{u}_0, \hat{u}_1\} \sim \mathcal{U}(0,1)$
  if $\{0 \le \hat{u}_0 \le 1/4\}$ **then**
    Compute: $\hat{x}_i := L\left(\sqrt{\hat{u}_0} - 1/2\right) \sim f_X(x)$
  else if $\{1/4 \le \hat{u}_0 \le 3/4\}$ **then**
    Compute: $\hat{x}_i := L\left(\hat{u}_0 - 1/4\right) \sim f_X(x)$
  else if $\{3/4 \le \hat{u}_0 \le 1\}$ **then**
    Compute: $\hat{x}_i := L\left(1 - \sqrt{1 - \hat{u}_0}\right) \sim f_X(x)$
  end if
  if $\{-L/2 \le \hat{x}_i \le 0\}$ **then**
    Compute: $\hat{y}_i := \sqrt{3}\left\{\hat{x}_i\left(\hat{u}_1 - 1\right) + L\hat{u}_1/2\right\} \sim \mathcal{U}_Y\left(-\sqrt{3}\hat{x}_i, \sqrt{3}L/2\right)$
  else if $\{0 \le \hat{x}_i \le L/2\}$ **then**
    Compute: $\hat{y}_i := \sqrt{3}L\hat{u}_1/2 \sim \mathcal{U}_Y\left(0, \sqrt{3}L/2\right)$
  else if $\{L/2 \le \hat{x}_i \le L\}$ **then**
    Compute: $\hat{y}_i := \sqrt{3}\hat{u}_1\left(L - \hat{x}_i\right) \sim \mathcal{U}_Y\left(0, \sqrt{3}\left(L - \hat{x}_i\right)\right)$
  end if
end for
Return: $\{\hat{x}_i, \hat{y}_i\} : i = 1, 2, \cdots, n_S$

Figure 4.36 – Pseudocode for spatial random deployment within a rhombus lattice

By the same token, the deployment surface for an equilateral triangular lattice is represented in Figure 4.37. The depicted area is equal to:

$$A_T = \iint_{(x,y) \in D_T \subset \mathbb{R}_+^2} dA = \sqrt{3}L^2/4 \approx 0.433L^2 \tag{4.114}$$

where the support domain is given by:

$$D_T = \left\{ \begin{matrix} (x,y) \in \mathbb{R}_+^2; \\ L \in \mathbb{R}_+^* \end{matrix} \middle| \begin{matrix} 0 \le y \le \sqrt{3}x: \ 0 \le x \le L/2 \\ 0 \le y \le \sqrt{3}(L - x): \ L/2 \le x \le L \end{matrix} \right\} \tag{4.115}$$

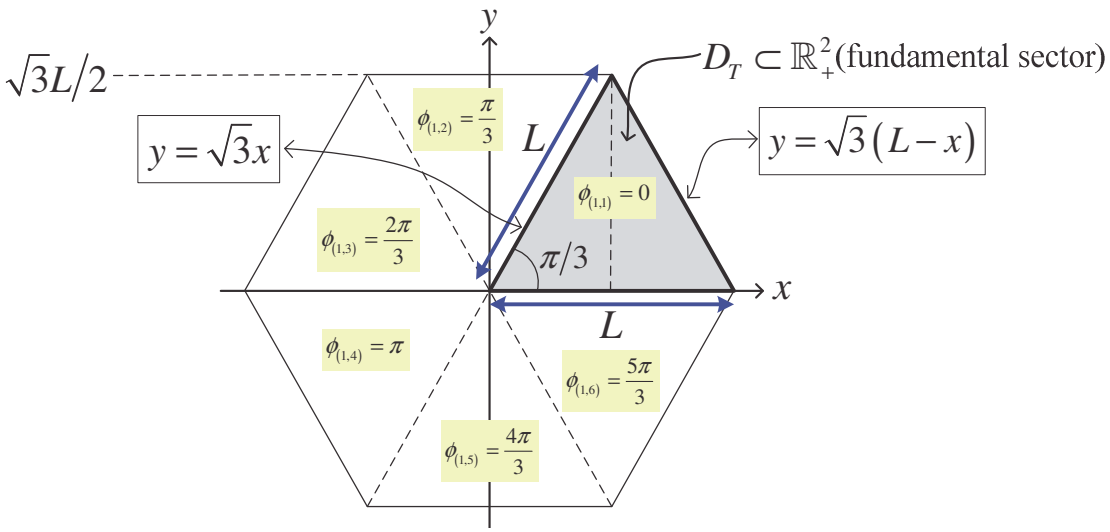

Figure 4.37 – Deployment surface of the triangular lattice

With this realization, we can acquire the corresponding spatial density function:

$$f_{XY}(x,y)=1/A_T=4/\sqrt{3}L^2 \quad (x,y)\in D_T\subset\mathbb{R}^2_+ \tag{4.116}$$

Next, by (4.116) we formulate the marginal PDF along the *x*-axis:

$$\begin{aligned} f_X(x) &= \int_{(x,y)\in D_T} f_{XY}(x,y)\,dy \\ &= \left\{4x/L^2\right\}\cdot\mathbf{1}(0\le x\le L/2)+\left\{4(L-x)/L^2\right\}\cdot\mathbf{1}(L/2\le x\le L) \end{aligned} \tag{4.117}$$

And, the marginal CDF is accordingly derived:

$$\begin{aligned} F_X(x) &= \Pr(X\le x)=\int_{\tilde{x}=-\infty}^{x} f_X(\tilde{x})\,d\tilde{x} \\ &= \left\{2(x/L)^2\right\}\cdot\mathbf{1}(0\le x\le L/2)+\left\{1-2(x/L-1)^2\right\}\cdot\mathbf{1}(L/2\le x\le L) \end{aligned} \tag{4.118}$$

If we solve for the ICDF, we then get:

$$\hat{x}=\hat{x}(\hat{u},L)=\left\{L\sqrt{\hat{u}/2}\right\}\cdot\mathbf{1}(0\le\hat{u}\le 1/2)+\left\{L\left(1-\sqrt{(1-\hat{u})/2}\right)\right\}\cdot\mathbf{1}(1/2\le\hat{u}\le 1) \tag{4.119}$$

In Figure 4.38, we tested the analyzed random generation over different cellular sizes. Definitely, we notice that the densities via MC simulations properly overlap the theoretical derivation of the marginal PDF.

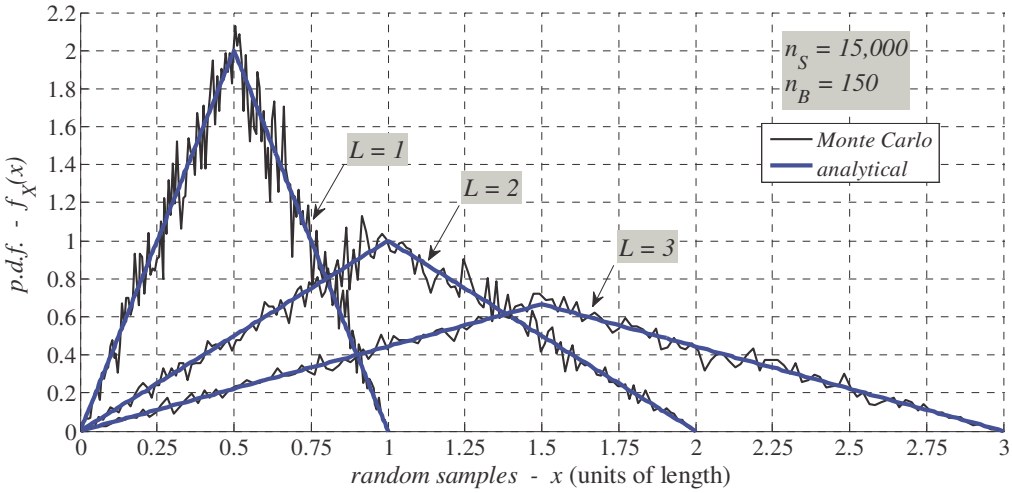

Figure 4.38 – Marginal PDF of nodal geometry for a triangular network along the *x*-axis

Now, using the statements in (4.115), (4.116) and (4.117), we find the conditional density:

$$f_{Y|X=\hat{x}}(y) = \mathcal{U}_Y\left(0,\sqrt{3}\hat{x}\right)\cdot\mathbf{1}\left(0\le\hat{x}\le L/2\right)+\mathcal{U}_Y\left(0,\sqrt{3}\left(L-\hat{x}\right)\right)\cdot\mathbf{1}\left(L/2\le\hat{x}\le L\right) \qquad (4.120)$$

Having these explicit stochastic notations, at presented, we simulated the various random networks of Figure 4.39 using the algorithm detailed in Figure 4.40. The experimental outcomes are further justifications to the performed analysis.

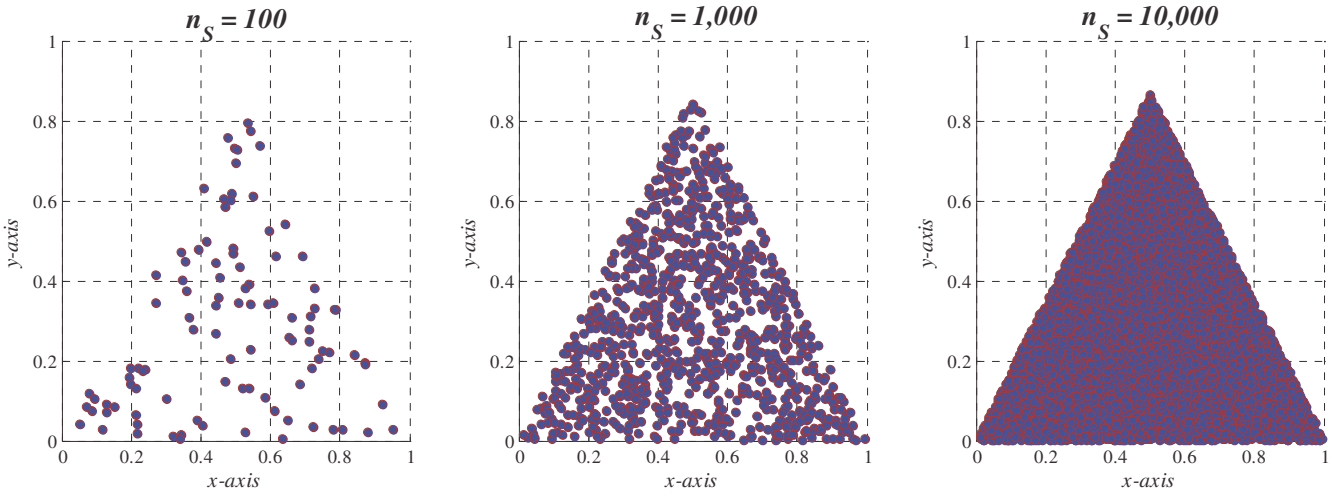

Figure 4.39 – Random triangular networks

Algorithm 12 - Random Deployment for a Triangular Network

Require: $n_S \in \mathbb{N}^* \quad L \in \mathbb{R}_+^*$
for $i = 1, 2, \cdots, n_S$ **do**
  Generate two i.i.d. RVs: $\{\hat{u}_0, \hat{u}_1\} \sim \mathcal{U}(0,1)$
  if $\{0 \le \hat{u}_0 \le 1/2\}$ **then**
    Compute: $\hat{x}_i := L\sqrt{\hat{u}_0/2} \sim f_X(x)$
  else if $\{1/2 \le \hat{u}_0 \le 1\}$ **then**
    Compute: $\hat{x}_i := L\left(1 - \sqrt{(1-\hat{u}_0)/2}\right) \sim f_X(x)$
  end if
  if $\{0 \le \hat{x}_i \le L/2\}$ **then**
    Compute: $\hat{y}_i := \sqrt{3}\hat{u}_1\hat{x}_i \sim \mathcal{U}_Y\left(0, \sqrt{3}\hat{x}_i\right)$
  else if $\{L/2 \le \hat{x}_i \le L\}$ **then**
    Compute: $\hat{y}_i := \sqrt{3}\hat{u}_1(L - \hat{x}_i) \sim \mathcal{U}_Y\left(0, \sqrt{3}(L - \hat{x}_i)\right)$
  end if
end for
Return: $\{\hat{x}_i, \hat{y}_i\} : i = 1, 2, \cdots, n_S$

Figure 4.40 – Pseudocode for spatial random deployment within a triangular lattice

4.5.4 – Geometrical Transformation of a Random Network

Before proceeding forward in the development of an inhomogeneous spatial algorithm for MCN, we must first formulate a number of geometrical tools useful for transforming a random network.

- **<u>Cluster Reflection</u>**: In Figure 4.41, we demonstrated three different ways for reflecting a random cluster; namely with respect to the: *x*-axis, *y*-axis, and origin.

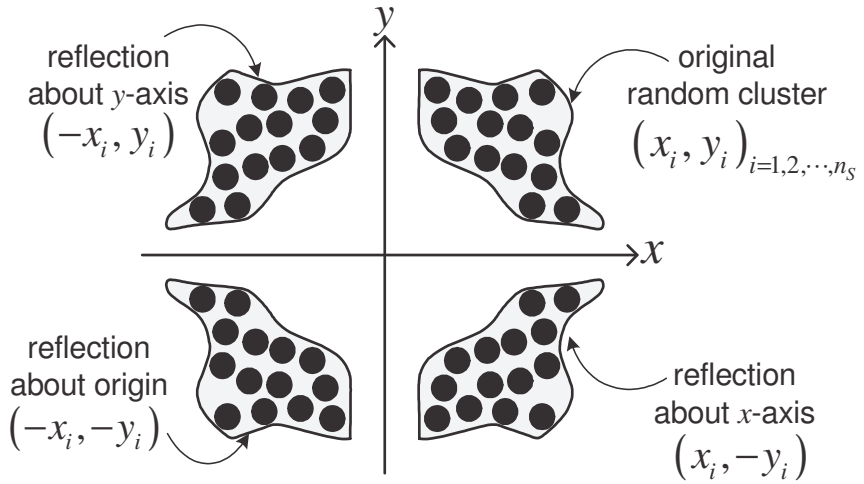

Figure 4.41 – Different perspectives for reflecting a random cluster

- **Cluster Rotation**: Consider Figure 4.42, where a random cluster is rotated about the origin of a Euclidian plane. In this model, a counterclockwise rotation results into a positive angle, i.e. $\phi \in \mathbb{R}^+$; otherwise, the angle will be negative. To determine the relation between the original coordinates $(x_i, y_i) \in \mathbb{R}^2$ of the random nodes, and the new positions $(\tilde{x}_i, \tilde{y}_i) \in \mathbb{R}^2$ obtained via rotation, the cluster should initially be characterized in polar format by the $(r_i, \theta_i) \in \mathbb{R}^2$ pair. After performing this task, we get:

$$\begin{bmatrix} \tilde{x}_i \\ \tilde{y}_i \end{bmatrix} = \begin{bmatrix} r_i \cos(\theta_i + \phi) \\ r_i \sin(\theta_i + \phi) \end{bmatrix} = \begin{bmatrix} r_i \{\cos(\theta_i)\cos(\phi) - \sin(\theta_i)\sin(\phi)\} \\ r_i \{\sin(\theta_i)\cos(\phi) + \cos(\theta_i)\sin(\phi)\} \end{bmatrix}$$

$$= \begin{bmatrix} \underbrace{r_i \cos(\theta_i)}_{=x_i} \cdot \cos(\phi) - \underbrace{r_i \sin(\theta_i)}_{=y_i} \cdot \sin(\phi) \\ \underbrace{r_i \sin(\theta_i)}_{=y_i} \cdot \cos(\phi) + \underbrace{r_i \cos(\theta_i)}_{=x_i} \cdot \sin(\phi) \end{bmatrix} = \begin{bmatrix} x_i \cdot \cos(\phi) - y_i \cdot \sin(\phi) \\ x_i \cdot \sin(\phi) + y_i \cdot \cos(\phi) \end{bmatrix}$$

$$= \begin{bmatrix} \cos(\phi) & -\sin(\phi) \\ \sin(\phi) & \cos(\phi) \end{bmatrix} \begin{bmatrix} x_i \\ y_i \end{bmatrix} \qquad i = 1, 2, \cdots, n_S$$

(4.121)

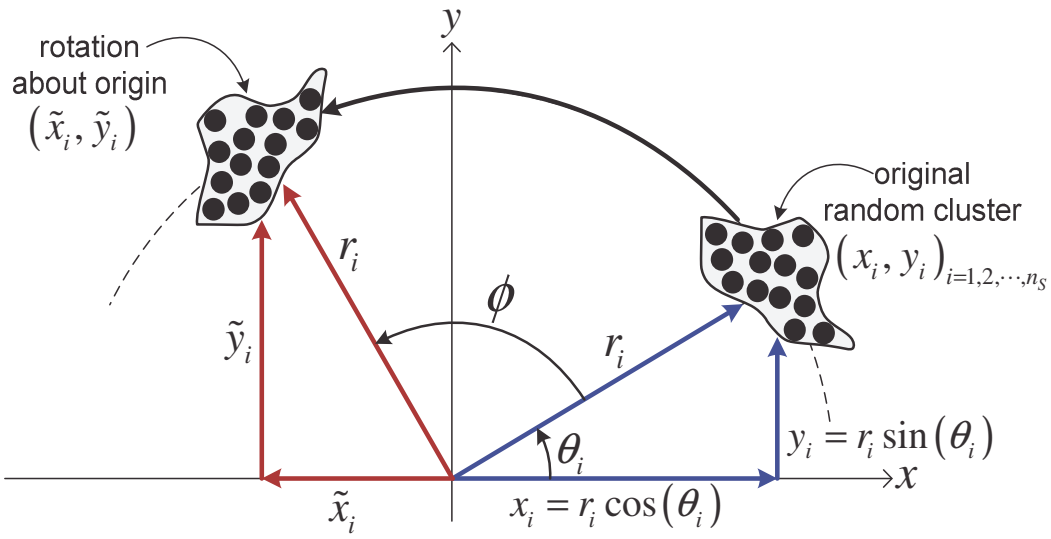

Figure 4.42 – Applying rotation to a random cluster

Certainly, the derived spatial emulation algorithms of Figures 4.36 and 4.40 for rhombus and triangular lattices are only valid in the fundamental sector that commences in the first quadrant of the Cartesian coordinate system. During MCN deployment, the rotation process of (4.121) is then required in order to relocate the random geometries in the appropriate sector within the cell. To facilitate this, the lattice models can be mapped to a numerical digit based on the following convention:

$$\left\{\begin{matrix}\text{triangular}\\ \text{rhombus}\\ \text{hexagonal}\end{matrix}\right\} \longleftrightarrow \left\{\begin{matrix}1\\ 2\\ 3\end{matrix}\right\} = \vec{l} \tag{4.122}$$

With this definition, the rotation angle $\phi_{(l,j)} \in \mathbb{R}^{+}$ of a random cluster for MCN modeling can generically be expressed by:

$$\phi_{(l,j)} = l \cdot \pi \cdot (j-1)/3 \qquad l = 1,2,3 \qquad j = 1,2,\cdots,6/l! \tag{4.123}$$

From this compact representation, the angular value for each sector can be obtained as explicitly shown in Figures 4.33 and 4.37.

In Figure 4.43, we performed a multi-density simulation of $n_S = 1{,}000$ random nodes per cell. In fact, the manner by which the terminals are partitioned is expressed in Table 4.6, where the rate of nodal quantity per cellular sector is obtained by:

$$\forall n_S \in \mathbb{N}^{*} : \exists n_j \in \mathbb{N}^{*} : r_j \triangleq n_j / n_S \qquad l = 1,2,3 \qquad j = 1,2,\cdots,6/l! \tag{4.124}$$

such that n_j is the portion of nodes inside the j-th sector out of the overall quantity n_S, and the obtained rate is limited by:

$$\left\{ r_j \in \mathbb{R}_{+}^{*} \;\middle|\; r_j \le 1 \right\} \tag{4.125}$$

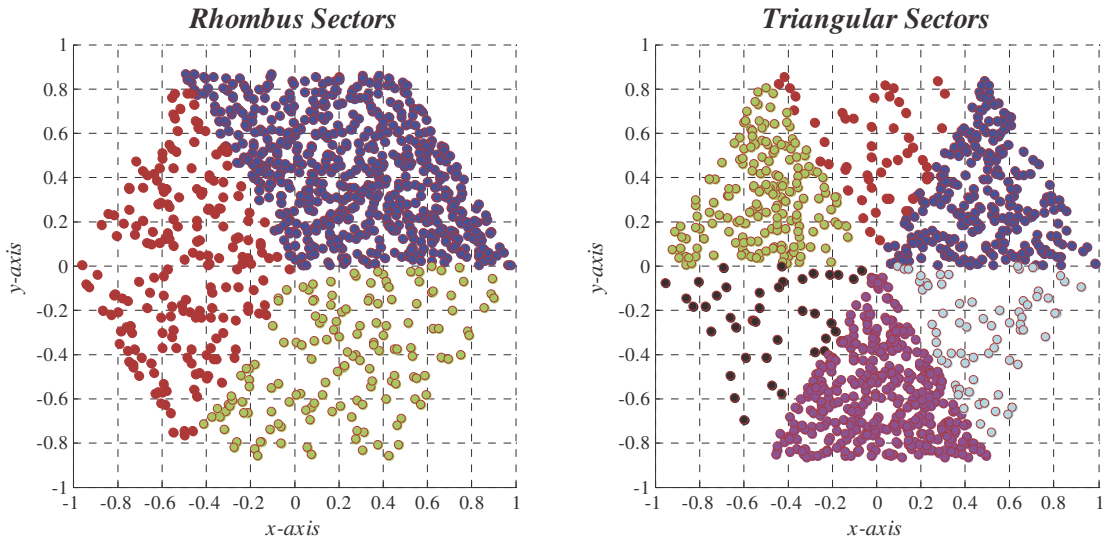

Figure 4.43 – Random network emulation with cellular sectoring

Table 4.6 – Rate of nodal quantity and areal density per cellular sector

no. of sectors	**rhombus sectors**		**triangular sectors**	
j	r_j	$\rho_A\left(\mathrm{k}/\mathrm{units}^2\right)$	r_j	$\rho_A\left(\mathrm{k}/\mathrm{units}^2\right)$
1	0.65	0.7506	0.26	0.6004
2	0.20	0.2309	0.05	0.1155
3	0.15	0.1732	0.19	0.4388
4	–	–	0.04	0.0924
5	–	–	0.39	0.9007
6	–	–	0.07	0.1617

- **<u>Cluster Scaling</u>**: Scaling the geometrical position of a node can be explained differently, but the most general characterization is of the following form:

$$\begin{bmatrix}\tilde{x}_i\\ \tilde{y}_i\end{bmatrix}=\begin{bmatrix}s_x & 0\\ 0 & s_y\end{bmatrix}\begin{bmatrix}x_i\\ y_i\end{bmatrix}=\begin{bmatrix}s_x x_i\\ s_y y_i\end{bmatrix} \qquad i=1,2,\cdots,n_S \tag{4.126}$$

where the entries of the diagonal scaling matrix are in $\mathbb{R}$. If for instance, we are interested to generate a densely or sparsely populated network, then we could assume a unique scaling factor $s\in\mathbb{R}_+^*$, and therefore (4.126) changes to:

$$\begin{bmatrix}\tilde{x}_i & \tilde{y}_i\end{bmatrix}^T = s\begin{bmatrix}x_i & y_i\end{bmatrix}^T \qquad i = 1,2,\cdots,n_S \tag{4.127}$$

In Figure 4.44, we display six example of $n_S = 500$ nodes randomly deployed in a square box of $[-1,1]^2$ dimensions. At every run of the generation, the nodes are accordingly remapped to their new positions by their corresponding scaling factor s. From the simulation results, we notice how the network areal density changes from highly dense to sparsely located deployment as the value of s is tuned. In other words, the generated random network is categorized by:

$$\begin{aligned} 0 < s < 1 &\leftrightarrow \textit{condense network} \\ s = 1 &\leftrightarrow \textit{unscaled network} \\ s > 1 &\leftrightarrow \textit{dispersed network} \end{aligned} \tag{4.128}$$

In fact, this occurs not because the volume of nodes vary, but because the deployment area is altered; thus changing the surface density $\rho_A = n_S / A_N$.

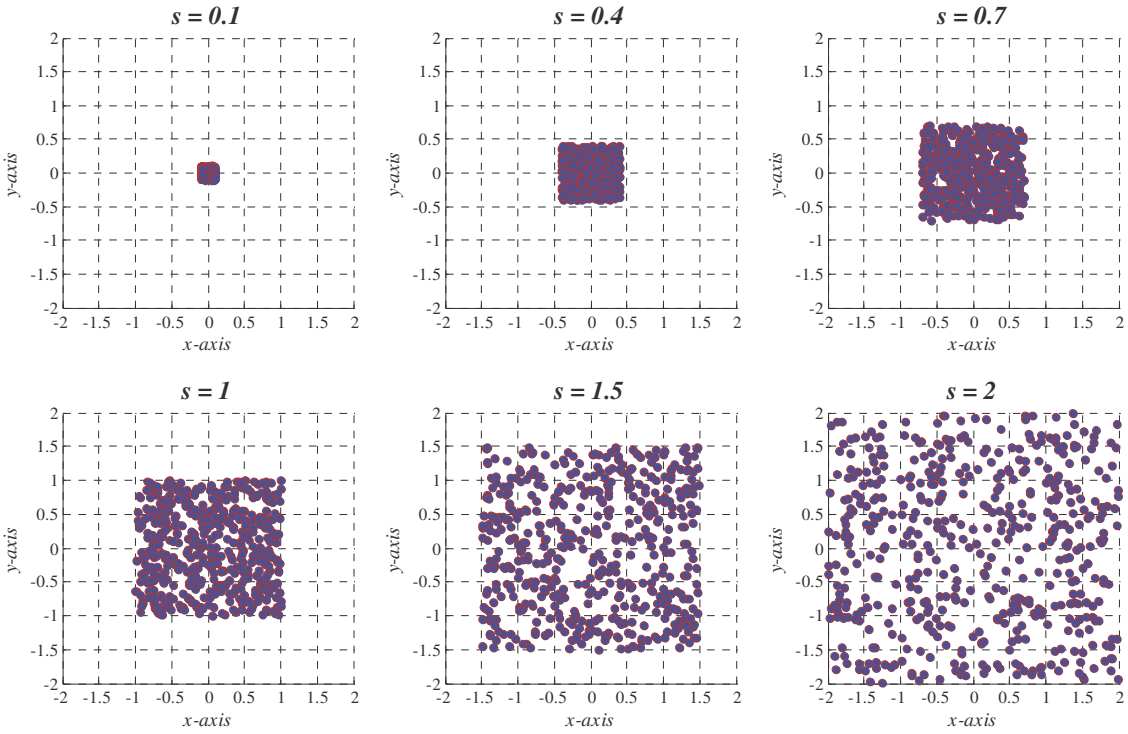

Figure 4.44 – Random networks as a function of different scaling values

- **Cluster Translation**: As shown in Figure 4.45, the translation of a random cluster is achieved by a shift along the x and y axes via $(h,k)\in\mathbb{R}^2$; the new positions are thus given by:

$$\begin{bmatrix}\tilde{x}_i\\ \tilde{y}_i\end{bmatrix}=\begin{bmatrix}x_i\\ y_i\end{bmatrix}+\begin{bmatrix}h\\ k\end{bmatrix}=\begin{bmatrix}x_i+h\\ y_i+k\end{bmatrix}\qquad i=1,2,\cdots,n_S \tag{4.129}$$

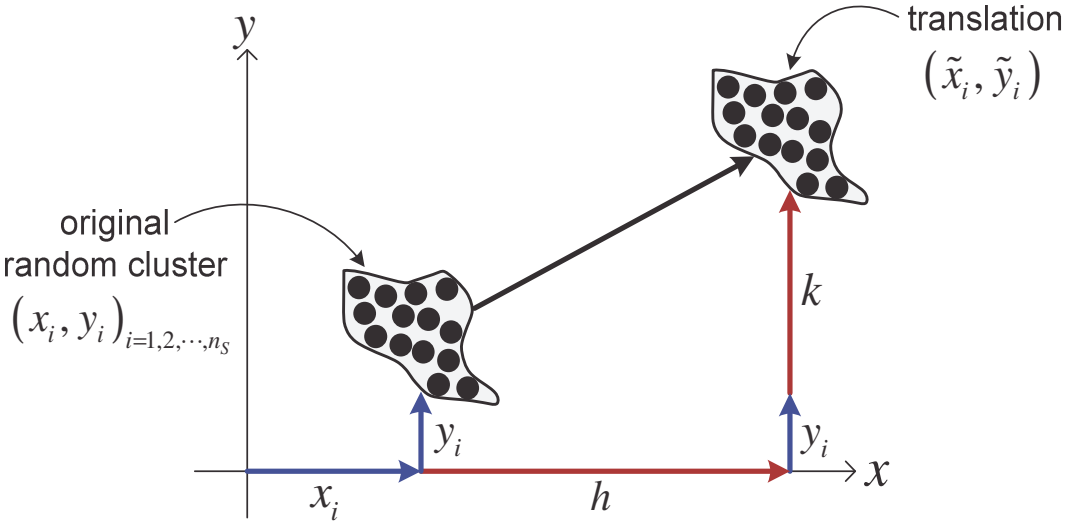

Figure 4.45 – Applying translation to a random cluster

All the manipulation tools formulated above for a random cluster can jointly and elegantly come together as expressed by:

$$\underset{2\times1}{\tilde{\mathbf{P}}_i}=\underset{2\times2}{\mathbf{S}_C}\ \underset{2\times2}{\mathbf{R}_C}\ \underset{2\times1}{\mathbf{P}_i}+\underset{2\times1}{\mathbf{T}_C}\qquad i=1,2,\cdots,n_S \tag{4.130}$$

where $\mathbf{P}_i$ and $\tilde{\mathbf{P}}_i$ are the original and new positions of a node within the cluster; and $\mathbf{R}_C$ is the rotation matrix, $\mathbf{S}_C$ is the scaling matrix, and $\mathbf{T}_C$ is the translation vector for a random cluster. For convenience, we expanded this compact representation by inserting (4.121), (4.126) and (4.129) into (4.130) in order to get:

$$\begin{bmatrix}\tilde{x}_i\\ \tilde{y}_i\end{bmatrix}=\begin{bmatrix}s_x & 0\\ 0 & s_y\end{bmatrix}\begin{bmatrix}\cos(\phi) & -\sin(\phi)\\ \sin(\phi) & \cos(\phi)\end{bmatrix}\begin{bmatrix}x_i\\ y_i\end{bmatrix}+\begin{bmatrix}h\\ k\end{bmatrix}$$
$$=\begin{bmatrix}s_x\left(x_i\cos(\phi)-y_i\sin(\phi)\right)+h\\ s_y\left(x_i\sin(\phi)+y_i\cos(\phi)\right)+k\end{bmatrix}\qquad i=1,2,\cdots,n_S \tag{4.131}$$

We could at this point make several noteworthy observations regarding the assembled generic expression of (4.131):

1. In Figure 4.41, the only reflection that can be obtained by rotation is the one performed about the origin; in particular, for this case $\phi=\pi$.

2. Alternatively, all three reflections can be achieved by setting the appropriate minus sign in the scaling matrix.

3. When a cluster is not intended for rotation, then $\phi=0$; and therefore, the rotation matrix will simplify to the identity matrix, i.e. $\mathbf{R}_C=\mathbf{I}_2$.

4. To model a multi-density deployment such as that shown in Figure 4.44, then the scaling matrix reduces to: $\mathbf{S}_C=s\cdot\mathbf{I}_2$.

Ultimately, for MCN emulation, we are interested to deploy wireless devices in a vast geographical area. Therefore, a cluster is initially generated via MC simulations about the origin of the coordinate system. Then, the random network is positioned in the proper location of the architecture footprint by the use of the geometrical manipulation tools formulated here.

4.5.5 – MCN Algorithm for Heterogeneous Random Deployment

In this section, we obtained exact expressions for random nodal deployment surrounded by tessellating forms identified by hexagonal, rhombus, and triangular lattice shapes. We also showed the analytical formulation for geometrical maneuvering of a random cluster. Now, we

aim to merge all these results defined and derived throughout this section in order to build a modular subroutine that enables a spatially flexible random deployment over a MCN.

The anticipated heterogeneous spatial deployment algorithm will actually be based on the ASD approach proposed earlier in this chapter. To be precise, the purpose of the ASD technique is formulated for randomly mapping a non-homogeneous cellular network by taking apart a deployment terrain and then reassembling the sectors; namely geometrical analysis followed by synthesis. This superposition principle of targeted distribution method is in fact applied in order to ensure a more realistic inhomogeneous stochastic pattern caused by users' tendency to cluster.

To create a generic modeling tool that can support a large and complex network, at first, we need to explain the layout of the MCN grid. Thus, in Figure 4.46 we illustrated the deployment model for a large network containing multiple hexagonal cells.

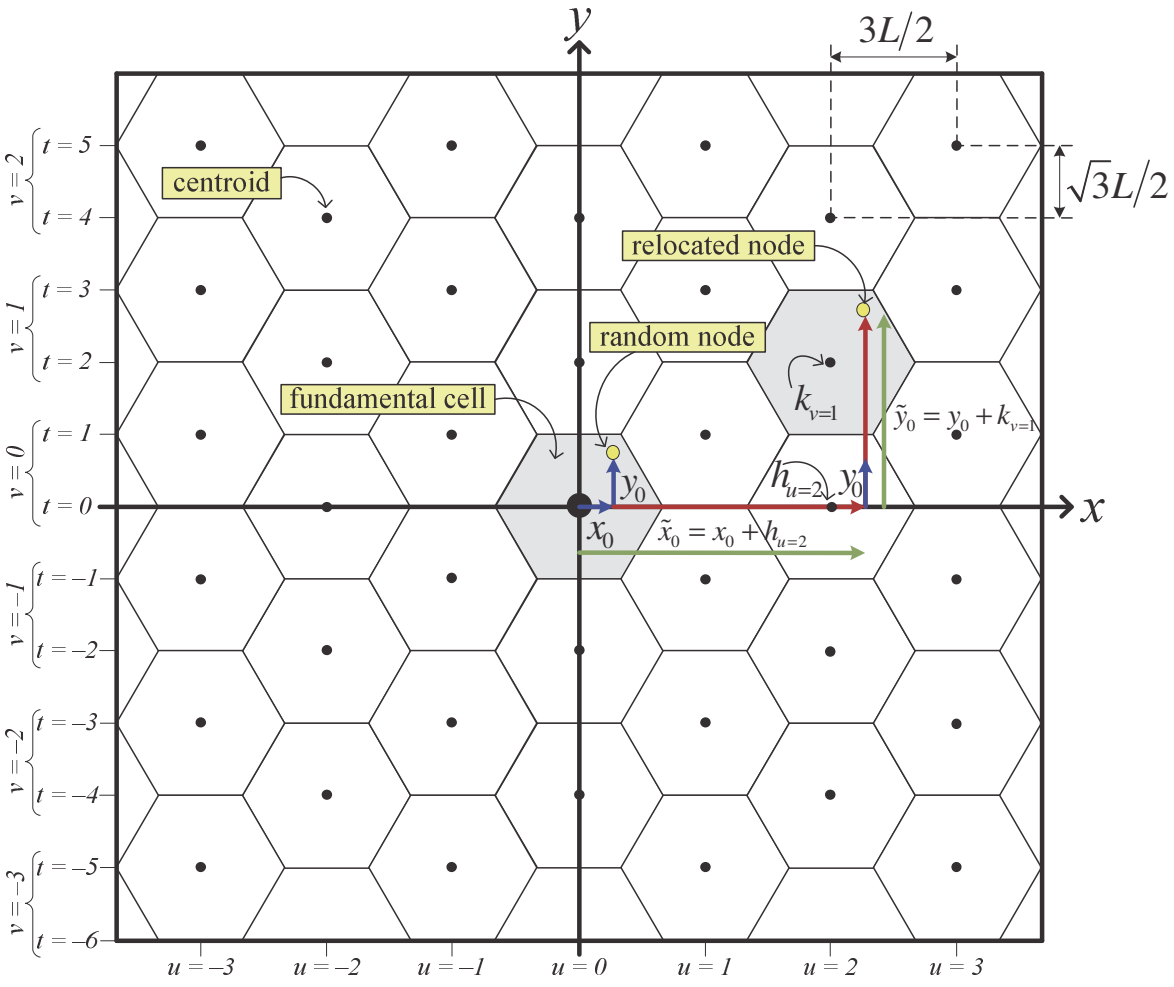

Figure 4.46 – Layout of a large MCN grid

As graphically explained, nodes will randomly be positioned in the fundamental cell centered at the origin of the Euclidian plane. Then, a sequence of geometrical steps can be applied to move the generated cluster to its desired position without an overlap of the borders. To do this task, we most importantly need to mathematically characterize the centroids of the network, which we can do by identifying the appropriate indices of a particular cell.

In Figure 4.46, we set the index along the *x*-axis to the $u \in \mathbb{Z}$ integer, and $t \in \mathbb{Z}$ for the *y*-axis. Indeed, identifying a cell with the (u,t) pair is problematic because not all combinations are valid cellular centroids, e.g. $(u,t) = (1,0)$ or $(1,2)$. In fact, from the network grid model, we recognize that if u is even, then t must also be even; otherwise both will be odd. Therefore, we rather remedy this reality by mapping (u,t) to an all-inclusive and compatible pair, say (u,v), where v is yet another integer variable. With some thought, we determined the relationship among the two pair of indices; thus we established the centroids for all possible cells:

$$\{u\ ,\ t\} = \{u\ ,\ t(u,v)\} = \{u\ ,\ (u \bmod 2 + 2 \cdot v)\} \qquad (u,v) \in \mathbb{Z}^2 \tag{4.132}$$

where **mod** is the modulo operator used to obtain the remainder of a rational number. To expand this operator, say we have the following rational number:

$$a/b = q + r/b \tag{4.133}$$

such that $a \in \mathbb{Z}$ is the dividend, $b \in \mathbb{N}^*$ is the divisor, $q \in \mathbb{Z}$ is the quotient, $r \in \mathbb{Z}$ is the remainder. Knowing that the quotient will always equal $\lfloor a/b \rfloor$, we could therefore isolate for the remainder in (4.133); hence we get:

$$r = a \bmod b = b(a/b - q) = a - b \cdot q = a - b \cdot \lfloor a/b \rfloor \qquad a \in \mathbb{Z}, b \in \mathbb{N}^* \tag{4.134}$$

With the geometrical help of Figure 4.46 and the compact generalization of (4.132), we can find the corresponding shifting vector for each cell by:

$$h_u = (3L/2)\cdot u \qquad u \in \mathbb{Z} \tag{4.135}$$

$$k_v = \left(\sqrt{3}L/2\right)t = \left(\sqrt{3}L/2\right)\cdot(u \bmod 2 + 2\cdot v) \qquad (u,v) \in \mathbb{Z}^2 \tag{4.136}$$

If we use the equality of (4.134), we can more appropriately rewrite (4.136) as follows:

$$k_v = k_v(u) = \sqrt{3}L\cdot\{u/2 - \lfloor u/2 \rfloor + v\} \qquad (u,v) \in \mathbb{Z}^2 \tag{4.137}$$

So basically, having the position indices (u,v) for the cellular of interest is enough for us to get the required centroid position within the larger honeycomb network grid by the use of (4.135) and (4.137). For an entire large network, these indices are inscribed in the cellular location matrix $\mathbf{L} \in \mathbb{Z}^{n_C \times 2}$, defined as:

$$\underset{n_C \times 2}{\mathbf{L}} = \begin{bmatrix} u_1 & u_2 & \cdots & u_{n_C} \\ v_1 & v_2 & \cdots & v_{n_C} \end{bmatrix}^T = \left[u_i, v_i\right]_{i=1,2,\cdots,n_C} \tag{4.138}$$

where $n_C \in \mathbb{N}^*$ is the overall number of cells considered for emulating a heterogeneous MCN deployment.

Beyond the location, particular cells may be partitioned differently; therefore, the sectors information will be indicated in the $\mathbf{S} \in \mathbb{N}_*^{n_C}$ array, namely:

$$\underset{n_C \times 1}{\mathbf{S}} = \begin{bmatrix} s_1 & s_2 & \cdots & s_{n_C} \end{bmatrix}^T = \left[s_i\right]_{i=1,2,\cdots,n_C} \tag{4.139}$$

such that $s_i \in \{1,3,6\}$ which basically refers to the number of sectors within the i-th cell.

As for the network scale, it will be registered in $\mathbf{N} \in \mathbb{N}^{n_C \times 6}$, which is the MCN deployment matrix for nodal quantity per sector per cell; this component is equal to:

$$\underset{n_C\times 6}{\mathbf{N}}=\begin{bmatrix} n_{(1,1)} & n_{(1,2)} & \cdots & n_{(1,s_1)} & \underbrace{0\cdots 0}_{6-s_1} \\ n_{(2,1)} & n_{(2,2)} & \cdots & n_{(2,s_2)} & \underbrace{0\cdots 0}_{6-s_2} \\ \vdots & \vdots & \vdots & \vdots & \vdots \\ n_{(n_C,1)} & n_{(n_C,2)} & \cdots & n_{(n_C,s_{n_C})} & \underbrace{0\cdots 0}_{6-s_{n_C}} \end{bmatrix}=\Big[\, n_{(i,j)}\in\mathbb{N}^{*}\,\Big]_{\substack{i=1,2,\cdots,n_C \\ j=1,2,\cdots,s_i}} \tag{4.140}$$

For easily managing the emulation process during its reusability for different network projects, we could combine (4.138), (4.139) and (4.140) together in the network plan matrix $\mathbf{P}\in\mathbb{Z}^{n_C\times 9}$, so as to form:

$$\underset{n_C\times 9}{\mathbf{P}}=\Big[\underset{n_C\times 2}{\mathbf{L}}\;\Big|\;\underset{n_C\times 1}{\mathbf{S}}\;\Big|\;\underset{n_C\times 6}{\mathbf{N}}\Big]=\Big[\,p_{(i,j)}\,\Big]_{\substack{i=1,2,\cdots,n_C \\ j=1,2,\cdots,9}}=\Big[\,u_i\quad v_i\quad s_i\quad n_{(i,j)}\,\Big]_{\substack{i=1,2,\cdots,n_C \\ j=1,2,\cdots,s_i}} \tag{4.141}$$

At this level, we can also quantify the overall number of sectors considered in the MCN emulation by:

$$n_{\text{sec-total}}=\sum\nolimits_{i=1}^{n_C}p_{(i,3)}=\sum\nolimits_{i=1}^{n_C}s_i \tag{4.142}$$

Having clear and explicit stochastic expressions derived for non-sectored and sectored hexagonal lattices, and geometrical ways to manage a random cluster, at present these components can coherently converge to produce the algorithm for MCN deployment of Figure 4.47. As it can be observed, this inhomogeneous spatial approach has a modular format, because as needed the appropriate random deployment algorithm for a particular sector lattice is accordingly called. Notably, **Algorithms 10**, **11**, and **12** shown in this pseudocode respectively refer to the code detailed in Figures 4.30, 4.36, and 4.40.

Moreover, the algorithm of Figure 4.47 is generic because it can support a host of complex non-homogeneous random networks effortlessly with simple, obvious and intuitive inputs. Indeed, this is possible due to the changeable attributes of the associated network plan enabled by adjusting:

Algorithm 13 - Emulating a Wide Inhomogeneous Random Network

Require: $n_C \in \mathbb{N}^* \quad L \in \mathbb{R}_+^* \quad \mathbf{P} = \left[p_{(i,j)} \in \mathbb{Z} \right]_{\substack{i=1,2,\cdots,n_C \\ j=1,2,\cdots,9}}$

Initialize: $n_{\text{sec-total}} = 0 \quad n_S = 0$

for $i = 1, 2, \cdots, n_C$ **do**

  Compute: $h_i \coloneqq (3L/2) \cdot p_{(i,1)}$

  Compute: $k_i \coloneqq \sqrt{3}L \cdot \left\{ p_{(i,1)}/2 - \left\lfloor p_{(i,1)}/2 \right\rfloor + p_{(i,2)} \right\}$

  $n_{\text{sec-total}} \coloneqq n_{\text{sec-total}} + p_{(i,3)}$

  for $j = 1, 2, \cdots, p_{(i,3)}$ **do**

    if $\left\{ p_{(i,3)} = 1 \right\}$ **then**

      Algorithm 10: $\left(p_{(i,j+3)}, L \right) \mapsto \left\{ \hat{x}_m, \hat{y}_m \right\} : m = 1, 2, \cdots, p_{(i,j+3)}$

      Set/Compute: $\phi_j \coloneqq 0$

    else if $\left\{ p_{(i,3)} = 3 \right\}$ **then**

      Algorithm 11: $\left(p_{(i,j+3)}, L \right) \mapsto \left\{ \hat{x}_m, \hat{y}_m \right\} : m = 1, 2, \cdots, p_{(i,j+3)}$

      Set/Compute: $\phi_j \coloneqq 2\pi (j-1)/3$

    else if $\left\{ p_{(i,3)} = 6 \right\}$ **then**

      Algorithm 12: $\left(p_{(i,j+3)}, L \right) \mapsto \left\{ \hat{x}_m, \hat{y}_m \right\} : m = 1, 2, \cdots, p_{(i,j+3)}$

      Set/Compute: $\phi_j \coloneqq \pi (j-1)/3$

    end if

    for $m = 1, 2, \cdots, p_{(i,j+3)}$ **do**

      Compute: $\tilde{x}_{n_S+m} \coloneqq \hat{x}_m \cdot \cos\left(\phi_j\right) - \hat{y}_m \cdot \sin\left(\phi_j\right) + h_i$

      Compute: $\tilde{y}_{n_S+m} \coloneqq \hat{x}_m \cdot \sin\left(\phi_j\right) + \hat{y}_m \cdot \cos\left(\phi_j\right) + k_i$

    end for

    $n_S \coloneqq n_S + p_{(i,j+3)}$

  end for

end for

Return: $\left\{ \tilde{x}_t, \tilde{y}_t \right\} : t = 1, 2, \cdots, n_S \quad n_{\text{sec-total}} \in \mathbb{N}^*$

Figure 4.47 – Pseudocode for random heterogeneous MCN spatial deployment

- the size of the cellular network: L
- the number of deployed cells: n_C
- the geographical position of the cell: (u_i, v_i)
- the sectoring capability of the cell: s_i
- the network scale of the cluster: $n_{(i,j)}$

Furthermore, the computational complexity of the above algorithm is given in (4.143), such that $n_S \in \mathbb{N}^*$ is the overall amount of randomly positioned nodes over the entire service area of the MCN.

$$O\left(\sum_{i=1}^{n_C}\sum_{j=1}^{p_{(i,3)}} p_{(i,j+3)}\right) = O\left(\sum_{i=1}^{n_C}\sum_{j=1}^{s_i} n_{(i,j)}\right) = O\left(n_S\right) \tag{4.143}$$

To demonstrate this algorithm, in Figure 4.48 we displayed the footmark of the network plan for a large architecture example composed of 19-cells, where users nodal quantity is inscribed in each zone. From this visual aid, we can straightforwardly express the heterogeneous deployment information in its equivalent canonical matrix format by:

$$\underset{19\times 9}{\mathbf{P}} = \begin{bmatrix} -2 & -2 & -2 & -1 & -1 & -1 & -1 & 0 & 0 & 0 & 0 & 0 & 1 & 1 & 1 & 1 & 2 & 2 & 2 \\ 1 & 0 & -1 & 1 & 0 & -1 & -2 & 2 & 1 & 0 & -1 & -2 & 1 & 0 & -1 & -2 & 1 & 0 & -1 \\ 3 & 1 & 6 & 6 & 1 & 6 & 3 & 1 & 3 & 1 & 3 & 1 & 3 & 6 & 1 & 6 & 6 & 1 & 3 \\ 80 & 400 & 150 & 60 & 300 & 50 & 220 & 250 & 300 & 1,200 & 400 & 500 & 30 & 150 & 400 & 150 & 30 & 100 & 90 \\ 130 & 0 & 25 & 35 & 0 & 120 & 300 & 0 & 100 & 0 & 150 & 0 & 130 & 80 & 0 & 75 & 150 & 0 & 150 \\ 150 & 0 & 90 & 80 & 0 & 150 & 190 & 0 & 100 & 0 & 170 & 0 & 90 & 200 & 0 & 150 & 50 & 0 & 130 \\ 0 & 0 & 150 & 150 & 0 & 190 & 0 & 0 & 0 & 0 & 0 & 0 & 0 & 100 & 0 & 45 & 40 & 0 & 0 \\ 0 & 0 & 65 & 80 & 0 & 50 & 0 & 0 & 0 & 0 & 0 & 0 & 0 & 50 & 0 & 15 & 150 & 0 & 0 \\ 0 & 0 & 200 & 250 & 0 & 85 & 0 & 0 & 0 & 0 & 0 & 0 & 0 & 150 & 0 & 25 & 350 & 0 & 0 \end{bmatrix}^T \tag{4.144}$$

From (4.142) and (4.144), we realize that in this network example $n_{\text{sec-total}} = 61$ sectors; and by (4.143) we can compute that $n_S = 10,000$ wireless nodes. If we simulate this described structure, we obtain in Figure 4.49 one possible random instance of the generated network.

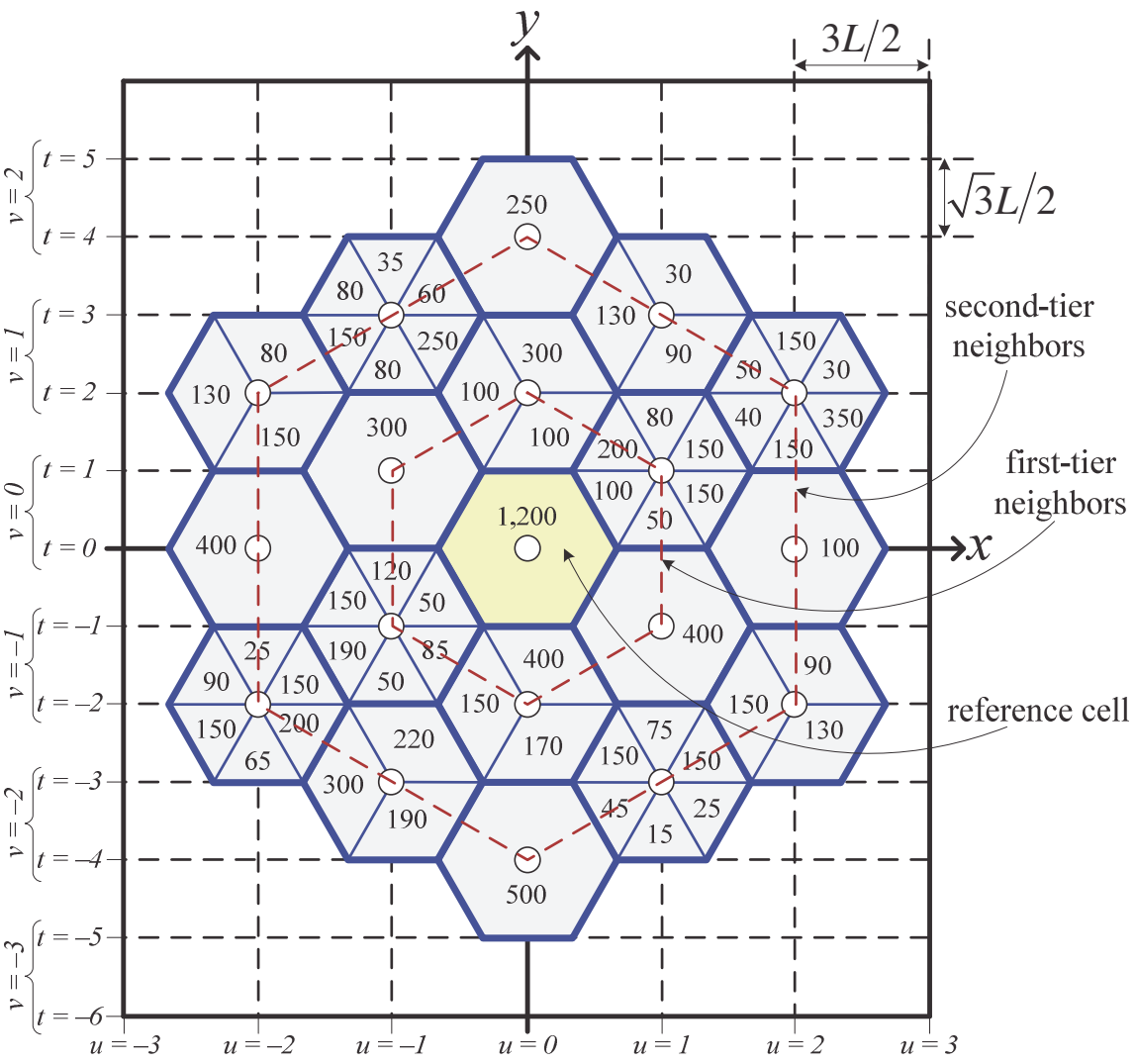

Figure 4.48 – Network footprint for a complex non-homogeneous MCN example

Although we did not do that in Figure 4.49, yet coloring could have been used to distinguish the various clusters of the MCN. This was in fact performed in the example that we demonstrated in [72].

Overall, the conceptualized algorithm tool can emulate heterogeneous MCN models that have the advantage of being flexible and scalable based on unbiased random sampling so as to reflect the desired network plan. Indeed, this generic deployment algorithm supports random structures with varying size, capacity, density, and sectoring capability. Thus, a designer could utilize this subroutine to simulate a large inhomogeneous mobile network straightforwardly and in a timely manner due mainly to its ease of configuration and modular complexion.

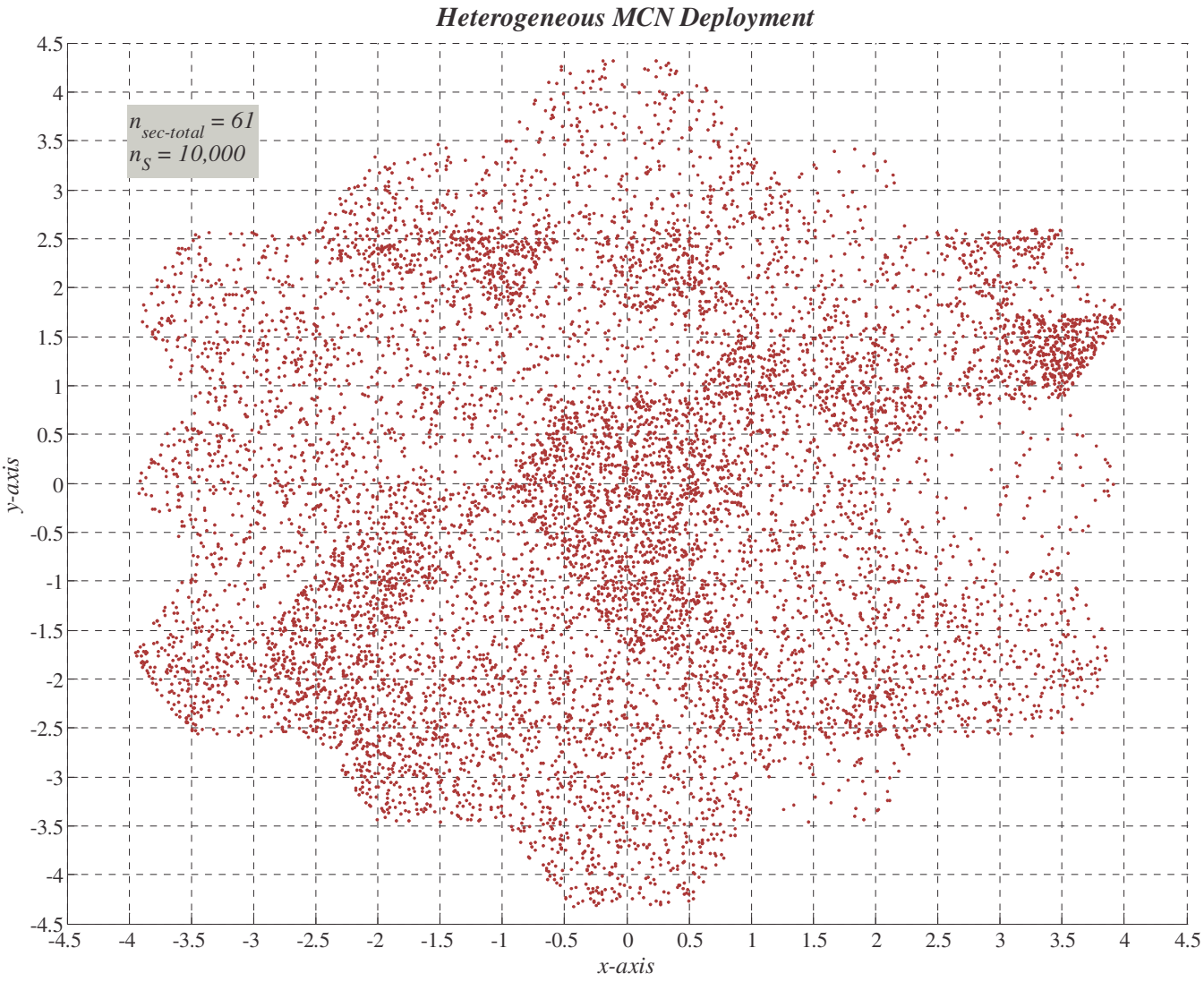

Figure 4.49 – Random heterogeneous spatial deployment for a 19-cell MCN example

Although the point here is to show how it is possible to emulate a random heterogeneous MCN; yet once constructed by the simulator tool, the hexagonal-based stochastic map can be used to effectively study various performance indicators. In particular, interference is a crucial system-level metric worthy of investigation, mainly for exploring: adjacent-channel interference, co-channel interference, and coexistence analysis due to spectrum overlapping.

To incite such potential, in the MCN footprint of Figure 4.48, we identified the first- and second-tier neighbors of a reference cell located at the origin of the Cartesian plane. As it is usually the case with CDMA and LTE networks, the reference is assumed to operate with FR factor of unity. In this setting, we may for instance explore the deteriorating impact of

interference on a randomly positioned MS in the reference network from these outer cells containing diverse multi-pattern sectoring. In fact, the analysis can be performed over different network planning, scaling, and coverage scenarios in order to observe outcomes and deduce valuable conclusions regarding the spatial layout of the architecture.

Following the in-depth characterization of the heterogeneous MCN, at this juncture we could concisely recapitulate and compare the various emulating algorithms formulated in this chapter. In Table 4.7, the major distinctive highlights between UCN and MCN inhomogeneous approaches are featured[6]. From the presented dichotomy, we can clearly identify and select the appropriate algorithm feasible for a certain deployment project. Generally speaking, macrocells are used for planning low-traffic network demands commonly encountered in rural conditions [73]; whereas microcells are considered in densely populated regions such as large urban cities with multiple BSs having directional antenna schemes.

Also, from the table we notice that the notion of spatial clustering can carry different meanings depending on the considered approach and the deployment settings. For instance, for the UCN case, clustering is founded as a function of terrain features. On the other hand, for the MCN case, it makes more sense due to the cell geometry to consider clustering as a function of the BS position within the MCN grid, and the sectoring capability of its antenna by the use of directional emitters.

Table 4.7 – Comparing the emulation algorithms for uni- and multi-cellular networks

spatial attributes	**inhomogeneity algorithms**	
	UCN	**MCN**
network location	suburban	urban
network scale	sparsely populated	densely populated
network dimension	macrocell	microcells
lattice structure	circular	hexagonal
spatial clustering	terrain features	BS positions and antenna sectoring
algorithm cost	$\underbrace{O(n_S)}_{\text{controlled}}, \underbrace{O(n_S + n_{L-\max} \cdot \log_2 n_{L-\max})}_{\text{uncontrolled}}$	$O(n_S)$

[6] We should remark that the associations outlined in Table 4.7 are typically valid, but are not necessarily true for all deployment scenarios; e.g. we may have a non-sparse UCN which is overloaded with active users as in Figure 4.26.

4.5.6 – Formulating the Spatial Density for Heterogeneous Networks

Similar to the spatial density analysis and verification conducted in Subsection 4.2.2 for the UCN structure; in this part, we are interested to formulate the related expressions for MCN deployment. Furthermore, we aim to derive a PDF estimation expression tailored specifically for approximating the spatial density of an inhomogeneous random network deployment realized via the proposed ASD algorithm.

In Figure 4.50, we provided the bivariate histogram for the random simulation of $n_S = 10,000$ samples estimated with $n_B = 25$ bins for a triangular, rhombus and hexagonal lattices by using the algorithms detailed in earlier subsections of this chapter.

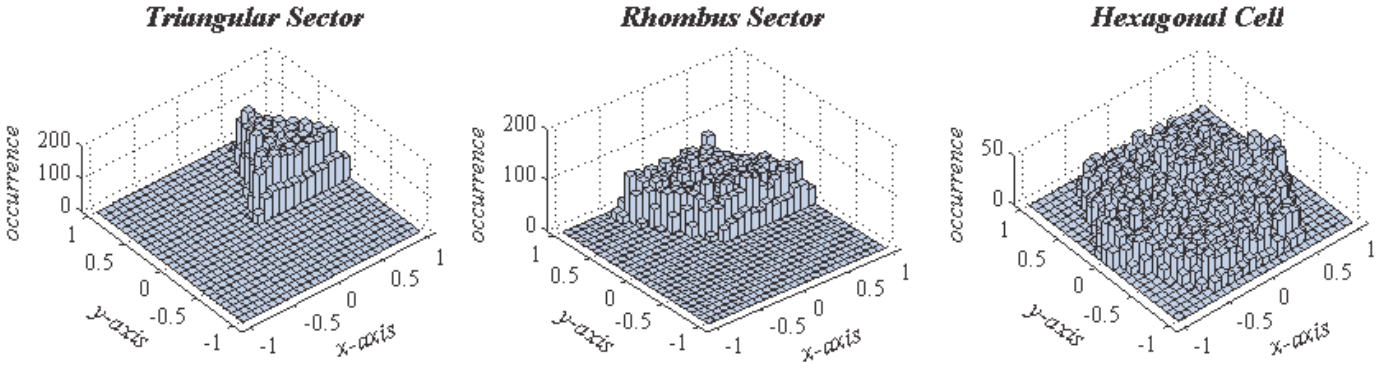

Figure 4.50 – Spatial densities of hexagonal-based random networks

Now, we want to analytically predict this spatial density estimation shown above. To do this, we could begin by unifying the relevant deployment areas of (4.96), (4.107), and (4.114) into:

$$A_H^{(l)} = \sqrt{3} \cdot L^2 \cdot l! / 4 \qquad l = 1,2,3 \tag{4.145}$$

where l follows the notational convention of (4.122). To facilitate this derivation, the footprint of Figure 4.51 can be utilized. In this illustration, we notice the bivariate estimation grid as equally-spaced bin regions; thus, the average histogram density can analytically be obtained by:

$$\begin{aligned} h_{XY}^{\text{analytical}} &= \langle h_{XY} \rangle = \rho_A \cdot A_{bin} = \left(n_S / A_N \right) \cdot \Delta_B^2 \\ &= \left(n_S / A_H^{(l)} \right) \cdot \left(2L / n_B \right)^2 = 16 \cdot n_S / \sqrt{3} \cdot n_B^2 \cdot l! \qquad l = 1,2,3 \end{aligned} \tag{4.146}$$

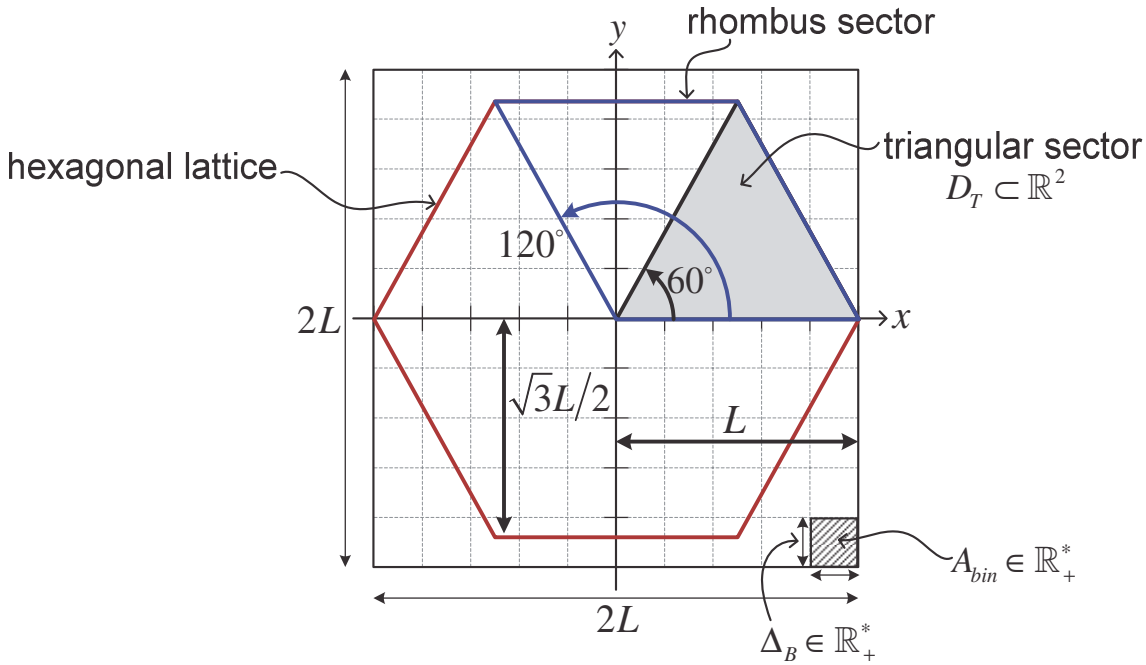

Figure 4.51 – Footprint of a hexagonal network for spatial density estimation

To verify this result, we performed a set of MC simulations with $n_S = 100,000$ samples over different histogram resolutions. The results are indicated in Table 4.8, such that $h_{XY}^{\text{simulation}}$ is given in (4.26), and the error measure ε_A is defined in (4.28). The small percentage error of the spatial density among analysis and simulation insinuates the correctness of the derivation.

Table 4.8 – Contrasting spatial density estimation for a hexagonal-based network

random network models	A_H (units^2)	n_S (no.)	ρ_A $(\text{k/units})^2$	n_B (no.)	$h_{XY}^{\text{analytical}}$ (no./bin area)	$h_{XY}^{\text{simulation}}$ (no./bin area)	ε_A (%)
triangular sector	0.4330	10^5	0.2309	300	10.2640	10.1708	0.91
rhombus sector	0.8660	10^5	0.1155	200	11.5470	11.4147	1.15
hexagonal cell	2.5981	10^5	0.0385	100	15.3960	15.0742	2.09

In the previous subsection, we conceptualize a MCN algorithm for heterogeneous random deployment. Then, we experimented the inhomogeneous spatial generation for a 19-cell example, and one instance of the random 2D deployment was shown in Figure 4.49. Here, its related spatial density is estimated in Figure 4.52 based on $n_B = 50$ resolution along each axis.

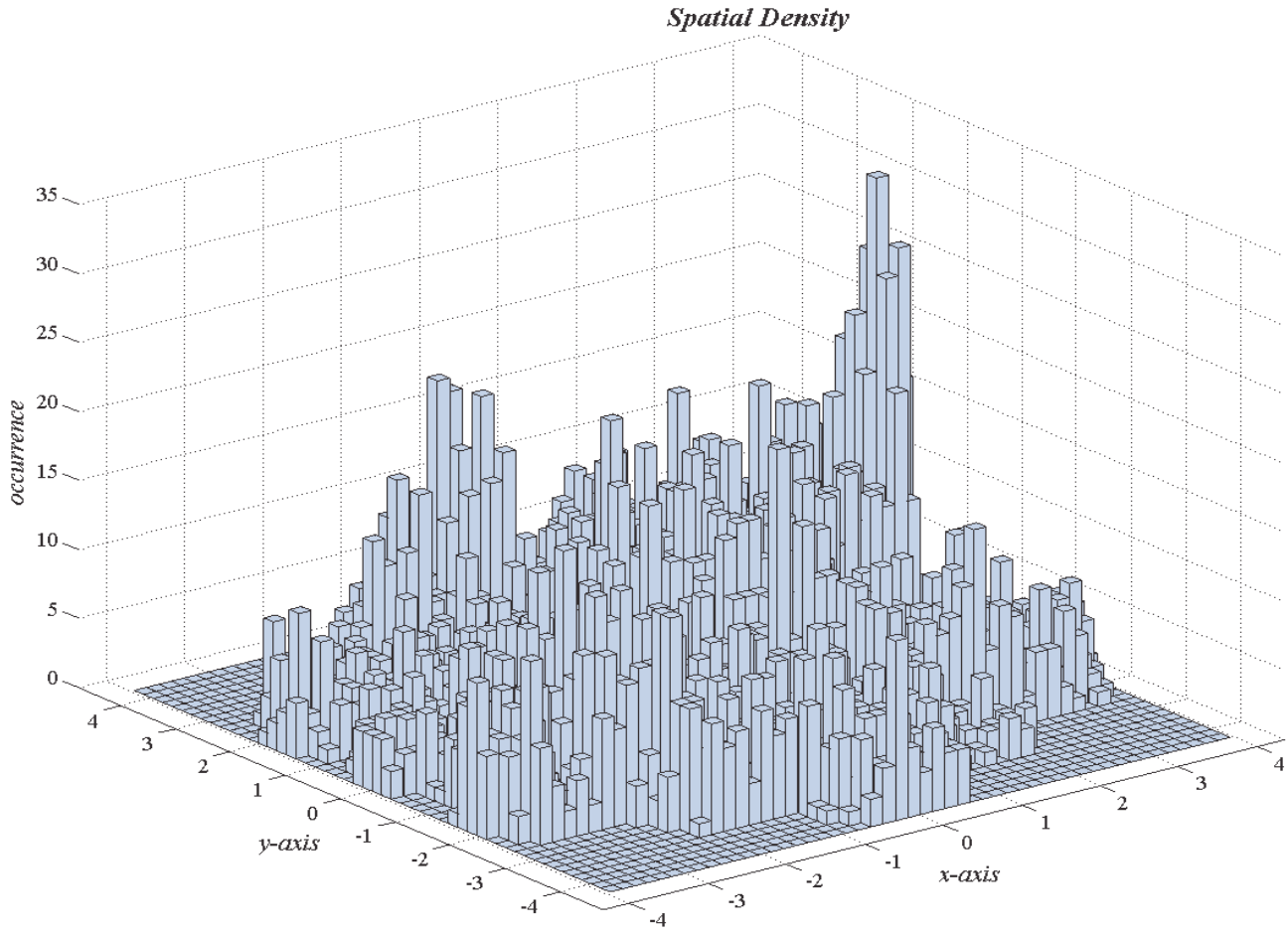

Figure 4.52 – Inhomogeneous spatial density estimation for a 19-cell MCN example

As apparent from Figure 4.52, the overall spatial distribution is non-homogeneous. At this stage, the intrigue is to develop a mathematical mechanism that can effectively approximate heterogeneously deployed networks such as the one estimated above. For this purpose, we define the spatial density histogram $H_{ASD}(x,y):\mathbb{R}^2 \mapsto \mathbb{N}$ for heterogeneous ASD deployment:

$$H_{ASD}(x,y)=\sum_{j=1}^{n_{B-Y}}\sum_{i=1}^{n_{B-X}} h_{(i,j)}^{ASD}\cdot\delta_B\left(x-x_i,y-y_j\right) \tag{4.147}$$

As it can be observed, this expression is similar to the notation of (4.19) except that here we consider multiple deployment regions as opposed to a single one. As a consequence, $h_{(i,j)}^{ASD}\in\mathbb{N}$ will equal the aggregate of the multi-density sectors:

$$h_{(i,j)}^{ASD} = h_{(i,j)}^{(1)} + h_{(i,j)}^{(2)} + \cdots + h_{(i,j)}^{(n_{\text{sec-total}})} = \sum\nolimits_{k=1}^{n_{\text{sec-total}}} h_{(i,j)}^{(k)} \tag{4.148}$$

And for this generalized case, the overall deployment surface $[x_L, x_H] \times [y_L, y_H]$ is obtained by:

$$x_L = \min_{k=1,2,\cdots,n_{\text{sec-total}}} \left\{ x_L^{(k)} \right\}; \qquad x_H = \max_{k=1,2,\cdots,n_{\text{sec-total}}} \left\{ x_H^{(k)} \right\} \tag{4.149}$$

$$y_L = \min_{k=1,2,\cdots,n_{\text{sec-total}}} \left\{ y_L^{(k)} \right\}; \qquad y_H = \max_{k=1,2,\cdots,n_{\text{sec-total}}} \left\{ y_H^{(k)} \right\} \tag{4.150}$$

Indeed, these expressions will basically determine the smallest and largest extremities of the sub-regions. As a result, (4.147) can be rewritten as follows:

$$H_{ASD}(x,y) = \sum\nolimits_{j=1}^{n_{B-Y}} \sum\nolimits_{i=1}^{n_{B-X}} \sum\nolimits_{k=1}^{n_{\text{sec-total}}} h_{(i,j)}^{(k)} \cdot \delta_B \left(x - x_L + (1/2 - i)\Delta x_B;\ y - y_L + (1/2 - j)\Delta y_B \right) \tag{4.151}$$

where the dimensions of the bivariate histogram bin are computed by:

$$\Delta x_B = (x_H - x_L) / n_{B-X} = \left(\max_{k=1,2,\cdots,n_{\text{sec-total}}} \left\{ x_H^{(k)} \right\} - \min_{k=1,2,\cdots,n_{\text{sec-total}}} \left\{ x_L^{(k)} \right\} \right) \Big/ n_{B-X} \tag{4.152}$$

$$\Delta y_B = (y_H - y_L) / n_{B-Y} = \left(\max_{k=1,2,\cdots,n_{\text{sec-total}}} \left\{ y_H^{(k)} \right\} - \min_{k=1,2,\cdots,n_{\text{sec-total}}} \left\{ y_L^{(k)} \right\} \right) \Big/ n_{B-Y} \tag{4.153}$$

To determine the density of (4.151), we need to go over the fundamentals of stochastic theory. Evidently, the probability of some arbitrary event A obtained for a bivariate PDF will be equal to:

$$\Pr\left(A \to (x,y) \in D \right) = \iint_{(x,y) \in D} f_{XY}(x,y)\, dx\, dy \tag{4.154}$$

This expression can be approximated by looking at the left and right hand sides of (4.154) separately and then equating them together, namely:

$$\Pr\left(A \to (x,y) \in D\right) \approx H_{ASD}(x,y)/n_S \approx \tilde{f}_{XY}(x,y) \cdot \Delta x_B \cdot \Delta y_B \tag{4.155}$$

such that $\tilde{f}_{XY}(x,y)$ is the numerical probability density estimation for spatial inhomogeneous deployment. If we isolate for the density function, we obtain the final result as follows:

$$\begin{aligned} f_{XY}(x,y) &= \lim_{n_S \to \infty} \lim_{\substack{n_{B-X} \to \infty \\ \Delta x_B \to 0}} \lim_{\substack{n_{B-Y} \to \infty \\ \Delta y_B \to 0}} \tilde{f}_{XY}(x,y) \\ &= \lim_{n_S \to \infty} \lim_{\substack{n_{B-X} \to \infty \\ \Delta x_B \to 0}} \lim_{\substack{n_{B-Y} \to \infty \\ \Delta y_B \to 0}} \sum_{j=1}^{n_{B-Y}} \sum_{i=1}^{n_{B-X}} \sum_{k=1}^{n_{\text{sec-total}}} h_{(i,j)}^{(k)} \cdot \delta_B\left(x - x_i, y - y_j\right) \Big/ n_S \cdot \Delta x_B \cdot \Delta y_B \end{aligned}$$

- $\delta_B(x,y) = \mathbf{1}\left(|x| \le \Delta x_B/2;\ |y| \le \Delta y_B/2\right)$
- $\Delta x_B = (x_H - x_L)/n_{B-X}$ $\quad$ • $\Delta y_B = (y_H - y_L)/n_{B-Y}$
- $x_L = \min_{k=1,2,\cdots,n_{\text{sec-total}}} \left\{x_L^{(k)}\right\}$ $\quad$ • $x_H = \max_{k=1,2,\cdots,n_{\text{sec-total}}} \left\{x_H^{(k)}\right\}$
- $y_L = \min_{k=1,2,\cdots,n_{\text{sec-total}}} \left\{y_L^{(k)}\right\}$ $\quad$ • $y_H = \max_{k=1,2,\cdots,n_{\text{sec-total}}} \left\{y_H^{(k)}\right\}$
- $x_i = x_L + (i - 1/2)\Delta x_B$ $\quad$ • $y_j = y_L + (j - 1/2)\Delta y_B$

■

(4.156)

As noted by the limits in this statement, the spatial density estimation can be improved by augmenting the quantity of MC samples n_S. Also, increasing the histogram resolution through the number of bars along each axis is expected to ameliorate the numerical computation of the 2D density function. However, rising n_S and n_B (assuming $n_{B-X} = n_{B-Y}$) simultaneously by a certain level does not necessarily improve the result. This is in fact the case because by (4.156) these elements oppositely impact the spatial density function, i.e.:

$$\tilde{f}_{XY}(x,y) \propto 1/n_S \cdot \Delta x_B \cdot \Delta y_B \propto n_{B-X} \cdot n_{B-Y}/n_S \propto n_B^2/n_S \tag{4.157}$$

Therefore, a better understanding of the joint relationship between these estimation factors is needed in order to fine-tune the approximation process.

On the whole, we should emphasize that the tractable statement of (4.156) offers an analytical formula for estimating users' inhomogeneous geometrical trend over a geographical service area. In fact, this statement is tailored specifically for approximating the spatial density function of an ASD-based heterogeneous network. Thus, the result is applicative for all the inhomogeneous algorithms derived in this chapter, i.e. controlled/uncontrolled UCN and MCN deployments. In other words, so long as the random position generation is based on the ASD approach, then the developed expression will be valid.

4.6 – Conclusion

The importance of all variations of wireless communications, and in particular cellular technologies, are still and even more significant as we move toward newer network generations. Therefore, analysis and planning of such systems through time- and cost-efficient simulations is rather vital. As a result, the central focus of this chapter was based on the random emulation of terminals spatial position. In fact, in order to enable the effective geometrical modeling of a network, we had to undertake this research challenge from different viewpoints targeting a specific deployment situation.

To this end, we began by identifying that it is a common practice by researchers and design engineers to spread random nodes in a disk-shaped circular cell representing an ideal EM radiation profile of a BS. Also, we noted that spatial distribution in an annulus is often conducted in order to study edge related aspects. However, despite this reality, no comprehensive stochastic method exists for nodal emplacement in different mutations of a circular cell without relying on biased sampling. Thus, we improved the spatial geometry of terminals by deriving exact expressions for versatile nodal deployment. To be precise, our UCN deployment derivation has a number of direct and cascading advantages; notably:

- It is more generic than currently available models; hence it enables spatial flexibility.
- It is based on more efficient position generation when compared to heuristic approaches.

- It ensures the preservation of unbiased randomness.
- It is analytically useful for rigorously obtaining a tractable large-scale fading density.
- It can be used as a foundation for spatially emulating an inhomogeneous multipurpose cellular network.

Next, as an alternative to exhaustive MC techniques, using the above steppingstone, we derived a closed-form large-scale fading predictor for a flexibly versatile random UCN. This finding essentially generalizes the result in [19], which basically determined the PL distribution for a fixed deployment coverage. Indeed, the impact of far-field was also overlooked in this previously reported result. In fact, the consideration of this phenomenon is critical because the large-scale fading is only valid and defined for interpoint distances that extends beyond the close-in range. On the other hand, our density derivation is more accurate because this fundamental propagation factor was explicitly accounted for in the spatial deployment, the channel-loss model, the stochastical transformation, and the theoretical analysis. Following the large-scale fading formulation, MC simulations were used to reaffirm the validity of the theoretical analysis. Also, various permutations of the UCN were evaluated from a PL perspective in order to study the interplay between the deployment structure of the network, the random nodal geometry, and its impact on the channel-loss behavior.

Furthermore, we remarked that typical spatial distribution densities, though practical to some degree, have their own limitations. For example, the uniform case is mainly valid when the terrain of interest is flat with no topographical features. And, this is the case because humans, who for the most part are the carriers of mobile devices, will favor one location as opposed to another. Likewise, the Gaussian spatial geometry is applicable in scenarios where the center of a cell has greater nodal concentration, and for modeling the airdropping of terminals.

Therefore, by means of the determined results for versatile nodal deployment, an inhomogeneous UCN algorithm based on the superposition principle of targeted spatial distribution was proposed. This conceptualized heterogeneous networking approach, which we refer to as ASD, is certainly more manageable because it breaks down a fairly complicated task of finding the wholesome density of users' spatial pattern in a vast terrain to that of smaller regions. Then, the principle of superposition can be applied to merge the spatial clusters together, and hence establish the entire random mobile distribution of the cell in order to investigate

various network-based integrity measures. Overall, this controlled spatial emulation algorithm is a coherent, easily configured tool, with greater emulation flexibility, useful for approximately modeling and attaining a heterogeneous random arrangement.

In addition to the above controlled UCN algorithm, we derived an automatic emulator to arbitrarily simulate an inhomogeneous wireless network. This uncontrolled heterogeneous spatial generator method is practical when no specific information about a network site is known or asserted; i.e., the designer is not aware of the actual deployment environment. The key advantage of this tool is that it can randomly construct a unique heterogeneous geometry suitable for small, medium or large scale networks while necessitating very few input parameters.

Moreover, we described an adjustable computer simulation mechanism for unbiased random deployment of nodes over a large MCN. This was done by first acknowledging that during the analysis of a cellular-based network, it is common to model the BS coverage area by assuming ideal cell shapes such as a circle or a hexagon. In fact, for MCN deployment, the hexagonal model is more appropriate because it eliminates overlapping and coverage holes. Consequently, we methodically derived the exact random generation approach for deploying nodes within non-sectored and sectored hexagonal-based network lattices; the outcomes were then verified through stochastic simulations. Using these findings, we subsequently demonstrated the implementation of a comprehensive stochastic model that can be applied to generically simulate a complex non-homogeneous cellular structure with varying parameters, such as: size, capacity, density, and sectoring capability. The systematic and modular nature of the obtained algorithm promotes its flexibility for different large coverage MCN projects. In general, this inhomogeneous simulator model can be used for studying a host of factors that affects the link-layer of the network, among others: channel losses, interference, and resource consumption.

Chapter 5

Channel-Loss Predictor for Gaussianly Deployed Network

5.1 – Introduction

5.1.1 – Objective

The Gaussian random network has been considered as an effective model for cellular systems and air deployed devices. Meanwhile, for the analysis of such LWN, profiling and predicting the behavior of the propagation channel is fundamental. By and large, the only way to obtain an estimate of the channel-loss distribution for a specific random network relies on computationally expensive MC simulation for each topology under investigation. For efficiency and tractably purposes, the large-scale fading distributions over various random uniform deployment models have already been formulated and analyzed in literature [19], [74], [75], and in previous parts of this dissertation. However, there is yet an analytical reporting to be made for the Gaussian network model.

Given the wide interest and practicality of the Gaussian network, as a result, in this chapter, we will derive a generic and exact closed-form PDF expression for the large-scale fading between an AP and a randomly deployed node based on a generalized truncated realization. The expected formulation will essentially characterize the propagation attributes while remaining fully generic and compatible to different cellular sizes, spatial intensities, channel parameters and operating environments. Overall, the result will be an insightful mechanism for planning, analyzing, and designing large RF networks that exhibit or emulate a Gaussian spatial pattern.

5.1.2 – Organization

The rest of this chapter is organized as follows. In Section 5.2, the motivation, geometry, and behavior of the Gaussian random network model will be detailed. Then, in Section 5.3, an exact closed-form analytical derivation for the large-scale fading density will be shown. After, in Section 5.4, the validity of the formulation will be demonstrated and analyzed via stochastic MC simulations. Next, in Section 5.5, some key implications of the large-scale fading PDF derived throughout this dissertation will be described. Finally, Section 5.6 will close the chapter.

5.2 – Gaussian Random Network Model

5.2.1 – Motivation

Besides the homogeneous network discussed previously, researchers have also considered the Gaussian geometry for modeling a snapshot of users in a cellular configuration, where mobiles concentration near or away from the AP is analyzed [24]–[26], [35]–[39]. Further, it was reported that the Gaussian distribution is an effective way to model nodes deployment from an air moving vehicle [42]–[45]. This realization is depicted in Figure 5.1, where a set of radios are deployed about a pre-positioned processing reference (e.g. tank). Once airdropped, the nodes are expected to be anywhere in a cloud around the AP due to factors such as wind, speed, height, etc.

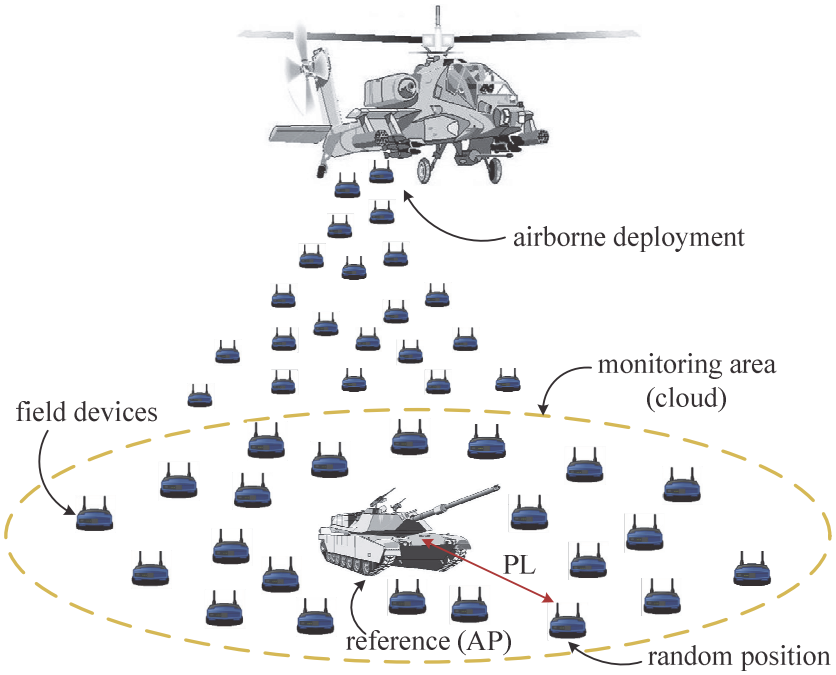

Figure 5.1 – Aerial network deployment

5.2.2 – Network Geometry

The network spatial configuration is based on Gaussianly deployed nodes, with a joint PDF governed by:

$$(X,Y) \sim f_{XY}(x,y) = \mathcal{N}(\boldsymbol{m},\boldsymbol{\Sigma}) = \frac{1}{2\pi|\boldsymbol{\Sigma}|^{1/2}} \exp\left\{-([x,y]-\boldsymbol{m})\boldsymbol{\Sigma}^{-1}([x,y]-\boldsymbol{m})^{T}/2\right\} \quad (5.1)$$

where the random spatial position is given by $(x,y) \in \mathbb{R}^2$, with mean vector $\boldsymbol{m} = (m_X, m_Y) \in \mathbb{R}^2$, and the covariance matrix $\boldsymbol{\Sigma} \in \mathbb{R}^{2\times 2}$ contains the spread $(\sigma_X, \sigma_Y) \in \mathbb{R}^2_{+,*}$ and correlation coefficient $\rho_{XY} \in \mathbb{R} : |\rho_{XY}| \le 1$ of the PDF:

$$\boldsymbol{\Sigma} = \begin{pmatrix} \sigma_X^2 & \rho_{XY}\sigma_X\sigma_Y \\ \rho_{XY}\sigma_X\sigma_Y & \sigma_Y^2 \end{pmatrix} \quad (5.2)$$

Taking into consideration that the reference AP will be located at the origin of the Euclidian space, implies that $m_X = m_Y = 0$. Further, it is assumed that the spatial axes are uncorrelated, or $\rho_{XY} = 0$. This is done not only for the sake of simplicity, but is rather instinctive because no *a priori* statistical insight of users' trends or terrain limitations is known. Moreover, in order to have a single controllable dispersion element, we will consider the SD to be the same along each direction; hence: $\sigma_X = \sigma_Y = \sigma_G$. Overall, the per-dimension samples for each nodal position are i.i.d.; and nodes geometrical emplacements among themselves are also i.i.d.

5.2.3 – Network Behavior

It is important to note that in comparison to the nonflexible uniform layout, the Gaussian model has the ability for controlling nodes deployment via the SD $\sigma_G \in \mathbb{R}^*_+$ of the joint spatial PDF. In particular, the reach and intensity of the spatial network can be adjusted by first realizing that a cellular radius of $3\sigma_G$ covers almost 0.997 of the surface area. If we assign L for the radius,

we could then parameterize the SD by: $\forall L \in \mathbb{R}_{+}^{*} : \exists a \in [3,\infty) : \sigma_G \approx L/a$. In light of this interpretation, simple examples that demonstrate the tunable flexibility of the network topology are demonstrated in Figure 5.2. Specifically, the cell size and the amount of nodes are held constant (e.g. $L=1;\ n_S=10{,}000$); however a is made variable so as to produce different realizations. When $a=3$ the nodes presence is all over the network surface, hence a sparse configuration is resulted. Otherwise, say for instance that $a=5$, then a condense outcome is obtained. And, as this variable grows, e.g. $a=7$, then the concentration further intensifies and a highly-centric structure near the BS is realized.

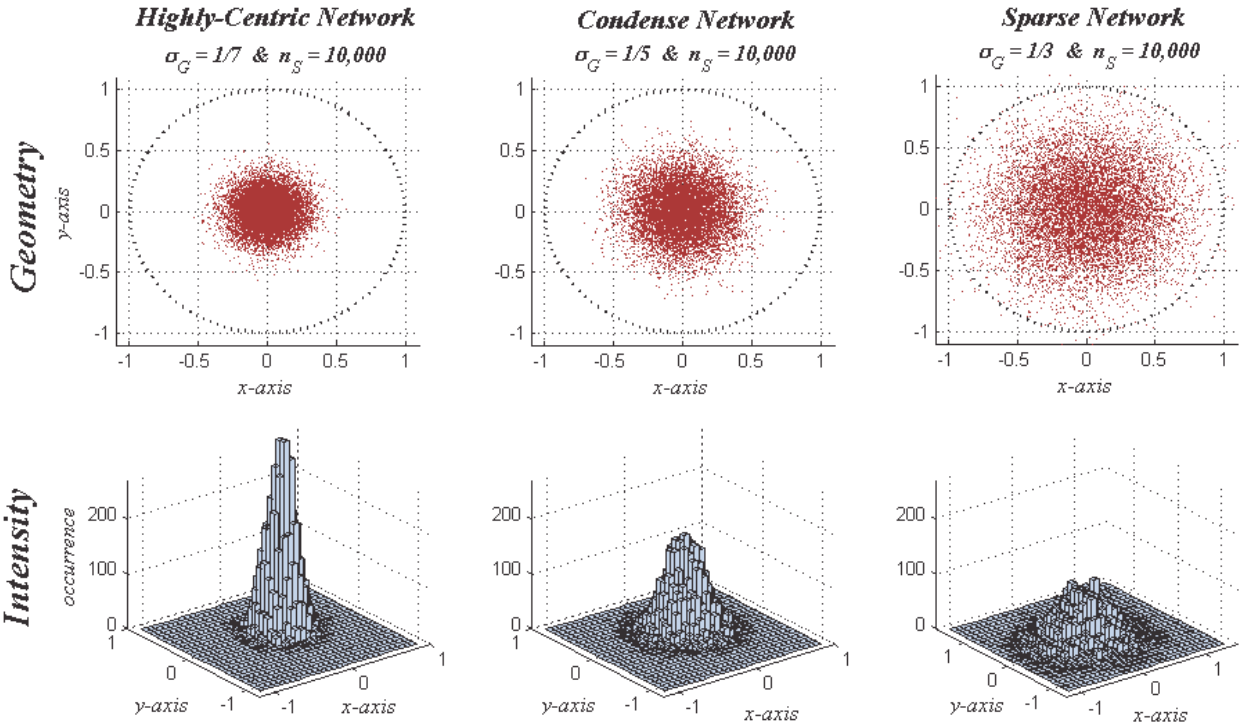

Figure 5.2 – Parameterizing the geographical spread and spatial intensity of the model

5.3 – Distribution of the Large-Scale Fading

5.3.1 – Internodal Distance PDF

At this point, we are interested to find the density of r, which is the distance between a random node and the corresponding AP. To achieve this, it becomes natural to transform (5.1) from its Cartesian representation to polar notation, where $J(r,\theta)$ is a 2D Jacobian matrix:

$$f_{R\theta}(r,\theta)=\left\{\mathcal{N}(\vec{m},\Sigma)\right\}_{\substack{x=r\cos\theta\\ y=r\cos\theta}}\left|J(r,\theta)\right|=\left\{\mathcal{N}_X\left(0,\sigma_G^2\right)\mathcal{N}_Y\left(0,\sigma_G^2\right)\right\}_{\substack{x=r\cos\theta\\ y=r\cos\theta}}\left|J(r,\theta)\right| \quad (5.3)$$

Then, we determine the marginal density along the radius, which can be shown to reduce to a Rayleigh distribution:

$$R\sim f_R(r)=\int_{\theta=0}^{2\pi} f_{R\theta}(r,\theta)\,d\theta=r\exp\left\{-r^2/2\sigma_G^2\right\}\Big/\sigma_G^2=Rayleigh(\sigma_G)\qquad r\in\mathbb{R}^+ \quad (5.4)$$

Evidently, the geometrical position of nodes will follow a Gaussian spatial pattern; but in particular, we will consider its truncated counterpart, which is a conditional realization of the original PDF [76]. In Cartesian format, the spatial density thus changes to:

$$f_{XY}^T(x,y)=f_{XY}\left(x,y\middle|D^T\right)=f_{XY}\left((x,y)\in\mathbb{R}^2;(r_0,L)\in\mathbb{R}^2_{+,*}\middle|\,r_0^2\le x^2+y^2\le L^2\right) \quad (5.5)$$

Specifically, this modification is performed because the large-scale fading model is valid for interpoint distances that extends beyond the far-field region r_0 . Moreover, this adjustment ensures that all nodes will be positioned within a preset delineation of the cell radius L . Thus, as shown by Figure 5.3, the radial density will be truncated, i.e.: $[0,\infty)\to[r_0,L]$; thus further generalizing the analysis.

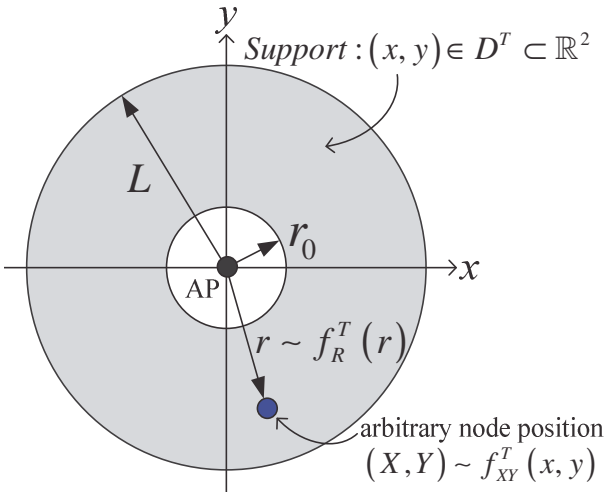

Figure 5.3 – Truncated deployment surface

Therefore, after readjusting (5.4), the radial equivalent of (5.5) becomes:

$$R \sim f_R^T(r) = f_R\left(r \middle| r_0 \le r \le L\right) = Rayleigh(\sigma_G) \Big/ \left\{F_R(r)\right\}_{r_0}^{L} \qquad r \in [r_0, L] \tag{5.6}$$

where $F_R(r) = 1 - \exp\left\{-r^2/2\sigma_G^2\right\} : \mathbb{R}^+ \mapsto [0,1]$ is the CDF of the Rayleigh PDF. After several manipulations, we obtain:

$$f_R^T(r) = r \exp\left\{\left(L^2 + r_0^2 - 2r^2\right)/4\sigma_G^2\right\} \Big/ 2\sigma_G^2 \sinh\left\{\left(L^2 - r_0^2\right)/4\sigma_G^2\right\} \qquad r \in [r_0, L] \tag{5.7}$$

As it will be explained later on, the CDF of (5.7) is also needed in order to generate random samples. Following some analysis, and with the support of Appendix-B, we then get:

$$\begin{aligned} F_R^T(r) = \Pr(R \le r) &= \int_{\tilde{r}=r_0}^{r} f_R^T(\tilde{r})\, d\tilde{r} \qquad r \in [r_0, L] \\ &= \exp\left\{\left(L^2 - r^2\right)/4\sigma_G^2\right\} \cdot \sinh\left\{\left(r^2 - r_0^2\right)/4\sigma_G^2\right\} \Big/ \sinh\left\{\left(L^2 - r_0^2\right)/4\sigma_G^2\right\} \end{aligned} \tag{5.8}$$

In Figure 5.4 the analytical PDF and CDF for the prolonged and truncated internodal density are accordingly plotted, where from the CDF curve the authenticity of the derivation is revealed.

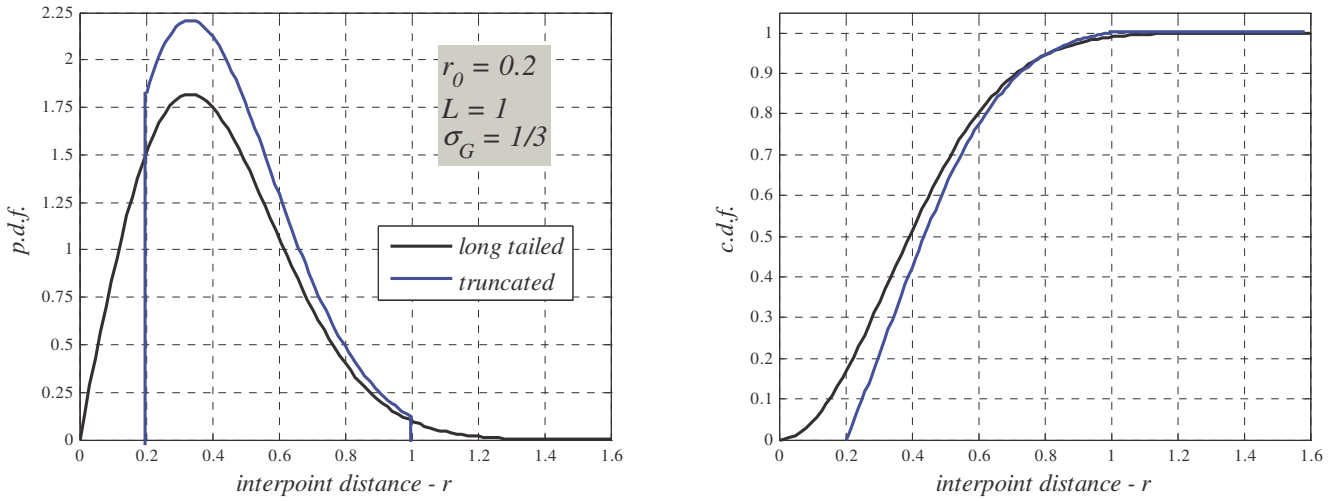

Figure 5.4 – Analytical plots for the internodal distance distribution

5.3.2 – Path-Loss PDF

Now, the aim is to obtain a PDF for the average PL over the intended Gaussian geometry and the supported surface region, namely:

$$w\left(r \sim f_R^T(r)\right) \equiv \overline{L_{PL}(r)}_{dB} = \left\{\alpha + \beta \log_{10}(r)\right\} \sim f_W(w) \qquad r \in [r_0, L] \tag{5.9}$$

where for theoretical convenience we assigned this average power loss to some RV $w = w(r) : \{0 < r_0 \le r \le L\} \mapsto \mathbb{R}_+^*$. And, as shown in Figure 5.5, the values of w are exclusively limited to $(w_0, w_L) \in \mathbb{R}_{+,*}^2 : w_L > w_0$.

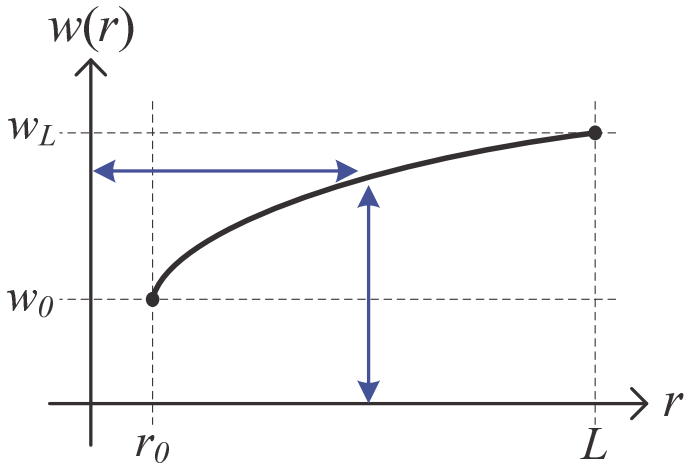

Figure 5.5 – Mapping truncated radius to the average path-loss

Further, in order to obtain the density of w, the transformation function must be:

- Continuous: $\lim_{r \to \delta} w(r) = w(\delta)$ for $\forall \delta \in [r_0, L]$.
- Memoryless: output at a given moment is only dependant on the input at the same instant.
- Bijective: a unique $r \leftrightarrow w$ correspondence as illustrated by the arrows of Figure 5.5.

Substantiating the above for the treated average PL, allows us to express the distribution of w by the derivation of (5.10).

$$
\begin{aligned}
f_W(w) &= f_R^T\left(r=r(w)\right)\Big/\left|dw(r)/dr\right|_{r=r(w)} = f_R^T\left(10^{(w-\alpha)/\beta}\right)\Big/\left|\beta/\ln(10)\,r\right|_{r=10^{(w-\alpha)/\beta}} \\
&= \left\{\ln(10)\exp\left\{\left(L^2+r_0^2\right)\Big/4\sigma_G^2\right\}\Big/2\beta\sigma_G^2\sinh\left\{\left(L^2-r_0^2\right)\Big/4\sigma_G^2\right\}\right\} \\
&\quad\times 10^{2(w-\alpha)/\beta}\cdot\exp\left\{-10^{2(w-\alpha)/\beta}\Big/2\sigma_G^2\right\}\cdot\mathbf{1}\left(w_0\le w\le w_L\right)
\end{aligned}
\tag{5.10}
$$

For certainty purposes, we can quickly verify the legitimacy of the above density function by noting that $f_W(w)\ge 0$ for $\forall w\in\mathbb{R}$ because the various exponential parts will inherently be positive; and given that $L>r_0$, the hyperbolic sine component will also produce a positive value. Also, it can analytically be demonstrated that (5.10) integrates to unity.

5.3.3 – Large-Scale Fading PDF

In this part, we will complement the PL density model of (5.10) by incorporating the stochastic influence of channel scatterers. Namely, we intend to find the distribution of:

$$
L_{PL}(r)_{dB} = \left[\left\{w(r)\sim f_W(w)\right\}+\left\{\Psi_{S-dB}\sim\mathcal{N}_S\left(0,\sigma_\Psi^2\right)\right\}\right]\sim f_{L_{PL}}(l)\qquad r\in[r_0,L] \tag{5.11}
$$

Since the average PL $w(r)$ and the shadowing factor Ψ_{S-dB} are statistically independent; i.e. $\mathrm{E}\left[w(r)\cdot\Psi_{S-dB}\right]=\mathrm{E}\left[w(r)\right]\cdot\mathrm{E}\left[\Psi_{S-dB}\right]$; therefore, the overall large-scale fading PDF $f_{L_{PL}}(l)$ can be obtained by convolving their respective densities, where $l\in\mathbb{R}_+^*$ is a sample value of the PL in dB:

$$
f_{L_{PL}}(l) = \left(f_W * f_\Psi\right)(l) = \int_{\tau=-\infty}^{\infty} f_W(\tau)\,f_\Psi(l-\tau)\,d\tau \triangleq \int_{\tau=-\infty}^{\infty} f_0(\tau)\,d\tau \tag{5.12}
$$

As for $f_W(\tau)$, it is obtained from (5.10) after switching w to the integration variable τ. And, the shadowing contribution $f_\Psi(l-\tau)$ was previously derived in (3.88). All together, the integrand of (5.12) is then obtained as follows:

$$f_0(\tau) = f_W(\tau)\, f_\Psi(l-\tau) = f_W(\tau)\, \mathcal{N}_S\left(l, \sigma_\Psi^2\right) \qquad \tau \in [w_0, w_L]$$

$$= \left\{ \ln(10) \exp\left\{ \left(L^2 + r_0^2\right) / 4\sigma_G^2 \right\} / 2\sqrt{2\pi}\beta\sigma_\Psi\sigma_G^2 \sinh\left\{ \left(L^2 - r_0^2\right) / 4\sigma_G^2 \right\} \right\}$$
$$\times \exp\left\{ -10^{2(\tau-\alpha)/\beta} / 2\sigma_G^2 \right\} \cdot \underbrace{10^{2(\tau-\alpha)/\beta}}_{\text{Equation (3.92)}} \cdot \exp\left\{ -(\tau-l)^2 / 2\sigma_\Psi^2 \right\}$$

$$= \left\{ \ln(10) \exp\left\{ \left(L^2 + r_0^2\right) / 4\sigma_G^2 \right\} \cdot 10^{-2\alpha/\beta} / 2\sqrt{2\pi}\beta\sigma_\Psi\sigma_G^2 \sinh\left\{ \left(L^2 - r_0^2\right) / 4\sigma_G^2 \right\} \right\}$$
$$\times \exp\left\{ -10^{2(\tau-\alpha)/\beta} / 2\sigma_G^2 \right\} \cdot \underbrace{\exp\left\{ 2\ln(10)\tau/\beta - (\tau-l)^2 / 2\sigma_\Psi^2 \right\}}_{\text{Equation (3.102)}}$$

$$= \frac{\ln(10) \cdot 10^{2(l-\alpha)/\beta}}{\sqrt{2^3\pi}\beta\sigma_\Psi\sigma_G^2 \sinh\left\{ \left(L^2 - r_0^2\right) / 4\sigma_G^2 \right\}} \cdot \exp\left\{ \left(L^2 + r_0^2\right) / 4\sigma_G^2 + \left(\sqrt{2}\ln(10)\sigma_\Psi / \beta \right)^2 \right\}$$
$$\times \exp\left\{ -10^{2(\tau-\alpha)/\beta} / 2\sigma_G^2 \right\} \cdot \exp\left\{ -\left(\tau - \left\{ l + 2\ln(10)\sigma_\Psi^2 / \beta \right\} \right)^2 / 2\sigma_\Psi^2 \right\} \tag{5.13}$$

After inserting (5.13) into (5.12), we then get:

$$f_{L_{PL}}(l) = \frac{\ln(10) \cdot 10^{2(l-\alpha)/\beta}}{\sqrt{2^3\pi}\beta\sigma_\Psi\sigma_G^2 \sinh\left\{ \left(L^2 - r_0^2\right) / 4\sigma_G^2 \right\}} \cdot \exp\left\{ \left(L^2 + r_0^2\right) / 4\sigma_G^2 + \left(\sqrt{2}\ln(10)\sigma_\Psi / \beta \right)^2 \right\}$$
$$\times \int_{\tau=w_0}^{w_L} \exp\left\{ -10^{2(\tau-\alpha)/\beta} / 2\sigma_G^2 \right\} \cdot \exp\left\{ -\left(\tau - \left\{ l + 2\ln(10)\sigma_\Psi^2 / \beta \right\} \right)^2 / 2\sigma_\Psi^2 \right\} d\tau \tag{5.14}$$

At this point, we may further simplify (5.14) by noticing that the second exponential of the integrand resembles a Gaussian PDF with distribution: $\mathcal{N}_\tau\left(l + 2\ln(10)\sigma_\Psi^2 / \beta, \sigma_\Psi^2 \right)$

along the τ variable. As a consequence of this observation, the indicated expression can be simplified by standardizing it to $\mathcal{N}_{\mu}(0,1)$ using the following transformation:

$$\mu = \left\{ \tau - \left(l + 2\ln(10)\sigma_{\Psi}^2 / \beta \right) \right\} \Big/ \sigma_{\Psi} \tag{5.15}$$

where we can isolate for $\tau = \sigma_{\Psi}\mu + l + 2\ln(10)\sigma_{\Psi}^2/\beta$, and thus: $d\tau = \sigma_{\Psi} d\mu$. After taking into account these remarks, followed by several maneuvering steps, we finally obtain in (5.16) the exact closed-form PDF of the large-scale fading between a reference AP and a random node deployed over a truncated Gaussian pattern.

$$f_{L_{PL}}\left(l, \vec{\Lambda}\right) = \frac{\ln(10)\cdot 10^{2(l-\alpha)/\beta}}{\sqrt{2^3\pi}\cdot\beta\cdot\sigma_G^2\cdot\sinh\left\{\left(L^2 - r_0^2\right)/4\sigma_G^2\right\}} \cdot \exp\left\{ \left(L^2 + r_0^2\right)/4\sigma_G^2 + \left(\sqrt{2}\ln(10)\sigma_{\Psi}/\beta\right)^2 \right\}$$
$$\times \int_{\mu=\mu_0(l)}^{\mu_L(l)} \exp\left(-\mu^2/2\right) \cdot \exp\left(-10^{2\sigma_{\Psi}\mu/\beta} \cdot 10^{2\left\{\beta\cdot(l-\alpha)+2\ln(10)\sigma_{\Psi}^2\right\}/\beta^2} \Big/ 2\sigma_G^2 \right) d\mu$$

$$0 < \tilde{l}_0 \lesssim l \lesssim \tilde{l}_L < \infty$$

- $\vec{\Lambda} = \{\alpha, \beta, \sigma_{\Psi}, r_0, L, \sigma_G\} \in \mathbb{R}_{+,*}^6$
- $\mu_0(l) = \left\{ \alpha - l + \ln\left(r_0^{\beta/\ln(10)} / 10^{2\sigma_{\Psi}^2/\beta} \right) \right\} \Big/ \sigma_{\Psi}$
- $\mu_L(l) = \left\{ \alpha - l + \ln\left(L^{\beta/\ln(10)} / 10^{2\sigma_{\Psi}^2/\beta} \right) \right\} \Big/ \sigma_{\Psi}$
- $\tilde{l}_0 = \alpha + \beta\log_{10}(r_0) - 3\sigma_{\Psi}$
- $\tilde{l}_L = \alpha + \beta\log_{10}(L) + 3\sigma_{\Psi}$ ■

(5.16)

And as suggested by $f_{L_{PL}}(l) = f_{L_{PL}}\left(l, \vec{\Lambda}\right)$, the derived stochastic expression has generic parameters, and it is therefore adaptable to different cellular dimensions, spatial intensities, channel parameters, and operating conditions.

5.4 – Experimental Analysis and Results

5.4.1 – Estimation Model

In order to verify the analytical derivation that was obtained above, in this section we will perform a set of stochastic simulations. But before we begin, it is necessary to explicitly define and analyze the model for numerical estimation. To do this, our derivation in this subsection will be based on the estimation of some representative PDF $f_Z(z): \mathbb{R} \mapsto \mathbb{R}^+$. The attained principles and results may then be personalized for the approximation of interpoint and large-scale fading density functions.

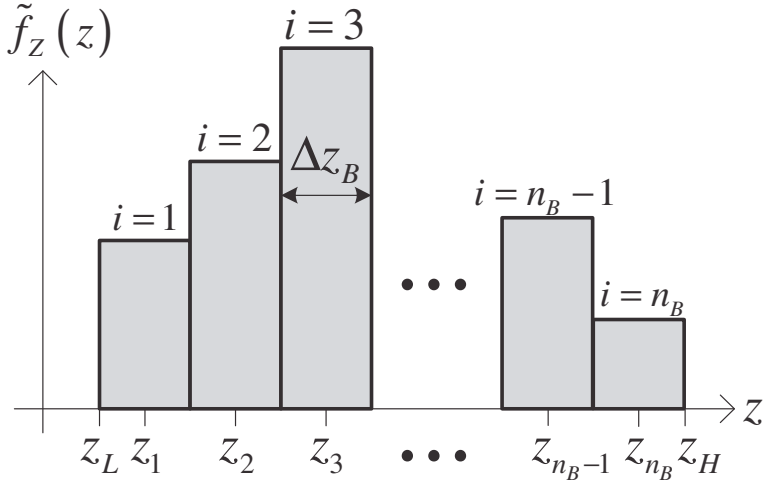

Figure 5.6 – Illustrating density estimation from random samples

To proceed, we respectively characterize the lower/higher extremities of the density domain by: $z_L = \inf \vec{z}_S$ and $z_H = \sup \vec{z}_S$, such that $\vec{z}_S \in \mathbb{R}^{n_S}$ is a vector of $n_S \in \mathbb{N}^*$ i.i.d. randomly generated samples. For density approximation, $n_B \in \mathbb{N}^*$ histogram bins are considered, where consecutive adjacent bars are aligned with no gap among them as depicted by Figure 5.6. Further, all bins are assumed to have equal width of size: $\Delta z_B = (z_H - z_L)/n_B$. For analytical purposes, the fundamental bin positioned at the origin may then be expressed by:

$$\delta_B(z) = \mathbf{1}(|z| \le \Delta z_B/2) \tag{5.17}$$

As for bins center position $z_i \in \mathbb{R}$, it can be shown to equal:

$$z_i = z_L + (i - 1/2) \cdot \Delta z_B \qquad i = 1, 2, \cdots, n_B \tag{5.18}$$

At this level, we can straightforwardly remark that the probability for each bin is thus:

$$\Pr\{z \in D_i\} = \pi_i^o / n_S \qquad i = 1, 2, \cdots, n_B \tag{5.19}$$

where $\pi_i^o \in \mathbb{N}^*$ is the number of occurrence per bar, such that the total number of samples is $n_S = \sum_{i=1}^{n_B} \pi_i^o$, and $D_i = \left\{ (z, z_i) \in \mathbb{R}^2, \Delta z_B \in \mathbb{R}_+^* \;\middle|\; |z - z_i| \le \Delta z_B / 2 \right\}$ is the associated domain. Further, from stochastic analysis, the probability measure for some arbitrary event A in sample space Ω, mapped to a RV Z element in $\mathbb{R}$, is given by:

$$\Pr\{z \in D\} = P\left(A \subseteq \Omega : Z(A) \in D\right) = \int_{z \in D} f_Z(z)\, dz \tag{5.20}$$

In light of (5.20), we can approximate the probability value by:

$$\Pr\{z \in D_i\} \approx f_Z(z \in D_i)\, \Delta z_B \qquad i = 1, 2, \cdots, n_B \tag{5.21}$$

With the insight of (5.19) and (5.21), we solve for the density function and then aggregate for all bins so as to obtain an exclusive mathematical notation for PDF estimation.

$$f_Z(z) \approx \tilde{f}_Z(z) = \sum_{i=1}^{n_B} \frac{\pi_i^o}{n_S \cdot \Delta z_B} \cdot \delta_B(z - z_i) \tag{5.22}$$

Several instrumental remarks regarding this estimation model can be noted. In part, the approximation can be enhanced by: increasing the number of samples, increasing the amount of

bars, or equally reducing the bin width. As a consequence, MC results would idealistically match the theoretical analysis provided:

$$f_Z(z) = \lim_{\substack{n_S \to \infty \\ \Delta z_B \to 0}} \lim_{n_B \to \infty} \tilde{f}_Z(z) = \lim_{\substack{n_S \to \infty \\ \Delta z_B \to 0}} \lim_{n_B \to \infty} \sum_{i=1}^{n_B} \frac{\pi_i^o}{n_S \cdot \Delta z_B} \cdot \delta_B(z - z_i) \tag{5.23}$$

5.4.2 – Internodal Random Generation

To simulate the channel behavior, we initially need to generate random values for interpoint distances between the AP and an arbitrarily deployed node. In particular, we produce a stochastic sample $\hat{u} \sim \mathcal{U}(0,1)$, such that $\mathcal{U}(a,b)$ over $[a,b] \mapsto [0,1/(b-a)]$ is a uniform distribution for $\forall x \in \mathbb{R} : \exists a,b \in \mathbb{R}^2$. Next, we assign this value to the CDF of the interpoint density derived in (5.8), i.e. $F_R^T(\hat{r}) = \hat{u}$. Then, provided the corresponding ICDF is available in closed-form, we solve for the interspace distance: $\hat{r} = \left(F_R^T\right)^{-1}(\hat{u})$. To emphasize the various interdependence of this generation, the above process can be represented by:

$$G(\hat{u}, r_0, L, \sigma_G) : \left\{ \exists \hat{u} \in \mathbb{R}_+^* : 0 < \hat{u} < 1 \right\} \mapsto (r_0, L) \tag{5.24}$$

And with some derivation, it can be shown that:

$$\hat{r} = \sigma_G \sqrt{-2 \cdot \ln\left\{ (1-\hat{u}) \cdot \exp\left(-r_0^2 / 2\sigma_G^2\right) + \hat{u} \cdot \exp\left(-L^2 / 2\sigma_G^2\right) \right\}} \tag{5.25}$$

Equipped with the above analysis, we could now verify the generation process by the formation of 10,000 random samples. From the results, a 100 bin histogram is constructed and scaled as explained in the PDF estimation model of the previous subsection. In Figure 5.7, the MC approximation and the analytical internodal distribution derived in (5.7) are accordingly plotted. The results clearly demonstrate the generation accuracy.

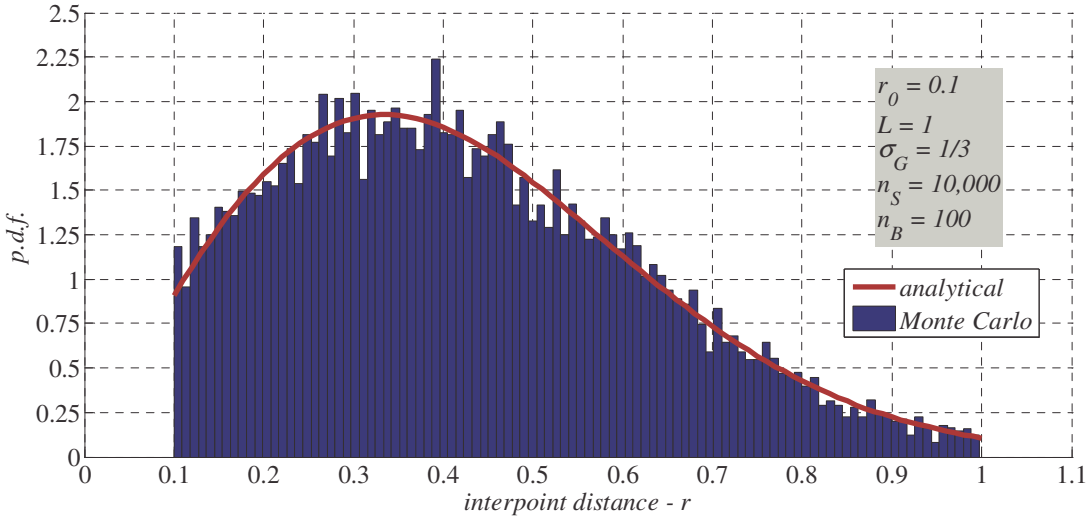

Figure 5.7 – Internodal distribution through analysis and simulations

5.4.3 – MC Simulations

To experimentally evaluate the channel behavior, we will utilize parameters from the IEEE 802.20 mobile broadband wireless access (MBWA) standard [52]. For a concise yet elaborate overview of MBWA peculiarities, interested readers may for instance refer to [77] and [78]. Generally speaking, MBWA supports three channel environments: urban macrocell, suburban macrocell, and urban microcell. In this chapter, we will specifically authenticate our analytical derivation based on the urban microcell channel detailed in Table 5.1. Parameters and investigation results of the other two channels were previously reported in [79].

Table 5.1 – MBWA channel model for urban microcell

IEEE 802.20 Propagation Parameters		
Propagation Model :	*COST*-231 *Walfisch-Ikegami*	
Operating Frequency :	1.9 GHz	
Support Range :	$r_0 = 20 \text{ m} \le r \le L$ $200 \le L \le 300 \text{ m}$	
Path Obstruction :	*LOS*	*NLOS*
Channel - Loss :	$\alpha = 30.18$ dB $\beta = 26$ dB	$\alpha = 34.53$ dB $\beta = 38$ dB
Shadowing :	$\sigma_\Psi = 4$ dB	$\sigma_\Psi = 10$ dB

To obtain an estimate of the large-scale fading distribution, we will utilize the elaborations reported in the previous two subsections. From these steps, the MC estimation algorithm of Figure 5.8 is obtained. This algorithm is basically divided into three major parts. First, random instances of the large-scale fading are obtained based on the stochastic nature of nodes geometry and shadowing. Once completed, a histogram for the PL frequency of occurrence is constructed with bin resolution n_B. Also, due to its faster convergence, the cumulative frequency is realized using a recursive relationship. Then, both of these values are appropriately scaled so as to produce the density of the channel attenuation.

Algorithm 14 - Path-Loss Density Function via Monte Carlo Simulation

Require: $\alpha \in \mathbb{R}_+^* \quad \beta \in \mathbb{R}_+^* \quad \sigma_\Psi \in \mathbb{R}_+^* \quad r_0 \in \mathbb{R}_+^*$
$L \in \mathbb{R}_+^* \quad \sigma_G \in \mathbb{R}_+^* \quad n_S \in \mathbb{N}^* \quad n_B \in \mathbb{N}^*$
Initialize: $\hat{l}_L = \infty \quad \hat{l}_H = 0 \quad \pi_i^O = 0 \quad i = 1, 2, \cdots, n_B$
for $j = 1, 2, \cdots, n_S$ **do**
  Generate RV: $\hat{u}_j \sim \mathcal{U}(0,1) \rightarrow \hat{r}_j = G\left(\hat{u}_j, r_0, L, \sigma_G\right) \sim f_R^T(r)$
  Generate RV: $\hat{n}_j \sim \mathcal{N}(0,1) \rightarrow \hat{\psi}_j = \sigma_\Psi \hat{n}_j \sim \mathcal{N}_S\left(0, \sigma_\Psi^2\right)$
  Compute: $\hat{l}_j = L_{PL}\left(\hat{r}_j\right)_{dB} = \alpha + \beta \log_{10}\left(\hat{r}_j\right) + \hat{\psi}_j \sim f_{L_{PL}}\left(l, \vec{\Lambda}\right)$
  if $\left\{\hat{l}_j < \hat{l}_L\right\}$ **then** $\hat{l}_L \coloneqq \hat{l}_j$ **end if** & **if** $\left\{\hat{l}_j > \hat{l}_H\right\}$ **then** $\hat{l}_H \coloneqq \hat{l}_j$ **end if**
end for
Compute: $\Delta l_B = \left(\hat{l}_H - \hat{l}_L\right) / n_B$
for $j = 1, 2, \cdots, n_S$ **do**
  for $i = 1, 2, \cdots, n_B$ **do**
    if $\left\{\left|\hat{l}_j - \hat{l}_L - (i - 1/2)\Delta l_B\right| \le \Delta l_B / 2\right\}$ **then**
      $\pi_i^O \coloneqq \pi_i^O + 1$ **break for**
    end if
  end for
end for
Initialize: $\pi_1^C = \pi_1^O$
for $i = 2, 3, \cdots, n_B$ **do**
  $\pi_i^C = \pi_i^O + \pi_{i-1}^C$
end for
Return/Compute: $\left\{\hat{r}_j;\ \hat{l}_j\right\} : j = 1, 2, \cdots, n_S$
$\left\{l_i;\ pdf_i;\ cdf_i\right\} = \left\{\hat{l}_L + (i - 1/2)\Delta l_B;\ \pi_i^O / n_S \Delta l_B;\ \pi_i^C / n_S\right\} : i = 1, 2, \cdots, n_B$

Figure 5.8 – Pseudocode for estimating the large-scale fading distribution

The computational running time complexity of the estimation algorithm of Figure 5.8 can be assessed by:

$$O\left(T_{cost}\left(\vec{\Lambda}, n_S, n_B\right)\right) \sim O\left(n_S n_B\right) \tag{5.26}$$

where attributes of $\vec{\Lambda}$ are defined in (5.16). Taking into account the observations made for (5.23), at present we remark that an increase in the sample size and the quantity of bins improves the density estimation at the cost of complexity. Consequently, from an estimation point of view, these competing requirements will result in a computational cost-benefit tradeoff.

In Figure 5.9, we substantiated our exact analytical derivation of (5.16) by means of random instances over two particular IEEE 802.20 channels: line-of-sight (LOS) and non-LOS (NLOS) propagations. From Table 5.1, we note that the size of the supported urban cell can go up to 300 m; in the simulation however, we assumed a transmission radius of 250 m.

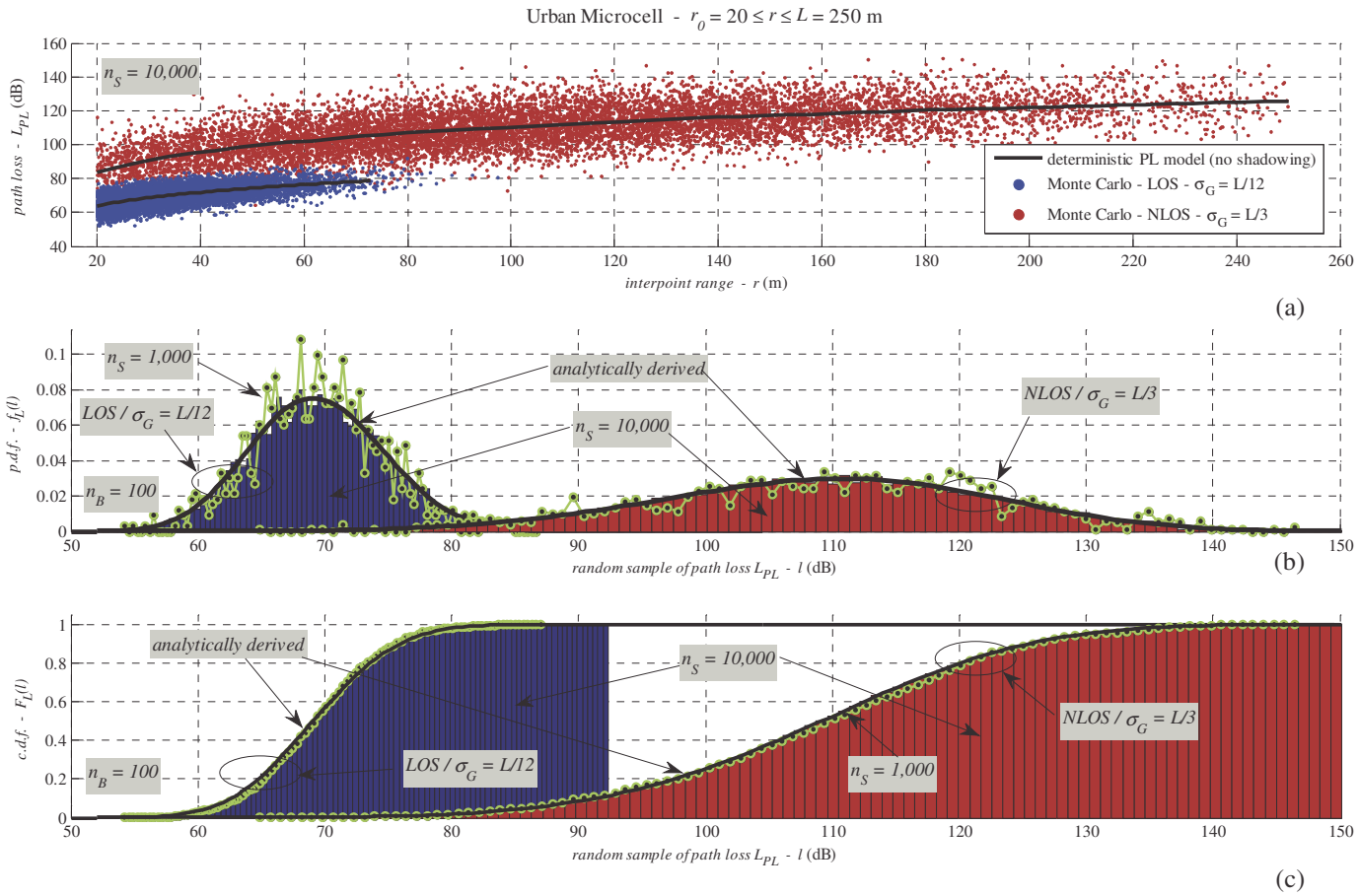

Figure 5.9 – Substantiating analytical derivation using the IEEE 802.20 channel

The plot of Figure 5.9a shows a scatter display based on 10,000 MC samples for each of the channel cases. Particularly for the LOS setting, we considered a densely populated network in the vicinity of the AP with $\sigma_G = L/12$. As for the NLOS channel, the experimentation was performed for spatial intensity $\sigma_G = L/3$, which translates into a sparsely populated network that extends throughout the entire cell. Also, it is interesting to observe that random instances of PL are exclusively limited between r_0 and L. Further, for greater perspective, we overlaid the average PL $\overline{L_{PL}(r)}_{dB}$ onto the scatter points, which is basically an oversimplified deterministic model for the channel-loss. In fact, when compared to MC simulation values, this nonrandom realization gives a justifiable representation of the average decay.

In the plot of Figure 5.9b, based on the above estimation model, algorithm, and the prior scatter diagram, a histogram for the PL density is constructed. In this plot, we clearly note that our analytically derived large-scale fading PDF completely coincides with the 10,000 MC samples over a bin resolution set to 100. For the sake of demonstrating the impact that the size of samples has on the estimation process, we also plotted simulation results with 1,000 random instances. As it can be noted during this situation, PL for the condensed LOS network fluctuation is substantially high; whereas for the scarce NLOS case, it is moderately visible.

Last, in the diagram of Figure 5.9c, the CDF is accordingly obtained from the previous set of PDF plots. In fact, this is achieved by an aggregation of the occurrence followed by a scaling step.

As noted earlier the reported analytical derivation is adaptable to different channel parameters, transmission coverage and spatial intensity. In Figure 5.10, we plotted the large-scale fading density function for LOS and NLOS channels over four network scenarios: $\sigma_G = L/3,\ L/6,\ L/9,\ L/15$. In this figure, it can be observed that as the spatial network constellation varies from highly-centric to sparse; the PL span is accordingly extended. And this is an anticipated outcome because as the network concentration is set farther away from the AP, the amount of power lost in the channel will proportionately augment. By the same token, and because of the nature of the LOS channel, in Figure 5.10 we also note that for a particular intensity level, the PL attenuation median is always smaller when compared to the NLOS counterpart.

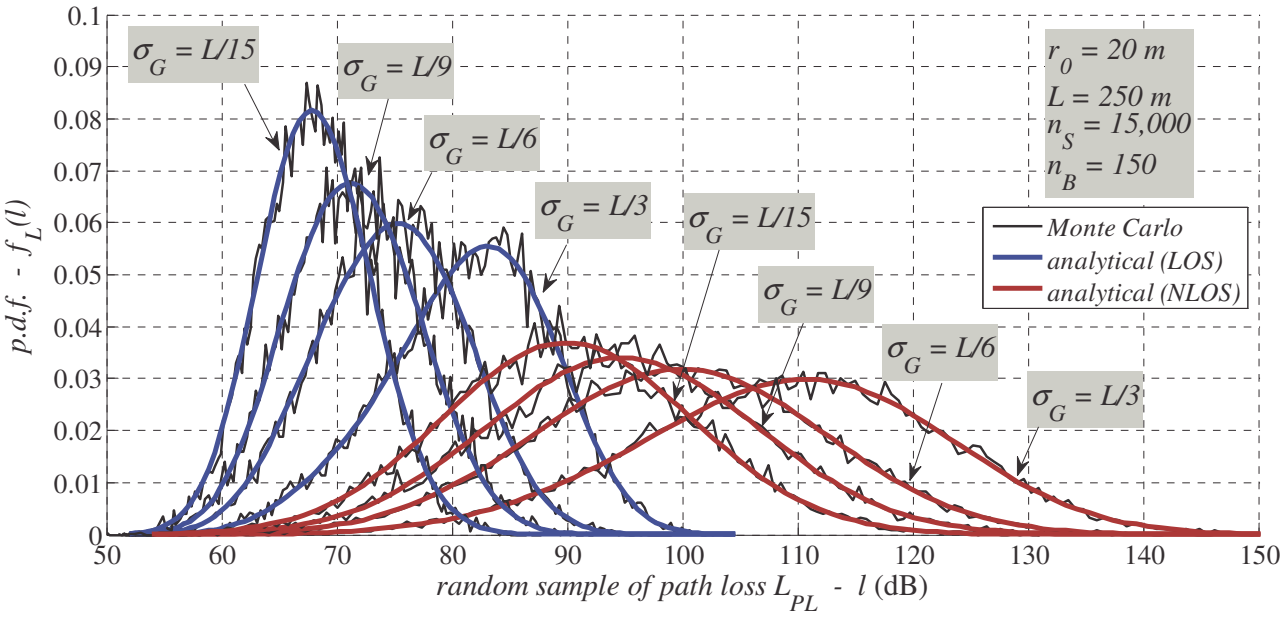

Figure 5.10 – Large-scale fading density functions over various spatial intensities

5.5 – Implications of the Large-Scale Fading Density

Throughout this dissertation, one of the principal objectives of our research investigation was to describe various probabilistic behaviors of random networks by tractably deriving exact closed-form expressions for the large-scale fading density. In fact, these channel-loss PDF results can be instrumental for explicitly approaching a number of network requirements and performance metrics in order to study factors that affect the QoS. Therefore, the purpose of this section is to briefly demonstrate several prospects and implications of the large-scale fading distributions by analytically assessing and detailing the necessary steps for: effective power management, connectivity, and detection capability. Once generically formulated, the actual derivations of these integrity measures for particular random deployment models can be evaluated.

5.5.1 – Power Consumption and Control

It has been identified that nearly 70% of the overall power depletion of a wireless node is attributed to the wireless interface [80]. In other words, this is a clear testament that the radio component is the most power hungry element of mobile units. Therefore, having the ability to analytically profile the channel-loss for an entire random network can be insightful in order to conceive and design sophisticated stochastical protocols that optimize consumption.

Meanwhile, in the event that a mobile is near the cell border; during uplink, the unit is expected to transmit with more power than another terminal located in the surrounding area of the BS. In other words, power control has to be used in order to eliminate the so-called near-far effect [48]. To be precise, in this setup, the power lost in the channel is projected by $f_{L_{PL}}\left(l,\vec{\Lambda}\right)$, and so from (5.27) we can forecast and thus control the necessary EIRP required in order to achieve the desired QoS level or tolerance designated at the receiver.

$$EIRP_{dBW} = P_{RX}\left(r\right)_{dBW} + L_{PL}\left(r\right)_{dB} \tag{5.27}$$

Also, in this scheme, the potential for intercell interference is to be expected. And so devices operating near the border should consider power control so as to minimize possible leakage to neighboring cells. Further, power control based on (5.27) can be enlightening during the analysis for effective horizontal-handoff.

5.5.2 – Outage Probability

On one hand, the outage probability performance metric characterizes the likelihood that the received power falls below a preset minimum threshold $P_{dBW}^{\min} \in \mathbb{R}$ [47]. On the other hand, outage probability may also be interpreted from a channel-loss viewpoint, where the probability that PL extends beyond a maximum target level $L_{dB}^{\max} \in \mathbb{R}_{+}^{*}$ is assessed [50]. In either case, selecting these thresholds is carried in order to meet the required quality of communications. In fact, as shown in (5.28), we may pass from one form to the other by fixing the EIRP of (5.27).

$$\begin{aligned} p_{out} &\triangleq \Pr\left\{P_{RX}\left(r\right)_{dBW} \le P_{dBW}^{\min}\right\} = \Pr\left\{EIRP_{dBW}^{0} - L_{PL}\left(r\right)_{dB} \le EIRP_{dBW}^{0} - L_{dB}^{\max}\right\} \\ &= \Pr\left\{L_{PL}\left(r\right)_{dB} \ge L_{dB}^{\max}\right\} = \int_{l=L_{dB}^{\max}}^{\infty} f_{L_{PL}}\left(l,\vec{\Lambda}\right)dl = \int_{l=L_{dB}^{\max}}^{l_L} f_{L_{PL}}\left(l,\vec{\Lambda}\right)dl \\ &= 1 - \int_{l=0}^{L_{dB}^{\max}} f_{L_{PL}}\left(l,\vec{\Lambda}\right)dl = 1 - \int_{l=l_0}^{L_{dB}^{\max}} f_{L_{PL}}\left(l,\vec{\Lambda}\right)dl \\ &\approx 1 - \int_{l=\tilde{l}_0}^{L_{dB}^{\max}} f_{L_{PL}}\left(l,\vec{\Lambda}\right)dl \end{aligned} \tag{5.28}$$

From this formulation, we observe that outage probability is minimized as the threshold approaches the higher extremity of the channel-loss PDF. Overall, we note that the derived large-scale fading distributions are paramount for quantifying the likelihood for nodal connectivity.

5.5.3 – Detection Capability

As it will be shown, the derived PDF results can also be instrumental for evaluating the surveillance quality of WSNs. To illustrate this, say we have an occurring event located at the origin of the Euclidean plane that emits EM radiation with a steady power $P_{dBW}^{T} \in \mathbb{R}$; we will refer to this point as the target. And, the monitoring area of the WSN that surrounding the target contains $n \in \mathbb{N}^{*}$ randomly positioned sensors. The detection distance of an arbitrary sensor $i \in \mathbb{N}^{*}$ for $1 \le i \le n$ is identified by r_i, which is a subset of $r \in \mathbb{R}_{+}^{*}$ having a distribution function $f_R(r):[r_0, L] \mapsto \mathbb{R}^{+}$. In this setup, the sensing capability for a particular random node is obtained by:

$$\begin{aligned} p_S &\triangleq \Pr\left\{P_{RX}(r)_{dBW} \ge \eta_{dBW}^{S}\right\} = 1 - \Pr\left\{P_{RX}(r)_{dBW} \le \eta_{dBW}^{S}\right\} \\ &= 1 - \Pr\left\{L_{PL}(r)_{dB} \ge P_{dBW}^{T} - \eta_{dBW}^{S}\right\} \end{aligned} \tag{5.29}$$

where $\eta_{dBW}^{S} \in \mathbb{R}$ is the sensor sensitivity. Using (5.29), we then derive in (5.30) a notation for the detection capability:

$$\begin{aligned} P_D &= 1 - \prod_{i=1}^{n}\left(1 - p_S\right) = 1 - \left(1 - p_S\right)^n = 1 - \left(\Pr\left\{L_{PL}(r)_{dB} \ge P_{dBW}^{T} - \eta_{dBW}^{S}\right\}\right)^n \\ &= 1 - \left\{\int_{l=P_{dBW}^{T}-\eta_{dBW}^{S}}^{\infty} f_{L_{PL}}\left(l, \vec{\Lambda}\right) dl\right\}^n \approx 1 - \left\{1 - \int_{l=\tilde{l}_0}^{P_{dBW}^{T}-\eta_{dBW}^{S}} f_{L_{PL}}\left(l, \vec{\Lambda}\right) dl\right\}^n \end{aligned} \tag{5.30}$$

To be exact, this expression is a metric for successful detection of an event at the target by n sensors [81]. In fact, this indicator is a key criterion in quantifying the performance of WSNs.

5.6 – Conclusion

The concept of random networks is inevitable in many wireless network situations. In particular, a random LWN constructed by a Gaussian profile has been considered due to its spatial flexibility for mobile and air deployed nodes. Precisely, the Gaussian scheme is easily malleable and can shift from a sparse to a dense network by a simple modification to the spatial intensity through the SD of the geometrical pattern.

Meanwhile, PL is a necessary element in order to understand, analyze, optimize, control and design RF network structures. For the Gaussian network geometry, the large-scale fading between a reference AP and an arbitrary node is only possible using MC simulations, with no analytical equivalent. As a consequence, in this chapter, we generically found an exact closed-form expression for the large-scale fading density that supports different: channel parameters, operating conditions, cellular sizes, and spatial intensities.

In fact, in doing so we progressed through various algebraical steps, where a random Gaussian network was modeled to deploy over a truncated surface region delimited radially between r_0 and L . Although for mobile communications the RCR ratio is generally superior by severalfold; we nonetheless took the close-in range into account in order to ensure a precise and accurate characterization of the channel-loss, and also for the sake of obtaining a generic result. Furthermore, shortening the spatial distribution to some predefined value L was applied, because in addition to generalizing the outcome, it will explicitly incorporate the cellular size within the analytical derivation of the large-scale fading density. Hence, it will enable greater leverage during network analysis and design.

Following the theoretical derivation, we then validated, analyzed, and discussed the result while comparing it to MC simulation techniques based on IEEE 802.20 specifications.

Finally, we identified various implications and prospects for the uncovered large-scale fading PDF results derived in this chapter and those that preceded it. In particular, we discussed various means useful for analytically quantifying critical QoS metrics, such as: power consumption, outage probability, and detection capability. We also provided the corresponding expressions for explicitly gaining theoretical insight to these random-based LWNs.

Chapter 6

Conclusion and Future Work

6.1 – Overall Synopsis

The broad objective for next generation wireless communications is to design networks that support ubiquitous connectivity, for a growing populace, over limited resources. Indeed, managing and planning such LWNs is complex, and optimizing its overall performance is relatively intricate to realize. To tackle this huge undertaking, diverse technical pathways can be regarded ranging from experimental techniques to analytical descriptions. In particular, insight into various aspects of the network can gradually be gained by modeling the deployment. Specifically, spatial modeling has emerged as an important topic worthy of investigation, not only in pure and applied applications, but also in communications and network theory. Hence, in this dissertation, we attempted to better understand the fundamentals of cellular radio networking by overlaying the principle of spatial geometry.

Despite some breakthroughs, until now, the concept of network geometry has been treated in a limited way. Therefore, in addition to surveying the notion of wireless spatial networking, we also tried to make some cohesive organization out of a still disordered research subject in order to serve as a guide throughout this treatment and beyond. From this arrangement, we identified numerous ways for obtaining a spatial pattern. Of course, the natural approach for constructing a LWN would be to find the actual location of users. However, besides empirical complications, this method does not produce well-behaved tractable results. Alternatively, stochastic geometry has been considered as an effective workaround for emulating the network and assessing its performance. As a consequence, the field of stochastic spatial modeling has attracted some researchers; yet, there are numerous aspects that require further insight.

In particular, quantifying the wireless propagation for random structures is critical for evaluating essential network metrics because the channel-loss indicator is the most fundamental

aspect in RF communications. To be precise, knowing or predicting the channel-loss behavior for mobile users is utterly dependent on the network geometry. Typically, the location of users is considered deterministic, and so the traditional approach is only based on modeling the random channel as a function of PL and shadowing. From this, we notice that the channel propagation is by itself an area of focus; and probabilistic network deployment is another standalone theme. Thus, the idea in this body of work was to cohesively amalgamate these two paradigms together by joining the randomness of the channel and the location of users in order to obtain an improved stochastic model for the large-scale fading density. As a result, the goal of this research consisted on conducting an in-depth study by analyzing important spatial models and verifying their effect on transmission losses.

Pursuing this further, it is important to highlight that large-scale fading is principal for all wireless links because it is the main attenuating source in the transmission. Also, its associated distribution function is a rudimentary element for profiling the channel behavior for a variety of random network models. Actually, obtaining the channel-loss density for multiple-access networks is realized through non-explicit MC simulations. Clearly, this estimation process via random numerical experimentation is both: computationally inefficient, and is analytically intractable. Therefore, theoretical parameterization of the large-scale fading PDF through variable notations for channel and network characteristics was established.

To be specific, we investigated the homogeneous random network model intended exclusively for MCN and UCN deployments. For these models, we analytically determined the exact closed-form distribution function of the large-scale fading among a reference AP and a randomly positioned user. In fact, we for the first time provided a precise and well-rounded density formulation that considered at once: the lattice profile, the users' random geometry, the effect of the far-field phenomenon, the PL behavior, and the stochastic impact of in-field scatterers. Indeed, the reported analytical PDFs were intentionally derived based on generic parameters. Therefore, the modeling results are compatible with an array of cellular networks having a unique: purpose, layout, scale, coverage size, and radio specifications; provided their designated channel propagation and spatial values are accordingly inserted in the stochastical expressions. As a case in point, the PL predictor for the MCN model is compliant to a host of networks, including: femtocells, picocells, microcells, and macrocells. Likewise, the large-scale fading distribution for UCN model can be useful during the analysis of a flexibly versatile nodal

deployment in sectored layers, annulus regions, and circular cells. Overall, these channel-loss PDFs will provide analytical insight into practical concerns during design and planning phases.

Furthermore, we also looked at the Gaussian random network structure, which is generally accepted for emulating snapshots of mobile units in a cellular-based architecture, and for modeling airborne deployments. For this tunable spatial distribution, we derived an explicit closed-form notation for the large-scale fading density between a set of Gaussianly deployed nodes with reference to an AP. Moreover, we explored the large-scale fading behavior for different deployment situations, such as instances where the size of the cell is unchangeable but the spatial intensity of the truncated Gaussian distribution is variable.

On the whole, the channel-loss distributions for MCN, UCN, and Gaussian random network models were verified using MC simulations. Although these probabilistic statements were generally formulated, yet the computational testing was founded on the MBWA propagation parameters. As expected, the random experimentations for the PL distributions appropriately match the theoretical results; thus signifying the correctness of the analysis.

Besides the explicit derivation for the PL distributions, an important portion of this dissertation was devoted to the conceptualization of inhomogeneous spatial algorithms. In fact, we considered this task because there was still a serious need to find robust, yet straightforwardly configured models that suitably emulates the most likely spatial position of random nodes over a specific deployment site. Even though formulating such geometrical nodal structure is a complex endeavor, we nonetheless attempted this challenge by proposing the ASD deployment principle. In general, this systematic mechanism is founded on three cascading steps: cluster planning, geometrical analysis, and synthesis of subnetworks. Also, apart from extensive empirical scrutiny, the ASD emulation technique has the advantage for only requiring limited geometrical-based network planning entries, which can be dependent on minimal social observations of the project site or by means of plausible assumptions. As a result, this concept produces a flexible deployment method useful to effectively plan the spatial traffic in order to realize a heterogeneous random network, while still preserving the stochastic character of users' position.

Equipped with the ASD principle, we then conceived various algorithms for generating heterogeneous random networks for UCN and MCN structures. Namely, we first derived a controlled inhomogeneous simulator tool for UCN deployment, which is generally practical for emulating a suburban network, where spatial clustering is subject to terrain features. We also

produced an uncontrolled UCN counterpart for non-homogeneous deployments. This latter algorithm is in fact useful when less information about the deployment footprint is known; thus it is particularly appropriate for automatically generating an inhomogeneous network in an arbitrary manner. Moreover, we applied the ASD procedure so as to randomly assemble a LWN for an urban-based wide coverage area. From this, we created a heterogeneous MCN modeling approach, where spatial clustering relies on the position of the BSs and the sectoring capability of its antennas. Altogether, these algorithms were generically developed; therefore, they could be designed for different: network situations, planning complexities, predefined assumptions, geographical locations, sizes, and scales. Evidently, the outcome of this research will be a significant step towards modeling and understanding stochastical schemes; especially emerging multi-scale and multi-coverage wireless networks. Actually, the scalability feature of the inhomogeneous algorithms makes these deployment models particularly feasible in response to a continuous increase of users' concentration and connectivity in current and future generation networks. Practically, these spatial-level tools are expected to serve as effective emulation mechanisms aimed for cellular mobile operators, deployment specialists, and system developers in order to examine the quality and performance for a specific network model.

Overall, we provided crucial breakthroughs in the area of spatial geometry so as to perform channel-level and system-level analysis of large random patterns. Indeed, the presented research is concentrated in the direction of network modeling by considering the fundamental results and interactions between: random geometry, channel losses, and inhomogeneous deployment. In fact, the broad idea was to: spatially emulate LWNs, extract interesting observations from the modeled structures, and utilize the results in order to better comprehend the characteristics, properties, and limitations of these networks. Accordingly, these original results are insightful for: planning the network deployment, performing connectivity analysis, and designing effective resource utilization intended for different cellular-based systems.

6.2 – Future Directions

Overall, the novel contributions of our presented work can be used as a foundation for diverse research directions. Therefore, before closing this dissertation, we will recommend some additional extensions by means of modeling, so as to further advance our insight into the concept of random networks.

- Analytical Tractability: It is technically valuable to assess critical QoS metrics for random network models. However, reusability of the derived channel-loss densities for these measures may sometimes result in an explicit, yet complicated formulation. Therefore, it would be interesting to analytically approximate the exact closed-form derivations by simpler expressions, while still preserving the generic and reliable properties of the notations, so that the evaluation of performance indicators is facilitated.

- Decentralized Connectivity: This body of work focused in part on determining stochastical expressions for the large-scale fading distributions over centralized communications. Since decentralized multihop networking continues to progress, it then becomes natural to also attempt to understand the behavior of channel losses under this condition. Thus, for future endeavors, it would be interesting to expand our research by attempting to derive channel-loss predictors for ad hoc interconnection.

- Spatial Inhomogeneity: In this research, we developed the ASD algorithm in order to generate a random heterogeneous deployment for UCN and MCN models. For this principle, it would be interesting to conceptualize an approach for characterizing the inhomogeneous level of a random spatial pattern via an index.

- Mobility and Dimensionality: For the purpose of obtaining solvable models, the analyzed random emulation techniques in this dissertation were considered motionless and over a flat Euclidian plane. To further add realism to the deployment, the effect of mobility and dimensionality can be superimposed to the random nodes of the network model. However, the challenge in this endeavor is to discover appropriate models that are reflective of users' patterns. Also, this spatio-temporal combination should be implemented in a careful manner in order to enable the deduction of well-behaved results.

On the whole, we hope that the motivation, analysis and insight of this dissertation will inspire, stimulate and foster research interest in order to exploit, complement and advance the reported stochastical modeling results, so as to enhance our understanding of random networks.

References

[1] J. Illian, *Statistical Analysis and Modelling of Spatial Point Patterns.* Chichester, England; Hoboken, N.J.: John Wiley, 2008, pp. 534.

[2] J. Møller and R. P. Waagepetersen, *Statistical Inference and Simulation for Spatial Point Processes.* Boca Raton, Fla.: Chapman & Hall/CRC, 2004, pp. 300.

[3] M. Franceschetti and R. Meester, *Random Networks for Communication: From Statistical Physics to Information Systems*. Cambridge University Press, 2008, pp. 216.

[4] M. Abdulla and Y. R. Shayan, "On the Influence of Terminals Spatial Location toward QoS," *The Centre for Advanced Systems and Communications Research Workshop* (*SYTACom'09*), Montréal, Québec, Canada, Apr. 28, 2009.

[5] D. Ashbrook and T. Starner, "Using GPS to Learn Significant Locations and Predict Movement Across Multiple Users," *Journal of Personal and Ubiquitous Computing*, vol. 7, no. 5, pp. 275–286, Oct. 2003.

[6] M. Abdulla, J. V. Svoboda and L. Rodrigues, "Avionics Made Simple," Dept. of Mechanical and Industrial Engineering, Concordia Univ., Montréal, Québec, Canada, 2005, pp. 173.

[7] D. Ganesan, S. Ratnasamy, H. Wang and D. Estrin, "Coping with Irregular Spatio-Temporal Sampling in Sensor Networks," In *Proc. of the 2nd Workshop on Hot Topics in Networks*, pp. 1-6, Cambridge, MA, USA, Nov. 2003.

[8] N. Eagle and A. Pentland, "Reality Mining: Sensing Complex Social Systems," *Journal of Personal and Ubiquitous Computing*, vol. 10, no. 4, pp. 255–268, May. 2006.

[9] C. Zhao and M. L. Sichitiu, "N-body: Social Based Mobility Model for Wireless Ad hoc Network Research," In *Proc. 7th IEEE SECON'10*, pp. 1-9, Boston, MA, USA, Jun. 21-25, 2010.

[10] B. Schmidt, "Human Factors in Complex Systems: The Modelling of Human Behaviour," In *Proc. of the 19th European Conference on Modelling and Simulation* (*ECMS'05*), pp.1-10, Riga, Latvia, Jun. 1-4, 2005.

[11] S. Shakkottai, R. Srikant and N. Shroff, "Unreliable Sensor Grids: Coverage, Connectivity and Diameter," In *Proc. 22nd IEEE INFOCOM'03*, pp. 1073-1083, San Francisco, CA, USA, Apr. 2003.

[12] D. J. Y. Lee and W. C. Y. Lee, "Impact of Mobile Distribution on CDMA Capacity," In *Proc. 7th IEEE PIMRC'96*, pp. 123-127, Taipei, Taiwan, Oct. 15-18, 1996.

[13] Y. Zou and K. Chakrabarty, "Sensor Deployment and Target Localization Based on Virtual Forces," In *Proc. 22nd IEEE INFOCOM'03*, pp. 1293-1303, San Francisco, CA, USA, Apr. 2003.

[14] T. Clouqueur, V. Phipatanasuphorn, P. Ramanathan and K. K. Saluja, "Sensor Deployment Strategy for Target Detection", In *Proc. ACM International Workshop on Wireless Sensor Networks and Applications* (*WSNA'02*), pp. 42-48, Atlanta, Georgia, USA, Sep. 2002.

[15] S. Tilak, N. B. Abu-Ghazaleh and W. Heinzelman, "Infrastructure Tradeoffs for Sensor Networks," In *Proc. ACM International Workshop on Wireless Sensor Networks and Applications* (*WSNA'02*), pp. 49-58, Atlanta, Georgia, USA, Sep. 2002.

[16] M. P. Lotter and P. Van Rooyen, "Modeling Spatial Aspects of Cellular CDMA/SDMA Systems," *IEEE Communications Letters,* vol. 3, no. 5, pp. 128-131, May. 1999.

[17] R. Ganesh and K. Joseph, "Effect of Non-Uniform Traffic Distributions on Performance of a Cellular CDMA System," In *Proc. of the 6th IEEE International Conference on Universal Personal Communications Record*, pp. 598-602, San Diego, CA, USA, Oct. 12-16, 1997.

[18] L. Dong, A. P. Petropulu and H. V. Poor, "A Cross-Layer Approach to Collaborative Beamforming for Wireless Ad hoc Networks," *IEEE Trans. on Signal Processing,* vol. 56, no. 7, pp. 2981-2993, Jul. 2008.

[19] Z. Bharucha and H. Haas, "The Distribution of Path Losses for Uniformly Distributed Nodes in a Circle," *Research Letters in Communications*, vol. 2008, Article ID 376895, 4 pages, 2008.

[20] P. Omiyi, H. Haas and G. Auer, "Analysis of TDD Cellular Interference Mitigation Using Busy-Bursts," *IEEE Trans. on Wireless Communications,* vol. 6, no. 7, pp. 2721-2731, Jul. 2007.

[21] S. Mukherjee, D. Avidor and K. Hartman, "Connectivity, Power, and Energy in a Multihop Cellular-Packet System," *IEEE Trans. on Vehicular Technology,* vol. 56, no. 2, pp. 818-836, Mar. 2007.

[22] H. Ochiai, P. Mitran, H. V. Poor and V. Tarokh, "Collaborative Beamforming for Distributed Wireless Ad hoc Sensor Networks," *IEEE Trans. on Signal Processing,* vol. 53, no. 11, pp. 4110-4124, Nov. 2005.

[23] H. Haas and G. J. R. Povey, "A Capacity Investigation on UTRA-TDD Utilising Underused UTRA-FDD Uplink Resources," In *Proc. IEE Colloquium on UMTS Terminals and Software Radio*, pp. 7:1-6, Glasgow, Scotland, Apr. 1999.

[24] C. Bettstetter, "On the Connectivity of Ad hoc Networks," *Computer Journal*, vol. 47, no. 4, pp. 432-447, 2004.

[25] K. Goto, T. Suzuki and T. Hattori, "Cell Size Adaptation in W-CDMA Cellular System," In *Proc. 55th IEEE VTC 2002-Spring*, pp. 444-448, Birmingham, AL, USA, May. 4-9, 2002.

[26] E. Yanmaz and O. K. Tonguz, "Location Dependent Dynamic Load Balancing," In *Proc. IEEE GLOBECOM'05*, pp. 587-591, St. Louis, MO, USA, Dec. 2005.

[27] J. Nasreddine and X. Lagrange, "Performance of TD-CDMA Systems During Crossed Slots," In *Proc. 60th IEEE VTC 2004-Fall*, pp. 798-802, Los Angeles, CA, USA, Sep. 26-29, 2004.

[28] S. Hamouda, P. Godlewski and S. Tabbane, "On Stability and Radio Capacity in UMTS System," In *Proc. IEEE International Conference on Signal Processing and Communications* (*ICSPC'07*), pp. 1299-1302, Dubai, UAE, Nov. 24-27, 2007.

[29] P. K. Jain and H. Haas, "Effects of User Distributions on CDMA System Performance," In *Proc. 16th IEEE PIMRC'05*, pp. 1652-1656, Berlin, Germany, Sep. 11-14, 2005.

[30] D. Wang, L. Xu, J. Peng and S. Robila, "Subdividing Hexagon-Clustered Wireless Sensor Networks for Power-Efficiency," In *Proc. IEEE International Conference on Communications and Mobile Computing* (*CMC'09*), pp. 454-458, Kunming, Yunnan, China, Jan. 6-8, 2009.

[31] C. Bettstetter, M. Gyarmati and U. Schilcher, "An Inhomogeneous Spatial Node Distribution and its Stochastic Properties," In *Proc. ACM MSWiM'07*, pp. 400-404, Chania, Crete Island, Greece, Oct. 22-26, 2007.

[32] U. Schilcher, M. Gyarmati, C. Bettstetter, Y. W. Chung and Y. H. Kim, "Measuring Inhomogeneity in Spatial Distributions," In *Proc. 67th IEEE VTC 2008-Spring*, pp. 2690-2694, Marina Bay, Singapore, May. 11-14, 2008.

[33] P. Xie and H. Sugimoto, "Link Capacity Analysis of a Wideband CDMA System," In *Proc. 9th IEEE PIMRC'98*, pp. 188-192, Boston, MA, USA, Sep. 8-11, 1998.

[34] M. Newton and J. Thompson, "Classification and Generation of Non-Uniform User Distributions for Cellular Multi-Hop Networks," In *Proc. IEEE ICC'06*, pp. 4549-4553, Istanbul, Turkey, Jun. 11-15, 2006.

[35] Z. Lei, D. J. Goodman and N. B. Mandayam, "Location-Dependent Other-Cell Interference and its Effect on the Uplink Capacity of a Cellular CDMA System," In *Proc. 49th IEEE VTC 1999-Spring*, pp. 2164-2168, Houston, TX, USA, May. 16-20, 1999.

[36] M. Abdulla, "Quantifying the Channel Loss of a Gaussian Random Network," *Joint Workshop on Control and Communications* (*JWCC'10*), McGill University, Montréal, Québec, Canada, May 27-28, 2010.

[37] D. Avidor and S. Mukherjee, "Hidden Issues in the Simulation of Fixed Wireless Systems," *Wireless Networks*, vol. 7, no.2, pp.187-200, Mar. 2001.

[38] G. D. Nguyen, J. E. Wieselthier and A. Ephremides, "Capture in Wireless Random-Access Networks with Multiple Destinations and a Physical Channel Model," In *Proc. IEEE MILCOM'05*, pp. 1200-1205, Atlantic City, NJ, USA, Oct. 17-20, 2005.

[39] J. Cho and Z. J. Haas, "Throughput Enhancement by Multi-hop Relaying in Cellular Radio Networks with Non-Uniform Traffic Distribution," In *Proc. 58th IEEE VTC 2003-Fall*, pp. 3065-3069, Orlando, FL, USA, Oct. 6-9, 2003.

[40] X. Liu and M. Haenggi, "Toward Quasiregular Sensor Networks: Topology Control Algorithms for Improved Energy Efficiency," *IEEE Trans. on Parallel and Distributed Systems,* vol. 17, no. 9, pp. 975-986, Sep. 2006.

[41] R. Vilzmann, J. Widmer, I. Aad and C. Hartmann, "Low-Complexity Beamforming Techniques for Wireless Multihop Networks," In *Proc. 3rd IEEE SECON'06*, pp. 489-497, Reston, VA, USA, Sep. 25-28, 2006.

[42] K. Chakrabarty and S. S. Iyengar, *Scalable Infrastructure for Distributed Sensor Networks*. Springer, 2005, pp. 194.

[43] M. F. A. Ahmed and S. A. Vorobyov, "Collaborative Beamforming for Wireless Sensor Networks with Gaussian Distributed Sensor Nodes," *IEEE Trans. on Wireless Communications,* vol. 8, no. 2, pp. 638-643, Feb. 2009.

[44] M. Leoncini, G. Resta and P. Santi, "Analysis of a Wireless Sensor Dropping Problem in Wide-Area Environmental Monitoring," In *Proc. 4th ACM/IEEE IPSN'05*, pp. 239-245, Los Angeles, CA, USA, Apr. 25-27, 2005.

[45] M. Ishizuka and M. Aida, "Achieving Power-Law Placement in Wireless Sensor Networks," In *Proc. 7th IEEE International Symposium on Autonomous Decentralized Systems* (*ISADS'05*), pp. 661-666, Chengdu, China, Apr. 4-8, 2005.

[46] "Specification of the Bluetooth System, Covered Core Package – Version 4.0" Jun. 2010.

[47] T. S. Rappaport, *Wireless Communications: Principles and Practice*. 2nd Ed. Upper Saddle River, N.J.: Prentice Hall PTR, 2002, pp. 707.

[48] A. Goldsmith, *Wireless Communications.* Cambridge, New York: Cambridge University Press, 2005, pp. 644.

[49] S. R. Saunders, *Antennas and Propagation for Wireless Communication Systems.* John Wiley & Sons Canada Ltd., 1999, pp. 426.

[50] J. S. Seybold, *Introduction to RF Propagation.* Hoboken, N.J: Wiley, 2005, pp. 352.

[51] V. Garg, *Wireless Communications and Networking.* San Francisco, CA: Morgan Kaufmann Publishers, 2007, pp. 840.

[52] IEEE 802.20 WG, "IEEE 802.20 Channel Models Document," IEEE 802.20 PD-08r1.

[53] J. G. Andrews, R. K. Ganti, M. Haenggi, N. Jindal and S. Weber, "A Primer on Spatial Modeling and Analysis in Wireless Networks," *IEEE Communications Magazine*, vol. 48, no. 11, pp. 156-163, Nov. 2010.

[54] M. Haenggi, J. G. Andrews, F. Baccelli, O. Dousse and M. Franceschetti, "Stochastic Geometry and Random Graphs for the Analysis and Design of Wireless Networks," *IEEE Journal on Selected Areas in Communications,* vol. 27, no. 7, pp. 1029-1046, Sep. 2009.

[55] P. Gupta and P. R. Kumar, "Critical Power for Asymptotic Connectivity in Wireless Networks," *Stochastic Analysis, Control, Optimization and Applications: A Volume in Honor of W. H. Fleming*, W. M. McEneaney, G. Yin, and Q. Zhang (Eds.), Birkhauser, Boston, 1998.

[56] S. Srinivasa and M. Haenggi, "Distance Distributions in Finite Uniformly Random Networks: Theory and Applications," *IEEE Trans. on Vehicular Technology*, vol. 59, no.2, pp. 940-949, Feb. 2010.

[57] M. Haenggi, "On Distances in Uniformly Random Networks," *IEEE Trans. on Information Theory*, vol. 51, no. 10, pp. 3584-3586, Oct. 2005.

[58] T. Camp, J. Boleng and V. Davies, "A Survey of Mobility Models for Ad hoc Network Research", *Wireless Communications and Mobile Computing* (*WCMC*)*: special issue on Mobile Ad hoc Networking: Research, Trends and Applications*, vol. 2, no. 5, pp. 483-502, 2002.

[59] F. Bai and A. Helmy, "A Survey of Mobility Models in Wireless Ad hoc Networks" Book Chapter in *Wireless Ad hoc and Sensor Networks*, *Springer*, Oct. 2006.

[60] D. P. Agrawal and Q. Zeng, *Introduction to Wireless and Mobile Systems.* 3rd Ed. CL-Engineering, 2010, pp. 608.

[61] M. Dohler, R. W. Heath Jr., A. Lozano, C. Papadias and R. A. Valenzuela, "Is the PHY Layer Dead?," *IEEE Communications Magazine*, vol. 49, no. 4, pp. 159-165, Apr. 2011.

[62] "IEEE Standard for Local and Metropolitan Area Networks Part 20: Air Interface for Mobile Broadband Wireless Access Systems Supporting Vehicular Mobility - Physical and Media Access Control Layer Specification," *IEEE Std. 802.20-2008,* pp. 1-1039, 2008.

[63] W. Bolton, Yang Xiao and M. Guizani, "IEEE 802.20: Mobile Broadband Wireless Access," *IEEE Wireless Communications Magazine,* vol. 14, no. 1, pp. 84-95, Feb. 2007.

[64] WiMAX Forum, "Mobile WiMAX: A Performance and Comparative Summary," Sep. 2006.

[65] A. Greenspan, M. Klerer, J. Tomcik, R. Canchi and J. Wilson, "IEEE 802.20: Mobile Broadband Wireless Access for the Twenty-First Century," *IEEE Communications Magazine,* vol. 46, no. 7, pp. 56-63, Jul. 2008.

[66] C. B. Moler, *Numerical Computing with MATLAB.* Philadelphia: Society for Industrial and Applied Mathematics, 2004, pp. 336.

[67] V. Krishnan, *Probability and Random Processes.* Hoboken, N.J.: Wiley-Interscience, 2006, pp. 723.

[68] S. R. Saunders and A. Aragón-Zavala, *Antennas and Propagation for Wireless Communication Systems*. 2nd Ed. Hoboken, N.J.: John Wiley & Sons, 2007, pp. 524.

[69] I. N. Bronshtein, *Handbook of Mathematics*. 5th Ed. New York: Springer, 2007, pp. 1159.

[70] Y. R. Shayan and M. Abdulla, "Terrestrial Wireless Communications," *Applied Vehicle Technology-Health Management for Munitions Task Group* (*AVT-160*), NATO Research and Technology Organisation (RTO), CD-ROM, Montréal, Québec , Canada , Oct. 14-16, 2008.

[71] I. F. Akyildiz, W. Su, Y. Sankarasubramaniam and E. Cayirci, "A Survey on Sensor Networks," *IEEE Communications Magazine,* vol. 40, no. 4, pp. 102-114, Aug. 2002.

[72] M. Abdulla and Y. R. Shayan, "Cellular-Based Statistical Model for Mobile Dispersion," In *Proc. of the 14th IEEE International Workshop on Computer-Aided Modeling, Analysis and Design of Communication Links and Networks* (*CAMAD'09*), pp. 1-5, Pisa, Tuscany, Italy, Jun. 12, 2009.

[73] J. C. Creput, A. Koukam, T. Lissajoux and A. Caminada, "Automatic Mesh Generation for Mobile Network Dimensioning Using Evolutionary Approach," *IEEE Trans. on Evolutionary Computation,* vol. 9, no. 1, pp. 18-30, Feb. 2005.

[74] M. Abdulla, Y. R. Shayan and J. H. Baek, "Revisiting Circular-Based Random Node Simulation," In *Proc. of the 9th IEEE International Symposium on Communication and Information Technology* (*ISCIT'09*), pp. 731-732, Incheon, South Korea, Sep. 28-30, 2009.

[75] M. Abdulla and Y. R. Shayan, "An Exact Path-Loss Density Model for Mobiles in a Cellular System," In *Proc. of the 7th ACM International Symposium on Mobility Management and Wireless Access* (*MobiWac'09*), *held in conjunction with MSWiM'09*, pp. 118-122, Tenerife, Canary Islands, Spain, Oct. 26-30, 2009.

[76] A. Papoulis and S. U. Pillai, *Probability, Random Variables, and Stochastic Processes*, 4th Ed. Boston: McGraw-Hill, 2002, pp. 852.

[77] M. Abdulla and Y. R. Shayan, "Harnessing Simultaneously the Benefits of UWB and MBWA: A Practical Scenario," In *Proc. of the 22nd IEEE Canadian Conference on Electrical and Computer Engineering* (*CCECE'09*), pp. 508-513, St. John's, Newfoundland and Labrador, Canada, May 3-6, 2009.

[78] M. Abdulla and Y. R. Shayan, “Analytical Coexistence Benchmark for Assessing the Utmost Interference Tolerated by IEEE 802.20,” *Journal of Information Processing Systems*, vol. 7, no. 1, pp. 43-52, Mar. 2011.

[79] M. Abdulla and Y. R. Shayan, “Closed-Form Path-Loss Predictor for Gaussianly Distributed Nodes,” In *Proc. of IEEE International Conference on Communications* (*ICC'10*), pp. 1-6, Cape Town, South Africa, May 23-27, 2010.

[80] T. Pering, Y. Agarwal, R. Gupta and R. Want, “Coolspots: Reducing the Power Consumption of Wireless Mobile Devices with Multiple Radio Interfaces,” In *Proc. ACM MobiSys’06*, pp. 220-232, Uppsala, Sweden, Jun. 19-22, 2006.

[81] S.-L. Wu and Y.-C. Tseng, *Wireless Ad hoc Networking: Personal-Area, Local-Area, and Sensory-Area Networks*. Auerbach Pub., 2007, pp. 664.

Appendices

Appendix A – Deriving the Differentiation of $Q\left(\left(x-A\right)/B\right)$

First, by (3.113), we express this notation in terms of the error function:

$$Q\left(\left(x-A\right)/B\right)=\left\{1-erf\left(\left(x-A\right)/\sqrt{2}B\right)\right\}\Big/2 \tag{A.1}$$

After taking the derivative of (A.1), we obtain:

$$d\left\{Q\left(\left(x-A\right)/B\right)\right\}\Big/dx=-d\left\{erf\left(\left(x-A\right)/\sqrt{2}B\right)\right\}\Big/2dx \tag{A.2}$$

In particular, the error function in (A.2) is defined as:

$$erf\left(x\right)=\left(2/\sqrt{\pi}\right)\cdot\int_{t=0}^{x}\exp\left(-t^2\right)dt \tag{A.3}$$

Meanwhile, from the fundamentals of definite integrals, we know that the differentiation with respect to the upper limit for some continuous function $f\left(x\right)$ has the following property [69, p. 443, 8.43]:

$$d\left\{\int_{t=a}^{x}f\left(t\right)dt\right\}\Big/dx=f\left(x\right) \tag{A.4}$$

With the aid of (A.4), we therefore can find the derivative of (A.3) by:

$$d\left\{erf\left(x\right)\right\}\Big/dx=2d\left\{\int_{t=0}^{x}\exp\left(-t^2\right)dt\right\}\Big/\sqrt{\pi}dx=2\exp\left(-x^2\right)\Big/\sqrt{\pi} \tag{A.5}$$

However, the derivative of the ERF in (A.2) is based on a generalized linear argument, which is obviously different from that in (A.5). Therefore, we apply the chain rule with $u=(x-A)/\sqrt{2}B$ in order to obtain:

$$\begin{aligned} d\left\{erf\left((x-A)/\sqrt{2}B\right)\right\}/dx &= \left[d\left\{erf(u)\right\}/du\right]_{u=(x-A)/\sqrt{2}B}\cdot du/dx \\ &= \left[2\exp\left(-u^2\right)/\sqrt{\pi}\right]_{u=(x-A)/\sqrt{2}B}\cdot d\left\{(x-A)/\sqrt{2}B\right\}/dx \\ &= \sqrt{2/\pi}\cdot\exp\left\{-(x-A)^2/2B^2\right\}/B \end{aligned} \tag{A.6}$$

Inserting (A.6) into (A.2) thus produces:

$$d\left\{Q\left((x-A)/B\right)\right\}/dx = -\exp\left\{-(x-A)^2/2B^2\right\}/\sqrt{2\pi}B = -\mathcal{N}_X\left(A,B^2\right) \tag{A.7}$$

Appendix B – A Hyperbolic Expression for $\exp(a)\pm\exp(b)$

First, following several manipulations, it can be demonstrated that:

$$\exp(a)\pm\exp(b) = \exp\left\{(a+b)/2\right\}\cdot\left(\exp\left\{(a-b)/2\right\}\pm\exp\left\{-(a-b)/2\right\}\right) \tag{B.1}$$

Then, from definition, the hyperbolic cosine and sine are respectively defined by $\cosh(x)=\left\{\exp(x)+\exp(-x)\right\}/2$ and $\sinh(x)=\left\{\exp(x)-\exp(-x)\right\}/2$; with this insight, we finally can express (B.1) by a more tractable arrangement, namely:

$$\exp(a)+\exp(b) = 2\cdot\exp\left\{(a+b)/2\right\}\cdot\cosh\left\{(a-b)/2\right\} \tag{B.2}$$

$$\exp(a)-\exp(b) = 2\cdot\exp\left\{(a+b)/2\right\}\cdot\sinh\left\{(a-b)/2\right\} \tag{B.3}$$